ADVANCED MATERIALS FOR SUPERCAPACITORS

EDITED BY: Wenyao Li, Min Zeng, Yuanlong Shao and Xiulin Fan
PUBLISHED IN: Frontiers in Chemistry and Frontiers in Materials

frontiers Research Topics

frontiers

ISSN 1664-8714
ISBN 978-2-88963-893-2
DOI 10.3389/978-2-88963-893-2

About Frontiers

Frontiers is more than just an open-access publisher of scholarly articles: it is a pioneering approach to the world of academia, radically improving the way scholarly research is managed. The grand vision of Frontiers is a world where all people have an equal opportunity to seek, share and generate knowledge. Frontiers provides immediate and permanent online open access to all its publications, but this alone is not enough to realize our grand goals.

Frontiers Journal Series

The Frontiers Journal Series is a multi-tier and interdisciplinary set of open-access, online journals, promising a paradigm shift from the current review, selection and dissemination processes in academic publishing. All Frontiers journals are driven by researchers for researchers; therefore, they constitute a service to the scholarly community. At the same time, the Frontiers Journal Series operates on a revolutionary invention, the tiered publishing system, initially addressing specific communities of scholars, and gradually climbing up to broader public understanding, thus serving the interests of the lay society, too.

Dedication to Quality

Each Frontiers article is a landmark of the highest quality, thanks to genuinely collaborative interactions between authors and review editors, who include some of the world's best academicians. Research must be certified by peers before entering a stream of knowledge that may eventually reach the public - and shape society; therefore, Frontiers only applies the most rigorous and unbiased reviews.
Frontiers revolutionizes research publishing by freely delivering the most outstanding research, evaluated with no bias from both the academic and social point of view. By applying the most advanced information technologies, Frontiers is catapulting scholarly publishing into a new generation.

What are Frontiers Research Topics?

Frontiers Research Topics are very popular trademarks of the Frontiers Journals Series: they are collections of at least ten articles, all centered on a particular subject. With their unique mix of varied contributions from Original Research to Review Articles, Frontiers Research Topics unify the most influential researchers, the latest key findings and historical advances in a hot research area! Find out more on how to host your own Frontiers Research Topic or contribute to one as an author by contacting the Frontiers Editorial Office: researchtopics@frontiersin.org

ADVANCED MATERIALS FOR SUPERCAPACITORS

Topic Editors:
Wenyao Li, University College London, United Kingdom
Min Zeng, Lanzhou Institute of Chemical Physics (CAS), China
Yuanlong Shao, Soochow University, China
Xiulin Fan, University of Maryland, College Park, United States

Citation: Li, W., Zeng, M., Shao, Y., Fan, X., eds. (2020). Advanced Materials for Supercapacitors. Lausanne: Frontiers Media SA. doi: 10.3389/978-2-88963-893-2

Table of Contents

05 ***Performance of Na-ion Supercapacitors Under Non-ambient Conditions—From Temperature to Magnetic Field Dependent Variation in Specific Capacitance***
Sudipta Biswas, Ananya Chowdhury and Amreesh Chandra

16 ***Biomass-Derived Porous Carbon Materials for Supercapacitor***
Hui Yang, Shewen Ye, Jiaming Zhou and Tongxiang Liang

33 ***Preparation of Flexible Substrate Electrode for Supercapacitor With High-Performance MnO_2 Stalagmite Nanorod Arrays***
Yuanyu Ge, Xianfeng Wang and Tao Zhao

39 **In situ** ***Growth of Cu_2O/CuO Nanosheets on Cu Coating Carbon Cloths as a Binder-Free Electrode for Asymmetric Supercapacitors***
Lina Xu, Jiao Li, Haibin Sun, Xue Guo, Jiakun Xu, Hua Zhang and Xiaojiao Zhang

48 ***Construction of Ultrathin Nitrogen-Doped Porous Carbon Nanospheres Coated With Polyaniline Nanorods for Asymmetric Supercapacitors***
Pingping Yu, Qunliang Wang, Lingxia Zheng and Yanfeng Jiang

59 ***Highly Ordered Mesoporous $NiCo_2O_4$ as a High Performance Anode Material for Li-Ion Batteries***
Qilong Ren, Guangyu Wu, Weinan Xing, Jiangang Han, Pingping Li, Bo Li, Junye Cheng, Shuilin Wu, Rujia Zou and Junqing Hu

66 ***Corrigendum: Highly Ordered Mesoporous $NiCo_2O_4$ as a High Performance Anode Material for Li-Ion Batteries***
Qilong Ren, Guangyu Wu, Weinan Xing, Jiangang Han, Pingping Li, Bo Li, Junye Cheng, Shuilin Wu, Rujia Zou and Junqing Hu

67 ***Liquid Phase Exfoliated Hexagonal Boron Nitride/Graphene Heterostructure Based Electrode Toward Asymmetric Supercapacitor Application***
Xuan Zheng, Guangjin Wang, Fei Huang, Hai Liu, Chunli Gong, Sheng Wen, Yuanqiang Hu, Genwen Zheng and Dongchu Chen

76 ***Facile Synthesis of Novel $V_{0.13}Mo_{0.87}O_{2.935}$ Nanowires With High-Rate Supercapacitive Performance***
Haishun Jiang, Wenjing Sun, Wenyao Li, Zhe Wang, Xiying Zhou, Zexing Wu and Jinbo Bai

83 ***Fabrication and Electrochemical Performance of Al-Doped ZnO Nanosheets on Graphene-Based Flexible Substrates***
Qi Yu, Ping Rong, Shuai Ren, Liyun Jiang and Yapeng Li

89 ***Three-Dimensional Graphene-Based Composite Hydrogel Materials for Flexible Supercapacitor Electrodes***
Enping Lai, Xinxia Yue, Wan'e Ning, Jiwei Huang, Xinlong Ling and Haitao Lin

94 ***Capacity Contribution Induced by Pseudo-Capacitance Adsorption Mechanism of Anode Carbonaceous Materials Applied in Potassium-ion Battery***
Jiahao Liu, Ziqiang Xu, Mengqiang Wu, Yuesheng Wang and Zaghib Karim

100 ***N-Propyl-N-Methylpyrrolidinium Difluoro(oxalato)borate as a Novel Electrolyte for High-Voltage Supercapacitor***
Weili Zhang, Fuming Zhang, Peng Zhang, Shuo Liang and Zhiqiang Shi

108 ***Hollow Co_3O_4@MnO_2 Cubic Derived From ZIF-67@Mn-ZIF as Electrode Materials for Supercapacitors***
Jiani Xu, Chaoting Xu, Yanhong Zhao, Jianghong Wu and Junqing Hu

114 ***Nitrogen and Phosphorus Co-doped Porous Carbon for High-Performance Supercapacitors***
Jiaming Zhou, Shewen Ye, Qinqin Zeng, Hui Yang, Jiahao Chen, Ziting Guo, Honghui Jiang and Karthikeyan Rajan

frontiers in Materials

ORIGINAL RESEARCH
published: 09 April 2019
doi: 10.3389/fmats.2019.00054

Performance of Na-ion Supercapacitors Under Non-ambient Conditions—From Temperature to Magnetic Field Dependent Variation in Specific Capacitance

*Sudipta Biswas, Ananya Chowdhury and Amreesh Chandra**

Department of Physics, Indian Institute of Technology Kharagpur, Kharagpur, India

Single phase $NaFePO_4$ can works as economically viable cathode material for Na-systems similar to $LiFePO_4$–a material that led to the commercialization of Li-ion based energy systems. The reported microstructures of hollow $NaFePO_4$ particles, with porous walls, establish their advantages over solid morphologies. The hollow structures deliver stable electrochemical specific capacitance of 115 F g^{-1} in 2 M NaOH electrolyte, over a large number of cycles. This observation is directly attributed to the increased surface area, transport channels and redox sites, which become available in the porous-hollow particles. Hitherto unreported electrochemical performance under non-ambient environment is also discussed. In contrast to recently reported in Fe-based metal oxides, where significant change in specific capacitance has been reported as a function of magnetic field, it is observed that $NaFePO_4$ can protect itself and suppress modifications. More importantly, $NaFePO_4$ can work as an efficient electrode material in the temperature range RT to 65°C, which makes it useful for automotive industry.

Keywords: electrochemical, non-ambient conditions, hollow structure, energy storage, supercapacitor

OPEN ACCESS

Edited by:
Yuanlong Shao,
King Abdullah University of Science and Technology, Saudi Arabia

Reviewed by:
Liang Zhou,
Wuhan University of Technology, China
Wei Kong Pang,
University of Wollongong, Australia

****Correspondence:***
Amreesh Chandra
achandra@phy.iitkgp.ac.in

Specialty section:
This article was submitted to Energy Materials, a section of the journal Frontiers in Materials

Received: *15 January 2019*
Accepted: *18 March 2019*
Published: *09 April 2019*

Citation:
Biswas S, Chowdhury A and Chandra A (2019) Performance of Na-ion Supercapacitors Under Non-ambient Conditions—From Temperature to Magnetic Field Dependent Variation in Specific Capacitance. Front. Mater. 6:54. doi: 10.3389/fmats.2019.00054

INTRODUCTION

The rapidly expanding consumer market of mobile and wearable electronics is driving the research for supplementary energy storage systems, which can complement or even compete with Li-ion technologies. A recent statistical study has predicted that the energy storage capacity required only by mobile technologies like phone, tablets and laptops will be more than 25 GW h by 2025[1]. For the major part of the last 4 decades, Na-ion based energy storage systems remained under the shadow of their more illustrious counterparts based on Li-ion (Zhao et al., 2011). Infact, careful examination of literature shows that Na-ion energy storage systems (ESS) were actually investigated before Li-ion technologies. In 1960s, Kummer and Weber of Ford Motor Co extensively investigated β-Al_2O_3 Na^+ion conducting solid electrolyte based battery, which eventually led to the development of sodium/sulfur technologies[2]. Even after large-scale commercialization of Li-batteries, it was always known that sodium, with similar oxidation state and electronic configuration, can deliver characteristics similar Li^+ based energy storage devices. The re-emergence of interests in Na-ion energy storage devices is also linked to the constraints associated with most Li-ion based materials/technologies (Zhang et al., 2017). These range from

[1]http://energystorage.org/system/files/attachments/esa_vision_2025_final.pdf 06-09-2018
[2]https://patentimages.storage.googleapis.com/1a/51/27/63e4b6a1229db4/US3413150.pdf 06-09-2018

geo-economical/political, availability, increasing demand, environmental impacts, and countering the IP protection.

The primary reason, which restricted the use of Na-ion based technologies, was the limited number of materials that could handle the chemistry of bigger ion like Na^+. The growing understanding and expertise to develop novel nanoparticles ranging from solid, hierarchical to hollow, has allowed the resurgence of Na-ion based energy storage systems (Yabuuchi et al., 2014; Fang et al., 2015; de la Llave et al., 2016; Guo et al., 2016; Wang et al., 2019; Zhu et al., 2019). Different sodium based materials viz. $Na_4Ti_5O_{12}$, $NaTiO_2$, $Na_2Ti_3O_7$, $Na_3V_2(PO_4)_3$, $Na_4Fe(CN)_6$, $NaVO_2$, etc., are now being investigated (Didier et al., 2011; Yin et al., 2012; Li et al., 2015; Guo et al., 2016),(Jiang et al., 2016).

It is well known that the discovery and fabrication of $LiFePO_4$ led to rapid commercialization of the Li-ion batteries (Liang et al., 2015). Similar to it, $NaFePO_4$ has been suggested as a promising cathode material for Na-ion batteries (Liu et al., 2018). The major problem associated with this material is related to the difficulty of synthesizing it in single phase. Recently, there have been reports that have presented synthesis protocols, which have led to single phase $NaFePO_4$ with simple morphologies and broad particle size

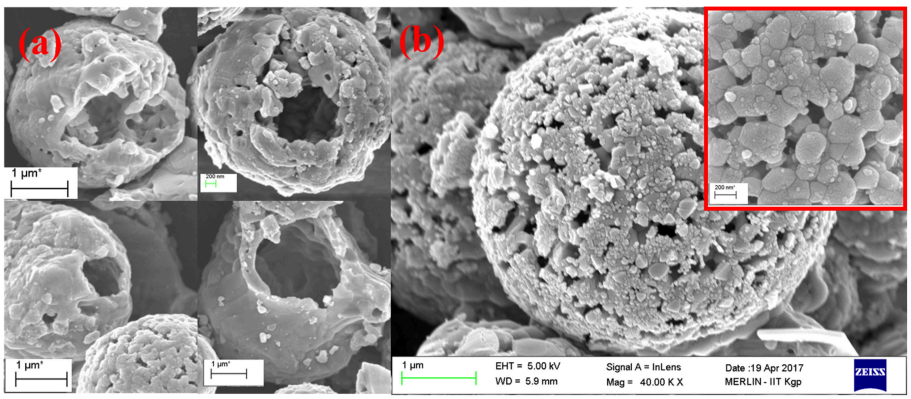

FIGURE 1 | (a) SEM image showing uniform microsphere, **(b)** SEM confirms porous and hollow structure.

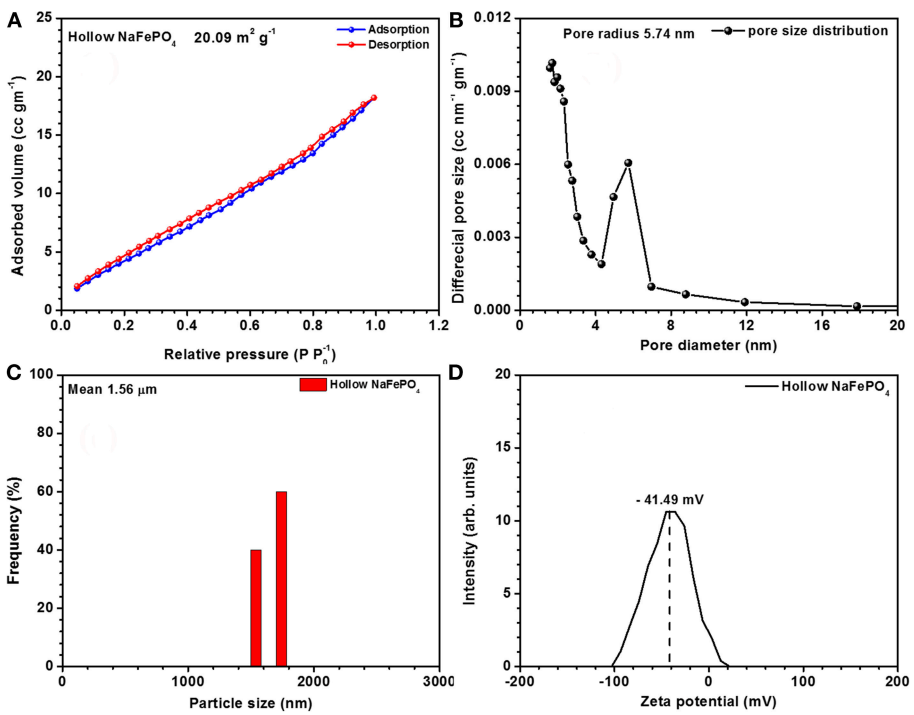

FIGURE 2 | (A) Adsorption-desorption isotherm curves, **(B)** pore size distribution curves, **(C)** particle size distribution, and **(D)** zeta potential curves of hollow $NaFePO_4$.

distributions (Minakshi et al., 2016; Rahman et al., 2017). The electrochemical response of these particles has been investigated only in batteries (Park et al., 2013; Slater et al., 2013). Typical energy densities that have been reported are ∼210–600 W h kg^{-1}. Intriguingly, its capacitive behavior remains ignored or mostly limited (Lu et al., 2015; Lim et al., 2016; Zhang et al., 2017; Ramakrishnan et al., 2018). For application in supercapacitors, tuning of morphology, surface area, pore size/dimension, and redox sites becomes essential.

In this paper, it is established that $NaFePO_4$ can also be used as efficient electrode material in supercapacitors, provided the morphology is carefully tuned. The results clearly prove that the hollow particles of $NaFePO_4$ have much higher capacitive behavior, in comparison to the solid counterparts. Superior performance of hollow structures can be attributed to the availability of more channels/sites for redox activities, while the enhanced surface area enforces increased contribution from the pseudo-capacitance (Sharma et al., 2018c).

Unlike the common strategy of reporting the supercapacitor response only at ambient conditions, the paper also discusses the behavior under non-ambient conditions. It is observed that $NaFePO_4$ can be easily used at elevated temperatures, which is essential if they are to be utilized in hybrid vehicles. The specific capacitance remains nearly same, even when the operating temperature is increased from RT to 65°C. Infact, slight increase in the specific capacitance is observed at elevated temperatures. The observation can be explained in terms of improved diffusion and accessibility of inner core for electrolyte ions insertion/de-insertion.

Very recently, few papers have indicated that Fe-based metal oxides used in supercapacitors will have to thoroughly re-characterized near magnetic field. Significant variation in specific capacitance can occur in such oxides as a function of varying dc-magnetic field, owing to modulated electron flow caused by the Lorentz force (Sharma et al., 2018a). It is demonstrated here that $NaFePO_4$ does show variation under magnetic field but the changes are much lower than that observed in pure Fe_2O_3. Therefore, $NaFePO_4$ based Na-ion capacitors can also be used near magnetic without disturbing the associated electronic circuitry.

EXPERIMENTAL

Material Used

Ferric nitrate nonahydrate ($Fe(NO_3)_3$, $9H_2O$), stearic acid, ammonium dihydrogen phosphate ($(NH_4)H_2PO_4$), tri-sodium citrate di-hydrate ($Na_3C_6H_5O_7$, $2H_2O$), citric acid, ethylene glycol, and sodium nitrate ($NaNO_3$) were procured from LobaChemie Pvt. Ltd. (India) and MerckSpecialities Pvt. Ltd. (India). All the analytical grade precursors were used directly without further purification.

Material Synthesis

Synthesis of Hollow and Porous structures

Porous and hollow $NaFePO_4$ microstructures were synthesized using one pot facile hydrothermal route followed by calcination in air. In a typical experimental procedure, 25 ml of 0.1 M ferric nitrate solution was mixed with 25 ml of 0.1 M stearic acid

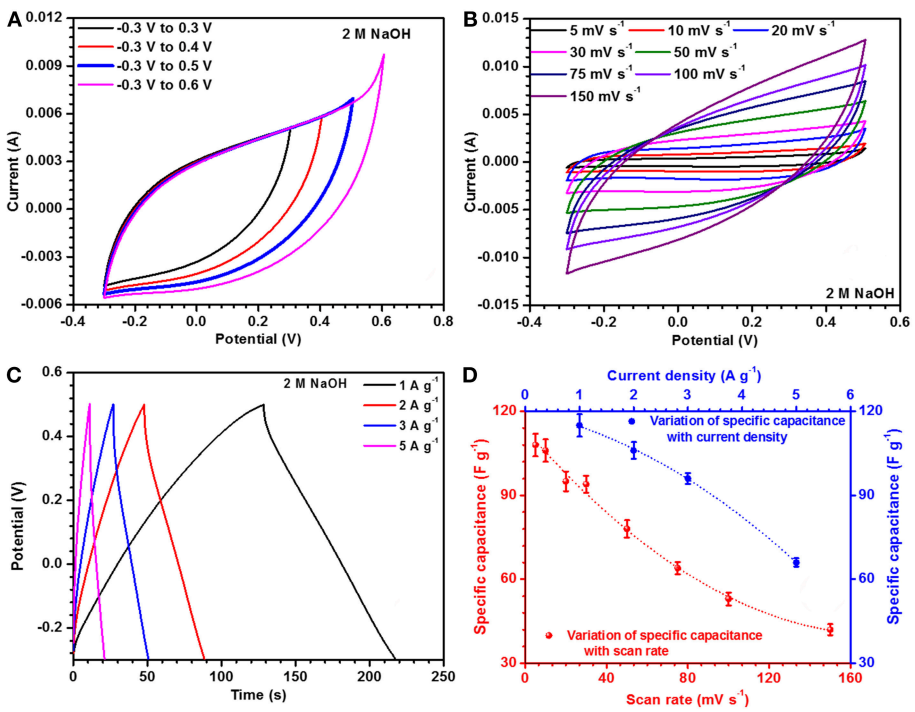

FIGURE 3 | (A) Window optimization, **(B)** CV profiles, **(C)** CD profiles, and **(D)** change in specific capacitance with scan rate and current density of hollow and porous $NaFePO_4$ in 2 M NaOH electrolyte.

solution. Subsequently, 245.1 mg trisodium citrate ($Na_3C_6H_5O_7$, $2H_2O$) was added and the solution was stirred for 2 h. Appropriate amount of ammonium dihydrogen phosphate ($(NH_4)H_2PO_4$) was added to the precursor solution so as to ensure Na:Fe:PO_4 concentration ratio was 1:1:1. 50 ml of this yellow colored solution was then transferred to a teflon-lined stainless steel (capacity 250 ml) autoclave. The autoclave was kept at 180°C for 24 h, before allowing it to slowly cool down to the room temperature. The precipitate was collected by centrifugation at 3,200 rpm. The precipitate was subsequentially washed three times using de-ionized water and dried overnight in a vacuum oven at 70°C. Dried sample was crushed and annealed at 600°C for 4 h in air to obtain hollow $NaFePO_4$ powder. To compare the performance of these hollow microstructures, solid nanoparticles of $NaFePO_4$ were also prepared. The corresponding synthesis protocol is given in the **Supplementary Information**.

Material Characterization

The phase formation of $NaFePO_4$ was confirmed by analyzing powder X-ray diffraction (XRD) profile obtained using a Rigaku MiniFlex600 diffractometer with Cu-Kα ($\lambda = 0.15406$ nm) as the incident wavelength.

For surface and particle morphological studies, both scanning and transmission electron micrographs were collected. For SEM data, CARL ZEISS SUPRA 40 SEM was used, while the TEM data were obtained utilizing a TEM FEI-TECHNAI G220S-Twin microscope operated at 200 kV. Brunauer-Emmett-Teller (BET) surface area and porosity were determined with a Quantachrome Nova Touch surface area and pore size analyzer. Zeta potential and particle size distribution were inferred by analyzing the DLS data obtained from a Horiba Scientific Nano Particle Analyzer SZ-100.

TABLE 1 | Specific capacitance of hollow and porous $NaFePO_4$ form CV curves in 2M NaOH electrolyte.

Scan Rate (mV s^{-1})	Specific Capacitance (F g^{-1})
5	108
10	106
20	95
30	94
50	78
75	64
100	53
150	42

TABLE 2 | Specific capacitance of hollow and porous $NaFePO_4$ form CD curves in 2M NaOH electrolyte.

Current Density (A g^{-1})	Specific capacitance (F g^{-1})
1	115
2	106
3	96
5	66

FTIR measurements were performed using Nexus 870 instrument in the range of 500–1,400 cm^{-1}. The spectrum was acquired in transmittance mode with a resolution of 1 cm^{-1}.

For the electrochemical characterization of the synthesized materials and fabricated devices, typical cyclic voltammetry (CV), and galvanostatic charge-discharge (GCD) were performed using the MetrohmAutolab (PGSTAT302N) potentiostat-galvanostat. The measurements were undertaken both in three- and two-electrode configurations, using an aqueous electrolyte. For impedance data of the electrochemical systems, in the frequency range of 50 mHz to 1 MHz, a N4L-PSM 1735 impedance analyzer was used.

Electrode Preparation and Electrochemical Characterization

A slurry was prepared by mixing 80 wt % active material, 10 wt % activated charcoal, and 10 wt % polyvinylidenefluoride-co-hexafluoropropylene (PVDF- HMP) using N-Methyl-2-pyrrolidone as the mixing media. All electrochemical measurements were performed in 1 M Na_2SO_4, 1 M $NaNO_3$, and 1 M NaOH electrolyte solutions, which allowed determination of an optimum electrolyte. Best performance was observed in NaOH and the corresponding results are presented in the paper. Platinum wire and Ag/AgCl/3.0 M KCl were used as the counter and reference electrodes, respectively.

RESULT AND DISCUSSION

It is now well established that, for useful electrochemically active materials, parameters such as: phase, particle morphology/size along with the nature of pores and pore-size/volume are critical (Singh and Chandra, 2015; Akhtar et al., 2016; Sharma et al., 2018b). The XRD plot obtained shown in **Figure S1** could be indexed using the *Pnmb* space group of $NaFePO_4$ following the JCPDS card no. 04-012-9665 (Kosova et al., 2014). XRD pattern for solid particle are shown in **Figure S2**.

Figures 1a,b shows the SEM micrographs of $NaFePO_4$ observed at various magnifications. It is clear that particles, with a cavity in the middle were stabilizing. Recently, hollow nanostructures of metal oxides have been suggested as electrode materials for next generation supercapacitors (Sharma et al., 2018b; Wei et al., 2018). Till date, there have been no reports, which have suggested formation of hollow $NaFePO_4$ particles/microspheres. The size of the synthesized $NaFePO_4$ microspheres varied in the range 1–3 μm. The micrographs also indicated that the wall surface of the hollow microspheres was not solid but porous. This can be an additional advantage of such particles because all the desired parameters i.e., surface area, pores, and transport channels, will be able to contribute in the final electrochemical reactions and/or specific capacitance. The particle growth mechanism is discussed in the supporting evidence (see **Figure S3**). The growth process was found to be a convoluted picture of reaction as well as diffusion kinetics. Corresponding SEM micrographs for solid $NaFePO_4$ structures are shown in **Figure S4** (see Supplementary Information).

The corresponding TEM images of the microspheres are given in supporting evidence (**Figure S5**). The associated elemental mapping and EDAX data for the $NaFePO_4$ microspheres are also described in the supporting evidence (**Figure S6**). The atomic ratio of Na:Fe:P:O was found to be 1.05:1:1.08:3.57, which confirmed the formation of $NaFePO_4$ with nominal composition and homogeneous distribution of the elements throughout the sample.

The surface area, pore size/volume and particle size distribution values are shown in **Figures 2A–D**. The BET adsorption-desorption curves showed typical type IV isotherms, indicating slit shaped mesopores of ∼6 nm. BET surface area was 20 m^2 g^{-1}.

Zeta potential denotes the electro kinetic potential in colloidal dispersions. In any chemical reaction, electro-positivity of the surface is determined by the overall pH of the solution. In the present studies, hollow nanostructures returned higher electro-positivity. This can only happen when there is an increased capacity to facilitate OH^- accommodation. This phenomenon helps to attract ions toward surface and hence increases the capacitance of the material. The surface charge (zeta potential) was −41.49 mV, as shown in **Figure 2D**.

It has been demonstrated that vibrational spectroscopy is very useful for probing fundamental sodium ion intercalation in a variety of crystalline sodium based electrode materials (Sharma et al., 2018c). The FTIR spectra of $NaFePO_4$ showed symmetric, asymmetric vibration as well as bending modes. The absorption bands at 1,009, 1,068, and 1,133 cm^{-1}, shown in the **Figure S7a**, could be assigned to the ν_3 type asymmetric stretching modes between P-O in PO_4^{3-}. The $\nu_1$modes near 980 and 947 cm^{-1} are attributed to the PO_4^{3-} intramolecular symmetric stretching vibrations (Sharma et al., 2018b). The asymmetric bending modes of the PO_4^{3-} anion, assigned as ν_4, were observed at 629, 577, and 540 cm^{-1} (see **Figure S7b**).

Before starting exhaustive electrochemical characterizations, it is critical to optimize the operating potential window. CV studies were performed at a scan rate of 50 mV s^{-1} in three different aqueous electrolytes viz., 1 M Na_2SO_4, $NaNO_3$, and NaOH. The mass of the electrode was kept at ∼1 mg. The observed CV curves in different voltage windows are shown in **Figures S8a–c**. The analysis clearly indicated that the electrolytes: Na_2SO_4 and $NaNO_3$ provided an electrochemical window ranging from −0.2 to 0.7 V. By using NaOH as electrolyte, voltage window of −0.3 to 0.5 V could be obtained. The CV curves as a function of varying scan rates, in the respective stabilized operational potential windows for the three electrolytes are shown in **Figures S8d–f**. After studying the electrochemical behavior of the hollow $NaFePO_4$ in three different electrolytes, NaOH was found to return the highest specific capacitance.

The estimated specific capacitance, with varying scan rates, is tabulated in **Table S1**. As expected, the specific capacitance showed appreciable dependence of the scan rates. The maximum specific capacitance, at 5 mV s^{-1} scan rate, was ∼75 F g^{-1} when 1 M NaOH electrolyte was used. When scan rate increased to 150 mV s^{-1} it was 20 F g^{-1}. The capacitance retention was found to be only ∼29%, when the scan rate was enhanced by 30 times.

The capacity to deliver the power of a commercial supercapacitor is obtained by the values of specific capacitance measured in galvanostatic charge discharge (CD) curves. The CD curves for the working electrode, in three different electrolytes are shown in **Figures S8g–i**.

The specific capacitance values, at different current densities, in three different electrolytes are listed in **Table S2**. The maximum capacitance of 87 F g^{-1} was obtained by using NaOH as electrolyte, which corroborated the results obtained from CV measurements. At higher specific currents, the specific capacitance decreased. This happens due to the underutilization of bulk capacitance, which is a normal behavior for supercapacitor electrode materials. At higher specific currents, the transfer of electrons toward the electrode is faster and hence the increase of potential would be higher. Consequently, the electrode gets reduced time to stay at a certain voltage and lower specific capacitance value is observed.

The electrolyte concentration has major effect on the electrochemical performance of an electrode material and is linked to the material's storage capacity. In the present case, the optimized concentration was found to be ∼ 2 M (NaOH). Operational window of the material was rechecked in 2 M NaOH and corresponding data is shown in **Figure 3A**. CV curves, at different scan rates, were collected in 2 M NaOH electrolyte and are shown in **Figure 3B**. Maximum specific capacitance was found to be 108 F g^{-1} at a scan rate of 5 mV s^{-1}. In the same potential window, CD profiles were also collected at different current densities. These are depicted in **Figure 3C**. The maximum specific capacitance in this case was found to be ∼115 F g^{-1} at 1 A g^{-1}. The specific capacitance values for the porous and hollow $NaFePO_4$, utilizing 2 M NaOH as electrolyte, at different scan rates and current densities are listed in **Tables 1**, **2**, respectively and corresponding graphs are shown in **Figure 3D**. It was also observed that the hollow structure based electrodes showed higher capacitance retention ability.

The performance of hollow structures was compared with that of $NaFePO_4$ solid particles. From the CV analysis, the maximum specific capacitance of 48 F g^{-1} was observed in the case of solid particles. The CD profiles gave the specific capacitance to be 81 F g^{-1}. Clearly, the hollow structures had much higher performance. The advantages of both outer/inner surfaces, low diffusion length, high availability of surface adsorption sites due to the hollow cavity of the particles would drive this enhanced performance. The CV and CD curves for solid structures are shown in **Figure S9** and the corresponding specific capacitance values are given in **Tables S3**, **S4**, respectively.

Cyclic stability of an electrode is one of the important property that decides its industrial application. In the present case, 93.7% of capacity retention was found after 1,500 cycles for hollow microsphere [see **Figure 4A**]. Solid structures also showed similar capacity retention after 1,500 cycles. This can be expected because the redox reactions would be similar as the chemical formula or composition was not varying as a function of particle morphology. The advantages rendered by hollow particles was leading to higher specific capacitance. Hollow and solid structures had BET surface areas of 20 and 6 m^2 g^{-1}, respectively. Hollow structures, with pore radius

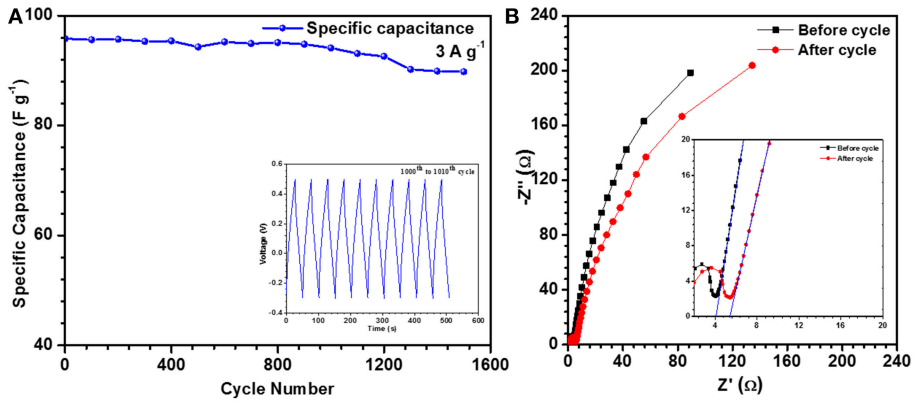

FIGURE 4 | (A) Cycling test for $NaFePO_4$ electrode and CD from 1,001 to 1,010 cycle (inset) and **(B)** EIS of hollow $NaFePO_4$.

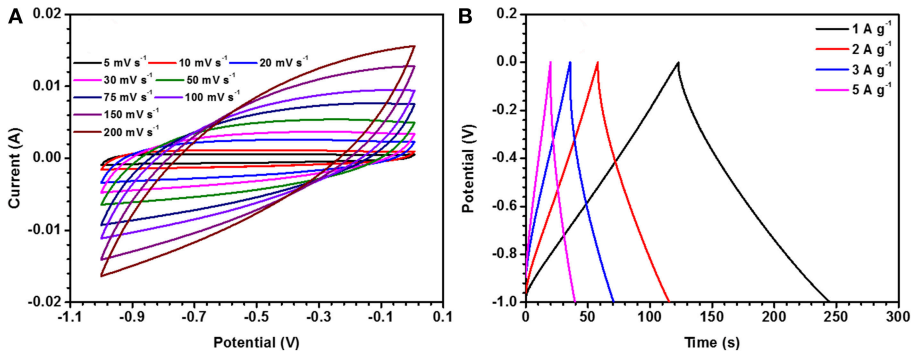

FIGURE 5 | (A) CV and **(B)** CD profiles for three electrode measurements of activated carbon (AC).

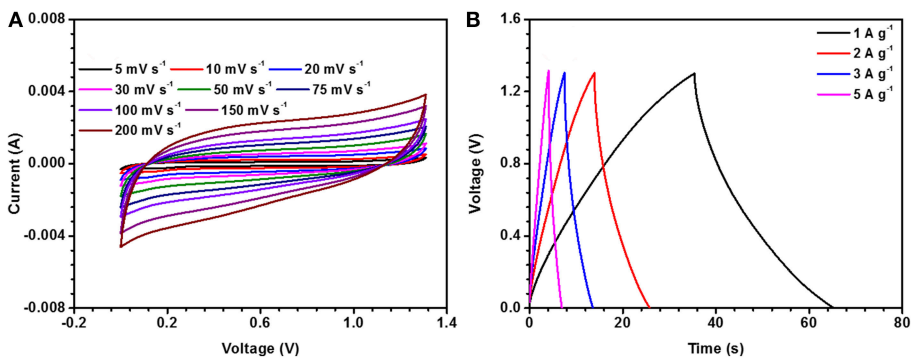

FIGURE 6 | (A) CV and **(B)** CD profiles of $NaFePO_4$//AC device at room temperature (25°C).

∼5.7 nm, would also allow better intercalation/ de-intercalation of electrolyte ions than the solid particles that showed pores of ∼1.7 nm radius. The surface area, pore size/volume, particle size distribution, and zeta potential of solid particles are depicted in **Figures S10a–d**.

The charge transport kinetics of the electrode was studied by the analysis of electrochemical impedance spectroscopy (EIS) data. Nyquist plots give the information about electrode-electrolyte interactions and equivalent series resistance (ESR). The ESR values for hollow microsphere and solid nanostructures were ∼4.0 Ω (**Figure 4B**) and ∼6.6 Ω (**Figure S11**), respectively. This indicated low charge transfer resistance at the working electrode and electrolyte interface in the case of hollow structures. Capacity retention for

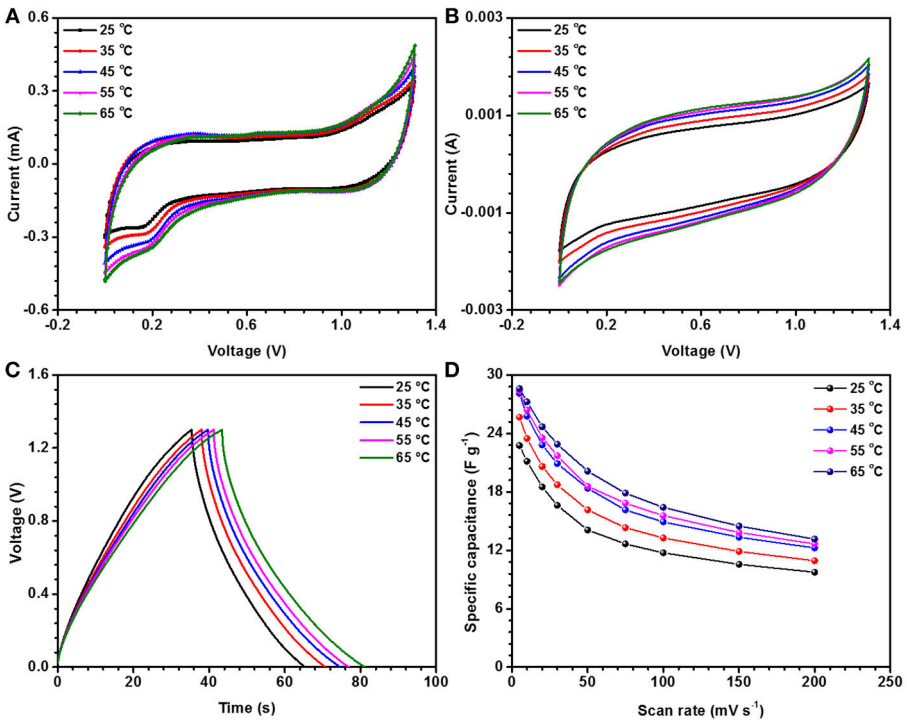

FIGURE 7 | CV measurements at different temperature for the device **(A)** at 5 mV s^{-1} and **(B)** at 50 mV s^{-1}, **(C)** CD measurements for $NaFePO_4$//AC device at different temperature, and **(D)** variation of specific capacitance with scan rate.

TABLE 3 | Values of specific capacitance at different scan rates at different temperature (screw cell device).

Scan rate (mV s^{-1})	Specific capacitance (F g^{-1})				
	Room temperature (25°C)	35°C	45°C	55°C	65°C
5	23	26	28	28	29
10	22	23	26	26	27
20	18	21	23	24	25
30	16	19	21	22	23
50	14	16	18	19	20
75	13	14	16	17	18
100	12	13	15	16	16
150	11	11	13	14	15
200	10	11	12	13	13

TABLE 4 | Values of specific capacitance at different current densities at different temperature (screw cell device).

Current Density (A g^{-1})	Specific capacitance (F g^{-1})				
	25°C (RT)	35°C	45°C	55°C	65°C
1	23	26	28	29	29
2	20	22	23	24	26
3	15	17	18	20	22
5	12	14	13	16	16

TABLE 5 | Values of resistance at different temperature.

Temperature (° C)	Resistance (Ω)
Room temperature (25)	7.63
35	7.49
45	7.30
55	6.94
65	6.52

hollow structures can be justified by the ESR measurements. The values of ESR increased from ∼4.0 to 5.4 Ω, in case of hollow $NaFePO_4$. This increment in the ESR values can be attributed to the electrode degradation and reduction in the available ion channels within the materials as a function of cycling. It is clear from the lower frequency regions in **Figure 4B**, that the capacitive behavior was lower in case of hollow structures.

Supercapacitor coin cell type device was fabricated using activated carbon as the negative and $NaFePO_4$ as the positive electrode. Activated carbon was tested in three-electrode configuration before making the device. **Figures 5A,B** shows the cyclic voltametric curves at different scan rates from 5 to 200 mV s^{-1} and charge discharge at different current density from 0.5 to 5 A g^{-1}. From the CV results, the working electrochemical window was found to be −1 to 0 V.

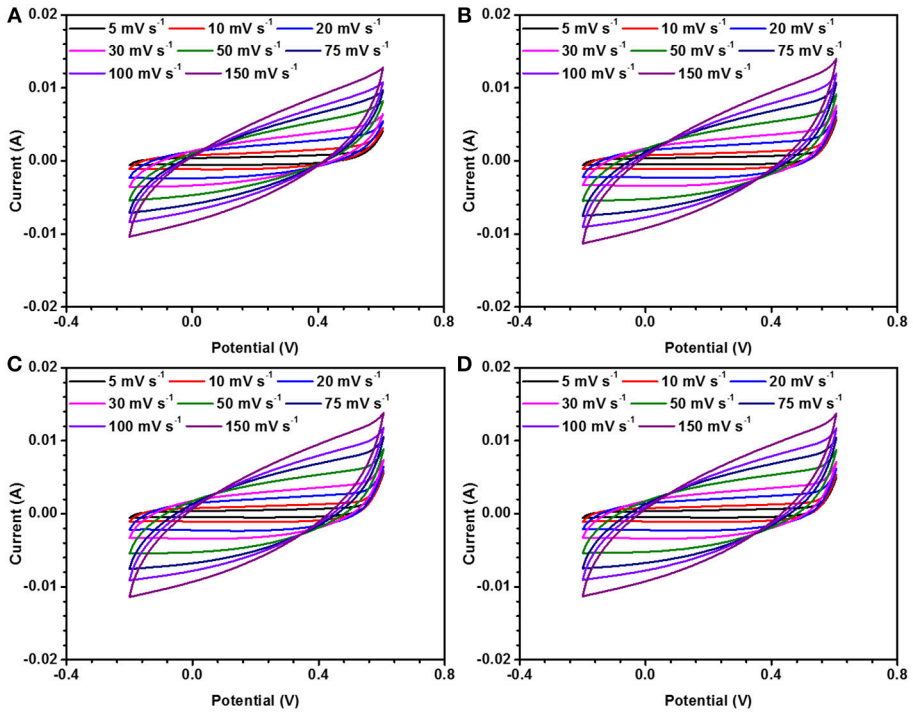

FIGURE 8 | CD measurements in three electrode set up for $NaFePO_4$ at **(A)** 0, **(B)** 10, **(C)** 20, and **(D)** 30 gauss magnetic field.

TABLE 6 | Values of specific capacitance at different scan rate under varying magnetic field (in three electrode configuration).

Scan rate (mV s^{-1})	Specific capacitance (F g^{-1})			
	No field	10 gauss	20 gauss	30 gauss
5	109	120	123	124
10	108	120	122	123
20	99	119	120	121
30	86	109	113	113
50	65	87	91	91
75	51	68	71	78
100	43	56	58	58
150	34	43	44	44

Highest specific capacitance observed from the CV measurement was 120 F g^{-1}, at a scan rate 5 mV s^{-1}. Using charge-discharge measurements, it was estimated as 126 F g^{-1} at current density of 1 A g^{-1}. Specific capacitance values from CV and CD for activated carbon are shown in **Tables S5**, **S6**, respectively.

Fabrication of asymmetric supercapacitor device needs charge balancing of the electrode materials. The optimal charge balance condition was estimated using the mass balance formula:

$$\frac{m_+}{m_-} = \frac{V_- C_-}{V_+ C_+} \quad (1)$$

where C_- and C_+ are the capacitances (in F g^{-1}) measured at the same scan rate, using the three electrode system, for negative and positive electrodes, respectively while ΔV_+ and ΔV_- denote the working potential window for the positive and negative electrodes, respectively. The required mass ratio for positive and negative electrode materials (m_+/m_-) was thus estimated as 1.5 at 5 mV s^{-1}.

Figure 6 shows the cyclic voltammetry and charge discharge curves for device. Whatman glass fiber paper was used as separator (pre-soaked in electrolyte) and 2 M NaOH was used as aqueous electrolyte. The electrochemical voltage window was found to be from 0 to 1.3 V. No H_2/O_2 evolution was discernible in this voltage window. From the CV measurements, maximum specific capacitance for the $NaFePO_4$//AC device was ~22 F g^{-1}. The device performance was found to decrease at higher scan rate, as a result of under-utilization bulk of the material. The maximum specific capacitance observed from CD was 23 F g^{-1}. Nearly linear charge discharge curves showed the dominance of the electric double layer capacitance (EDLC) in the device.

In most of the applications, there are few additional parameters, which contribute in determining the final electrochemical performance. These include: temperature, external frequency, magnetic field, etc., (Ramakrishnan et al., 2018; Sharma et al., 2018a). Till date, such studies have remained ignored in the Na-ion based supercapacitors. Given below are the performance of the $NaFePO_4$ based supercapacitors under variable temperature and magnetic field.

It has been suggested that, at elevated temperatures, contributions from additional factors such as ion conductivity, solubility limits, viscosity, thermal stability, etc., cannot be ignored. For investigating the thermal stability, the device was slowly heated at increments of 10°C. The device was equilibrated for 30 min at a given temperature before the electrochemical measurements were performed. As presented above, the specific capacitance in $NaFePO_4$ based screw cell type asymmetric device was ∼23 F g^{-1}. The CV and CD curves, with increasing temperature, are shown in **Figures S12**, **S13**. CV curves with increasing temperature at a scan rate of 5 and 50 mV s^{-1} are shown in **Figures 7A,B**, respectively. Comparison of charge discharge curve at 1 A g^{-1} with increase in temperature and variation of specific capacitance with scan rate is shown in **Figures 7C,D**, respectively. Clear signature was obtained, which suggested increase in the specific capacitance with increasing temperature. At 65°C, the specific capacitance increased to 29 F g^{-1}, which was nearly 25% higher than the value obtained at room temperature. Additionally, the device continued to show the characteristics expected from a capacitive system. The corresponding values of specific capacitance from CV and CD analysis are listed in **Tables 3**, **4**, respectively. The intrinsic internal resistance decreased with increasing temperature and the values are given in **Table 5**.

On comparing with literature dealing with elevated temperature behavior in supercapacitors fabricated using metal oxides, it was interesting to note that the Na-ion based device showed much lower variation as a function of temperature. This can be directly correlated with the fact that the olivine structures show much lower thermal expansion than the other relevant metal oxides. Therefore, change of ∼50°C will not lead to appreciable change in the surface area or pore structure in the $NaFePO_4$ particles. It is known that, with increasing temperature, the reaction kinetics increases. Therefore, in the Na-based olivines, the increase in specific capacitance with increasing temperature will only be dominated by the enhanced electrochemical reactions near the electrolyte-electrode interface, which will vary too much in the temperature window of ∼40°C.

It has been very recently reported that electrode materials based on ferromagentic ions may have to revisited because devices fabricated using them can have appreciable effect under/near variable magnetic field. $NaFePO_4$ also has Fe, which is a well-known ferromagnetic atom. The magnetic field dependent studies in $NaFePO_4$, while it is being used as an electrode material in storage device, has never been reported. Cyclic voltammetry (CV) and galvanostatic charge-discharge (CD) measurements were performed under varying magnetic fields (B = 0, 10, 20, and 30 gauss). CV curves at different scan rate and at different current densities under varying magnetic fields (B = 0, 10, 20, and 30 gauss) are shown in **Figure 8** and **Figure S14**. Schematic of experimental arrangement for performing the magnetic field dependent measurements is shown in **Figure S15** of the supplementary information. The calculated specific capacitance values are listed in **Table 5**. It was clear that the specific capacitance showed an increasing trend, with increasing magnetic field. On reaching the magnetic field of 30 gauss, the specific capacitance at 5 mV s^{-1} increased to 124 F g^{-1} from 109 F g^{-1}, which was observed at 0 Gauss. This corresponded to a mere 14% change. Additionally, no change was observed even by further increasing the magnetic field. In comparison, nearly 75% increase has been reported in Fe_2O_3 or MnO_2. So, $NaFePO_4$ clearly showed stability near magnetic field, which would make this material even more important for industrial use. The values of specific capacitance at different scan rates is shown in **Table 6** and corresponding specific capacitance values from charge discharge is shown in **Table S7**.

One of the reasons behind the increase in capacitance response in magnetic field is magneto hydrodynamic (MHD) effect. This increases the magnetic current in the system because of the feedback mechanism and increase in vigorous hydrodynamic stirring. Further, the change of electronic energy state due to the applied magnetic field may also improve the performance of electrode material. The suppressed magnetic field dependence can be easily explained if we examine the expected valence state of the elements in $NaFePO_4$. Fe is expected to be in a +2 state, which is known to be non-magnetic. If magnetism has to be induced in it then large magnetic field has to be applied as per the Van Vleck paramagnets (Smolenski et al., 2016). Additional, Na (valency +1) is a known diamagnetic. Therefore, it will oppose the realignment in transport channels, which may

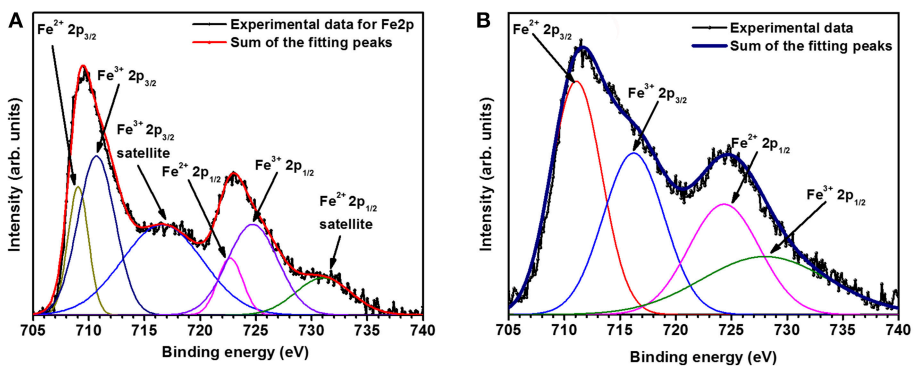

FIGURE 9 | XPS spectra for Fe present in (A) Fe_2O_3 and (B) $NaFePO_4$.

occur owing to structural reorientation driven by the magnetic iron (Fe^{3+}, which can also stabilize during material synthesis). To confirm the presence of ionized state of Fe analysis, XPS data was collected (shown in **Figure 9**) and analyzed. XPS result showed that the percentage of Fe^{2+} and Fe^{3+} was ∼55 and 45%, respectively, in $NaFePO_4$. As Fe^{2+} is nonmagnetic, Fe^{3+} drives the response under external magnetic field. The effect is more pronounced in Fe_2O_3 that had much higher percentage of Fe^{3+} (70%) with respect to the Fe^{2+} state (30%). This makes $NaFePO_4$ useful for application near the magnetic environment.

CONCLUSION

Single phase $NaFePO_4$ particles, with hollow cavity having porous walls, are reported. This microstructure allows efficient utilization of active surface area and pore structure, leading to high specific capacitance. Bulk structures return specific capacitance of ∼48 F g^{-1} at a scan rate 5 mV s^{-1} and 81 F g^{-1} at a current density of 1 A g^{-1}. For hollow microstructures structure, the specific capacitance is found to be 108 F g^{-1} at a scan rate 5 mV s^{-1} and 115 F g^{-1} at a current density 1 A g^{-1}. $NaFePO_4$ also shows long term stability under non-ambient conditions, where parameters such as magnetic field or temperature are varied. $NaFePO_4$ has the capacity to deliver performance similar to $LiFePO_4$ and make Na-ion based energy systems industrially and economically viable.

AUTHOR CONTRIBUTIONS

SB and AnC have contributed equally in sample preparation and data analysis under direct supervision of AmC as part of their Ph.D. program. AmC has also contribute in data analysis and interpretation.

FUNDING

MES program of the Department of Science and Technology, India.

ACKNOWLEDGMENTS

The authors acknowledge the financial support received from DST (India) under the MES scheme to pursue work under the project entitled: Hierarchically nanostructures energy materials for next generation Na-ion based energy storage technologies and their use in renewable energy systems.

SUPPLEMENTARY MATERIAL

The Supplementary Material for this article can be found online at: https://www.frontiersin.org/articles/10.3389/fmats.2019.00054/full#supplementary-material

REFERENCES

Akhtar, M. A., Sharma, V., Biswas, S., and Chandra, A. (2016). Tuning porous nanostructures of $MnCo_2O_4$ for application in supercapacitors and catalysis. *RSC Adv.* 6, 96296–96305. doi: 10.1039/C6RA20004D

de la Llave, E., Borgel, V., Park, K. J., Hwang, J. Y., Sun, Y. K., Hartmann, P., et al. (2016). Comparison between Na-ion and Li-ion cells: understanding the critical role of the cathodes stability and the anodes pretreatment on the cells behavior. *ACS Appl. Mater. Interfaces* 8, 1867–1875. doi: 10.1021/acsami.5b09835

Didier, C., Guignard, M., Denage, C., Szajwaj, O., Ito, S., Saadoune, I., et al. (2011). Electrochemical Na-deintercalation from $NaVO_2$. electrochem. *Solid-State Lett.* 14:A75. doi: 10.1149/1.3555102

Fang, Y., Liu, Q., Xiao, L., Ai, X., Yang, H., and Cao, Y. (2015). High-performance olivine $NaFePO_4$ microsphere cathode synthesized by aqueous electrochemical displacement method for sodium ion batteries. *ACS Appl. Mater. Interfaces* 7, 17977–17984. doi: 10.1021/acsami.5b04691

Guo, S., Yi, J., Sun, Y., and Zhou, H. (2016). Recent advances in titanium-based electrode materials for stationary sodium-ion batteries. *Energy Environ. Sci.* 9, 2978–3006. doi: 10.1039/C6EE01807F

Jiang, X., Yang, L., Ding, B., Qu, B., Ji, G., and Lee, J. Y. (2016). Extending the cycle life of $Na_3V_2(PO_4)_3$ cathodes in sodium-ion batteries through interdigitated carbon scaffolding. *J. Mater. Chem. A* 4, 14669–14674. doi: 10.1039/C6TA05030A

Kosova, N. V., Podugolnikov, V. R., Devyatkina, E. T., and Slobodyuk, A. B. (2014). Structure and electrochemistry of $NaFePO_4$ and Na_2FePO_4F cathode materials prepared via mechanochemical route. *Mater. Res. Bull.* 60, 849–857. doi: 10.1016/j.materresbull.2014.09.081

Li, W.-J., Chou, S.-L., Wang, J.-Z., Kang, Y.-M., Wang, J.-L., Liu, Y., et al. (2015). Facile method to synthesize Na-enriched $Na_{1+x}FeFe(CN)_6$ frameworks as cathode with superior electrochemical performance for sodium-ion batteries. *Chem. Mater.* 27, 1997–2003. doi: 10.1021/cm504091z

Liang, Y., Wen, K., Mao, Y., Liu, Z., Zhu, G., Yang, F., et al. (2015). Shape and size control of $LiFePO_4$ for high-performance lithium-ion batteries. *ChemElectroChem* 2, 1227–1237. doi: 10.1002/celc.201500114

Lim, E., Jo, C., Kim, M. S., Kim, M.-H., Chun, J., Kim, H., et al. (2016). High-performance sodium-ion hybrid supercapacitor based on Nb_2O_5@Carbon core-shell nanoparticles and reduced graphene oxide nanocomposites. *Adv. Funct. Mater.* 26, 3711–3719. doi: 10.1002/adfm.201505548

Liu, Y., Zhang, N., Wang, F., Liu, X., Jiao, L., and Fan, L.-Z. (2018). Approaching the downsizing limit of maricite $NaFePO_4$ toward high-performance cathode for sodium-ion batteries. *Adv. Funct. Mater.* 28:1801917. doi: 10.1002/adfm.201801917

Lu, K., Li, D., Gao, X., Dai, H., Wang, N., and Ma, H. (2015). An advanced aqueous sodium-ion supercapacitor with a manganous hexacyanoferrate cathode and a Fe_3O_4/rGO anode. *J. Mater. Chem. A* 3, 16013–16019. doi: 10.1039/C5TA04244E

Minakshi, M., Mitchell, D., Jones, R., Alenazey, F., Watcharatharapong, T., Chakraborty, S., et al. (2016). Synthesis, structural and electrochemical properties of sodium nickel phosphate for energy storage devices. *Nanoscale* 8, 11291–11305. doi: 10.1039/C6NR01179A

Park, Y. U., Seo, D. H., Kwon, H. S., Kim, B., Kim, J., Kim, H., et al. (2013). A new high-energy cathode for a Na-ion battery with ultrahigh stability. *J. Am. Chem. Soc.* 135, 13870–13878. doi: 10.1021/ja406016j

Rahman, M. M., Sultana, I., Mateti, S., Liu, J., Sharma, N., and Chen, Y. (2017). Maricite $NaFePO_4$/C/graphene: a novel hybrid cathode for sodium-ion batteries. *J. Mater. Chem. A* 5, 16616–16621. doi: 10.1039/C7TA04946C

Ramakrishnan, K., Nithya, C., and Karvembu, R. (2018). High-performance sodium ion capacitor based on MoO_2@rGO nanocomposite and goat hair derived carbon electrodes. *ACS Appl. Energy Mater.* 1, 841–850. doi: 10.1021/acsaem.7b00284

Sharma, V., Biswas, S., and Chandra, A. (2018a). Need for revisiting the use of magnetic oxides as electrode materials in supercapacitors: unequivocal evidence of significant variation in specific capacitance under variable magnetic field. *Adv. Energy Mater.* 2018:1800573. doi: 10.1002/aenm.201800573

Sharma, V., Singh, I., and Chandra, A. (2018b). Hollow nanostructures of metal oxides as next generation electrode materials for supercapacitors. *Sci. Rep.* 8:1307. doi: 10.1038/s41598-018-19815-y

Sharma, V., Singh, I., and Chandra, A. (2018c). Origin of superior catalytic activity in copper (II) oxide nanoflakes in comparison to solid or even hollow particles. Mater. *Lett*. 211, 285–288. doi: 10.1016/j.matlet.2017.10.030

Singh, A., and Chandra, A. (2015). Significant performance enhancement in asymmetric supercapacitors based on metal oxides, carbon nanotubes and neutral aqueous electrolyte. *Sci. Rep.* 5:15551. doi: 10.1038/srep15551

Slater, M. D., Kim, D., Lee, E., and Johnson, C. S. (2013). Sodium-ion batteries. *Adv. Funct. Mater*. 23, 947–958. doi: 10.1002/adfm.201200691

Smolenski, T., Kazimierczuk, T., Kobak, J., Goryca, M., Golnik, A., Kossacki, P., et al. (2016). Magnetic ground state of an individual Fe(2+) ion in strained semiconductor nanostructure. *Nat. Commun*. 7:10484. doi: 10.1038/ncomms10484

Wang, X., Niu, C., Meng, J., Hu, P., Xu, X., Wei, X., et al. (2019). Novel $K_3V_2(PO_4)_3$/C bundled nanowires as superior sodium-ion battery electrode with ultrahigh cycling stability. *Adv. Energy Mater*. 5, 1500716–1500723. doi: 10.1002/aenm.201500716

Wei, J., Li, X., Xue, H., Shao, J., Zhu, R., and Pang, H. (2018). Hollow structural transition metal oxide for advanced supercapacitors. *Adv. Mater. Interf*. 5:1701509. doi: 10.1002/admi.201701509

Yabuuchi, N., Kubota, K., Dahbi, M., and Komaba, S. (2014). Research development on sodium-ion batteries. *Chem. Rev*. 114, 11636–11682. doi: 10.1021/cr500192f

Yin, J., Qi, L., and Wang, H. (2012). Sodium titanate nanotubes as negative electrode materials for sodium-ion capacitors. *ACS Appl. Mater. Interfaces* 4, 2762–2768. doi: 10.1021/am300385r

Zhang, S., Liu, Y., Han, Q., He, S., Zhang, N., and Yang, J. (2017). Development and characterization of aqueous sodium-ion hybrid supercapacitor based on $NaTi_2(PO_4)_3$ //activated carbon. *J. Alloys Compd*. 729, 850–857. doi: 10.1016/j.jallcom.2017.08.256

Zhao, D. D., Wang, Y., and Zhang, Y. F. (2011). High-performance Li-ion batteries and supercapacitors based on prospective 1-D nanomaterials. *Nano-Micro Lett*. 3, 62–71. doi: 10.1007/BF03353653

Zhu, T., Hu, P., Wang, X., Liu, Z., Luo, W., Owusu, K. A., et al. (2019). Realizing three-electron redox reactions in NASICON-structured $Na_3MnTi(PO_4)_3$ for sodium-ion batteries. *Adv. Energy Mater*. 2019:1803436. doi: 10.1002/aenm.201803436

Conflict of Interest Statement: The authors declare that the research was conducted in the absence of any commercial or financial relationships that could be construed as a potential conflict of interest.

frontiers in Chemistry

REVIEW
published: 24 April 2019
doi: 10.3389/fchem.2019.00274

Biomass-Derived Porous Carbon Materials for Supercapacitor

Hui Yang†, Shewen Ye†, Jiaming Zhou and Tongxiang Liang**

School of Materials Science and Engineering, Jiangxi University of Science and Technology, Ganzhou, China

The fast consumption of fossil energy accompanied by the ever-worsening environment urge the development of a clean and novel energy storage system. As one of the most promising candidates, the supercapacitor owns unique advantages, and numerous electrodes materials have been exploited. Hence, biomass-derived porous carbon materials (BDPCs), at low cost, abundant and sustainable, with adjustable dimension, superb electrical conductivity, satisfactory specific surface area (SSA) and superior electrochemical stability have been attracting intense attention and highly trusted to be a capable candidate for supercapacitors. This review will highlight the recent lab-scale methods for preparing BDPCs, and analyze their effects on BDPCs' microstructure, electrical conductivity, chemical composition and electrochemical properties. Future research trends in this field also will be provided.

Keywords: biomass, porous carbon, supercapacitor, electrochemical performance, energy storage

OPEN ACCESS

Edited by:
Wenyao Li,
Shanghai University of Engineering Sciences, China

Reviewed by:
Kaibing Xu,
Donghua University, China
Guangjin Wang,
Hubei Engineering University, China

***Correspondence:**
Hui Yang
yanghui_2521@163.com
Tongxiang Liang
liang_tx@126.com

†*Co-first authors*

Specialty section:
This article was submitted to Electrochemistry, a section of the journal Frontiers in Chemistry

Received: *01 March 2019*
Accepted: *03 April 2019*
Published: *24 April 2019*

Citation:
Yang H, Ye S, Zhou J and Liang T (2019) Biomass-Derived Porous Carbon Materials for Supercapacitor. Front. Chem. 7:274. doi: 10.3389/fchem.2019.00274

INTRODUCTION

The ever-growing population, crisis of energy shortage, and environmental pollution caused by burning fossil fuels have brought about different kinds of problems, and they stimulate the process of developing clean and sustainable energy, such as solar energy, wind power etc. (Dunn et al., 2011; Chu and Majumdar, 2012; Dubal et al., 2015; Kamat, 2015; Kazmerski, 2016; Peng et al., 2017). All these closely relate to the development of the advanced energy storage system. Until now, for electrochemical energy storage systems, for example, various rechargeable batteries and supercapacitorsare identified as the most promising energy storage devices (Chmiola et al., 2006; Miller and Simon, 2008; Kim et al., 2010; Cheng et al., 2011; Xu et al., 2014; Gogotsi, 2015). Although batteries have a relatively longer life cycle, (<1,000 cycles), high-energy density and satisfactory rate performance, distinct from rechargeable batteries, supercapacitors possess the following characteristics: high-power energy, extremely long cycle life (>100,000 cycles) without losing capacitance and safety, it is quite essential to bridge the gap between conventional electrochemical capacitors and rechargeable batteries, and meet the demand of electric vehicles which require high power (Liu et al., 2018a; Xu et al., 2018).

Basically, supercapacitors can be classified under two categories according to their charge storage mechanism, which further affects the power density of supercapacitors. The electrical double layer (EDL) capacitance and pseudo-capacitance are quite different. For the former, charges are stored through ions' adsorption by electro-static interaction at the near-surface of active materials, where EDL forms; while the energy storage/release mechanism for pseudo-capacitance is by means of redox reaction, ions insertion/extrusion and under-potential depositions (Augustyn et al., 2014; Mccloskey, 2015). Both the aforementioned supercapacitors require chemical and structure stability, outstanding electrical conductivity, and high SSA. Hence, to satisfy the requirement of high capacity and superior rate performance for supercapacitors, the exploitation of advanced

electrode materials with low cost, adjustable composition, and microstructure (especially pore structure) turns increasingly important.

In the past decades, thanks to the excellent conductivity property, high SSA, variable pore structure and porosity, carbon materials, such as commercial activated carbons (Chan et al., 2004; Jänes et al., 2007; Zhang and Zhao, 2009; Lv et al., 2011; Wang et al., 2014), graphene (Wang et al., 2009; Liu et al., 2010; Zhang et al., 2010; Cao et al., 2011), graphene oxide (GO) (Li et al., 2013; Li and Yang, 2014; Down et al., 2018), carbon nanotubes (CNTs) (An et al., 2001; Futaba et al., 2006; Pushparaj et al., 2007), porous carbon (PC) (Lee et al., 2000; Vix-Guterl et al., 2005; Hou et al., 2015) and their composites (Salunkhe et al., 2015) have achieved various kinds of essential accomplishments on their volumetric performance. However, their high production cost, complicated and unsustainable preparation process greatly limited their wide application. Besides, the gravimetric capacitance for CAs is keeping at a relatively low level for several decades, that should be ascribed to the rich micro-pores, which are hard accessible for ions, especially at high-current density condition (Li et al., 2014). Therefore, enlarging the ion-accessible area through creating a suitable hierarchical porous structure is a key factor for achieving high specific capacitance (C_s) and rate performance (Zhao et al., 2016). Biomass materials abundantly present across our surroundings, and their low cost, accessible, environmentally friendly, and recyclable properties ensure they are ideal candidates for resources of carbon materials. At the same time, their naturally hierarchical porous structure and various elements (N, S) facilitate electrolyte penetration and extra active sites' generation, respectively (Chen et al., 2016).

In this review, we provide a summary of the recent and significant advances in hierarchical porous carbon (HPC) derived from biomass materials, emphasizing on the relationship between interconnectivity of the pore structure and electrochemical efficiency, and synthetic strategies for preparing HPC as supercapacitors. Finally, the current challenges and future directions are briefly discussed.

RELATION BETWEEN PORE FEATURES AND CAPACITIES

In general, the capacitance of PC materials relies on the pore size distribution, connectivity and hydrophilicity; these factors will be further influencing the ion diffusion process and energy density of active materials. According to the findings by Dubinin (1960) and the classification by the International Union of Pure and Applied Chemistry (IUPAC) in 1985 (Sing, 1985), pores with different widths can be divided among three categories: macropores (>50 nm), mesopores (2–50 nm) and micropores (<2 nm). With the development of porous materials, three new pore types have been classified since 2015, they are nanopores (<100 nm), supermicropores (0.7–2 nm) and ultramicropores (<0.7 nm).

Pore Size Distribution

Although intense efforts are focused on improving the surface area and redox active sites of PC materials, optimization of pore size distribution is also an effective mode to enhance capacitance, especially for EDL capacitors. Generally, nanoporous carbons consist of pores ranging from micropores to mesopores, and most of them cannot maintain long-range ordering, or be accessible to ions from the electrolyte, though we know the electrochemical performance of PC is dependent on the interface of carbon and electrolyte. The macropore, mesopore and micropore have different functions in the electrochemical charge/discharge process. Macropores serve as ion-buffing reservoirs for meso- and micropores; mesopores provide abundant transport channels for ions' diffusion; in spite of some regions of micropores are inaccessible to adsorb ions, it still affects the charge status through controlling the diffusion of ions and molecular sieve effects, and then changing the capacitance of PC materials (Liu et al., 2018c); in addition, as the size of pores decreases toward <1 nm, an anomalous capacitance increase occurred in the organic electrolyte due to ion dissolution. Chmiola and co-workers reported that PC could achieve the highest capacitance as its average pore size matched the size of desolvated ions (Chmiola et al., 2006). Kondrat (Kondrat et al., 2012) found that different carbon materials with the same average pore size will display very different capacitive properties, because of the difference in pore size distribution; besides, for the monodisperse porous electrode, its energy density and pore size do not fit a non-monotonic function (**Figure 1**). Moreover, Cheng (Wang et al., 2008) believed that high micropore volume and the micropore-to-total-pore ratio are crucial for gaining a high-rate electrochemical performance of PC.

Pore Connectivity

interconnected pores at different size dimensions are qualified as a hierarchical porous structure, which facilitates electrolyte infiltration and ion diffusion through a different pore canal (Borchardt et al., 2013). Until now, it is still a big challenge to construct carbon materials with 3D-interconnected, long-range order macroporous and mesoporous structures. These structures, combined with decent SSA and proper pore size distribution, allow efficient diffusion of any substance, such as electrolytes, ions etc., to the interior space of all channels. The strategies for fabrication HPC mainly includes templating (hard/soft) (Yuan et al., 2016; Xiong et al., 2017; Zhu et al., 2017) and non-templating ways (Lv et al., 2012), while these methods are time-consuming and highly costly. As a promising renewable resource, Biomass always possess a naturally interconnected, multichannel and porous structure, hence, they are the excellent candidates for preparing HPC. Wang and co-workers used pomelo peel as the carbon sources, in virtue of its foamy fibrous layer and abundant oxygen-containing functional groups, HPC was obtained after KOH activation, it gained a capacitance of 222.6 F/g at relatively low discharge current density (0.5 A/g), at the same time, it

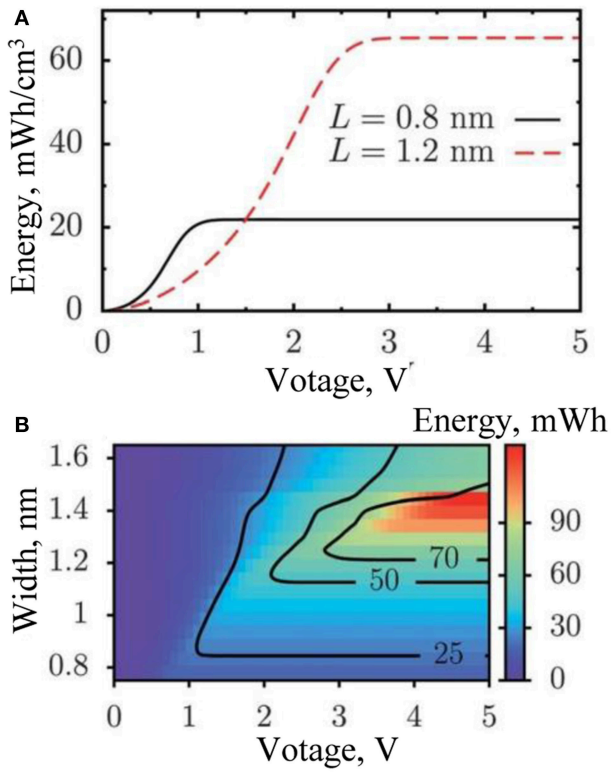

FIGURE 1 | (A) The relationship between energy density and working voltage in PC supercapacitor. **(B)** The energy density correlates with pore size and working voltage. Reprinted with permission from Kondrat et al. (2012). Copyright 2012 Royal Society of Chemistry.

maintained a good rate of performance and a suitable cycling stability (Li et al., 2017a).

Pores' Hydrophilicity

Until recently, the charging mechanism for supercapacitors is derived from ions into the PC network by applied potential driving. Hence, the pore wettability, also named as surface hydrophobic/hydrophilic balance, closely relates to pores' surface functional groups, and has a great impact on the penetration of guest species into the pore systems and transfer of electrons (Xiao et al., 2016). Therefore, the functionalization of PC materials through surface modification gradually becomes an important issue to achieve appropriate wettability (**Figure 2**). The modification techniques always involve post-treatment of PC materials in oxidizing media, or doping carbons with oxygen, nitrogen and other elements (Lin et al., 2015; Chen et al., 2017b). Generally, N- and O-doping, introduced by grafting different functional groups, facilitate adsorption of ions and further improve the hydrophilicity of the carbon matrix. Therefore, moderate oxidation accompanied by heteroatom doping provide faradic pseudocapacitance, and then increase the capacitance value of electrode materials. However, overoxidation results in collapse of pore structure and large interface resistance (Wei et al., 2016). Moreover, most natural biomass contains nitrogen, boron, sulfur and other trace elements, which would be doped into the carbon framework as heteroatoms, and that will generate a more active site, and decrease the hydrophobicity of PC. Li utilized corncob as a precursor, and obtained nitrogen-doped activated carbons with N content up to 4 wt%, the corresponding hybrid-type supercapacitor achieved high-energy density and rate performance (Li et al., 2015a).

BRIEF OVERVIEW OF FABRICATION STRATEGIES FOR PC

Up to now, various synthetic methods have been developed for preparing biomass-derived PC. The carbonization methods, such as pyrolysis (Dubal et al., 2016) and hydrothermal carbonization (Enterría et al., 2016), are used earliest to obtain PC. The pyrolysis is a dry-carbonization reaction, which usually takes place in an inert atmosphere or low oxygen environment at an elevated temperature condition (300–900°C), the main components of biomass are gradually transferred into biochar through a series of reaction, such as cross-linking depolymerization, fragmentation reactions etc. The performance of biochar depends on the reaction temperature, time and catalyst (Li et al., 2016b); For the hydrothermal carbonization, it is carried out in aqueous environment at elevated temperature (<300°C) and autogenous high pressure, it is a chemical process for conversion of biomass to carbonaceous materials, whose properties are determined by reaction temperature, time, pressure, and water/biomass ratio. Furthermore, Compared with the pyrolysis reaction, hydrothermal carbonization results in higher biochar yield. However, biochars obtained through the aforementioned methods have low SSA and porosity. Hence, as the most common strategies for increasing SSA of carbon materials, activation, including physical and chemical activation, have been wildly used.

Physical activation is carried out at a high temperature (>700°C) in the presence of gases like CO_2, H_2O, air and ozone (Abioye and Ani, 2015; Chang et al., 2016; Lota et al., 2016). The process of physical activation has two steps: firstly, carbonization happens at a low temperature in an inert atmosphere, and during this process, volatile matters are eliminated and biochar is formed. Subsequently, gasification reaction leads to the formation of abundant open pores because of the introduction of oxidizing gas at a high temperature. It should be noteworthy that increasing reaction temperature and prolonging treating time are helpful to improve the porosity of carbon materials, while the pore size distribution will be broadened.

Prior to carbonization, biochar is pre-mixed with certain chemicals, such as an acid (Sun et al., 2015), strong base (Qu et al., 2015), or a salt (Sevilla and Fuertes, 2016), then the mixture is carbonized at relatively low temperatures (450–900°C). Although there are drawbacks for chemical activation, for example, high cost, apparatus corrosion, and non-recoverable chemicals, it is still preferred over physical activation owing to its lower reaction temperature, shorter reaction time and larger SSA. Among

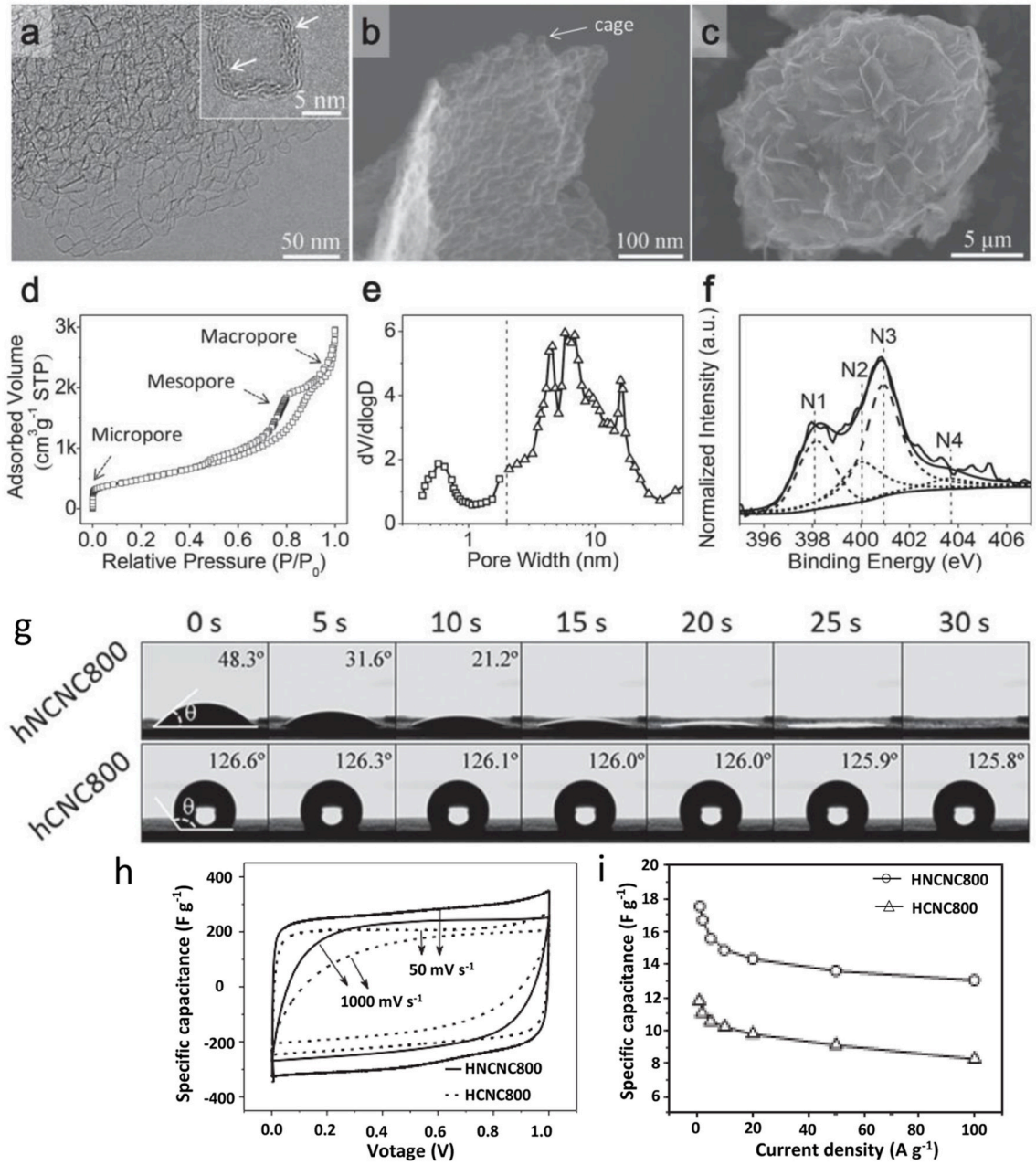

FIGURE 2 | (a–c) TEM and SEM images of N-doped PC; **(d-f)** N_2 adsorption/desorption isothermal, pore size distribution and XPS spectra of the sample; **(g)** wettability tests; **(h,i)** electrochemical performance analysis. Reprinted with permission from Zhao et al. (2015). Copyright 2015 Willey VCH.

various kinds of activating reagents, KOH (Lv et al., 2011) is the most wildly used chemical. The activation mechanism of KOH activation (**Figure 3**) can be summarized and shown as the following reaction equations.

$$KOH + C \leftrightarrow K + CO_2 + H_2O \quad (1)$$

$$KOH + CO_2 \leftrightarrow K + CO_2 + H_2O \quad (2)$$

$$KOH + C \leftrightarrow K + H_2 + K_2CO_3 \quad (3)$$

$$C + CO_2 \leftrightarrow CO \quad (4)$$

Cellulose-Derived PC

As the most abundant and sustainable natural polymer, cellulose is the main component of green plants' primary cell wall and consists of a linear chain of D-glucose. Cellulose fibers exhibit high surface area and aspect ratios, excellent mechanics and flexibility, broad chemical-modification capacity, so it has attracted intense attention in the past several years for supercapacitor (Yang et al., 2015; Yu et al., 2016). Generally, according to the origin of cellulose, it can be classified in two ways: commercial cellulose and isolated cellulose from lignocellulose for PC precursor. After carbonization and

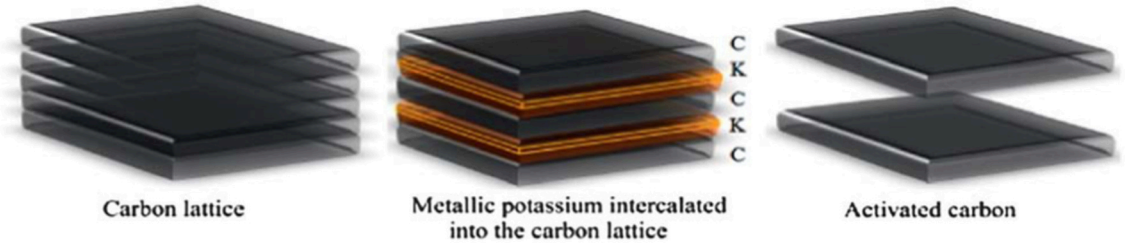

FIGURE 3 | KOH activation mechanism. Reprinted with permission from Wang and Kaskel (2012). Copyright 2012 Royal Society of Chemistry.

activation through a physical or chemical process at elevated temperature, then PC was gained. Although they have extremely high SSA, compared with HPC, it exhibited limited C_s because of low wettability, slow ions' diffusion rate and relatively small amount of the effective active site. Hence, recently, many efforts have been focusing on the fabrication of HPC derived from cellulose.

The unique structure of carbon aerogels provides high SSA, hierarchical porous structure, interconnected macro-/meso-/micropores, efficient ions diffusion rate, and abundant active sites. Nanocellulose microcrystalline would be gelling at the base condition, after freeze-drying and CO_2 activation process, carbon aerogel with interconnected 3D nanostructure could be prepared. The final products showed high SSA (1,873 m^2/g) and high pore volume (2.65 cm^3/g); besides, the C_s reached 302 F/g and 205 F/g at 0.5 A/g and 20 A/g, respectively (Zu et al., 2016). "leavening" strategy (**Figure 4**) is applicable to various biomass and their derivatives, the corresponding electrode materials exhibited a C_s of 253 F/g with superior cycling stability (Deng et al., 2015). Zhuo et al. synthesized HPC through a dissolving-gelling process, after carbonization process, carbon aerogel with abundant macropores, mesopores and micropores was obtained, and gained high C_s of 328 F/g at 0.5 A/g with 96% of the capacitance retention after 5,000 cycles (Zhuo et al., 2016). Sodium carboxymethyl cellulose aerogels derived PC could be obtained through sol-gel and KOH activation, its relative low C_s (152 F/g at 0.5 A/g) might be attributed to the limited SSA (<500 m2/g) (Yu et al., 2016). What's more, Long et al. cellulose nanofibrils and short cellulose nanofibrils were assembled into macro/micro/mesoporous structure by Li and co-workers, who found the hierarchical structure maintained high surface area (1,244 cm^2/g), good C_s (170 F/g) at high current densities (Li et al., 2017b). Waste paper is also a promising candidate for preparing PC. Kraft pulp was mixed with KOH solution and freeze-dried, then the mixture was calcined at an elevated temperature under an inert atmosphere. Dense graphene-like HPC was fabricated, and its gravimetric and volumetric C_s is 309 F/g and 309 F/cm^3 at 1 A/g, respectively (Mo et al., 2018).

It is believed that increasing surface functional groups into the carbon framework contribute to the enhancement of the capacitance of supercapacitors. Hence, introducing of N, B, P, and O, which act as electron donor or electron acceptor, have the following effects: improving wettability between PC and electrolyte; facilitate the binding between carbon materials and ions; enhancing the active sites in the carbon framework (Chen et al., 2013, 2017d; Wu et al., 2015; An et al., 2017). Contrary to oxygenic functional groups, N-containing functional groups own basic characters, which leads to donor-acceptor properties, and improves the final electrochemical properties of electrode materials (Wang et al., 2008). As the carbon sources and as a template, cellulose nanocrystals were used to control the growth of melamine-formaldehyde, then rod-like porous N-doped carbon particles were fabricated; they achieved 352 F/g at 5 A/g and maintained over 95% C_s retention after 2000 cycles (Wu et al., 2015). Through pyrolysis and activation procedure, PC nanosheets (PCN) were doped by N and S, the co-doped PCN had a C_s of 298 and 233 F/g at charge/discharge current density of 0.5 and 50 A/g. Besides, only 2% capacitance lost after 10,000 cycles (Li et al., 2016b). Phosphorus (P) doped HPC possessed outstanding rate capability, and it showed a C_s of 133 F/g (146 mF/cm^2) at 10 A/g with ∼98% capacitance retention after 10,000 cycles (Yi et al., 2017).

Lignin-Derived PC

As the most abundant natural aromatic polymer and the second raw material from plants, lignin, with a production ∼ 50 million tons per year, is known as one of the most promising candidates for carbon sources considering environmental and economic aspects (Suhas and Carrott, 2007). Recently, the lignin-based PC nanocomposite gradually has attracted much attention because of its excellent electrochemical performance (Kai et al., 2016; Ma et al., 2016; Wang et al., 2016a). Generally, it is quite difficult to isolate the lignin because of the potential oxidation and condensation reaction during the isolation process; besides, the mass production and purity of lignin, isolated through hydrolysis or solubilization of plants, also limit the wide application of lignin-based PC for supercapacitor. However, series of works have been published and some progress has been made. Physical and chemical activations are the most common strategy to prepare lignin-based HPC. Zhang (Zhang et al., 2015a) utilized KOH as the template and activating agent and successfully prepared lignin-derived HPC with an interconnected 3D network. Its abundant oxygen-containing group ensures a relatively good pseudocapacitance performance (165 F/g in 1 M H_2SO_4 at 50 mA/g). Increasing SSA of carbon materials is a good choice for promoting the C_s of electrode materials; hence, a higher HPC derived from lignin was obtained by KOH activation,

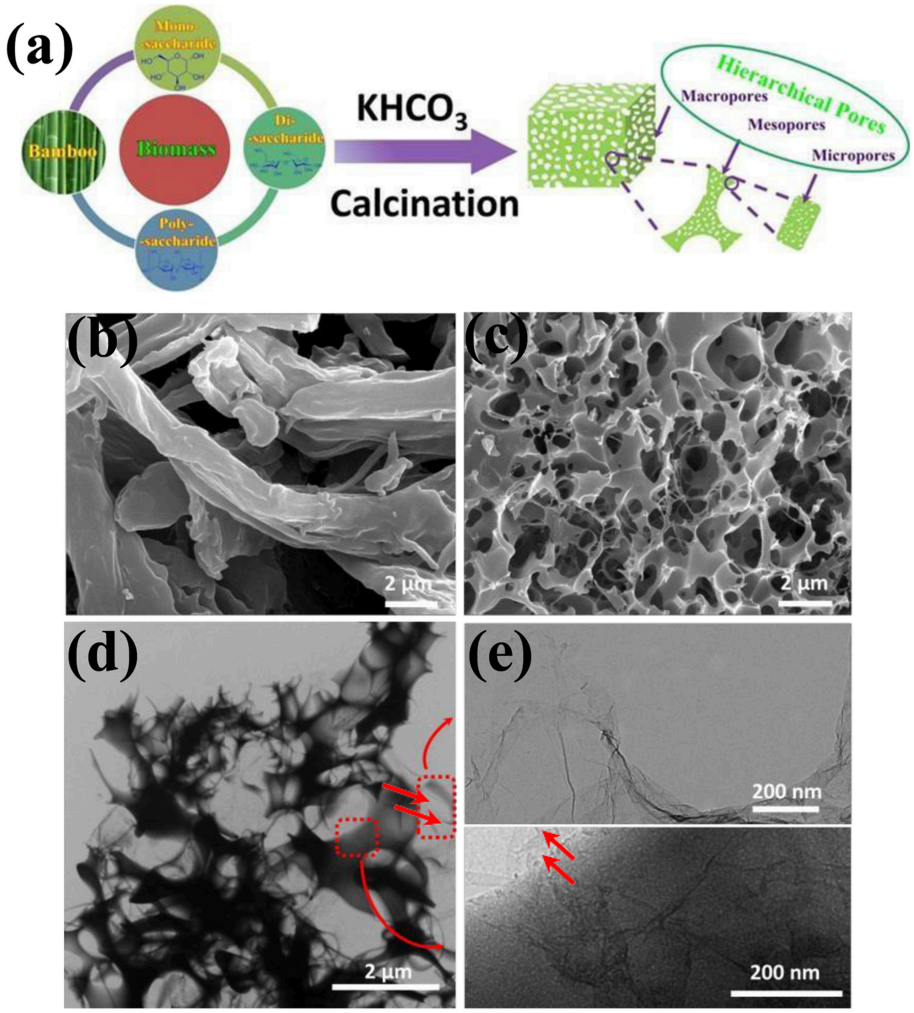

FIGURE 4 | (a) Scheme diagram of the formation of HPC by "leavening" agent; **(b–e)** SEM and TEM images of HPC. Reprinted with permission from Deng et al. (2015). Copyright 2015 Royal Society of Chemistry.

the corresponding products provided a C_s of 286.7 F/g at 0.2 A/g (Zhang et al., 2015b). In addition, a hard template, such as zeolite, was used to control the assembly of lignin, and then control the pore structure of the final products, this lignin-based templated PC showed a high C_s (250 F/g at 50 mA/g) (Ruiz-Rosas et al., 2014). One dimension of PC fibers derived from lignin not only contributed to faster electron conduction, but also facilitated the electrolyte infiltration by providing abundant pore structure, Hu et al. reported that porous fiber activated by KOH achieved a total capacitance of 1 F at 10 mg loading (Hu et al., 2014). Besides, lignin-based HPC film was developed by Chang and co-workers, as shown in **Figure 5**, a flexible film consists of lignin, PVP and Mg $(NO_3)_2$ was synthesized through electrospinning, then the precursor was carbonized and pickling to remove the MgO, the final PC film exhibited C_s of 248 F/g and outstanding rate and cyclic performance (Ma et al., 2018).

To enhance the performance of lignin-derived PC, surfactant, organic solvent and silica were added into the mixture of lignin, after carbonization and activation by 2 M NaOH, the carbon film (~310 μm) was used as an electrode, because of its hierarchical pore structure and superb electrical conductivity, this novel carbon electrode achieved an ultrahigh areal capacitance of 3 F/cm^2 and a high volumetric capacitance of 97.1 F/cm^3, high mass loading and excellent electrochemical performance ensure it is a promising candidate for supercapacitor (Li et al., 2016a). Furthermore, lignin-derived byproducts were used as carbon resources by hydrothermal treatment and activation, the as-prepared N-doped PC with hierarchical bowl-like pore structure exhibited a high conductivity (4.8 S/cm), favorable C_s (312 F/g at 1 A/g in 6 M KOH) and excellent rate capability (81% retention at 80 A/g) (Wang et al., 2017). Moreover, Wang reported that N-doped PC derived by KOH activated urea-modified lignin could be obtained; it possessed a well-developed porous structure and extremely high SSA (3,130 m^2/g). The corresponding supercapacitors achieved C_s of 273 and 306 F/g in 6 M KOH and KOH-PVA solid electrolytes, respectively (Wang et al., 2016b).

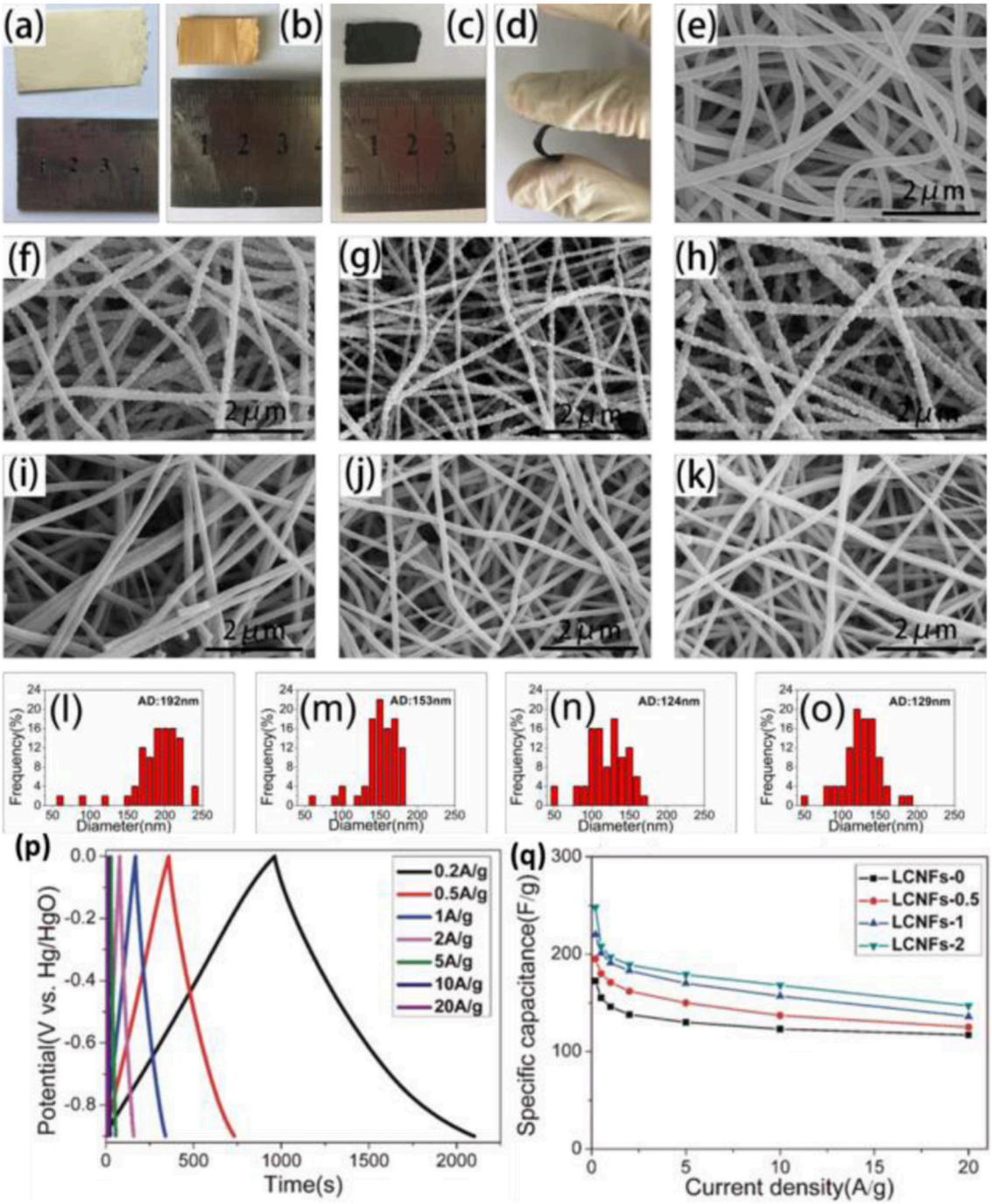

FIGURE 5 | Optical images **(a–c)** and SEM images **(e–k)** of fiber film; **(l–o)** size distribution of carbon fiber; galvanostatic charge and discharge curves **(p)** and rate capability **(q)** of fiber film. Reprinted with permission from Ma et al. (2018). Copyright 2018 Elsevier.

Alginate-Derived PC

Except for cellulose, other kinds of natural polysaccharides obtained by artificial extracting have been wildly used as PC precursor because of their low cost, accessibility and component stability.

Alginate is a polysaccharide composed by covalently linked mannuronate and guluronate, and widely distributed to the cell walls of brown algae. Furthermore, the chelation between metal ions and alginate results in gelling and forming an "egg-box" structure (Davis et al., 2003), which further being calcinated at 800°C, three-dimensional macro-meso-microporous HPC aerogels were prepared. The final products showed an excellent rate performance (65% capacity retention at 100 A/g) and decent capacity (188 F/g at 1 A/g) (Wang et al., 2018a). Li

and co-workers synthesized alginate gels with interconnected macropore structure utilizing freeze-drying process, then after activation by KOH and removal of Ca, interconnected HPC was obtained; it showed a high-rate capability with 222 F/g and long cycling life at 10 A/g (Li et al., 2015c). On account of the limited C_s of an EDLC capacitor, O- and N- enriched PC was prepared by calcining kelp in NH_3 atmosphere, the products acquired high volumetric C_s (>360 F/cm^3) and superb cycling performance (Li et al., 2015b). In addition, Nitrogen-doped PC fibers derived from cobalt alginate with egg-box structure, which led into the formation of abundant large mesopores, and the product presented an excellent capacitive behavior of 197 F/g at 1 A/g and superb cycling ability (Tang et al., 2018). Geng (Geng et al., 2016) reported a facile method to synthesis HPC derived from sodium alginate by pre-carbonization and NaOH activation, and it exhibited a capacity of 451 F/g in 2 M KOH solution; while its rate performance, which greatly depends on the electrical conductivity of the electrode materials, was not satisfied.

Starch-Derived PC

As the most common carbohydrate in the human diet, starch, a polymeric carbohydrate consisting of glucose units jointed by glycosidic bonds, is a promising candidate for supercapacitors as its low cost, accessibility (Lei et al., 2016; **Figure 6**). Direct carbonization of starch with the aid of activated agents is easy and commonly used by researchers for preparing PC. Guo (Guo et al., 2018) synthesized starch-derived PC through one-pot carbonization, the as-prepared PC achieved a C_s of 385 F/g at 1 A/g. Zhang (Zhang et al., 2015b) proposed a simple strategy to fabricate hierarchical hollow porous spherical carbon using starch as raw materials and $KHCO_3$ as the activation agent. The relatively large SSA and rich porous structure endowed the electrode materials with a high capacitance (265.4 F/g at 1 A/g) and excellent rate capacitance (137 F/g at 100 A/g). Hence, carbon derived by different botanical origin would influence the electrochemical performance of the products, and this was verified by Bakierska (Bakierska et al., 2017). In addition, hydrothermal treatment of starch is useful for improving the hydrophilic of carbon materials by introducing the oxygen-containing functional group. Therefore, before carbonization and activation at elevated temperature, hydrothermal carbonization was performed, the potato-derived PC spheres displayed a high C_s (245 F/g) and good rate performance (61% capacitance retention at 10 A/g) (Qiang et al., 2015); similar processing procedure was used by Hong with sweet potato starch as the carbon source, a C_s of 208 F/g at 1 A/g was gained (Hong et al., 2018).

The foaming process (Wang et al., 2016b) through physical or chemical blowing with the aid of carbonate of urea leads to the formation of abundant macropores. For this reason, inspired by bread leavening, Deng (Deng et al., 2015) proposed a non-casting and template-free method to fabricate HPC by mixing the starch with $KHCO_3$ followed by carbonization at a high-temperature condition. The as-prepared samples owned a C_s of 253 F/g and with no distict capacitance loss after 10,000 cycles. At the same time, Chang (Chang et al., 2017) employed a chemical blowing strategy to synthesis N-doping sheet-like PC by graphitization and chemical activation. The samples gained extremely high surface area (2,129 m^2/g), large pore volume (0.97 cm^3/g), good C_s (337 F/g at 0.5 A/g) and reasonable cycle stability. Similar preparation strategies were employed to treat starch by other researchers to investigate the electrochemical properties of the PC (Pang et al., 2016a; Yang et al., 2016; Du et al., 2017). Calcium acetate was used as the hard template and mixed with starch before carbonization, the PC with tunable pore size by adjusting the ratio of starch/calcium acetate was prepared. When the current density increased from 0.1 A/g to 10 A/g, the C_s of the electrode materials transformed from 277 F/g to 182 F/g, and the cycling results indicated that the PC owned an extremely outstanding cycle stability even after 20,000 cycles (Zhang et al., 2016b). Compared with other kinds of biomass, corn starch is a relatively pure resource as its high-yield character. PC derived corn starch by hydrothermal carbonization, and activation acquired high SSA (1,239 cm^2/g), good capacitance (144 F/g) and energy density (19.9 Wh/kg), that were performed slightly better than commercial PC (Pang et al., 2016b). The rate performance of the electrode can be improved by combining PC and carbon cloth together. Zhong (Zhong et al., 2018) synthesized a binder-free activated carbon electrode via sol-gel and KOH activation; the corresponding electrodes achieved 272 F/g (1 A/g) and C_s retention of 75.9% at 50 A/g.

Chitin-Derived PC

As one of the most abundant natural polymers, chitins, with stiff chain conformation and considerable nitrogen concentration (∼6.9 wt%), can be completely dissolved into the mixture solution of NaOH and urea. Generally, the addition of PETF hampers the electron transport and restrains the rate capacity of electrode materials. Zhang (Zhang et al., 2016a) employed a one-step synthesis strategy for preparing a binder-free PC electrode by sol-gel method. After KOH activation, the electrode achieved gravimetric C_s of 272 F/g and 75.9% C_s retention at 50 A/g. By means of emulsification and carbonization at high temperature, N-doped microsphere with ample interconnected porous structure, high SSA, unique elasticity and outstanding rate performance were obtained (Suhas and Carrott, 2007). Gao employed prawn shells as a carbon precursor, the obtained N-doped activated carbon exhibited very fine C_s of 357 F/g (6 M KOH) and 695 F/g (1 M H_2SO_4) (Zhang et al., 2015b). The fungus was also used as PC sources, Long (Ruiz-Rosas et al., 2014) found the corresponding graphene-like carbon possessed high specific surface are (1,103 m^2/g), outstanding volumetric (360 F/cm^3) and cycle stability (99% capacitance retention after 10,000 cycles). At the same time, N-doped PC derived from shrimp shells with high surface area (1,271 m^2/g) by KOH activation also got a high C_s (239 F/g at 0.5 A/g). Moreover, as a renewable biomass mainly composed of chitin, cicada slough derived PC was obtained through carbonization in air and KOH etching in inert atmosphere, results showed that the products exhibited fairly high oxygen content (∼30%), moderate nitrogen content (∼4%) and high C_s (266 F/g at 0.5 A/g) (Hu et al., 2014).

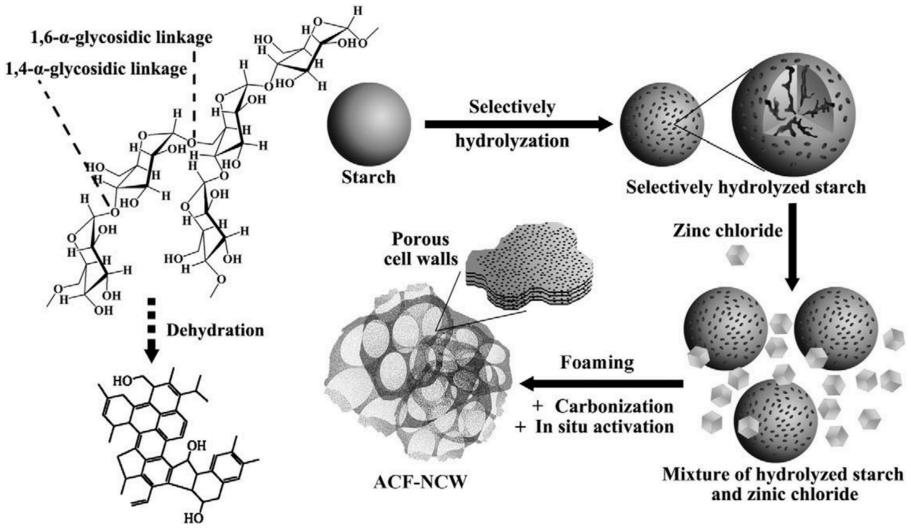

FIGURE 6 | Schematic illustration of the synthesis process of PC foam. Reprinted with permission from Lei et al. (2016). Copyright 2015 Elsevier.

Gelatin-Derived PC

As a renewable biomass resource, gelatin owns abundant rich –NH_3 groups, which ensure a good wettability after carbonization, and facilitates nitrogen atoms doped during the activation process. Hence, it is believed to be a promising candidate for the raw material of PC for supercapacitor. Recently, it is still a big challenge for preparing bio-sources derived carbon materials with 2D planar architectures, which promote ions transportation and electrons conduction, and further affecting the capacitance and rate performance of the electrode materials. Therefore, utilizing gelatin and dopamine as carbon and N sources, respectively, Fan and colleagues (Fan et al., 2015) developed a general strategy for synthesizing 2D PC nanosheets through a series of treatment, including intercalation, thermal treatment and chemical etching; meanwhile, layered montmorillonite was added to control the microstructure of gelatin, and brought about the formation of two-dimensional nanosheet-like PC. The final products exhibited an enhanced rate capability and a high C_s of 246 F/g; besides, the decent capacitance retention (81% at 100 A/g) indicates the electrode material is a good candidate of electrode material for supercapacitor. Furthermore, a free-standing N-doped PC film derived from gelatin/copper hydroxide nanostrands composite films were synthesized by Hu et al. (2016); the binder-free mesoporous N-doped carbon film possessed promoted specific energy (28.1 Wh/kg) and high specific capacity (316 F/g at 0.5 A/g), while its rate performance was not satisfied. Doping with multi-elements is another strategy to improve the electrochemical performance of PC because of the synergistic effect. Therefore, a facile yet sustainable approach was used to produce B/N co-doped PC. Boric acid was added into the gelatin solution, and it acted as hard templates after crystallization during the evaporation of aqueous solution at an elevated temperature. The plate-like shaped boric acid regulating the assembly of gelatin, after carbonization and activation, 2D plate-like PC formed. As the voltage windows is 0.8 and 1.0 V, the C_s of the PC is 240 and 230 F/g, respectively. It also showed improved capacitance retention (Zheng et al., 2016b). Except for boric acid, graphene oxide was applied as a regulator to modify the pore structure, composition, and microstructure of PC derived from gelatin, and results showed that the carbon nanosheets with thickness range from 10 to 30 nm, owned high C_s, decent rate capability and high capacitance retention (76% at 20 A/g). At the same time, Zhang applied a similar approach to preparing layer-like PC with the thickness ∼100 nm, which delivered a high discharge C_s (366 F/g at 1 A/g), good rate capability (221 F/g at 30 A/g) and suitable cycling performance (Zhang et al., 2015c).

Plant-Tissue-Derived PC

It is well-known that a thick electrode with high areal active materials loading is urgent in supercapacitor designs as it is closely related to the energy density of supercapacitor devices, and it is useful to reduce the cost of manufacturing through maximizing the packing density of electrode materials and decreasing the layers of inactive materials. What is noteworthy is that the transportation rates of the ion and electron are inversely proportional to the thickness of the electrode in the real-world application. However, natural wood possesses a unique anisotropic structure and plenty of open channel along the growth direction, which facilitates alleviating the electrode materials' tortuosity, promoting the ions transfer, and further increasing the rate capacity of the electrode materials (**Figure 7**). Hence, a surface modified porous wood carbon derived from poplar wood was prepared by Liu (Liu et al., 2012), and the products achieved a maximum gravimetric and volumetric capacitance of 234 F/g and 36 F/cm^3, respectively. Basswood was carbonized by multistep thermal treatment and CO_2 activation; the obtained HPC with extremely high mass loading of MnO2 gained high-energy density (1.6 mWh/cm^2) and power density

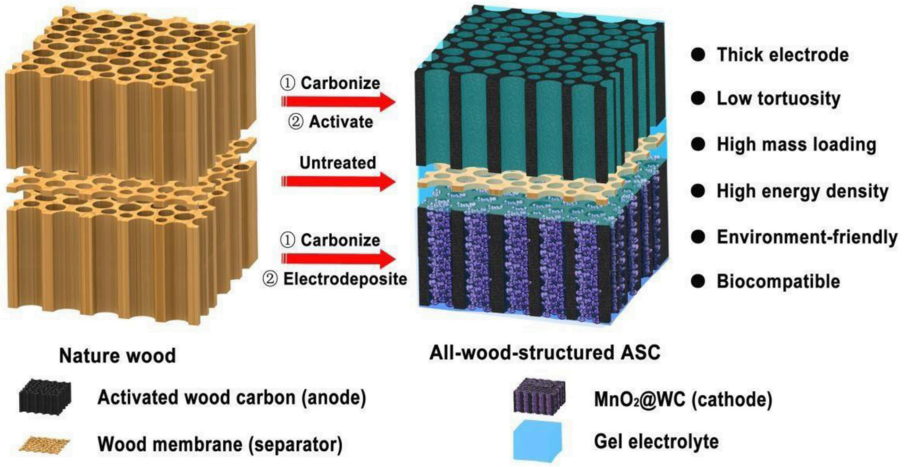

FIGURE 7 | Schematic illustration of hierarchical PC supercapacitor. Reprinted with permission from Chen et al. (2017a). Copyright 2017 Royal Society of Chemistry.

(24 W/cm^2) (Chen et al., 2017a). In addition, highly anisotropic, multichannel wood carbon doped by N and S were also exhibited well electrochemical properties, the PC showed a C_s of 704 F/g at 0.2 A/g, and still maintained a competitive C_s of 349 F/g at 4 A/g (Tang et al., 2018). Pinecone tree activated carbon was prepared by KOH activation at 800°C, and the products showed a C_s and energy density of 69 F/g at 0.5 A/g and 24.6 Wh/kg, respectively, besides, it exhibited excellent voltage stability after holding 110 h (Barzegar et al., 2017).

Similar to the wood's microstructure, bamboo-derived carbon was obtained by carbonization with the aid of KOH under N_2 atmosphere. After being doped by boron and nitrogen, the corresponding HPC exhibited a C_s of 281 F/g (1 M, KOH) and energy density (37.8 Wh/kg) (Chen et al., 2015). As N-enrich biomass, the bamboo shoot was carbonized by Chen (Chen et al., 2017c) to prepare N-doped PC materials, which was endowed with high SSA, highly interconnected pores and uniform nitrogen dopant distribution. Its outstanding C_s and rate performance ensured it is a promising candidate for supercapacitors. Wei employed broussonetia papyrifera as a biomass source, after hydrothermal treatment in KOH solution, then pyrolysis and activated at high temperature in Ar atmosphere, N-doped HPC with high SSA (1,212 m^2/g) and outstanding C_s (320 F/g at 0.5 A/g) were fabricated (Wei et al., 2015). Thubsuang reported that rubberwood waste treated with H_3PO_4 or NaOH led into the formation of carbon monoliths, which exhibited a maximum gravimetric capacitance, volumetric capacitance and energy density of 129 F/g, 104 F/cm^3, and 14.2 Wh/kg, respectively (Thubsuang et al., 2017). What's more, wood waste was used as raw material, and the N-doped PC-PANI composite possessed a decent C_s (347 F/g at 2 A/g) and high energy density (44.4 Wh/kg) (Yu et al., 2015). Compared with conventional KOH activation, impregnate-activation method resulted in PC derived from pine tree sawdust with higher surface area and richer interconnected pores, and achieved good C_s in the organic electrolyte (146 F/g) and IL electrolyte (224 F/g) (Wang et al., 2017). Except for these woody materials aforementioned, other woody wastes, such as spruce bark (Sun et al., 2018), Java Kapok tree (Kumar et al., 2018), plane tree (Yao et al., 2017), Melia azedarach (Morenocastilla et al., 2017), auriculiformis tree bark (Momodu et al., 2017), ginkgo leaves (Hao et al., 2017) (**Figure 8**) were developed as carbon for fabricating PC, whose C_s was all better than commercial activated carbon. Musa basjoo, which appears like a tree and have three layers of structure involves nano-/micro-/millimeter level, that endowed the PC with abundant interconnected pores after KOH activation. The products displayed high C_s and good cycling performance (Zheng et al., 2016a).

In addition to wood, plants with a similar structure like shrimp shell, which preserve its layered structure after carbonization and washing with an acid solution, should be a kind of promising candidate for HPC. The microstructure of these plants, such as the flower petals andtree leaves, could be kept by shape fixing via a salt recrystallization strategy, which involves the addition of salt crystals with a high melting point (Ding et al., 2015). Hence, the salt sealing strategy was utilized to fabricate graphene-like PC nanosheets (GPCN) derived from salvia splendens' flower petals. The obtained PC consisted of 10.26% O and 2.3% N through elemental analysis, and it owns high SSA (∼1,051 m^2/g). Thanks to these characteristics, the GPCN-based carbon materials exhibited ∼220 F/g at 20 A/g, and showed a high-rate capability (86.3% capacity retention from 1 to 100 A/g in 6 M KOH solution) (Liu et al., 2018b). In addition, PC derived from paulownia flower by pyrolysis carbonization and chemical activation also showed high SSA, suitable size distribution, superb wettability and partial graphitization phase, which endowed the electrode with a C_s of 297 F/g at 1 A/g in 1 M H_2SO_4 solution, and the corresponding electrode material exhibited high-energy densities of ∼22 Wh/kg as the power output is 3,781 W/kg (Chang et al., 2015). Moreover, other kinds of flower-derived carbon have been prepared by carbonization and activation process, such as camellia and pine cone flower

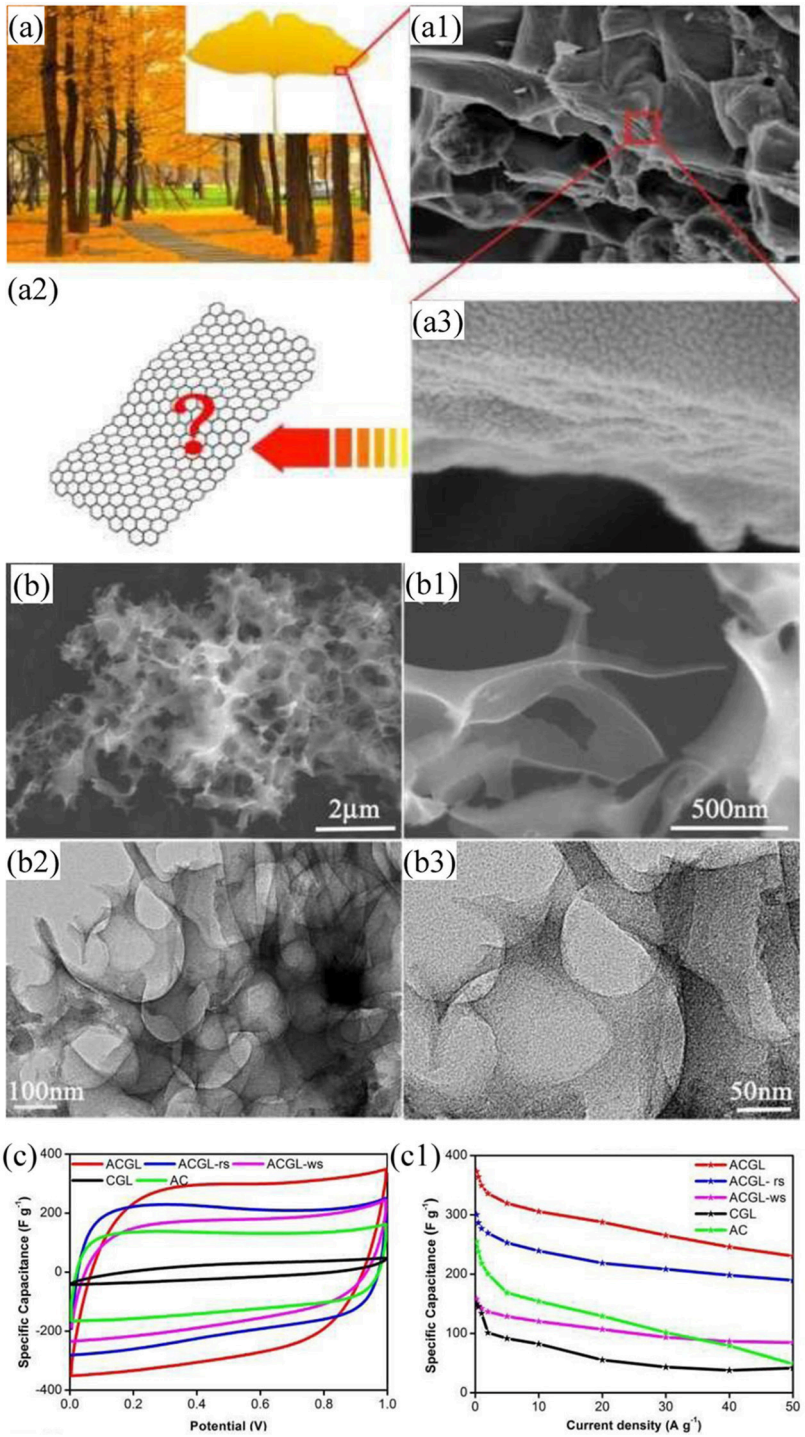

FIGURE 8 | Optical image **(a)** and SEM micrograph of ginkgo biloba **(a1–a3)**; **(b–b3)** SEM and TEM images of carbonized ginkgo biloba; **(c1–c2)** electrochemical performance of PC. Reprinted with permission from Hao et al. (2016). Copyright 2016 Royal Society of Chemistry.

(Nagaraju et al., 2016; Ma et al., 2017), Borassus flabellifer flower (Sivachidambaram et al., 2017), Osmanthu's flower (Zou et al., 2018), cornstalk (Wang et al., 2018b), rice husk (Dong et al., 2018), grape seeds (Guardia et al., 2019), rice straw (Liu et al., 2018d), walnut shell (Wang et al., 2019), wood sawdust (Sevilla et al., 2019) all of these PC electrode materials delivered a relative high C_s and good rate capacity owing to their fine microstructure and abundant N, O elements.

What's more, leaves with a delicate hierarchical structure, which promote the diffusion of electrolytes in living organisms, are also a good choice for transferring it into HPC materials. Li proposed a facile strategy to fabricate a free-standing bio-carbon supercapacitor derived from sisal leaves by being carbonized at 1,000°C for two times and by chemical activation afterwards, was removed and freeze-dried; the developed free-standing electrode exhibited a high C_s of 204 F/g at 1 A/g and good rate capacity; at the same time, it also delivered a relative steady capacity in an organic electrolyte (Wang et al., 2016c). It is worth noting that the combination of the physical and chemical activation method might bring about unexpected results. Li (Li et al., 2015d) proposed a novel strategy to treat the fallen leaves by the activations of mixed KOH and $KHCO_3$. The combination of KOH and $KHCO_3$ led to the enlargement of pore size, which benefited the diffusion of ions and is helpful to enhance the specific capacity and rate performance of carbon materials, the electrochemical characterizations' results revealed that this novel strategy endows the PC with a capacity of 242 F/g at 0.3 A/g in 6 M KOH solution, and it also showed a relative good cyclic performance. Although the activation process is a common method to fabricate biomass-derived PC materials, while the physical or chemical activates, reaction always accompanied with the collapse of the fine microstructure of the biomass, and further affecting the ion/electron diffusion during energy storage. Hence, a possible way should be developed to replace the activation process while endows the PC with high SSA and abundant pore structure. Huang (Huang et al., 2017) proposed a facile technique, which involves indicalamus leaves and polytetrafluoroethylene as carbon precursor and silica-*in-situ*-remover, respectively, the obtained PC owns a SSA of ∼1,800 m^2/g, and exhibited high capacitance (326 F/g in 1 V supercapacitor), high-energy density (23.7 Wh/kg at power density of 224.5 W/kg). Furthermore, hydrothermal treatment is a benefit to introducing rich oxygen-group into the framework of carbon, and dual-doped by N, S can promote the electron conduction and increase the active sites of PC materials. Hao and colleagues reported that HPC derived from gingko leaves by hydrothermal treatment in H_2SO_4 and then activated by KOH at elevated temperature in inert atmosphere, the final products contained small amount of N and S according to the EDS analysis; and the PC maintained a high C_s of 364 F/g at 0.5 A/g and excellent cycling capability (98% capacity retention after 30,000 cycles) (Hao et al., 2016). In addition the leaves aforementioned, other leaves, such as tea (Inal et al., 2015; Ma et al., 2017), euonymus japonicas (Zhu et al., 2015), corn (Yang et al., 2017), cabbage (Wang et al., 2016c), have been used as carbon precursors for synthesizing PC materials for supercapacitor electrodes.

CONCLUSION AND PROSPECTIVE

In the new era of energy storage, compared with traditional activated carbon materials, biomass-derived HPC has achieved superior performance because of their natural fine structure and rich race elements in the organic tissue. However, it is worth noting that their rate capability performance is not satisfied especially at a high charge/discharge electric current condition. That should be contributed to the high concentration of oxygen groups in carbon framework, which is helpful for enhancing the hydrophilic of carbon materials, and further facilitating the infiltration of electrolyte, while these oxygen groups hamper the electric conductivity of PC. Hence, it is urgent to develop an efficient strategy to balance the wettability and electric conductivity of the carbon matrix, and that calls for the joint from theoretical and experimental researches.

Till now, the chemical activation process through KOH, NaOH etc. is a common tool for preparing porous carbon with a rich porous structure, especially for micropores. It should be noteworthy that a large amount of volatile-gases will be formed because of the reaction between KOH and carbon matrix at elevated temperature, these volatile gases, including metal K, CO, CO_2, H_2, and H_2O, not only lead to the formation of abundant micropores, they also threaten the safety of the instrument because of the strong corrosiveness of metal K. Therefore, other activation strategies should be developed to meet the demand of industrialization.

Ion diffusion is a key issue in supercapacitor systems. Although molecular simulation provides different viewpoints for us to design electrode materials with high efficiency; recently, it mainly focuses on the ion-diffusion within ultra-small pores, and it is still a big challenge for us to investigate the diffusion process of ions in hierarchical pore structure, which is extremely important to enhance the electrochemical performance of PC. Moreover, from the perspective of the environment, security and cost, aqueous electrolyte, but not ionic liquids, should be a better choice for the wide application of supercapacitors in energy storage. However, most of the previous studies have been focused on simulating ion behavior in ionic liquids, which is quite different from the aqueous electrolytes, including ion size, solvation shell and diffusion coefficient. Hence, it is necessary to carry out related studies, and investigate the ion diffusion behavior in aqueous electrolytes, then push the development of supercapacitor.

The impact of carbon doping is still unclear, although doped PC materials provide great opportunities to meet the energy density gap between supercapacitor and battery. As we know, introducing nitrogen into the framework of carbon is always accompanied with the enhancement of electrical conductivity and increasing of electrochemically-active sites compared with commercial carbon, which further results in huge improvement of C_s because of an additional faradaic contribution, while the enhancement is quite limited in an aqueous electrolyte. Meanwhile, although the promising prospect of aqueous electrolyte, till now, ions liquids offer better capacitive performance, while it still needs to investigate numerous cations, anions and solvent molecules to achieve more excellent performance to meet the requirement of the industry. Therefore, high-throughput techniques, already applied in battery materials and electrolytes, is a powerful tool for the exploitation of promising systems among thousands of candidates for supercapacitors, and the systems-screening process is closely related to the results of *in-situ* experiments and simulation in molecular level.

Unveiling the ion adsorption and charge storage in PC materials for supercapacitor is essential for its applications; in the meantime, it also promotes the development of other energy storage system, for example, redox flow batteries, biofuel cells, flow capacitors. Hence, it is of central importance to combine the experimental and theoretical tools gained from supercapacitors to promote the development of other current/future technologies.

At last, it is noteworthy that previously reported electrode materials with high gravimetric/areal/volumetric capacitance is meaningless if we ignore the corresponding mass loading/working area/ total volume of the electrode. Hence, effective metrics are required to evaluate the performance of numerous materials for supercapacitors, including biomass-derived PC. As for gravimetric capacitance, ultra-small mass loading means the storage of a limited amount of charges. So, the mass loading of electrodes is a key parameter in comparing the capacitance variation, and it is still urgent to improve electrochemical performance of supercapacitor at high mass loading, but not the C_s of the electrode with small loading active materials.

AUTHOR CONTRIBUTIONS

SY and JZ were responsible for literature searching and drafting. All authors contributed equally to the final writing of the paper.

FUNDING

This research was supported by National Nature Science Foundation of China (51702139) and Youth Science Foundation (20151BAB216007, GJJ150637, 20161BAB216122).

REFERENCES

Abioye, A. M., and Ani, F. N. (2015). Recent development in the production of activated carbon electrodes from agricultural waste biomass for supercapacitors: a review. *Renew. Sustain. Energy Rev.* 52, 1282–1293. doi: 10.1016/j.rser.2015.07.129

An, K. H., Kim, W. S., Park, Y. S., Moon, J. M., Bae, D. J., Lim, S. C., et al. (2001). Electrochemical properties of high-power supercapacitors using single-walled carbon nanotube electrodes. *Adv. Funct. Mater.* 11, 387–392. doi: 10.1002/1616-3028(200110)11:5<;387::AID-ADFM387>3.0.CO;2-G

An, Y., Yang, Y., Hu, Z., Guo, B., Wang, X., Yang, X., et al. (2017). High-performance symmetric supercapacitors based on carbon nanosheets framework with graphene hydrogel architecture derived from cellulose acetate. *J. Power Sources* 337, 45–53. doi: 10.1016/j.jpowsour.2016.10.112

Augustyn, V., Simon, P., and Dunn, B. (2014). Pseudocapacitive oxide materials for high-rate electrochemical energy storage. *Energy Environ. Sci.* 7, 1597–1614. doi: 10.1039/c3ee44164d

Bakierska, M., Chojnacka, A., M, S., Natkanski, P., Gajewska, M., Rutkowska, M., et al. (2017). Multifunctional carbon aerogels derived by sol–gel process of natural polysaccharides of different botanical origin. *Materials.* 10:1336. doi: 10.3390/ma10111336

Barzegar, F., Bello, A., Dangbegnon, J. K., Manyala, N., and Xia, X. (2017). Asymmetric supercapacitor based on activated expanded graphite and pinecone tree activated carbon with excellent stability. *Appl. Energy* 207, 417–426. doi: 10.1016/j.apenergy.2017.05.110

Borchardt, L., Oschatz, M., and Kaskel, S. (2013). Tailoring porosity in carbon materials for supercapacitor applications. *Mater. Horizons* 1, 157–168. doi: 10.1039/C3MH00112A

Cao, X., Shi, Y., Shi, W., Lu, G., Huang, X., Yan, Q., et al. (2011). Preparation of novel 3D graphene networks for supercapacitor applications. *Small* 7, 3163–3168. doi: 10.1002/smll.201100990

Chan, K., Choi, Y. O., Lee, W. J., and Yang, K. S. (2004). Supercapacitor performances of activated carbon fiber webs prepared by electrospinning of PMDA-ODA poly(amic acid) solutions. *Electrochim. Acta* 50, 883–887. doi: 10.1016/j.electacta.2004.02.072

Chang, B., Yin, H., Zhang, X., Zhang, S., and Yang, B. (2017). Chemical blowing strategy synthesis of nitrogen-rich porous graphitized carbon nanosheets: morphology, pore structure and supercapacitor application. *Chem. Eng. J.* 312, 191–203. doi: 10.1016/j.cej.2016.11.129

Chang, H. K., Wee, J. H., Kim, Y. A., Yang, K. S., and Yang, C. M. (2016). Tailoring pore structure of carbon nanofiber for achieving ultrahigh-energy-density supercapacitors using ionic liquid as electrolyte. *J. Mater. Chem. A* 4, 4763–4770. doi: 10.1039/C5TA10500E

Chang, J., Gao, Z., Wang, X., Wu, D., Xu, F., Wang, X., et al. (2015). Activated porous carbon prepared from paulownia flower for high performance supercapacitor electrodes. *Electrochim. Acta* 157, 290–298. doi: 10.1016/j.electacta.2014.12.169

Chen, C., Zhang, Y., Li, Y., Dai, J., Song, J., Yao, Y., et al. (2017a). All-wood, low tortuosity, aqueous, biodegradable supercapacitors with ultra-high capacitance. *Energy Environ. Sci.* 10, 538–545. doi: 10.1039/C6EE03716J

Chen, H., Liu, D., Shen, Z., Bao, B., Zhao, S., and Wu, L. (2015). Functional biomass carbons with hierarchical porous structure for supercapacitor electrode materials. *Electrochim. Acta* 180, 241–251. doi: 10.1016/j.electacta.2015.08.133

Chen, L., Ji, T., Mu, L., and Zhu, J. (2016). Cotton fabric derived hierarchically porous carbon and nitrogen doping for sustainable capacitor electrode. *Carbon* 111, 839–848. doi: 10.1016/j.carbon.2016.10.054

Chen, L. F., Huang, Z. H., Liang, H. W., Yao, W. T., Yu, Z. Y., and Yu, S. H. (2013). Flexible all-solid-state high-power supercapacitor fabricated with nitrogen-doped carbon nanofiber electrode material derived from bacterial cellulose. *Energy Environ. Sci.* 6, 3331–3338. doi: 10.1039/c3ee42366b

Chen, L. F., Lu, Y., Yu, L., and Lou, X. W. (2017b). Designed formation of hollow particle-based nitrogen-doped carbon nanofibers for high-performance supercapacitors. *Energy Environ. Sci.* 10, 1777–1783. doi: 10.1039/C7EE00488E

Chen, X., Zhang, J., and Zhang, B. (2017c). A novel hierarchical porous nitrogen-doped carbon derived from bamboo shoot for high performance supercapacitor. *Sci. Rep.* 7:7362. doi: 10.1038/s41598-017-06730-x

Chen, Z., Peng, X., Zhang, X., Jing, S., Zhong, L., and Sun, R. (2017d). Facile synthesis of cellulose-based carbon with tunable N content for potential supercapacitor application. *Carbohydr. Polym.* 170, 107–116. doi: 10.1016/j.carbpol.2017.04.063

Cheng, F., Liang, J., Tao, Z., and Chen, J. (2011). Functional materials for rechargeable batteries. *Adv. Mater.* 23, 1695–1715. doi: 10.1002/adma.201003587

Chmiola, J., Yushin, G., Gogotsi, Y., Portet, C., Simon, P., and Taberna, P. L. (2006). Anomalous increase in carbon capacitance at pore sizes less than 1 nanometer. *Science* 313, 1760–1763. doi: 10.1126/science.1132195

Chu, S., and Majumdar, A. (2012). Opportunities and challenges for a sustainable energy future. *Nature* 488:294. doi: 10.1038/nature11475

Davis, T. A., Volesky, B., and Mucci, A. (2003). A review of the biochemistry of heavy metal biosorption by brown algae. *Water Res.* 37, 4311–4330. doi: 10.1016/S0043-1354(03)00293-8

Deng, J., Xiong, T., Xu, F., Li, M., Han, C., Gong, Y., et al. (2015). Inspired by bread leavening: one-pot synthesis of hierarchically porous carbon for supercapacitors. *Green Chem.* 17, 4053–4060. doi: 10.1039/C5GC00523J

Ding, W., Li, L., Xiong, K., Wang, Y., Li, W., Nie, Y., et al. (2015). Shape fixing via salt recrystallization: a morphology-controlled approach to convert nanostructured polymer to carbon nanomaterial as a highly active catalyst for oxygen reduction reaction. *J. Am. Chem. Soc.* 137:5414. doi: 10.1021/jacs.5b00292

Dong, S. A., He, X. J., Zhang, H. F., Xie, X. Y., Yu, M. X., Yu, C., et al. (2018). Surface modification of biomass-derived hard carbon by grafting porous

carbon nanosheets for high-performance supercapacitors. *J. Mater. Chem. A* 33, 15954–15960. doi: 10.1039/C8TA04080J

Down, M. P., Rowleyneale, S. J., Smith, G. C., and Banks, C. E. (2018). Fabrication of graphene oxide supercapacitor devices. *ACS Appl. Energy Mater.* 1, 707–714. doi: 10.1021/acsaem.7b00164

Du, G., Bian, Q., Zhang, J., and Yang, X. (2017). Facile fabrication of hierarchical porous carbon for a high-performance electrochemical capacitor. *RSC Adv.* 7, 46329–46335. doi: 10.1039/C7RA08402A

Dubal, D. P., Ayyad, O., Ruiz, V., and Gómezromero, P. (2015). Hybrid energy storage: the merging of battery and supercapacitor chemistries. *Cheminform* 44, 1777–1790. doi: 10.1039/c4cs00266k

Dubal, D. P., Chodankar, N. R., Caban-Huertas, Z., Wolfart, F., Vidotti, M., Holze, R., et al. (2016). Synthetic approach from polypyrrole nanotubes to nitrogen doped pyrolyzed carbon nanotubes for asymmetric supercapacitors. *J. Power Sources* 308, 158–165. doi: 10.1016/j.jpowsour.2016.01.074

Dubinin, M. M. (1960). The potential theory of adsorption of gases and vapors for adsorbents with energetically nonuniform surfaces. *Chem. Rev.* 60, 235–241. doi: 10.1021/cr60204a006

Dunn, B., Kamath, H., and Tarascon, J. M. (2011). Electrical energy storage for the grid: a battery of choices. *Science* 334, 928–935. doi: 10.1126/science.1212741

Enterría, M., Martín-Jimeno, F. J., Suárez-García, F., Paredes, J. I., Pereira, M. F. R., Martins, J. I., et al. (2016). Effect of nanostructure on the supercapacitor performance of activated carbon xerogels obtained from hydrothermally carbonized glucose-graphene oxide hybrids. *Carbon* 105, 474–483. doi: 10.1016/j.carbon.2016.04.071

Fan, X., Yu, C., Yang, J., Ling, Z., Hu, C., Zhang, M., et al. (2015). A layered-nanospace-confinement strategy for the synthesis of two-dimensional porous carbon nanosheets for high-rate performance supercapacitors. *Adv. Energy Mater.* 5:1401761. doi: 10.1002/aenm.201401761

Futaba, D. N., Hata, K., Yamada, T., Hiraoka, T., Hayamizu, Y., Kakudate, Y., et al. (2006). Shape-engineerable and highly densely packed single-walled carbon nanotubes and their application as super-capacitor electrodes. *Nat. Mater.* 5, 987–994. doi: 10.1038/nmat1782

Geng, Z., Wang, H., Wang, R., Zhang, P., Lang, J., and Wang, C. (2016). Facile synthesis of hierarchical porous carbon for supercapacitor with enhanced electrochemical performance. *Mater. Lett.* 182, 1–5. doi: 10.1016/j.matlet.2016.06.046

Gogotsi, Y. (2015). Materials for electrochemical capacitors. *Nat Mater.* 7, 845–854. doi: 10.1038/nmat2297

Guardia, L., Suarez, L., Querejeta, N., Vretenar, V., Kotrusz, P., Skakalova, V., et al. (2019). Biomass waste-carbon/reduced graphene oxide composite electrodes for enhanced supercapacitors. *Electrochimica Acta* 298, 910–917. doi: 10.1016/j.electacta.2018.12.160

Guo, J., Guo, H., Zhang, L., Yang, B., and Cui, J. (2018). Hierarchically porous carbon as a high-rate and long-life electrode material for high-performance supercapacitors. *Chemelectrochem* 5, 770–777. doi: 10.1002/celc.201701286

Hao, E., Liu, W., Liu, S., Zhang, Y., Wang, H., Chen, S., et al. (2016). Rich sulfur doped porous carbon materials derived from ginkgo leaves for multiple electrochemical energy storage devices. *J. Mater. Chem. A* 5, 2204–2214. doi: 10.1039/C6TA08169Jt

Hao, E., Liu, W., Liu, S., Zhang, Y., Wang, H., Chen, S., et al. (2017). Rich sulfur doped porous carbon materials derived from ginkgo leaves for multiple electrochemical energy storage devices. *J. Mater. Chem. A* 5, 2204–2214. doi: 10.1039/C6TA08169J

Hong, W., Wang, L., Liu, K., Han, X., Zhou, Y., Gao, P., et al. (2018). Asymmetric supercapacitor constructed by self-assembled camellia-like BiOCl and activated carbon microspheres derived from sweet potato starch. *J. Alloys Comp.* 746, 292–300. doi: 10.1016/j.jallcom.2018.02.231

Hou, J., Cao, C., Idrees, F., and Ma, X. (2015). Hierarchical porous nitrogen-doped carbon nanosheets derived from silk for ultrahigh-capacity battery anodes and supercapacitors. *ACS Nano* 9:2556. doi: 10.1021/nn506394r

Hu, P., Meng, D., Ren, G., Yan, R., and Peng, X. (2016). Nitrogen-doped mesoporous carbon thin film for binder-free supercapacitor. *Appl. Mater. Today* 5, 1–8. doi: 10.1016/j.apmt.2016.08.001

Hu, S., Zhang, S., Pan, N., and Hsieh, Y. L. (2014). High energy density supercapacitors from lignin derived submicron activated carbon fibers in aqueous electrolytes. *J. Power Sources* 270, 106–112. doi: 10.1016/j.jpowsour.2014.07.063

Huang, J., Chen, L., Dong, H., Zeng, Y., Hu, H., Zheng, M., et al. (2017). Hierarchical porous carbon with network morphology derived from natural leaf for superior aqueous symmetrical supercapacitors. *Electrochim. Acta* 258, 504–511. doi: 10.1016/j.electacta.2017.11.092

Inal, I. I. G., Holmes, S. M., Banford, A., and Aktas, Z. (2015). The performance of supercapacitor electrodes developed from chemically activated carbon produced from waste tea. *Appl. Surf. Sci.* 357, 696–703. doi: 10.1016/j.apsusc.2015.09.067

Jänes, A., Kurig, H., and Lust, E. (2007). Characterisation of activated nanoporous carbon for supercapacitor electrode materials. *Carbon* 45, 1226–1233. doi: 10.1016/j.carbon.2007.01.024

Kai, D., Tan, M. J., Pei, L. C., Yun, K. C., Yong, L. Y., and Xian, J. L. (2016). Towards lignin-based functional materials in a sustainable world. *Green Chem.* 18, 1175–1200. doi: 10.1039/C5GC02616D

Kamat, P. V. (2015). Meeting the clean energy demand: nanostructure architectures for solar energy conversion. *J. Phys. Chem. C* 111, 2834–2860. doi: 10.1021/jp066952u

Kazmerski, L. (2016). Renewable and sustainable energy reviews. *Renew. Sustain. Energy Rev.* 38, 834–847.

Kim, H., Seo, M., Park, M. H., and Cho, J. (2010). A critical size of silicon nano-anodes for lithium rechargeable batteries. *Angewandte Chemie Int. Edition* 122, 2192–2195. doi: 10.1002/ange.200906287

Kondrat, S., Presser, V., Gogotsi, Y., and Kornyshev, A. A. (2012). Effect of pore size and its dispersity on the energy storage in nanoporous supercapacitors. *Energy Environ. Sci.* 5, 6474–6479. doi: 10.1039/c2ee03092f

Kumar, K. T., Sundari, G. S., Kumar, E. S., Ashwini, A., Ramya, M., Varsha, P., et al. (2018). Synthesis of nanoporous carbon with new activating agent for high-performance supercapacitor. *Mater. Lett.* 218, 181–184. doi: 10.1016/j.matlet.2018.02.017

Lee, J., Yoon, S., Oh, S. M., Shin, C. H., and Hyeon, T. (2000). Development of a new mesoporous carbon using an HMS aluminosilicate template. *Adv. Mater.* 12, 359–362. doi: 10.1002/(SICI)1521-4095(200003)12:5<;359::AID-ADMA359>3.0.CO;2-1

Lei, H., Chen, D., and Huo, J. (2016). Blowing and in-situ activation of carbonaceous "lather" from starch: preparation and potential application. *Mater. Des.* 92, 362–370. doi: 10.1016/j.matdes.2015.12.063

Li, B., Dai, F., Xiao, Q., Yang, L., Shen, J., Zhang, C., et al. (2015a). Nitrogen-doped activated carbon for high energy hybrid supercapacitor. *Energy Environ. Sci.* 9, 102–106. doi: 10.1039/C5EE03149D

Li, H., Yuan, D., Tang, C., Wang, S., Sun, J., Li, Z., et al. (2016a). Lignin-derived interconnected hierarchical porous carbon monolith with large areal/volumetric capacitances for supercapacitor. *Carbon* 100, 151–157. doi: 10.1016/j.carbon.2015.12.075

Li, J., Liu, K., Gao, X., Yao, B., Huo, K., Cheng, Y., et al. (2015b). Oxygen and nitrogen enriched 3D porous carbon for supercapacitors of high volumetric capacity. *ACS Appl. Mater. Interfaces* 7, 24622–24628. doi: 10.1021/acsami.5b06698

Li, J., Liu, W., Xiao, D., and Wang, X. (2017a). Oxygen-rich hierarchical porous carbon made from pomelo peel fiber as electrode material for supercapacitor. *Appl. Surf. Sci.* 416, 918–924. doi: 10.1016/j.apsusc.2017.04.162

Li, J., Xie, H., and Li, Y. (2013). Fabrication of graphene oxide/polypyrrole nanowire composite for high performance supercapacitor electrodes. *J. Power Sources* 241, 388–395. doi: 10.1016/j.jpowsour.2013.04.144

Li, W., and Yang, Y. J. (2014). The reduction of graphene oxide by elemental copper and its application in the fabrication of graphene supercapacitor. *J. Solid State Electrochem.* 18, 1621–1626. doi: 10.1007/s10008-014-2391-5

Li, Y., Liu, Q., Kang, D., Gu, J., Zhang, W., and Zhang, D. (2015c). Freeze-drying assisted synthesis of hierarchical porous carbons for high-performance supercapacitors. *J. Mater. Chem. A* 3, 21016–21022. doi: 10.1039/C5TA04233J

Li, Y., Roy, S., Ben, T., Xu, S., and Qiu, S. (2014). Micropore engineering of carbonized porous aromatic framework (PAF-1) for supercapacitors application. *Phys. Chem. Chem. Phys.* 16, 12909–12917. doi: 10.1039/c4cp00550c

Li, Y., Wang, G., Wei, T., Fan, Z., and Yan, P. (2016b). Nitrogen and sulfur co-doped porous carbon nanosheets derived from willow catkin for supercapacitors. *Nano Energy* 19, 165–175. doi: 10.1016/j.nanoen.2015.10.038

Li, Y. T., Pi, Y. T., Lu, L. M., Xu, S. H., and Ren, T. Z. (2015d). Hierarchical porous active carbon from fallen leaves by synergy of K 2 CO 3 and their supercapacitor performance. *J. Power Sources* 299, 519–528. doi: 10.1016/j.jpowsour.2015.09.039

Li, Z., Ahadi, K., Jiang, K., Ahvazi, B., Li, P., Anyia, A. O., et al. (2017b). Freestanding hierarchical porous carbon film derived from hybrid nanocellulose for high-power supercapacitors. *Nano Res.* 10, 1847–1860. doi: 10.1007/s12274-017-1573-8

Lin, T., Chen, I. W., Liu, F., Yang, C., Bi, H., Xu, F., et al. (2015). Nitrogen-doped mesoporous carbon of extraordinary capacitance for electrochemical energy storage. *Science* 350, 1508–1513. doi: 10.1126/science.aab3798

Liu, B., Yang, M., Chen, H., Liu, Y., Yang, D., and Li, H. (2018b). Graphene-like porous carbon nanosheets derived from salvia splendens for high-rate performance supercapacitors. *J. Power Sources* 397, 1–10. doi: 10.1016/j.jpowsour.2018.06.100

Liu, C., Yan, X., Hu, F., Gao, G., Wu, G., and Yang, X. (2018c). Toward superior capacitive energy storage: recent advances in pore engineering for dense electrodes. *Adv. Mater.* 30:1705713. doi: 10.1002/adma.201705713

Liu, C., Yu, Z., Neff, D., Zhamu, A., and Jang, B. Z. (2010). Graphene-based supercapacitor with an ultrahigh energy density. *Nano Lett.* 10, 4863–4868. doi: 10.1021/nl102661q

Liu, J., Wang, J., Xu, C., Jiang, H., Li, C., Zhang, L. L., et al. (2018a). Advanced energy storage devices: basic principles, analytical methods, and rational materials design. *Adv. Sci.* 5:1700322. doi: 10.1002/advs.201700322

Liu, M. C., Kong, L. B., Zhang, P., Luo, Y. C., and Kang, L. (2012). Porous wood carbon monolith for high-performance supercapacitors. *Electrochim. Acta* 60, 443–448. doi: 10.1016/j.electacta.2011.11.100

Liu, S. B., Yang, Z., Zhang, B. H., Xia, H., Zhou, J. F., Xie, W. K., et al. (2018d). Nano-micro carbon spheres anchored on porous carbon derived from dual-biomass as high rate performance supercapacitor electrodes. *J. Power Sources* 381, 116–126. doi: 10.1016/j.jpowsour.2018.02.014

Lota, G., Krawczyk, P., Lota, K., Sierczynska, A., Kolanowski, Ł., Baraniak, M., et al. (2016). The application of activated carbon modified by ozone treatment for energy storage. *J. Solid State Electrochem.* 20:2857. doi: 10.1007/s10008-016-3293-5

Lv, Y., Gan, L., Liu, M., Xiong, W., Xu, Z., Zhu, D., et al. (2012). A self-template synthesis of hierarchical porous carbon foams based on banana peel for supercapacitor electrodes. *J. Power Sources* 209, 152–157. doi: 10.1016/j.jpowsour.2012.02.089

Lv, Y., Zhang, F., Dou, Y., Zhai, Y., Wang, J., Liu, H., et al. (2011). A comprehensive study on KOH activation of ordered mesoporous carbons and their supercapacitor application. *J. Mater. Chem.* 22, 93–99. doi: 10.1039/C1JM12742J

Ma, C., Li, Z., Li, J., Fan, Q., Wu, L., Shi, J., et al. (2018). Lignin-based hierarchical porous carbon nanofiber films with superior performance in supercapacitors. *Appl. Surf. Sci.* 456, 568–576. doi: 10.1016/j.apsusc.2018.06.189

Ma, G., Li, J., Sun, K., Peng, H., Feng, E., and Lei, Z. (2017). Tea-leaves based nitrogen-doped porous carbons for high-performance supercapacitors electrode. *J. Solid State Electrochem.* 21, 1–11. doi: 10.1007/s10008-016-3389-y

Ma, X., Kolla, P., Zhao, Y., Smirnova, A. L., and Hao, F. (2016). Electrospun lignin-derived carbon nanofiber mats surface-decorated with MnO 2 nanowhiskers as binder-free supercapacitor electrodes with high performance. *J. Power Sources* 325, 541–548. doi: 10.1016/j.jpowsour.2016.06.073

Mccloskey, B. D. (2015). Expanding the ragone plot: pushing the limits of energy storage. *J. Phys. Chem. Lett.* 6:3592. doi: 10.1021/acs.jpclett.5b01813

Miller, J. R., and Simon, P. (2008). Materials science. electrochemical capacitors for energy management. *Science* 321, 651–652. doi: 10.1126/science.1158736

Mo, R.-J., Zhao, Y., Zhao, M.-M., Wu, M., Wang, C., Li, J.-P., et al. (2018). Graphene-like porous carbon from sheet cellulose as electrodes for supercapacitors. *Chem. Eng. J.* 346, 104–112. doi: 10.1016/j.cej.2018.04.010

Momodu, D., Madito, M., Barzegar, F., Bello, A., Khaleed, A., Olaniyan, O., et al. (2017). Activated carbon derived from tree bark biomass with promising material properties for supercapacitors. *J. Solid State Electrochem.* 21, 859–872. doi: 10.1007/s10008-016-3432-z

Morenocastilla, C., Garcíarosero, H., and Carrascomarín, F. (2017). Symmetric supercapacitor electrodes from KOH activation of pristine, carbonized, and hydrothermally treated melia azedarach stones. *Materials.* 10:747. doi: 10.3390/ma10070747

Nagaraju, G., Lim, J. H., Cha, S. M., and Yu, J. S. (2016). Three-dimensional activated porous carbon with meso/macropore structures derived from fallen pine cone flowers: A low-cost counter electrode material in dye-sensitized solar cells. *J. Alloys Comp.* 693, 1297–1304. doi: 10.1016/j.jallcom.2016.10.015

Pang, L., Zou, B., Han, X., Cao, L., Wang, W., and Guo, Y. (2016a). One-step synthesis of high-performance porous carbon from corn starch for supercapacitor. *Mater. Lett.* 184, 88–91. doi: 10.1016/j.matlet.2016.07.147

Pang, L., Zou, B., Zou, Y., Han, X., Cao, L., Wang, W., et al. (2016b). A new route for the fabrication of corn starch-based porous carbon as electrochemical supercapacitor electrode material. *Colloids Surfaces A Physicochem. Eng. Aspects* 504, 26–33. doi: 10.1016/j.colsurfa.2016.05.049

Peng, H. J., Huang, J. Q., Cheng, X. B., and Zhang, Q. (2017). Review on high-loading and high-energy lithium–sulfur batteries. *Adv. Energy Mater.* 7:1700260. doi: 10.1002/aenm.201700260

Pushparaj, V. L., Shaijumon, M. M., Kumar, A., Murugesan, S., Ci, L., Vajtai, R., et al. (2007). Flexible energy storage devices based on nanocomposite paper. *Proc. Natl. Acad. Sci. USA.* 104, 13574–13577. doi: 10.1073/pnas.0706508104

Qiang, R., Hu, Z., Yang, Y., Li, Z., An, N., Ren, X., et al. (2015). Monodisperse carbon microspheres derived from potato starch for asymmetric supercapacitors. *Electrochim. Acta* 167, 303–310. doi: 10.1016/j.electacta.2015.03.190

Qu, W.-H., Xu, Y.-Y., Lu, A.-H., Zhang, X.-Q., and Li, W.-C. (2015). Converting biowaste corncob residue into high value added porous carbon for supercapacitor electrodes. *Bioresour. Technol.* 189, 285–291. doi: 10.1016/j.biortech.2015.04.005

Ruiz-Rosas, R., Valero-Romero, M. J., Salinas-Torres, D., Rodríguez-Mirasol, J., Cordero, T., Morallón, E., et al. (2014). Electrochemical performance of hierarchical porous carbon materials obtained from the infiltration of lignin into zeolite templates. *ChemSusChem* 7, 1458–1467. doi: 10.1002/cssc.201301408

Salunkhe, R. R., Lin, J., Malgras, V., Dou, S. X., Kim, J. H., and Yamauchi, Y. (2015). Large-scale synthesis of coaxial carbon nanotube/Ni(OH) 2 composites for asymmetric supercapacitor application. *Nano Energy* 11, 211–218. doi: 10.1016/j.nanoen.2014.09.030

Sevilla, M., Diez, N., Ferrero, G. A., and Fuertes, A. B. (2019). Sustainable supercapacitor electrodes produced by the activation of biomass with sodium thiosulfate. *Energy Storage Mater.* 18, 356–365. doi: 10.1016/j.ensm.2019.01.023

Sevilla, M., and Fuertes, A. B. (2016). A green approach to high-performance supercapacitor electrodes: the chemical activation of hydrochar with potassium bicarbonate. *ChemSusChem* 9, 1880–1888. doi: 10.1002/cssc.201600426

Sing, K. S. W. (1985). Reporting physisorption data for gas/solid systems-with special reference to the determination of surface area and porosity. *Pure Appl. Chem.* 57, 603–619. doi: 10.1351/pac198557040603

Sivachidambaram, M., Vijaya, J. J., Kennedy, L. J., Jothiramalingam, R., Allohedan, H. S. A., Munusamy, M. A., et al. (2017). Preparation and characterization of activated carbon derived from the borassus flabellifer flower as an electrode material for supercapacitor applications. *N. J. Chem.* 41, 3939–3949. doi: 10.1039/C6NJ03867K

Suhas, Carrott, P. J. M., and Carrott, M. M. L. R. (2007). Lignin – from natural adsorbent to activated carbon: a review. *Bioresour. Technol.* 98:2301. doi: 10.1016/j.biortech.2006.08.008

Sun, X., Cheng, P., Wang, H., Xu, H., Dang, L., Liu, Z., et al. (2015). Activation of graphene aerogel with phosphoric acid for enhanced electrocapacitive performance. *Carbon.* 92, 1–10. doi: 10.1016/j.carbon.2015.02.052

Sun, Z., Zheng, M., Hu, H., Dong, H., Liang, Y., Xiao, Y., et al. (2018). From biomass wastes to vertically aligned graphene nanosheet arrays: a catalyst-free synthetic strategy towards high-quality graphene for electrochemical energy storage. *Chem. Eng. J.* 336, 550–561. doi: 10.1016/j.cej.2017.12.019

Tang, Z., Pei, Z., Wang, Z., Li, H., Zeng, J., Ruan, Z., et al. (2018). Highly anisotropic, multichannel wood carbon with optimized heteroatom doping for supercapacitor and oxygen reduction reaction. *Carbon.* 130, 532–543. doi: 10.1016/j.carbon.2018.01.055

Thubsuang, U., Laebang, S., Manmuanpom, N., Wongkasemjit, S., and Chaisuwan, T. (2017). Tuning pore characteristics of porous carbon monoliths prepared from rubber wood waste treated with H 3 PO 4 or NaOH and their

potential as supercapacitor electrode materials. *J. Mater. Sci.* 52, 6837–6855. doi: 10.1007/s10853-017-0922-z

Vix-Guterl, C., Frackowiak, E., Jurewicz, K., Friebe, M., Parmentier, J., and Béguin, F. (2005). Electrochemical energy storage in ordered porous carbon materials. *Carbon* 43, 1293–1302. doi: 10.1016/j.carbon.2004.12.028

Wang, B., Li, D., Tang, M., Ma, H., Gui, Y., Tian, X., et al. (2018a). Alginate-based hierarchical porous carbon aerogel for high-performance supercapacitors. *J. Alloys Compd.* 749, 517–522. doi: 10.1016/j.jallcom.2018.03.223

Wang, C. J., Wu, D. P., Wang, H. J., Gao, Z. Y., Xu, F., and Jiang, K. (2018b). A green and scalable route to yield porous carbon sheets from biomass for supercapacitors with high capacity. *J. Mater. Chem. A* 6, 1244–1254. doi: 10.1039/C7TA07579K

Wang, D. W., Li, F., Liu, M., Lu, G. Q., and Cheng, H. M. (2008). 3D aperiodic hierarchical porous graphitic carbon material for high-rate electrochemical capacitive energy storage. *Angewandte Chemie* 120, 379–382. doi: 10.1002/ange.200702721

Wang, G., Wang, H., Lu, X., Ling, Y., Yu, M., Zhai, T., et al. (2014). Solid-state supercapacitor based on activated carbon cloths exhibits excellent rate capability. *Adv. Mater.* 26, 2676–2682. doi: 10.1002/adma.201304756

Wang, J., and Kaskel, S. (2012). KOH activation of carbon-based materials for energy storage. *J. Mater. Chem.* 22, 23710–23725. doi: 10.1039/c2jm34066f

Wang, K., Cao, Y., Wang, X., Castro, M. A., Luo, B., Gu, Z., et al. (2016a). Rod-shape porous carbon derived from aniline modified lignin for symmetric supercapacitors. *J. Power Sources* 307, 462–467. doi: 10.1016/j.jpowsour.2016.01.008

Wang, K., Xu, M., Gu, Y., Gu, Z., and Fan, Q. H. (2016b). Symmetric supercapacitors using urea-modified lignin derived N-doped porous carbon as electrode materials in liquid and solid electrolytes. *J. Power Sources* 332, 180–186. doi: 10.1016/j.jpowsour.2016.09.115

Wang, P., Wang, Q., Zhang, G., Jiao, H., Deng, X., and Liu, L. (2016c). Promising activated carbons derived from cabbage leaves and their application in high-performance supercapacitors electrodes. *J. Solid State Electrochem.* 20, 319–325. doi: 10.1007/s10008-015-3042-1

Wang, X., Li, Y., Lou, F., Buan, M. E. M., Sheridan, E., and Chen, D. (2017). Enhancing capacitance of supercapacitor with both organic electrolyte and ionic liquid electrolyte on a biomass-derived carbon. *RSC Adv.* 7:23859–23865. doi: 10.1039/C7RA01630A

Wang, Y., Shi, Z., Huang, Y., Ma, Y., Wang, C., Chen, M., et al. (2009). Supercapacitor devices based on graphene materials. *J. Phys. Chem. C* 113, 13103–13107. doi: 10.1021/jp902214f

Wang, Y. F., Jiang, H. H., Ye, S. W., Zhou, J. M., Chen, J. H., Zeng, Q. Q., et al. (2019). N-doped porous carbon derived from walnut shells with enhanced electrochemical performance for supercapacitor. *Funct. Mater. Lett.* doi: 10.1142/S1793604719500425. [Epub ahead of print].

Wei, T., Wei, X., Gao, Y., and Li, H. (2015). Large scale production of biomass-derived nitrogen-doped porous carbon materials for supercapacitors. *Electrochim. Acta* 169, 186–194. doi: 10.1016/j.electacta.2015.04.082

Wei, X., Jiang, X., Wei, J., and Gao, S. (2016). Functional groups and pore size distribution do matter to hierarchically porous carbons as high-rate-performance supercapacitors. *Chem. Mater.* 28, 445–458. doi: 10.1021/acs.chemmater.5b02336

Wu, X., Shi, Z., Tjandra, R., Cousins, A., Sy, S., Yu, A., et al. (2015). Nitrogen-enriched porous carbon nanorods templated by cellulose nanocrystals as high performance supercapacitor electrode. *J. Mater. Chem. A* 3, 23768–23777. doi: 10.1039/C5TA07252B

Xiao, K., Ding, L. X., Liu, G., Chen, H., Wang, S., and Wang, H. (2016). Freestanding, hydrophilic nitrogen-doped carbon foams for highly compressible all solid-state supercapacitors. *Adv. Mater.* 28, 5997–6002. doi: 10.1002/adma.201601125

Xiong, S., Fan, J., Wang, Y., Zhu, J., Yu, J., and Hu, Z. (2017). A facile template approach to nitrogen-doped hierarchical porous carbon nanospheres from polydopamine for high-performance supercapacitors. *J. Mater. Chem. A* 5, 18242–18252. doi: 10.1039/C7TA05880B

Xu, K. B., Yang, J. M., and Hu, J. Q. (2018). Synthesis of hollow NiCo2O4 nanospheres with large specific surface area for asymmetric supercapacitors. *J. Colloid Interface Sci.* 511, 456–462. doi: 10.1016/j.jcis.2017.09.113

Xu, W., Wang, J., Ding, F., Chen, X., Nasybulin, E., Zhang, Y., et al. (2014). Lithium metal anodes for rechargeable batteries. *Energy Environ. Sci.* 7, 513–537. doi: 10.1039/C3EE40795K

Yang, X., Du, G., Zhang, L., and Liu, Y. (2016). Preparation of hierarchical porous carbon material derived from starch for high-performance electrochemical capacitor. *Mater. Lett.* 183, 52–55. doi: 10.1016/j.matlet.2016.07.069

Yang, X., Li, C., and Chen, Y. (2017). Hierarchical porous carbon with ultrahigh surface area from corn leaf for high-performance supercapacitors application. *J. Phys. D Appl. Phys.* 50:055501. doi: 10.1088/1361-6463/50/5/055501

Yang, X., Shi, K., Zhitomirsky, I., and Cranston, E. D. (2015). Cellulose nanocrystal aerogels as universal 3D lightweight substrates for supercapacitor materials. *Adv. Mater.* 27, 6104–6109. doi: 10.1002/adma.201502284

Yao, Y., Zhang, Y., Li, L., Wang, S., Dou, S. X., and Liu, X. (2017). Fabrication of hierarchical porous carbon nanoflakes for high-performance supercapacitors. *ACS Appl. Mater. Interfaces* 9:34944. doi: 10.1021/acsami.7b10593

Yi, J., Yan, Q., Wu, C. T., Zeng, Y., Wu, Y., Lu, X., et al. (2017). Lignocellulose-derived porous phosphorus-doped carbon as advanced electrode for supercapacitors. *J. Power Sources* 351, 130–137. doi: 10.1016/j.jpowsour.2017.03.036

Yu, M., Li, J., and Wang, L. (2016). KOH-activated carbon aerogels derived from sodium carboxymethyl cellulose for high-performance supercapacitors and dye adsorption. *Chem. Eng. J.* 310, 300–306. doi: 10.1016/j.cej.2016.10.121

Yu, S., Liu, D., Zhao, S., Bao, B., Jin, C., Huang, W., et al. (2015). Synthesis of wood derived nitrogen-doped porous carbon–polyaniline composites for supercapacitor electrode materials. *RSC Adv.* 5:30943–30949. doi: 10.1039/C5RA01949D

Yuan, K., Hu, T., Xu, Y., Graf, R., Brunklaus, G., Forster, M., et al. (2016). Engineering the morphology of carbon materials: 2D porous carbon nanosheets for high-performance supercapacitors. *Chemelectrochem* 3, 822–828. doi: 10.1002/celc.201500516

Zhang, L., You, T., Tian, Z., Xia, Z., and Feng, X. (2016a). Interconnected hierarchical porous carbon from lignin-derived byproducts of bioethanol production for ultra-high performance supercapacitors. *ACS Appl. Mater. Interfaces* 8:13918. doi: 10.1021/acsami.6b02774

Zhang, L. L., and Zhao, X. S. (2009). Carbon-based materials as supercapacitor electrodes. *Chem. Soc. Rev.* 38:2520. doi: 10.1039/b813846j

Zhang, L. L., Zhou, R., and Zhao, X. S. (2010). Graphene-based materials as supercapacitor electrodes. *J. Mater. Chem.* 20, 5983–5992. doi: 10.1039/c000417k

Zhang, W., Lin, H., Lin, Z., Yin, J., Lu, H., Liu, D., et al. (2015a). 3 D hierarchical porous carbon for supercapacitors prepared from lignin through a facile template-free method. *ChemSusChem* 8, 2114–2122. doi: 10.1002/cssc.201403486

Zhang, W., Zhao, M., Liu, R., Wang, X., and Lin, H. (2015b). Hierarchical porous carbon derived from lignin for high performance supercapacitor. *Colloids Surfaces A Physicochem. Eng. Aspects* 484, 518–527. doi: 10.1016/j.colsurfa.2015.08.030

Zhang, X., Jiao, Y., Sun, L., Wang, L., Wu, A., Yan, H., et al. (2015c). GO-induced assembly of gelatin toward stacked layer-like porous carbon for advanced supercapacitors. *Nanoscale* 8, 2418–2427. doi: 10.1039/C5NR07857A

Zhang, Y., Jia, M., Yu, J., Fan, J., Wang, L., Zou, Y., et al. (2016b). A tunable hierarchical porous carbon from starch pretreated by calcium acetate for high performance supercapacitors. *J. Solid State Electrochem.* 20, 733–741. doi: 10.1007/s10008-015-3101-7

Zhao, J., Lai, H., Lyu, Z., Jiang, Y., Xie, K., Wang, X., et al. (2015). Hydrophilic hierarchical nitrogen-doped carbon nanocages for ultrahigh supercapacitive performance. *Adv. Mater.* 27, 3541–3545. doi: 10.1002/adma.201500945

Zhao, Y. Q., Lu, M., Tao, P. Y., Zhang, Y. J., Gong, X. T., Yang, Z., et al. (2016). Hierarchically porous and heteroatom doped carbon derived from tobacco rods for supercapacitors. *J. Power Sources* 307, 391–400. doi: 10.1016/j.jpowsour.2016.01.020

Zheng, K., Fan, X., Mao, Y., Lin, J., Dai, W., Zhang, J., et al. (2016a). The well-designed hierarchical structure of musa basjoo for supercapacitors. *Sci. Rep.* 6:20306. doi: 10.1038/srep20306

Zheng, L., Zhiyu, W., Mengdi, Z., Chang, Y., Gang, W., Yanfeng, D., et al. (2016b). Sustainable synthesis and assembly of biomass-derived b/n co-doped carbon nanosheets with ultrahigh aspect ratio for high-performance supercapacitors. *Adv. Funct. Mater.* 26, 111–119. doi: 10.1002/adfm.201504004

Zhong, Y., Shi, T., Huang, Y., Cheng, S., Liao, G., and Tang, Z. (2018). One-step synthesis of porous carbon derived from starch for all-carbon binder-free high-rate supercapacitor. *Electrochim. Acta* 269, 676–685. doi: 10.1016/j.electacta.2018.03.012

Zhu, D., Wang, Y., Lu, W., Zhang, H., Song, Z., Luo, D., et al. (2017). A novel synthesis of hierarchical porous carbons from interpenetrating polymer networks for high performance supercapacitor electrodes. *Carbon* 111, 667–674. doi: 10.1016/j.carbon.2016.10.016

Zhu, L., Gao, Q., Tan, Y., Tian, W., Xu, J., Yang, K., et al. (2015). Nitrogen and oxygen co-doped microporous carbons derived from theleaves of Euonymus japonicas as high performance supercapacitor electrode material. *Micropor. Mesopor. Mater.* 210, 1–9. doi: 10.1016/j.micromeso.2015.02.014

Zhuo, H., Hu, Y., Tong, X., Zhong, L., Peng, X., and Sun, R. (2016). Sustainable hierarchical porous carbon aerogel from cellulose for high-performance supercapacitor and CO2 capture. *Ind. Crops Prod.* 87, 229–235. doi: 10.1016/j.indcrop.2016.04.041

Zou, R., Quan, H., Wang, W., Gao, W., Dong, Y., and Chen, D. (2018). Porous carbon with interpenetrating framework from osmanthus flower as electrode materials for high-performance supercapacitor. *J. Environ. Chem. Eng.* 6, 258–265. doi: 10.1016/j.jece.2017.11.080

Zu, G., Shen, J., Zou, L., Wang, F., Wang, X., Zhang, Y., et al. (2016). Nanocellulose-derived highly porous carbon aerogels for supercapacitors. *Carbon* 99, 203–211. doi: 10.1016/j.carbon.2015.11.079

Conflict of Interest Statement: The authors declare that the research was conducted in the absence of any commercial or financial relationships that could be construed as a potential conflict of interest.

frontiers in Chemistry

ORIGINAL RESEARCH
published: 14 May 2019
doi: 10.3389/fchem.2019.00338

Preparation of Flexible Substrate Electrode for Supercapacitor With High-Performance MnO_2 Stalagmite Nanorod Arrays

*Yuanyu Ge, Xianfeng Wang and Tao Zhao**

College of Chemistry, Chemical Engineering and Biotechnology, Donghua University, Shanghai, China

A large-area MnO_2 stalagmite nanorod arrays (SNAs) growing vertically on flexible substrates were successfully fabricated by an easy heat-electrodeposition method. The large specific capacitance (646.4 F g^{-1} at 500 mA g^{-1}) and excellent rate capability (42.3% retention with 40 times of increase) indicate that the prepared MnO_2 SNAs flexible electrode has outstanding electrochemical performance. Furthermore, after 5,000 repetitions of CV tests, the overall specific capacitance could retain ~101.2% compared with the initial value meant a long cycling life. These outstanding properties could be ascribed to the effective conductive transport path between Ni substrate and MnO_2 nanorods, and owing to the stalagmite like structure of MnO_2 nanorods, the exposed sufficient active sites are beneficial to the electrolyte infiltration.

Keywords: large-area, manganese dioxide, stalagmite nanorod arrays, supercapacitors, flexible electrode

OPEN ACCESS

Edited by:
Wenyao Li,
Shanghai University of Engineering Sciences, China

Reviewed by:
Bo Li,
Shanghai Jiao Tong University, China
Guangjin Wang,
Hubei Engineering University, China

****Correspondence:***
Tao Zhao
tzhao@dhu.edu.cn

Specialty section:
This article was submitted to Electrochemistry, a section of the journal Frontiers in Chemistry

Received: *09 April 2019*
Accepted: *25 April 2019*
Published: *14 May 2019*

Citation:
Ge Y, Wang X and Zhao T (2019) Preparation of Flexible Substrate Electrode for Supercapacitor With High-Performance MnO_2 Stalagmite Nanorod Arrays. Front. Chem. 7:338. doi: 10.3389/fchem.2019.00338

INTRODUCTION

The expanding requirement for energy consumption has stimulated the development of electrochemical energy storage devices (Simon and Gogotsi, 2008). Supercapacitors (SCs) occupy an important position in the field of energy storage devices due to their high power density, high-speed of charging and discharging and long cycle life (Burke, 2000). Nowadays, the development of supercapacitors to higher mechanical flexibility has become one of the important trends. It is shown that materials, such as graphene, transition metal dichalcogenides, MXenes (Han et al., 2018), and nanocellulose-graphene composites (Xing et al., 2019) could be used to construct nanomaterials-based flexible electrodes with high performance for supercapacitors, and there were relationships between structures and properties.

There are many different SCs electrode materials, such as carbon-based material (Li G. et al., 2018; Takeuchi et al., 2018) for the electric double layer capacitors (EDLCs), transition metal oxides, nitrides (Yi et al., 2018) and nickel based materials (Feng et al., 2014; Li et al., 2018) for the pseudocapacitors (PCs). Manganese dioxide (MnO_2) is one of the rapid developed metal oxide electrode materials in recent years (Wang et al., 2015). α-MnO_2 has a high specific capacitance among the various crystallographic structures of MnO_2, which is mainly due to its largest tunnel (Sanger et al., 2016) that can store more foreign cations for charge balance. More importantly, the electrolytes used for MnO_2 electrodes are non-corrosive neutral solutions, which is green and fit for environmental protection (Li et al., 2012).

As we know, the effects of active materials on the performance of SCs include morphology, structure, contact with collector plate and active sites, etc. Unfortunately, during the redox reaction, the electrons transport of MnO_2 electrodes often restricted by its high electrical resistivity. In addition, the defect of the conventional powder electrode preparation is that the generated 'dead volume' by the bonding process of the active material to substrate could make a deterioration in the electrochemical properties of the electrodes (Liu et al., 2016). To solve the defects noted above, it could be a feasible way to manufacture binder-free MnO_2 supporting on 3D conductive substrates. The benefits of the 3D binder-free electrode are the enhanced electron transport and sufficient free space between the nanostructures, which contribute to the generation of more active sites for Faradaic reaction. Li et al. prepared the Ni foam-based ultrafine MnO_2 nanobelts with capacitance of 509 F g^{-1} at 0.2 A g^{-1} (Li et al., 2013). Davoglio et al. (2018) synthetized the α-MnO_2 particles at the aqueous-organic interface with capacitance of 289 F g^{-1} at 0.5 A g^{-1}. Although some achievements have been made in the preparation of MnO_2 electrodes on conductive substrates, there is still great potential to develop easy methods for the preparation of high performance MnO_2 nanowires with various forms.

In this paper, the heat-electrodeposition method was adopted to formulate a nanoarrays of stalagmite like MnO_2 on the flexible substrates. The prepared electrode gets capacitance of 646.4 F g^{-1} (500 mA g^{-1}) and 42.3% retention (current density increased 40 times) for a remarkable rate capability. And the total capacitance retention rate after 5,000 cycles is ∼101.2%. Furthermore, to verify the generality of the synthesis method, another flexible activated carbon fiber (ACF) was also used as the substrate for the growth of MnO_2 nanoarrays.

EXPERIMENTAL

Material Preparation

The preparing method in detail was: the heat-electrodeposition process carried on a 3D porous Ni foam. Before electrodeposition, the Ni foam was cut into ∼ 3 × 1 cm^2, and then immersed into a 5 mol/L HCl solutions along with supersonic wave treatment for 10 min to dissolve the NiO layer on the surface. The Ni foam obtained from the previous step was rinsed to neutral with distilled water, and then subjected to vacuum drying (60°C, 4 h). The heat-electrodeposition occurred in a cell with the water bath. The composition of the electrolyte was as follows: $Mn(CH_3COO)_2$ (0.01 M), CH_3COONH_4 (0.02 M) and dimethylsulfoxide (DMSO, 10 vol.%). The corresponding working electrode, the counter electrode and the reference electrode were the treated Ni foam, the Pt plate (1.5 × 1.5 cm^2) and saturated calomel electrode (SCE), respectively. The heat-electrodeposition condition was applied at a constant current (0.5 mA cm^{-2}) by the Autolab electrochemical workstation at ∼ 80°C for 60 min. After that rinsed the obtained sample to neutral and placed it in a 60°C vacuum dryer for 4 h. Finally, the sample was calcined in N_2 atmosphere (heating-up 0.5°C min^{-1}, 250°C, 2 h). The weight gain of the sample after the deposition was the active matter weight.

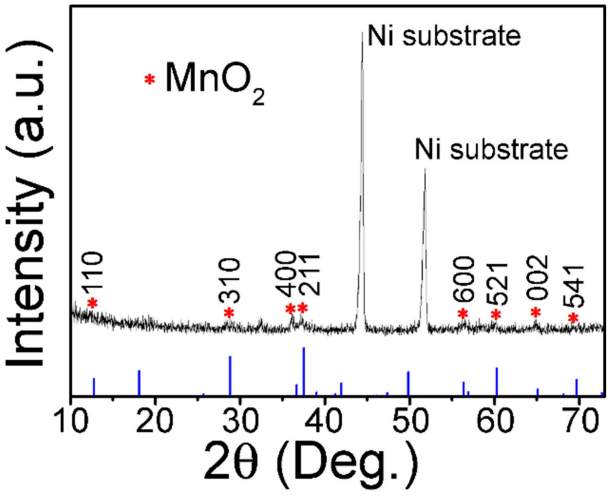

FIGURE 1 | XRD pattern of the prepared MnO_2 sample.

Material Characterizations

In order to analyze the samples qualitatively, the X-ray diffractometer (XRD; Rigaku D/max-2550 PC, Cu-Kα radiation) spectrum was utilized. To observe the microstructures, scanning electron microscope (SEM, Hitachi S-4800) and transmission electron microscope (TEM, JEOL JEM-2100F) were adopted. Mass weighing (Mettler Toledo XS105DU, δ = 0.01 mg).

Electrochemical Measurements

The Electrochemical Workstation (Autolab PGSTAT302N, electrolyte 0.5 M Na_2SO_4) was used to measure electrochemical performance. In the test, the obtained MnO_2 electrode (∼1 cm^2) was used as the working electrode. The counter and reference electrode were the same as mentioned above. Specific capacitance calculation (Guan et al., 2017):

$$C = I \cdot \Delta t / (\Delta V \cdot m) \quad (1)$$

where C (F g^{-1}) is the specific capacitance, I (A) is the discharge current, Δt (s) is the discharge time consumed in the potential range of ΔV, ΔV (V) is the potential window, m (g) is the mass of the active materials.

The weight of the 1 cm^2 MnO_2 electrode was ∼ 1.32 mg. The cyclic voltammetry (CV) potential window was −0.1 to 0.9 V. The scan rates increased from 1 to 100 mV s^{-1}. The galvanostatic charge-discharge (GCD) curves were measured under current densities from 0.5 to 20 A g^{-1}. The cycle life was obtained by CV test (50 mV s^{-1}) with repetitions of 5,000.

RESULTS AND DISCUSSIONS

Except for the two strong peaks of 3D Ni foam substrate, the XRD diffraction pattern in **Figure 1** shows that other peaks at 12.8, 28.8, 36.7, 37.5, 56.4, 60.3, 65.1, and 69.7°, which are characteristic (110), (310), (400), (211), (600), (521), (002), and

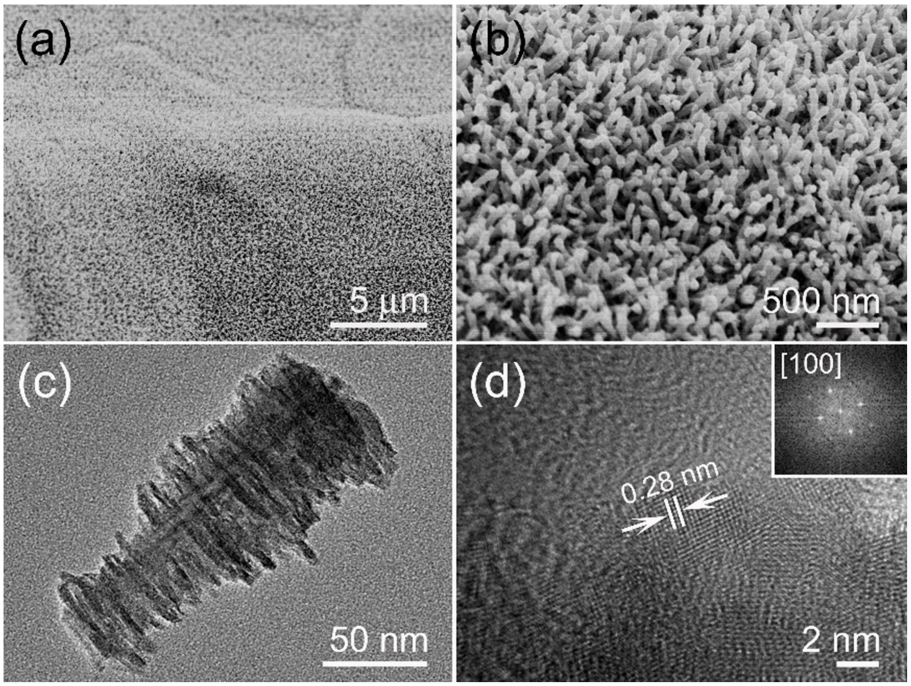

FIGURE 2 | (a) Low and **(b)** enlarged SEM photos of MnO_2 nanoarrays. **(c)** TEM image of the stalagmite MnO_2 nanorod. **(d)** Lattice resolved HRTEM image of a MnO_2 nanorod, an upper right inset showing its corresponding FFT pattern.

(541) reflections of α-MnO_2 (JCPDS 44-0141, a = b = 9.785 Å and c = 2.863 Å), respectively.

An aligned and dense MnO_2 nanoarray is presented in **Figure 2a** and there are no macroscopic defects among them. The enlarged SEM image of **Figure 2b** shows a highly open structure was formed by a vertical MnO_2 arrays on the substrate, which is conducive to the full entry of electrolytes. The TEM characterization was performed in order to get more structural information of the MnO_2 arrays. **Figure 2c** is a single stalagmite like MnO_2 nanorod which appears to be truncated cone-shaped with burrs on its surface. The typical diameters are ∼30 nm of the root and ∼80 nm of the top, and the length is up to ∼180 nm. HRTEM image of the single MnO_2 nanorod edge (**Figure 2d**) suggests that the surface is clearly with uniform single crystal and the interplanar spacing of 0.28 nm matches the (001) lattice plane of α-MnO_2 crystal. In addition, FFT diffraction pattern can also be associated with [100] zone axis of α-MnO_2 crystal (inset of **Figure 2d**).

In order to understand how the unique structure of stalagmite MnO_2 nanorod arrays (MnO_2 SNAs) was formed, the time-dependent electrodepositing experiments were carried out through controlling the electrodeposit reaction time. **Figure 3a** shows that after deposition of 2 min, nanoparticles can be seen on the surface of the substrate with the diameters of 10–20 nm. When the reaction time increases to 20 min, lots of well-distributed cylindrical nanorods began to appear, as displayed in **Figure 3b**. After doubling the reaction time, some irregular burrs were observed around the increased nanorods (**Figure 3c**). As shown in **Figure 3d**, after 60 min of the electrodeposition, it is found that large-scale and uniform nanorod arrays were formed. The change of the morphology of the samples after different electrochemical deposition time could help us estimate the formation process of the MnO_2 nanorod arrays. In the early stage of the reaction, the formation of the nucleus in the precursor solution and the 1D growth behavior of Mn^{2+} (Ding et al., 2011) occurs successively, which result in the deposition of some tiny nanorods randomly and fast all over the surface. As the deposition intensifies, nanoparticles develop into nanorods with burrs, similar to stalagmite. When the reaction time reached to 1 h, the nanorods presented a truncated cone-shaped and formed a high-density array. The formation process of MnO_2 SNAs was elucidated in **Figure 3e**.

Furthermore, to verify the generality of the synthesis method, another flexible ACF substrate was chosen to replace the Ni foam. **Figure S1** shows that the dense needle-like MnO_2 nanorod arrays were grown on the ACF, which proves that the heat-electrodeposition method could be used to fabricate electrodes with different flexible substrates.

Figure 4A shows that the MnO_2 SNAs electrode CV with scanning rate from 1 to 100 mV s^{-1} were approximate to rectangle and symmetrical. All CV curves feature exhibits the pseudocapacitive nature (**Figure S3**) and a high-speed charge and discharge process (Hu et al., 2016). The possible reason for this phenomenon could be that the active sites in the microstructures of the stalagmite MnO_2 SNAs were fully in contact with electrolytes. The symmetrical GCD curves of the MnO_2 SNAs shown in **Figure 4B** revealed that the reversible redox reaction

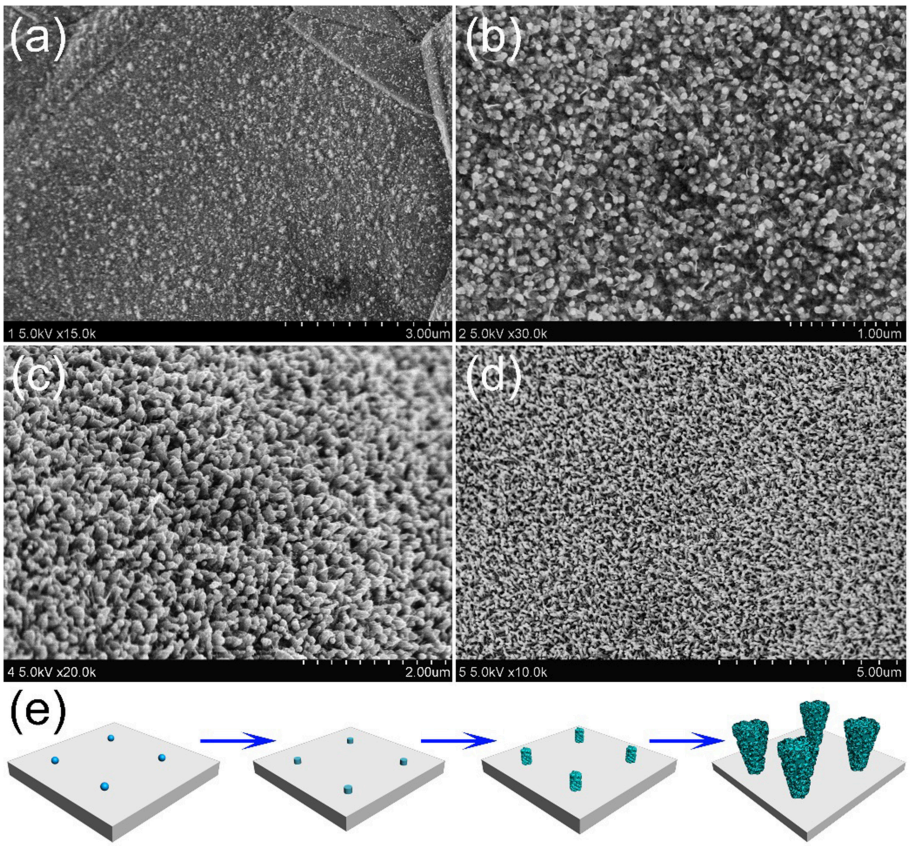

FIGURE 3 | SEM images of the stalagmite MnO_2 nanorod arrays for different electrodepositing time: **(a)** 2 min, **(b)** 20 min, **(c)** 40 min, and **(d)** 60 min; **(e)** Schematic diagram of the MnO_2 SNAs formation.

and good electrochemical capacitance characteristics of the system. In addition, by comparing the specific capacitance of the Ni foam substrate and the prepared MnO_2 SNAs electrode in **Figure S2**, it is found that the substrate has little effect on the capacitance value.

In **Figure 4C**, the calculated specific capacitance of the electrode were 646.4, 587.1, 538.1, 463.6, 387.6, and 273.6 F g^{-1} (Red Star), respectively, which were higher than reported works with similar MnO_2 structure (Li et al., 2013; Wang et al., 2017; Davoglio et al., 2018). **Figure 4C** also shows that the capacitance retention increased with the increase of current density. When it increased 40 times from 0.5 to 20 A g^{-1}, the corresponding specific capacitance reduced from 646.4 to 273.6 F g^{-1} with the retention of 42.3%. The excellent rate capability indicates the potential of the MnO_2 SNAs electrode in high-power applications, and it could be caused by the unique open structure. The advantages of the open structure are that it is favorable for electrolyte infiltration and it owns large electrolytic accessible area, which not only promote redox reaction but also facilitates intercalation and de-intercalation of active species.

Figure 4D shows that a beneficial cycle life of the electrode and the capacitances retention enlarged during the initial 3,000 loops. The possible explanation is that the initially inactive part of the MnO_2 SNAs electrode was activated by the permeated electrolyte and then the specific capacitance is increased (Xia et al., 2012).

After 5,000 cycles, a high specific capacitance retention of 101.2% indicated that the cyclical stability of the MnO_2 SNAs electrode was good. The strong contact between the active matters and the substrate facilitating the collection and enhancement of the electron participation reaction could be an important reason for the effective cycle stability. Thus, it is concluded that the electrode material of the as-synthesized MnO_2 SNAs demonstrates an excellent cycle life.

CONCLUSION

In conclusion, the stalagmite MnO_2 nanorod arrays successfully grew on the flexible substrate by heat-electrochemical deposition method. The prepared MnO_2 SNAs electrode has the high specific capacitance, the outstanding rate capability and the long cycle life, all of which all suggest its excellent electrochemical performance. In addition, this approach could pave the way for a facile low-temperature heat synthetic route for generating a variety of metal oxides arrays flexible substrate electrode.

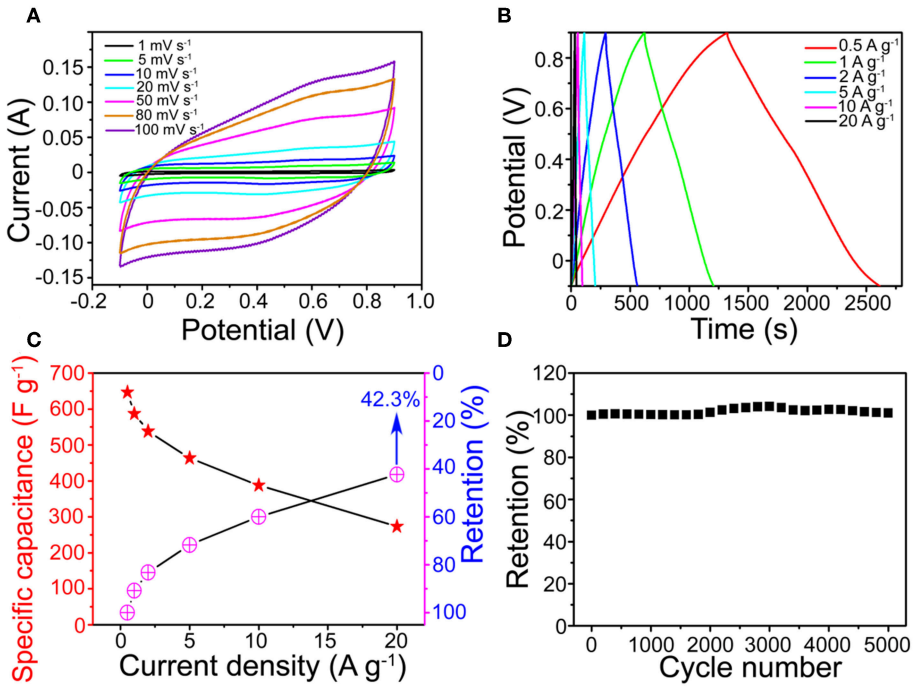

FIGURE 4 | (A) CV and **(B)** GCD curves of the MnO_2 SNAs electrode. **(C)** Specific capacitance and retention of the MnO_2 SNAs electrode. **(D)** CV cycling performance.

DATA AVAILABILITY

The raw data supporting the conclusions of this manuscript will be made available by the authors, without undue reservation, to any qualified researcher.

AUTHOR CONTRIBUTIONS

YG did the experiments and described the images of figures. XW helping with writing. TZ was the supervisor of this research work. All authors participated in the analysis of experimental data and manuscript preparation.

FUNDING

This work was supported by National Key R&D Program (2017YFB0309100) from Ministry of Science and Technology of the People's Republic of China.

SUPPLEMENTARY MATERIAL

The Supplementary Material for this article can be found online at: https://www.frontiersin.org/articles/10.3389/fchem.2019.00338/full#supplementary-material

REFERENCES

Burke, A. (2000). Ultracapacitors: why, how, and where is the technology. *J. Power Sources* 91, 37–50. doi: 10.1016/S0378-7753(00)00485-7

Davoglio, R. A., Cabello, G., Marco, J. F., and Biaggio, S. R. (2018). Synthesis and characterization of α-MnO_2 nanoneedles for electrochemical supercapacitors. *Electrochim. Acta* 261, 428–435. doi: 10.1016/j.electacta.2017.12.118

Ding, S., Zhu, T., Chen, J. S., Wang, Z., Yuan, C., and Lou, X. W. (2011). Controlled synthesis of hierarchical NiO nanosheet hollow spheres with enhanced supercapacitive performance. *J. Mater. Chem.* 21, 6602–6606. doi: 10.1039/c1jm00017a

Feng, L., Zhu, Y., Ding, H., and Ni, C. (2014). Recent progress in nickel based materials for high performance pseudocapacitor electrodes. *J. Power Sources* 267, 430–444. doi: 10.1016/j.jpowsour.2014.05.092

Guan, B. Y., Yu, L., Wang, X., Song, S., and Lou, X. W. D. (2017). Formation of onion-like $NiCo_2S_4$ particles via sequential ion-exchange for hybrid supercapacitors. *Adv. Mater. Deerfield Beach Fla* 29:1605051. doi: 10.1002/adma.201605051

Han, Y., Ge, Y., Chao, Y., Wang, C., and Wallace, G. G. (2018). Recent progress in 2D materials for flexible supercapacitors. *J. Energy Chem.* 27, 57–72. doi: 10.1016/j.jechem.2017.10.033

Hu, J., Qian, F., Song, G., Li, W., and Wang, L. (2016). Ultrafine MnO_2 nanowire arrays grown on carbon fibers for high-performance supercapacitors. *Nanoscale Res. Lett.* 11:469. doi: 10.1186/s11671-016-1693-1

Li, G., Gao, X., Wang, K., and Cheng, Z. (2018). Porous carbon nanospheres with high EDLC capacitance. *Diam. Relat. Mater.* 88, 12–17. doi: 10.1016/j.diamond.2018.06.010

Li, W., Liu, Q., Sun, Y., Sun, J., Zou, R., Li, G., et al. (2012). MnO_2 ultralong nanowires with better electrical conductivity and enhanced supercapacitor performances. *J. Mater. Chem.* 22, 14864–14867. doi: 10.1039/c2jm33368f

Li, W., Xu, K., An, L., Jiang, F., Zhou, X., Yang, J., et al. (2013). Effect of temperature on the performance of ultrafine MnO_2 nanobelt supercapacitors. *J. Mater. Chem. A* 2, 1443–1447. doi: 10.1039/C3TA14182A

Li, W., Zhang, B., Lin, R., Ho-Kimura, S., He, G., Zhou, X., et al. (2018). A dendritic nickel cobalt sulfide nanostructure for alkaline battery electrodes. *Adv. Funct. Mater.* 28:1705937. doi: 10.1002/adfm.201705937

Liu, X., Chen, G., Guan, H., Dong, C., Xiao, X., and Wang, Y. (2016). Binder-free NiO@MnO_2 core-shell electrode: rod-like NiO core prepared through corrosion by oxalic acid and enhanced pseudocapacitance with sphere-like MnO_2 shell. *Electrochim. Acta* 189, 83–92. doi: 10.1016/j.electacta.2015.12.076

Sanger, A., Kumar, A., Kumar, A., and Chandra, R. (2016). Highly sensitive and selective hydrogen gas sensor using sputtered grown Pd decorated MnO_2 nanowalls. *Sens. Actuators B Chem.* 234, 8–14. doi: 10.1016/j.snb.2016.04.152

Simon, P., and Gogotsi, Y. (2008). Materials for electrochemical capacitors. *Nat. Mater.* 7, 845–854. doi: 10.1038/nmat2297

Takeuchi, K., Fujishige, M., Ishida, N., Kunieda, Y., Kato, Y., Tanaka, Y., et al. (2018). High porous bio-nanocarbons prepared by carbonization and NaOH activation of polysaccharides for electrode material of EDLC. *J. Phys. Chem. Solids* 118, 137–143. doi: 10.1016/j.jpcs.2018.02.050

Wang, J.-G., Kang, F., and Wei, B. (2015). Engineering of MnO_2-based nanocomposites for high-performance supercapacitors. *Prog. Mater. Sci.* 74, 51–124. doi: 10.1016/j.pmatsci.2015.04.003

Wang, Y., Fu, A., Liu, X., Wang, Y., Li, Y., Guo, P., et al. (2017). Porous carbon directed growth of carbon modified MnO_2 porous spheres for pseudocapacitor applications. *J. Alloys Compd.* 717, 341–349. doi: 10.1016/j.jallcom.2017.05.035

Xia, X., Tu, J., Zhang, Y., Wang, X., Gu, C., Zhao, X., et al. (2012). High-quality metal oxide core/shell nanowire arrays on conductive substrates for electrochemical energy storage. *ACS Nano* 6, 5531–5538. doi: 10.1021/nn301454q

Xing, J., Tao, P., Wu, Z., Xing, C., Liao, X., and Nie, S. (2019). Nanocellulose-graphene composites: a promising nanomaterial for flexible supercapacitors. *Carbohydr. Polym.* 207, 447–459. doi: 10.1016/j.carbpol.2018.12.010

Yi, C., Zou, J., Yang, H., and Leng, X. (2018). Recent advances in pseudocapacitor electrode materials: transition metal oxides and nitrides. *Trans. Nonferrous Met. Soc.* 28, 1980–2001. doi: 10.1016/S1003-6326(18)64843-5

Conflict of Interest Statement: The authors declare that the research was conducted in the absence of any commercial or financial relationships that could be construed as a potential conflict of interest.

frontiers in Chemistry

ORIGINAL RESEARCH
published: 06 June 2019
doi: 10.3389/fchem.2019.00420

In situ Growth of Cu_2O/CuO Nanosheets on Cu Coating Carbon Cloths as a Binder-Free Electrode for Asymmetric Supercapacitors

Lina Xu[1], Jiao Li[1], Haibin Sun[1]*, Xue Guo[1], Jiakun Xu[2], Hua Zhang[1] and Xiaojiao Zhang[1]*

[1] School of Materials Science and Engineering, Shandong University of Technology, Zibo, China, [2] Yellow Sea Fisheries Research Institute, Chinese Academy of Fishery Sciences, Qingdao, China

Cu_2O/CuO nanosheets *in-situ* grown on Cu-Carbon cloths (Cu-CCs), namely Cu_2O/CuO@Cu-CCs, are constructed by a simple strategy with electroless copper plating, chemical etching, and thermal dehydration. The as-prepared material is directly used as binder-free electrodes for supercapacitors (SCs). CCs coated with Cu, as the current collector, can effectively promote the charge collection and electron transfer, while the hierarchical Cu_2O/CuO nanosheets provide massive active sites for fast faradic reactions. The composite electrode exhibits high specific capacitance [1.71 F cm^{-2}, equivalent to 835.2 F g^{-1}, at the current density of 10 mA cm^{-2} (3.57 A g^{-1})]. The asymmetric supercapacitor device using Cu_2O/CuO@Cu-CCs as the positive electrode and activated carbon as the negative electrode, achieves a superior energy density up to 60.26 Wh kg^{-1} at a power density of 299.73 W kg^{-1} and an excellent long-term cycling stability (9.65% loss of its initial capacitance after 5,000 cycles). The excellent electrochemical performance is mainly ascribed to the unique hierarchical structure of Cu_2O/CuO@Cu-CCs, making it attractive as a potential electrode material for high performance SCs.

Keywords: copper oxide, nanostructures, electrode, carbon cloth, asymmetric supercapacitor

OPEN ACCESS

Edited by:
Wenyao Li,
Shanghai University of Engineering Sciences, China

Reviewed by:
Pankaj Madhukar Koinkar,
Tokushima University, Japan
Edward Gillan,
The University of Iowa, United States

***Correspondence:**
Jiao Li
haiyan9943@163.com
Haibin Sun
hbsun@sdut.edu.cn

Specialty section:
This article was submitted to Electrochemistry, a section of the journal Frontiers in Chemistry

Received: *07 April 2019*
Accepted: *21 May 2019*
Published: *06 June 2019*

Citation:
Xu L, Li J, Sun H, Guo X, Xu J, Zhang H and Zhang X (2019) In situ Growth of Cu_2O/CuO Nanosheets on Cu Coating Carbon Cloths as a Binder-Free Electrode for Asymmetric Supercapacitors. Front. Chem. 7:420. doi: 10.3389/fchem.2019.00420

INTRODUCTION

Supercapacitors (SCs), one of the most promising energy storage devices, have received extensive attention owning to their high power density, fast charge/discharge speed, long cycling life span, and low-cost (Lu et al., 2014; Xiong et al., 2015; Sami et al., 2017; Dai et al., 2018). According to the reaction mechanisms, SCs can be classified into electrical double layer capacitors (EDLCs) and pseudocapacitors (PCs) (Wei et al., 2012). For EDLCs, the charges are stored electrostatically at the electrode/electrolyte interface while typically taking carbon materials as active materials (Surendran et al., 2018). For PCs, the energy is stored within the electrode through the faradic redox reaction while taking transition metal oxides/hydroxides and conducting polymers as the electrode materials, thus the PCs provide much higher energy density and specific capacitance than EDLCs. Nevertheless, there are many of problems scarcely understood which attract large numbers of investigator devote oneself to resolve, such as inadequate energy density and capacitance, poor electrochemical stability for practical applications.

In recent years, various transition metal oxides/hydroxides, such as RuO_2 (Wang et al., 2014), NiO (Ouyang et al., 2019), $Ni(OH)_2$ (Kim et al., 2017), MnO_2 (Huang et al., 2015), Co_3O_4 (Liu T. et al., 2018), $Co(OH)_2$ (Yang et al., 2018), V_2O_5 (Foo et al., 2014), CuO (Bu and Huang, 2017; Li et al., 2017; Liu Y. et al., 2018), Cu_2O (Zhang W. et al., 2016; Ji et al., 2017), have been applied to achieve excellent capacitive performance for PCs. Among these materials, CuO, Cu_2O, or Cu_2O/CuO nanostructures with different configurations including nanoneedle, nanoflowers, nanowires (Dong et al., 2014; Wang et al., 2015; Chen et al., 2016; Xu et al., 2016; Yang et al., 2016), are attracting considerable interest due to their environmental friendliness, numerous reserve, low-cost, chemical stability, and excellent electrochemical properties [theoretical capacitance of CuO up to 1,800 F g^{-1} (Liu Y. et al., 2018) and Cu_2O is up to 2,247 F g^{-1} (Wu et al., 2017)]. However, most of metal oxides/hydroxides were poor in electrical conductivity, making it difficult to achieve high specific capacitance (Xu et al., 2016). To resolve this issue, oxides/hydroxides are typically mixed with ancillary carbon black or binder and then bonded to current collector, but leading to a significant decrease of the overall specific capacitance (Yuan et al., 2017). An effective approach is that, nanostructured electrode materials directly grow on current collectors, forming binder-free electrodes, thus achieving higher energy density (Dong et al., 2014).

Carbon material containing carbon nanotube, graphene and carbon fiber is one kind of the preferred current collectors due to their excellent electrical conductivity and electrochemical stability (Prasad et al., 2011; Moosavifard et al., 2014; Bu and Huang, 2017). Among various carbon materials, carbon cloths (CCs) with low-cost, chemical stability and desirable conductivity, are regarded as novel carbonaceous materials, which are consist of numerous uniform carbon fibers with three-dimensional (3D) structure (Guo et al., 2014; Zhang Y. et al., 2016). The 3D network structure is conducive to shorten the diffusion pathway of ions and accelerate the flow of ions during the electrochemical process. Numerous electrode materials of PCs taking CCs as current collectors have been developed, such as NiCo-LDH@NiOOH (622 F g^{-1} at 1 A g^{-1}) (Liang et al., 2018), $MnNiCoO_4$@MnO_2 (1931 F g^{-1} at 0.8 A g^{-1}) (Saray and Hosseini, 2016), MnO_2 nanosheet arrays (2.16 F cm^{-2}, at 5 mA cm^{-2}) (Guo et al., 2014). Currently, copper oxide and its composite materials are mainly grown on copper foam and copper foil (Zhang et al., 2015; Singh and Sarkar, 2017), and the combination of CuO or Cu_2O with CCs is also in the developing situation. For example, Xu et al. (2016) fabricated CuO nanoflower arrays on CCs, the energy density and power density are 10.05 Wh kg^{-1} and 1,798.5 W kg^{-1}, respectively. Wan et al. (2017) developed forest-like cuprous oxide/copper with the energy density of 24.0 Wh kg^{-1} at 0.625 kW kg^{-1}. However, it is still challenging to evolve the commercially viable Cu oxides/hydroxides with high energy/power density, specific capacitance, and excellent cycling stability (Dong et al., 2014). Therefore, it will be worthy to make a thorough research on CuO or Cu2O electrodes grown on CCs.

In order to improve the kinetics and electrochemical performance of electrodes, two typical methods are usually employed. One straightforward approach is to increase the specific surface area of electrodes to provide more active sites for faradaic redox reaction (Daoping et al., 2014). The other method is to improve the conductivity of electrode material to accelerate electron conduction (Lu et al., 2013). Herein, we firstly synthesized Cu_2O/CuO nanosheets directly grown on CCs which is coated with Cu film by a simple strategy with electroless copper plating, chemical etching and thermal dehydration. The uniform Cu film on carbon microfiber cloth has a strong binding force. In addition, Cu_2O/CuO nanosheets *in situ* grown on CCs provide sufficient active sites for charge/discharge electronic, which is important for energy storage of supercapacitor. Finally, it is worth mentioning that there are still Cu films between CCs and Cu_2O/CuO nanosheets after chemical etching, which is important for promoting electronic conduction.

EXPERIMENTAL

Materials Synthesis

CCs (WOS1002) were purchased from CeTech. $(NH_4)_2S_2O_8$ (Tianjin Huachen Company) and all other reagents (from Aladdin) were of analytical grade without further treatment. In a typical electroless copper plating process, CCs, cut into squares (25 × 25 mm), were firstly heated to 400°C at a heating rate of 10°C min^{-1} and hold for 30 min in muffle furnace under air atmosphere to remove a part of impurities. And then, the CCs were immersed into concentrated nitric acid to make the surface rough, followed by the sensitization and activation treatment. Stannous chloride/hydrochloric acid and silver nitrate/ammonium hydroxide solutions were used as the sensitizer and activator, respectively (Yuan et al., 2017). The composition of the sensitizing and activating solution are shown in **Supplementary Tables 1, 2**. The sensitization and activator treatment adsorbs a layer of active silver particles on the surface of the carbon cloth as active metal particles, and copper ions were first reduced on the active metal particles, so that the reduction reaction of copper proceeds on the surface of the carbon cloth. Catalyzed CCs with a number of active sites were obtained after in NaOH (10%) for 3 min. Subsequently, the catalyzed CCs were immersed into plating solutions and stirred at a rotating speed of 200 r min^{-1} for 60 min at 25°C, during which Cu films were coated on CCs, thus obtaining Cu-CCs samples. The amount of copper retained is about 0.009 g cm^{-2} on the carbon cloth. The composition of the electroless copper plating solution is shown in **Supplementary Table 3**. Formaldehyde is used as a reducing agent, and the main chemical reactions in electroless copper plating solutions are as follows:

$$Cu^{2+} + 2HCHO + 4OH^- \rightarrow Cu + 2HCOO^- + H_2\uparrow + H_2O$$

$$2Cu^{2+} + HCHO + 5OH^- \rightarrow Cu_2O + HCOO^- + 3H_2O$$

$$Cu_2O + 2HCHO + 2OH^- \rightarrow 2Cu + 2HCOO^- + H_2\uparrow + H_2O$$

In the chemical etching process, the Cu-CCs were dipped into 100 mL mixed solutions with 2.5 mol L^{-1} NaOH and 0.1 mol L^{-1} $(NH_4)_2S_2O_8$ at 25°C for a while, $Cu(OH)_2$ arrays

were *in situ* grown on Cu-CCs. After being washed, $Cu(OH)_2$ arrays were decomposed into Cu_2O/CuO arrays through a thermal dehydration at 120°C in air for 3 h, thus obtaining Cu_2O/CuO@Cu-CCs electrodes.

Materials Characterization and Electrochemical Measurements

The phase compositions of the products were identified by X-ray diffraction analysis (XRD, Rigaku-Dmax 2500 diffractometer). The microstructure and morphology were observed by scanning electron microscopy (SEM, HITACHI S4800) and high-resolution transmission electron microscopy (HRTEM, Tecnai G2 F20 STWIN, FEI, USA). X-ray photoelectron spectroscopy (XPS, Kratos Axis Ultra DLD, Britain) was performed using Mg Ka as the exciting source.

Cyclic voltammetry (CV) and galvanostatic charge-discharge (GCD) tests of Cu_2O/CuO@Cu-CCs electrodes were tested on a CHI 660E electrochemical workstation (Shanghai Chenhua Instrument Company, China) in a three-electrode electrochemical cell using a 6 M KOH aqueous solution as the electrolyte at room temperature. The Cu_2O/CuO@Cu-CCs electrodes were used as the working electrode, while a platinum wire and an Ag/AgCl electrode as the counter and reference electrode, respectively. Electrochemical impedance spectroscopy (EIS) tests were performed in the frequency ranging from 106 to 0.01 Hz. The specific capacitances were calculated from the discharge part of the GCD curves using the following equation.

$$C = (I\int Vdt)/(SV^2) \tag{1}$$

where *C* represents the specific capacitance (F cm^{-2}), I represents the discharge current (A), Δt is the total discharging time (s), *S* is the area of the sample (cm^2), and ΔV is the potential change (V) within the discharge time Δt.

Fabrication and Electrochemical Measurements of Asymmetric Supercapacitor

Active carbon, acetylene black, and poly tetra fluoroethylene (PTFE) with a mass ratio of 80:10:10 were mixed with moderate amount of ethanol. The resulting mixture was brushed on carbon cloth and dried at 80°C for 10 h in a vacuum oven. Acetylene black and PTFE are acted as conductive agents and binders, respectively. The asymmetric supercapacitor (ASC) device was assembled by using Cu_2O/CuO@Cu-CCs electrode (with a diameter of 1 cm) and active carbon electrode as the positive and negative electrode, respectively. The filter papers soaked with 6 M KOH solution were taken as separators. As a electrochemical property's asymmetric supercapacitor, the charge stored between the two electrodes should keep the balance relationship ($q^+ = q^-$), which could be calculated by equation (Liu Y. et al., 2018).

$$q = C \bullet m \bullet \Delta V \tag{2}$$

where *C* represents the specific capacitance (F g^{-1}), m is the mass of active materials on both electrodes (g), ΔV is the potential window (V). Therefore, the mass ratio of electroactive material between the two electrodes could be calculated by equation (Li et al., 2019).

$$m^+/m^- = C^-\Delta V^-/C^+\Delta V^+ \tag{3}$$

where C^- (F g^{-1}) and ΔV^- (V) are the specific capacitance and the voltage range of scanning segment of the AC electrode, respectively. C^+ (F g^{-1}) and ΔV^+ (V) are the specific capacitance and the voltage range of scanning segment of the Cu_2O/CuO@Cu-CCs electrode. The specific capacitance, energy density and power density of the ACS device were calculated using the following equations (Ensafi et al., 2018; Liu Y. et al., 2018).

$$Cs = (2I\int Vdt)/(mV^2) \tag{4}$$

$$E = 1/2C\Delta V^2 \tag{5}$$

$$P = E/\Delta t \tag{6}$$

where *Cs* represents the specific capacitance (F g^{-1}), *I* is the discharge current (A), ΔV is the potential window (V), Δt is the discharge time (s), m is the mass of active materials on both electrodes (g), *E* and *P* correspond to the energy density (Wh kg^{-1}) and power density (W kg^{-1}), respectively (Guan et al., 2017).

RESULTS AND DISCUSSION

The schematic illustration of the growth process of Cu_2O/CuO@Cu-CCs electrodes is shown in **Figure 1**. Firstly, the Cu film is uniformly coated on the CCs through electroless copper plating, forming Cu-CCs samples. Subsequently, $Cu(OH)_2$ nanosheet arrays are *in situ* grown on Cu film by alkaline oxidative enchanting in NaOH and $(NH_4)_2S_2O_8$ solution, during which the oxidative $S_2O_8^{2-}$ is attached on the surface of Cu-CCs, and partial CuO are oxidized to Cu^{2+}(Chen et al., 2016). With the reaction of Cu^{2+} and OH^-, $Cu(OH)_2$ nanosheet arrays are formed and then are decomposed into Cu_2O/CuO nanosheets by thermal dehydration, thus obtaining Cu_2O/CuO@Cu-CCs electrodes

XRD patterns of CCs, Cu-CCs and Cu_2O/CuO@Cu-CCs are shown in **Figure 2a**. As can be seen by comparing peaks of CCs and Cu-CCs, the Cu films on CCs leads to the decrease of the characteristic peaks of carbon fiber at $2\theta = 26.4°$. For Cu-CCs samples, there are two strong diffraction peaks at $2\theta = 43.5$ and 50.6°, corresponding to the (111) and (200) planes of the metallic copper (JCPDS no. 04-0836), respectively (Chen et al., 2016). After the heat treatment at 120°C, the sample exhibits four peaks at 2θ of 35.6, 36.4, 39.1, 42.3°, in which $2\theta = 35.6$ and 39.1° correspond to (−111) and (200) planes of the CuO substrates (JCPDS no. 48-1548), while the else two peaks ($2\theta = 36.4$ and 42.3°) are attributed to the (111) and (200) reflections of Cu_2O (JCPDS no. 05-0667). It is worthy to note that Cu and CCs peaks are still observed, therefore, the composition is confirmed to be Cu_2O/CuO@Cu-CCs.

Shown in **Figure 2b** is the SEM image of bare CCs, it can be observed that the surface of the carbon fibers is smooth and

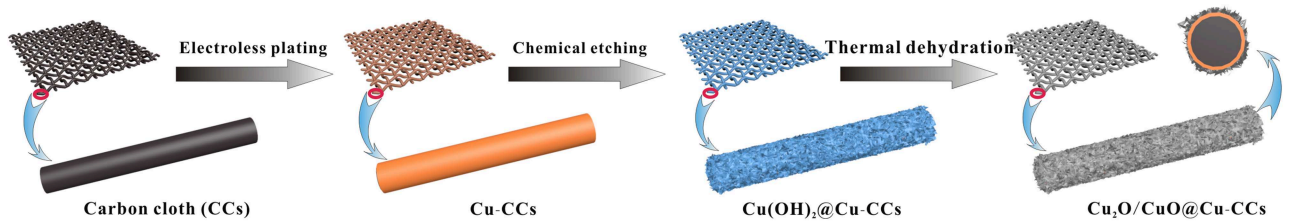

FIGURE 1 | Schematic illustration of the growth process of Cu_2O/CuO nanosheets on Cu coating carbon cloth to prepare Cu_2O/CuO@Cu-CCs electrodes.

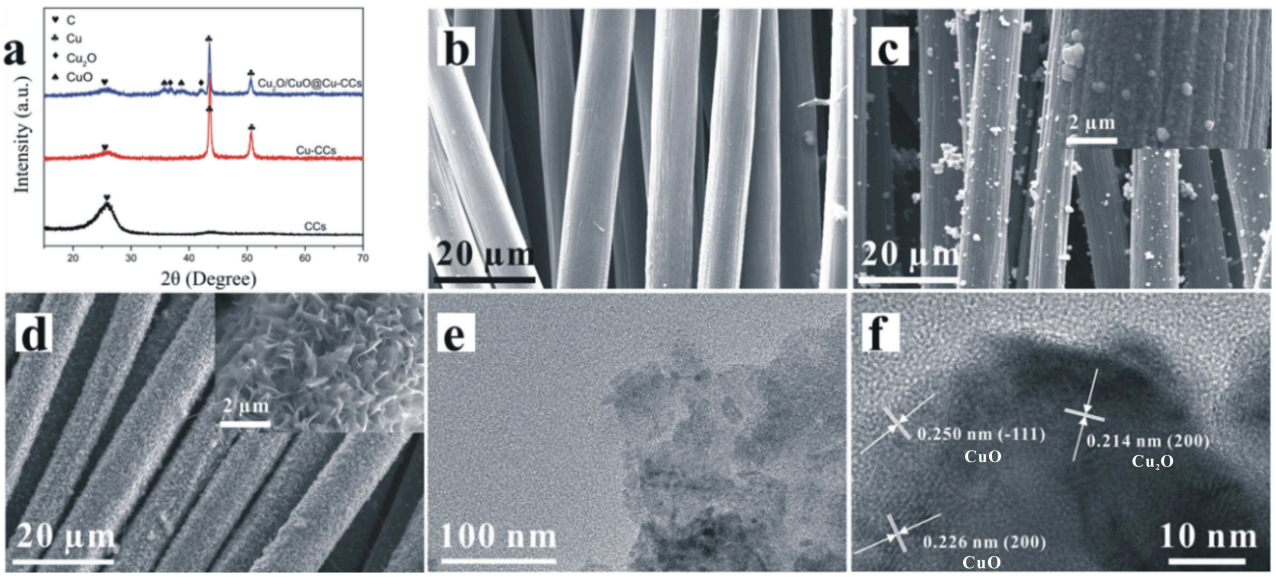

FIGURE 2 | (a) XRD patterns of bare CCs, Cu-CCs, and Cu_2O/CuO@Cu-CCs samples. SEM images of bare **(b)** CCs, **(c)** Cu-CCs, and **(d)** Cu_2O/CuO@Cu-CCs samples. **(e)** TEM image and **(f)** HRTEM image of Cu_2O/CuO nanosheets.

the diameter is around 8–10 μm. In **Figure 2c**, the carbon fibers are uniformly coated with copper films. After being etched in alkaline solution, the morphologies of Cu_2O/CuO nanosheets vary with the change of etching time (**Supplementary Figure 1**). With an etching time of 25 min, the sample exhibits a highly porous cross-linked structure with abundant thin Cu_2O/CuO nanosheets (**Figure 2d**). The lamellar nanosheets can effectively increase the number of active sites, which may be beneficial for promoting charge transfer and redox reaction (Liu Y. et al., 2018). As shown in **Figure 2e**, the porous Cu_2O/CuO nanosheets are ultra-thin, which may enlarge the specific surface area to accelerate the intercalation and de-intercalation of ions (Chen et al., 2016). In addition, the HRTEM image in **Figure 2f** shows that the measured interplanar spacing of 0.250 and 0.226 nm for the well- defined lattice fringes are consistent well with the (−111) and (200) plane of CuO (JCPDS no. 48-1548), and there is a part of interplanar distances calculated to be 0.214 nm, which can be directed as the (200) plane of Cu_2O (JCPDS no. 05-0667)

The XPS spectrums of the surface atomic composition and chemical state of the Cu_2O/CuO@Cu-CCs samples are obtained by Gaussian curve-fitting. As illustrated in **Figure 3A**, the complete spectrum indicates the existence of C, Cu, and O elements in the sample. As shown in **Figure 3B**, there are two sharp peaks located at 932.43 and 952.5 eV, which are correspond to Cu 2p3/2 and Cu 2p1/2, respectively, illustrating the coexistence of Cu^+ and Cu^0 species (Wan et al., 2017). At the same time, there are three satellite peaks with binding energies of 934.2, 943.1, and 953.9 eV indicated the existence of CuO in the samples. Therefore, it can be concluded that the copper is mainly Cu^{2+}, Cu^+, and Cu^0 (Liu Y. et al., 2018). The existence of Cu^0 can be beneficial for improving the electronic conduction of electrodes. As shown in **Figure 3C**, the O 1s XPS spectrum can be deconvoluted into two peaks, one is the peak at 530.3 eV, which represents the oxygen in Cu_2O lattice. Another is the high intensity peak at 531.1 eV, which is attributed to the CuO. This result further confirms the coexistence of CuO and Cu_2O (Singh and Sarkar, 2017). In the **Figure 3D**, C 1s spectrum shows a high intensity peak at 284.5 eV, demonstrating that the intensity of C-C functional group peak is notably strong, further illustrating carbon fiber is stable in Cu_2O/CuO@Cu-CCs.

The CV curves of CCs, Cu-CCs and Cu_2O/CuO@Cu-CCs at a scan rate of 30 mV s^{-1} are shown in **Figure 4A**. It is obvious

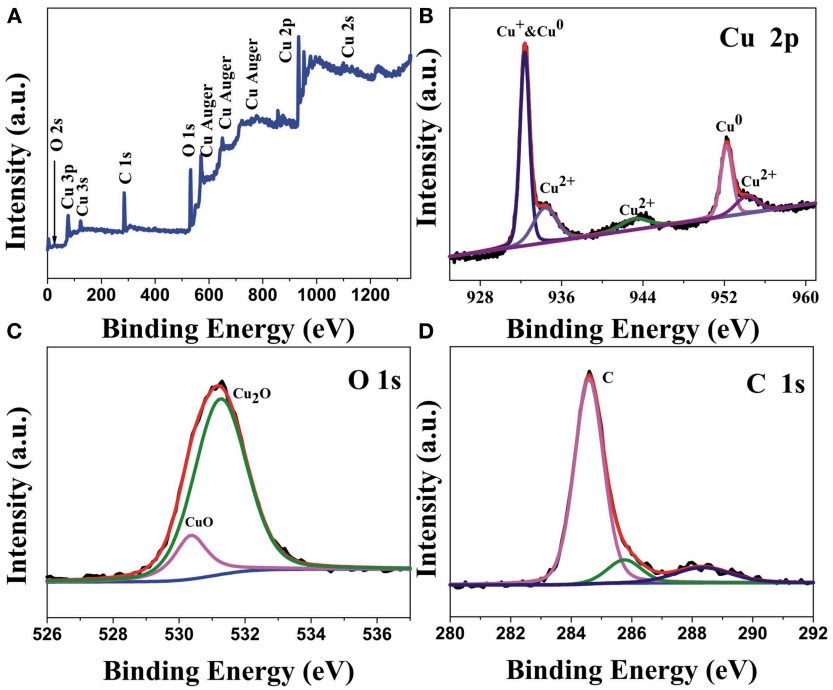

FIGURE 3 | (A) XPS survey spectrum of Cu_2O/CuO@Cu-CCs samples and high relation XPS spectra for **(B)** Cu 2p, **(C)** O 1s, **(D)** C 1s.

that strong pair of anodic and cathodic peaks is clearly visible for Cu_2O/CuO@Cu-CCs and Cu-CCs samples, mainly due to the Faradaic redox reaction (Dong et al., 2014). For Cu-CCs, copper ions mainly derive from the reaction of Cu and KOH electrolyte solution during electrochemical measurement. The pronounced pseudocapacitive characteristic of Cu_2O/CuO@Cu-CCs is mainly attributed to the porous cross-linked Cu_2O/CuO nanosheets while the contribution of capacitance for CCs can be negligible. **Figure 4B** shows the GCD curves of different electrodes at a constant current density of 10 mA cm^{-2}. The non-linear behavior of GCD curves further verifies that the main sources for charge storage originate from Faradaic reactions. The Cu_2O/CuO@Cu-CCs electrode discussed above is the sample etched for 25 min (CV and GCD curves of other samples are shown in **Supplementary Figures 2A,B**), and this sample shows the best pseudocapacitive characteristic with a specific capacitance of 1.71 F cm^{-2} (835.2 F g^{-1}) at 10 mA cm^{-2} (3.57 A g^{-1}) (**Figure 4C**), which is outperform the previously published values of Cu_2O/CuO-based electrodes (1.674 F cm^{-2}, equivalent to 594.27 F g^{-1}, at 2 mA cm^{-2}; 839.9 Fg^{-1}, at 1 mVs^{-1}; 357 F g^{-1}, at 10 A g^{-1}) and more exhaustive data were displayed in **Supplementary Table 4**. The EIS analysis was studied to further clarify the electrochemical behaviors of different electrodes. The Nyquist diagrams are shown in **Figure 4D**, which consist of an approximate semicircle in the high-frequency region and a line in the low-frequency region. All real-axis intercepts are as low as approximately 0.5 Ω, illustrating all the samples have excellent electronic conduction due to the CCs and Cu-CCs current collectors. The depressed semicircle at the high frequency region corresponds to charge transfer resistance (Rct) caused by Faradaic reactions (Ensafi et al., 2018). The Cu_2O/CuO@Cu-CCs electrode has the smallest semicircle, illustrating an enhanced charge transfer. Also, the straight line in low-frequency region can be ascribed to Warburg impedance related to the fast charge diffusion in the electrolyte (Ensafi et al., 2018).

The electrochemical performances of Cu_2O/CuO@Cu-CCs at various scan rates and current densities (**Figures 4E,F**) demonstrate a perfect reversibility during the charge-discharge process. Clearly, the slope of GCD curves decline suddenly at 0.18–0.25 V in charge part and the same as discharge part, corresponding the pseudocapacitance behavior in the CV scans, which is associated with the Faradaic redox reactions of Cu^{2+}/Cu^{+} redox pairs related to OH^{-} as bellows (Guan et al., 2017; Sami et al., 2017).

$$CuO + H_2O + 2e^{-} \leftrightarrow Cu_2O + 2OH^{-}$$
$$Cu_2O + H_2O + 2OH^{-} \leftrightarrow 2Cu(OH)_2 + 2e^{-}$$
$$CuOH + OH^{-} \leftrightarrow Cu(OH)_2 + e^{-}$$
$$CuOH + OH^{-} \leftrightarrow CuO + H_2O + e^{-}$$

Remarkable, with the current density increases from 5 to 30 mA cm^{-2}, the GCD curves present a gradually decreased discharge time but tends to preserve similar shape (**Figure 4F**) and the electrode retains 68.5% of its capacitance (**Figure 4G**), suggesting an excellent rate capability. Furthermore, the Cu_2O/CuO@Cu-CCs electrode delivers excellent cycling stability with only 14.4% loss in specific capacitance after 5,000 cycles at 5 mA cm^{-2} (**Figure 4H**), which can be explained by the stable structure of electrodes after cycling (the inset in **Figure 4H**).

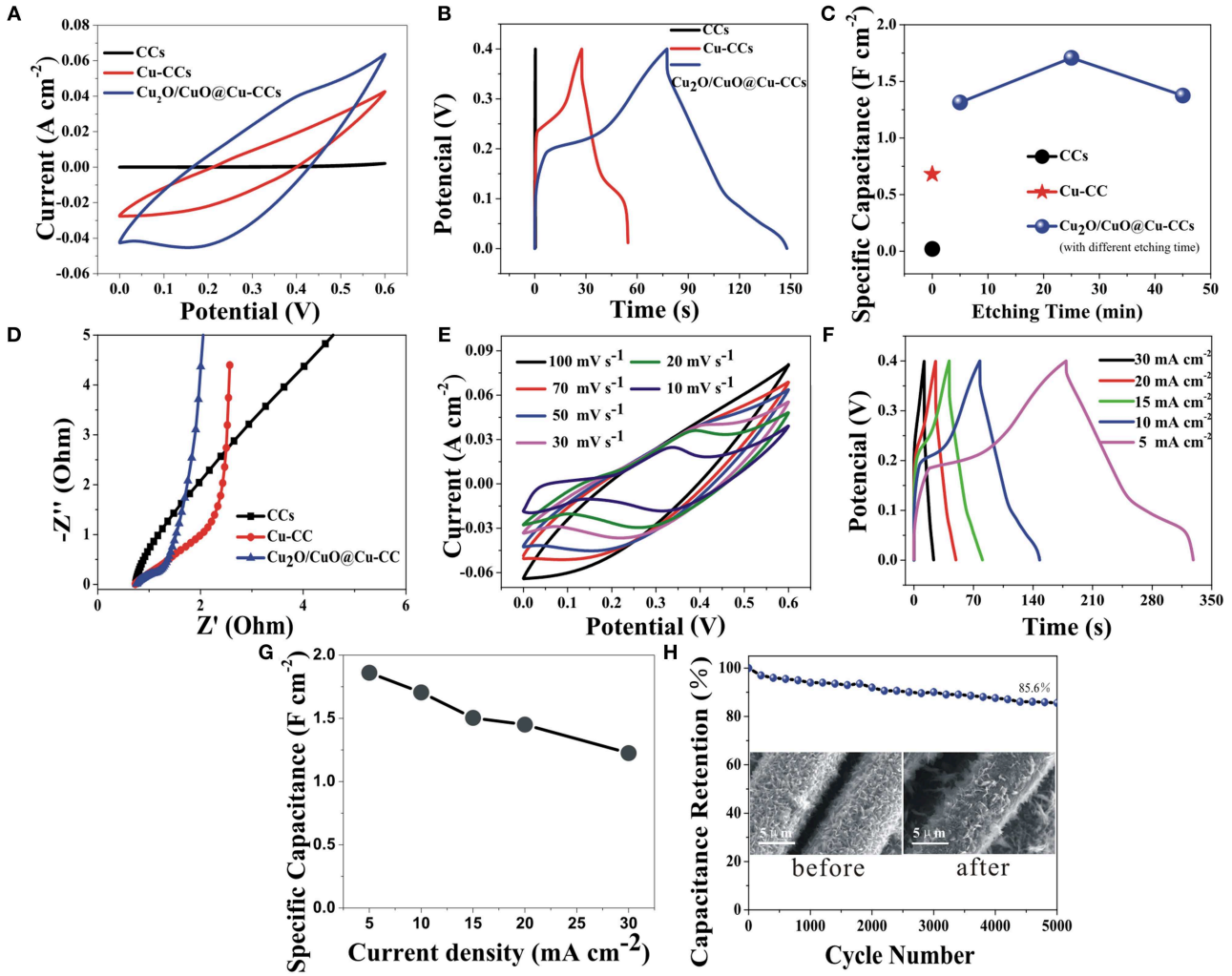

FIGURE 4 | CV curves at a scan rate of 30 mV s^{-1} **(A)**, GCD curves at a current density of 10 mA cm^{-2} **(B)**, the capacitance retention at 10 mA cm^{-2} **(C)**, and Nyquist plot **(D)** of CCs, Cu-CCs, and Cu_2O/CuO@Cu-CCs electrodes in a 3-electrode cell in 6 M KOH aqueous solution. CV curves at various scan rates **(E)**, GCD curves under different current densities **(F)**, specific capacitances under different current densities **(G)**, and the cycling performance at a current density of 5 mA cm^{-2} (the inset shows the SEM images before and after 5,000 cycles) **(H)** of Cu_2O/CuO@Cu-CCs electrode.

For further exploring of the application, the electrochemical performances of the ASC device are investigated. As shown in **Figure 5A**, the device is sandwiched with the Cu_2O/CuO@Cu-CCs positive electrode, active carbon negative electrode, and diaphragm separator soaked with 6 M KOH aqueous solution. **Figure 5B** shows the exactly complementary potential windows range of simple AC and Cu_2O/CuO@Cu-CCs electrode, which suggest the high potential window of the ACS device. Furthermore, the calculated mass ratio of the electroactive materials of negative and positive electrodes according to Equation (3) is about 1:20. **Figures 5C,D** show the CV curves at a scan rate of 30 mV s^{-1} and GCD curves at a current density of 1 A g^{-1} with different potential windows, respectively. It is obvious that the shapes of the CV curves stay nearly same at different potential windows and the maximum potential window is extended to 1.6 V. The perfect symmetry and nearly unchanged shapes at different potential windows of GCD curves also contribute to the outstanding capacitive performance of this ASC device.

Figure 5E shows the CV curves of the ASC device at a scan rate ranging from 10 to 100 mV s^{-1}. Apparently, the excellent synergy effect of the two electrodes leads to the high operation voltage of 1.6 V, which is three times as wide as the potential window of Cu_2O/CuO@Cu-CCs electrode in the three-electrode system. Meanwhile, the curve shape retains the same at different scan rates. The GCD curves at current densities from 0.5 to 10 A g^{-1} are shown in **Figure 5F**. It is obvious that very low voltage drops are visible compared with three-electrode test even at high current densities. And the symmetrical shape indicates high reversibility of the device. Thus, the device shows excellent rate capability (**Supplementary Figure 3**). In addition, owing to the broad potential window and huge specific capacitance, the ASC device shows a high energy density of 60.26 Wh kg^{-1} at a power density of 299.73 W kg^{-1}, higher

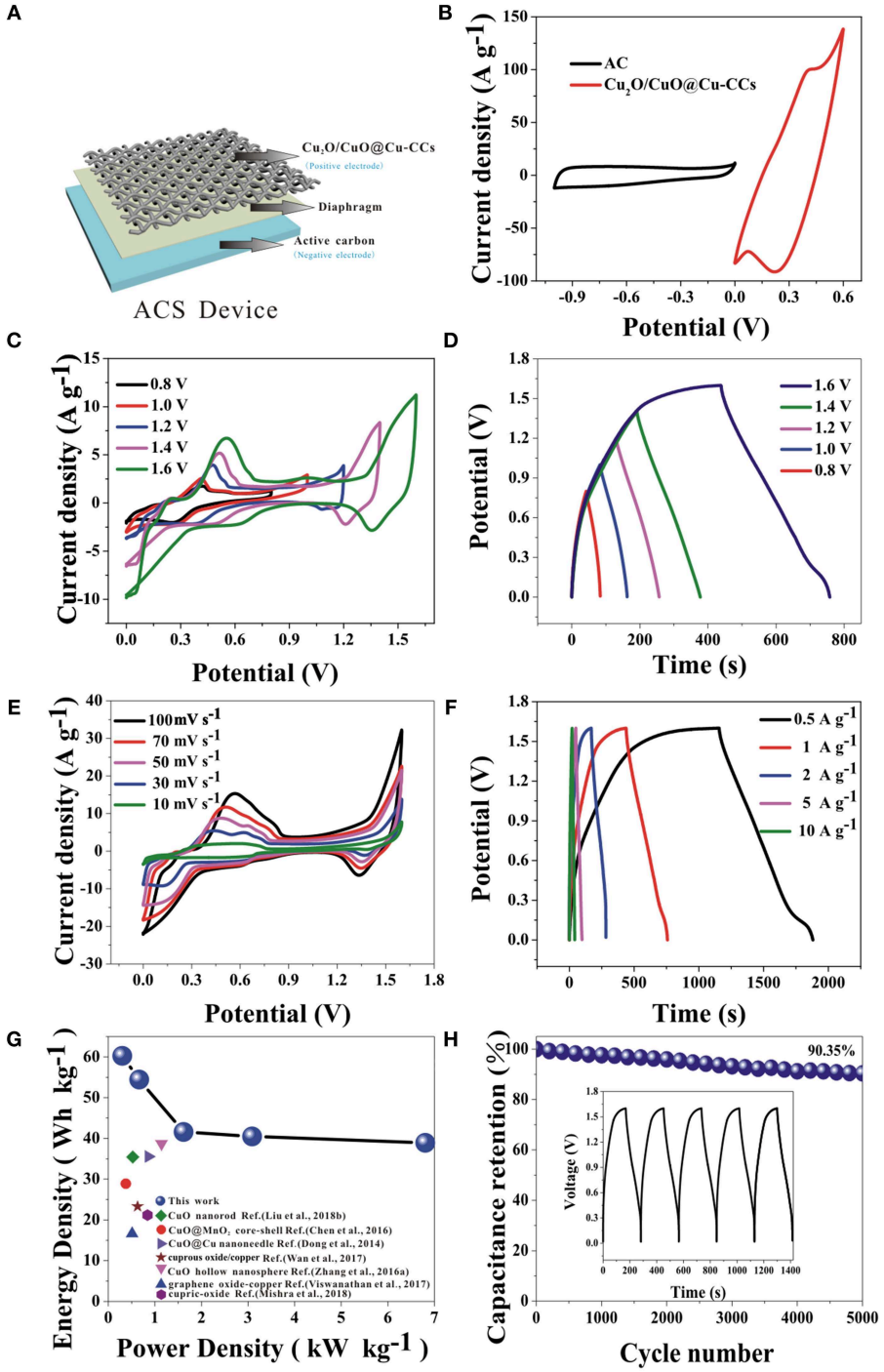

FIGURE 5 | The schematic illustration **(A)** and comparative CV curves of Cu_2O/CuO@Cu-CCs and AC electrodes at a scan rate of 30 mV s^{-1} in a three-electrode system **(B)**, electrochemical performances of the ASC device: **(C)** CV curves of at various potential windows at 30 mV s^{-1}, **(D)** GCD curves at different potential windows at a current density of 1 A g^{-1}, **(E)** CV curves at various scan rates, **(F)** GCD curves at increasing current densities, **(G)** the Ragone plot, and **(H)** the long-term cycling stability at a current density of 2 A g^{-1}, the inset is the last 5 cycles of GCD curves.

than some other literatures (**Figure 5G**). In order to investigate the long-term cycling stability and durability of the device, we performed 5,000 continuous GCD cycles at a current density of 2 A g^{-1}. The ASC device exhibits an excellent cycling stability with keeping 90.35% in its specific capacitance after 5,000 GCD cycles (**Figure 5H**). This kind of electrode material will

be a promising electrode for further engineering all-solid-state high-performance supercapacitor due to its excellent capacitor performance and flexibility characteristic.

CONCLUSIONS

In short, we constructed Cu_2O/CuO@Cu-CCs electrodes by a simple process with electroless copper plating, chemical etching and thermal dehydration. The ASC device with Cu_2O/CuO@Cu-CCs positive electrode and AC negative electrode showed high energy density of 60.26 Wh kg^{-1} at a power density of 299.73 W kg^{-1} using 6 M KOH aqueous solution as the electrolyte. Also, the ASC device express an excellent cycling stability with keeping 90.35% in its specific capacitance after 5,000 GCD cycles. Also, this kind of electrode material will be a promising electrode for further engineering all-solid-state high-performance supercapacitor.

DATA AVAILABILITY

The raw data supporting the conclusions of this manuscript will be made available by the authors, without undue reservation, to any qualified researcher.

AUTHOR CONTRIBUTIONS

LX synthesized Cu_2O/CuO@Cu-CCs samples and analyzed part of characterizations. JL was the supervisor of this research work. HS and XG helped with the data analysis. JX analyzed XPS measurements. HZ organized a part of the data. XZ supplemented a part of the experiment.

FUNDING

This work was supported by A Project of Shandong Province Higher Educational Science and Technology Program (Grant No. J18KA002), National Natural Science Foundation of China (Grant No. 51702189), and Natural Science Foundation of Shandong Province (Grant No. ZR2017BEM033).

SUPPLEMENTARY MATERIAL

The Supplementary Material for this article can be found online at: https://www.frontiersin.org/articles/10.3389/fchem.2019.00420/full#supplementary-material

REFERENCES

Bu, I. Y. Y., and Huang, R. (2017). Fabrication of CuO-decorated reduced graphene oxide nanosheets for supercapacitor applications. *Ceram. Int.* 43, 45–50. doi: 10.1016/j.ceramint.2016.08.136

Chen, H., Zhou, M., Wang, T., Li, F., and Zhang, Y. X. (2016). Construction of unique cupric oxide-manganese dioxide core-shell arrays on a copper grid for high-performance supercapacitors. *J. Mater. Chem. A* 4, 10786–10793. doi: 10.1039/C6TA04258A

Dai, S., Liu, Z., Zhao, B., Zeng, J., Hu, H., Zhang, Q., et al. (2018). A high-performance supercapacitor electrode based on N-doped porous graphene. *J. Power Sources* 387, 43–48. doi: 10.1016/j.jpowsour.2018.03.055

Daoping, C., Dandan, W., Bin, L., Lingling, W., Yuan, L., Han, L., et al. (2014). Three-dimensional Co3O4@NiMoO4 core/shell nanowire arrays on Ni foam for electrochemical energy storage. *ACS Appl. Mater. Interfaces* 6:5050. doi: 10.1021/am500060m

Dong, C., Wang, Y., Xu, J., Cheng, G., Yang, W., Kou, T., et al. (2014). 3D binder-free Cu2O@Cu nanoneedle arrays for high-performance asymmetric supercapacitors. *J. Mater. Chem. A* 2, 18229–18235. doi: 10.1039/C4TA04329D

Ensafi, A. A., Moosavifard, S. E., Rezaei, B., and Kaverlavani, S. K. (2018). Engineering onion-like nanoporous CuCo2O4 hollow spheres derived from bimetal–organic frameworks for high-performance asymmetric supercapacitors. *J. Mater. Chem. A* 6, 10497–10506. doi: 10.1039/C8TA02819B

Foo, C. Y., Sumboja, A., Tan, D. J. H., Wang, J., and Lee, P. S. (2014). Flexible and highly scalable V2O5-rGO electrodes in an organic electrolyte for supercapacitor devices. *Adv. Energy Mater.* 4:1400236. doi: 10.1002/aenm.201400236

Guan, B. Y., Yu, L., Wang, X., Song, S., and Lou, X. W. D. (2017). Formation of onion-like NiCo2S4 particles via sequential ion-exchange for hybrid supercapacitors. *Adv. Mater.* 29:1605051. doi: 10.1002/adma.201605051

Guo, D., Yu, X., Shi, W., Luo, Y., Li, Q., and Wang, T. (2014). Facile synthesis of well-ordered manganese oxide nanosheet arrays on carbon cloth for high-performance supercapacitors. *J. Mater. Chem. A* 2, 8833–8838. doi: 10.1039/c4ta01238k

Huang, M., Li, F., Dong, F., Zhang, Y., and Zhang, L. L. (2015). MnO2-based nanostructures for high-performance supercapacitors. *J. Mater. Chem. A* 3, 21380–21423. doi: 10.1039/C5TA05523G

Ji, Y., Liu, J., Liu, X., Yuen, M. M. F., Fu, X. Z., Yang, Y., et al. (2017). 3D porous Cu@Cu 2 O films supported Pd nanoparticles for glucose electrocatalytic oxidation. *Electrochim. Acta* 248, 299–306. doi: 10.1016/j.electacta.2017.07.100

Kim, S. W., Kim, I. H., Kim, S. I., and Jang, J. H. (2017). Nickel hydroxide supercapacitor with a theoretical capacitance and high rate capability based on hollow dendritic 3D-nickel current collectors. *Chem. Asian J.* 12, 1291–1296. doi: 10.1002/asia.201700454

Li, J., Liu, Z., Zhang, Q., Cheng, Y., Zhao, B., Dai, S., et al. (2019). Anion and cation substitution in transition-metal oxides nanosheets for high-performance hybrid supercapacitors. *Nano Energy* 57, 22–33. doi: 10.1016/j.nanoen.2018.12.011

Li, Y., Wang, X., Yang, Q., Javed, M. S., Liu, Q., Xu, W., et al. (2017). Ultra-fine CuO nanoparticles embedded in three-dimensional graphene network nano-structure for high-performance flexible supercapacitors. *Electrochim. Acta* 234, 63–70. doi: 10.1016/j.electacta.2017.02.167

Liang, H., Lin, J., Jia, H., Chen, S., Qi, J., Cao, J., et al. (2018). Hierarchical NiCo-LDH@NiOOH core-shell heterostructure on carbon fiber cloth as battery-like electrode for supercapacitor. *J. Power Sources* 378, 248–254. doi: 10.1016/j.jpowsour.2017.12.046

Liu, T., Zhang, L., You, W., and Yu, J. (2018). Core-shell nitrogen-doped carbon hollow spheres/Co3 O4 nanosheets as advanced electrode for high-performance supercapacitor. *Small* 14:e1702407. doi: 10.1002/smll.201702407

Liu, Y., Cao, X., Jiang, D., Jia, D., and Liu, J. (2018). Hierarchical CuO nanorod arrays *in situ* generated on three-dimensional copper foam via cyclic voltammetry oxidization for high-performance supercapacitors. *J. Mater. Chem. A* 6, 10474–10483. doi: 10.1039/C8TA00945G

Lu, Q., Chen, Y., Li, W., Chen, J. G., Xiao, J. Q., and Jiao, F. (2013). Ordered mesoporous nickel cobaltite spinel with ultra-high supercapacitance. *J. Mater. Chem. A* 1, 2331–2336. doi: 10.1039/c2ta00921h

Lu, X., Zeng, Y., Yu, M., Zhai, T., Liang, C., Xie, S., et al. (2014). Oxygen-deficient hematite nanorods as high-performance and novel negative electrodes for flexible asymmetric supercapacitors. *Adv. Mater.* 26, 3148–3155. doi: 10.1002/adma.201305851

Moosavifard, S. E., Shamsi, J., Fani, S., and Kadkhodazade, S. (2014). Facile synthesis of hierarchical CuO nanorod arrays on carbon nanofibers for high-performance supercapacitors. *Ceram. Int.* 40, 15973–15979. doi: 10.1016/j.ceramint.2014.07.126

Ouyang, Y., Huang, R., Xia, X., Ye, H., Jiao, X., Wang, L., et al. (2019). Hierarchical structure electrodes of NiO ultrathin nanosheets anchored to NiCo2O4 on carbon cloth with excellent cycle stability for asymmetric supercapacitors. *Chem. Eng. J.* 355, 416–427. doi: 10.1016/j.cej.2018.08.142

Prasad, K. P., Dhawale, D. S., Sivakumar, T., Aldeyab, S. S., Zaidi, J. S., Ariga, K., et al. (2011). Fabrication and textural characterization of nanoporous carbon electrodes embedded with CuO nanoparticles for supercapacitors. *Sci. Technol. Adv. Mater.* 12:044602. doi: 10.1088/1468-6996/12/4/044602

Sami, S. K., Siddiqui, S., Shrivastava, S., Lee, N. E., and Chung, C. H. (2017). The pine-needle-inspired structure of zinc oxide nanorods grown on electrospun nanofibers for high-performance flexible supercapacitors. *Small* 13:1702142. doi: 10.1002/smll.201702142

Saray, M. T., and Hosseini, H. (2016). Mesoporous MnNiCoO4@MnO 2 core-shell nanowire/nanosheet arrays on flexible carbon cloth for high-performance supercapacitors. *Electrochim. Acta* 222, 505–517. doi: 10.1016/j.electacta.2016.11.003

Singh, A. K., and Sarkar, D. (2017). Substrate-integrated core–shell Co3O4@Au@CuO hybrid nanowires as efficient cathode materials for high-performance asymmetric supercapacitors with excellent cycle life. *J. Mater. Chem. A* 5, 21715–21725. doi: 10.1039/C7TA07266J

Surendran, S., Shanmugapriya, S., Sivanantham, A., Shanmugam, S., and Kalai Selvan, R. (2018). Electrospun carbon nanofibers encapsulated with NiCoP: a multifunctional electrode for supercapattery and oxygen reduction, oxygen evolution, and hydrogen evolution reactions. *Adv. Energy Mater.* 8:1800555. doi: 10.1002/aenm.201800555

Wan, C., Jiao, Y., and Li, J. (2017). Cellulose fibers-supported hierarchical forest-like cuprous oxide/copper array architecture as flexible and free-standing electrodes for symmetric supercapacitors. *J. Mater. Chem. A* 5, 17267–17278. doi: 10.1039/C7TA04994C

Wang, K., Dong, X., Zhao, C., Qian, X., and Xu, Y. (2015). Facile synthesis of Cu 2 O/CuO/RGO nanocomposite and its superior cyclability in supercapacitor. *Electrochim. Acta* 152, 433–442. doi: 10.1016/j.electacta.2014.11.171

Wang, W., Guo, S., Lee, I., Ahmed, K., Zhong, J., Favors, Z., et al. (2014). Hydrous ruthenium oxide nanoparticles anchored to graphene and carbon nanotube hybrid foam for supercapacitors. *Sci. Rep.* 4:4452. doi: 10.1038/srep04452

Wei, D., Scherer, M. R., Bower, C., Andrew, P., Ryhänen, T., and Steiner, U. (2012). A nanostructured electrochromic supercapacitor. *Nano Lett.* 12, 1857–1862. doi: 10.1021/nl2042112

Wu, S., Lv, W., Lei, T., Han, Y., Jian, X., Deng, M., et al. (2017). Distinctive supercapacitive properties of copper and copper oxide nanocrystals sharing a similar colloidal synthetic route. *Adv. Energy Mater.* 7:1700105. doi: 10.1002/aenm.201700105

Xiong, X., Dong, D., Chen, D., Waller, G., Bu, Y., Wang, Z., et al. (2015). Three-dimensional ultrathin Ni(OH) 2 nanosheets grown on nickel foam for high-performance supercapacitors. *Nano Energy* 11, 154–161. doi: 10.1016/j.nanoen.2014.10.029

Xu, W., Dai, S., Liu, G., Xi, Y., Hu, C., and Wang, X. (2016). CuO nanoflowers growing on carbon fiber fabric for flexible high-performance supercapacitors. *Electrochim. Acta* 203, 1–8. doi: 10.1016/j.electacta.2016.03.170

Yang, W., Qu, G., Chen, M., Ma, W., Li, W., and Tang, Y. (2018). Effective NaBH4-exfoliated ultrathin multilayer Co(OH)2 nanosheets arrays and sulfidation for energy storage. *Nanotechnology* 29:295403. doi: 10.1088/1361-6528/aac158

Yang, Y., Pei, L., Xu, X., Xu, J., Shen, J., and Ye, M. (2016). *In-situ* growth of self-assembled 3D Cu 2 O@Cu foam with enhanced electrochemical properties. *Electrochim. Acta* 221, 56–61. doi: 10.1016/j.electacta.2016.10.150

Yuan, W., Luo, J., Pan, B., Qiu, Z., Huang, S., and Tang, Y. (2017). Hierarchical shell/core CuO nanowire/carbon fiber composites as binder-free anodes for lithium-ion batteries. *Electrochim. Acta* 241, 261–271. doi: 10.1016/j.electacta.2017.04.159

Zhang, L., Ding, Q., Huang, Y., Gu, H., Miao, Y. E., and Liu, T. (2015). Flexible hybrid membranes with Ni(OH)2 nanoplatelets vertically grown on electrospun carbon nanofibers for high-performance supercapacitors. *ACS Appl. Mater. Interfaces* 7:22669. doi: 10.1021/acsami.5b07528

Zhang, W., Yin, Z., Chun, A., Yoo, J., Diao, G., Kim, Y. S., et al. (2016). Rose rock-shaped nano Cu 2 O anchored graphene for high-performance supercapacitors via solvothermal route. *J. Power Sources* 318, 66–75. doi: 10.1016/j.jpowsour.2016.04.006

Zhang, Y., Hu, Z., An, Y., Guo, B., An, N., Liang, Y., et al. (2016). High-performance symmetric supercapacitor based on manganese oxyhydroxide nanosheets on carbon cloth as binder-free electrodes. *J. Power Sources* 311, 121–129. doi: 10.1016/j.jpowsour.2016.02.017

Conflict of Interest Statement: The authors declare that the research was conducted in the absence of any commercial or financial relationships that could be construed as a potential conflict of interest.

frontiers in Chemistry

ORIGINAL RESEARCH
published: 26 June 2019
doi: 10.3389/fchem.2019.00455

Construction of Ultrathin Nitrogen-Doped Porous Carbon Nanospheres Coated With Polyaniline Nanorods for Asymmetric Supercapacitors

Pingping Yu[1], *Qunliang Wang*[1], *Lingxia Zheng*[2] *and Yanfeng Jiang*[1]*

[1] Department of Electronic Engineering, College of Internet-of-Things, Jiangnan University, Wuxi, China, [2] Department of Applied Chemistry, Zhejiang University of Technology, Hangzhou, China

Porous carbon materials produced by biomass have been widely studied for high performance supercapacitor due to their abundance, low price, and renewable. In this paper, the series of nitrogen-doped hierarchical porous carbon nanospheres (HPCN)/polyaniline (HPCN/PANI) nanocomposites is reported, which is prepared via *in-situ* polymerization. A novel approach with one-step pyrolysis of wheat flour mixed with urea and $ZnCl_2$ is proposed to prepare the HPCN with surface area of 930 m^2/g. Ultrathin HPCN pyrolysised at 900°C (~3 nm in thickness) electrode displays a gravimetric capacitance of 168 F/g and remarkable cyclability with losing 5% of the maximum capacitance after 5,000 cycles. The interconnected porous texture permits depositing of well-ordered polyaniline nanorods and allows a fast absorption/desorption of electrolyte. HPCN/PANI with short diffusion pathway possesses high gravimetric capacitance of 783 F/g. It can qualify HPCN/PANI to be used as cathode in assembling asymmetric supercapacitor with HPCN as anode, and which displays an exceptional specific capacitance of 81.2 F/g. Moreover, HPCN/PANI//HPCN device presents excellent cyclability with 88.4% retention of initial capacity over 10,000 cycles. This work will provide a simple and economical protocol to prepare the sustainable biomass materials based electrodes for energy storage applications.

Keywords: sustainable sources, ultrathin porous nanospheres, polyaniline nanorods, nitrogen-doped, supercapacitors

OPEN ACCESS

Edited by:
Wenyao Li,
Shanghai University of Engineering Sciences, China

Reviewed by:
Linfeng Hu,
Fudan University, China
Anqi Ju,
Donghua University, China

***Correspondence:**
Yanfeng Jiang
jiangyf@jiangnan.edu.cn

Specialty section:
This article was submitted to Electrochemistry, a section of the journal Frontiers in Chemistry

Received: *14 May 2019*
Accepted: *07 June 2019*
Published: *26 June 2019*

Citation:
Yu P, Wang Q, Zheng L and Jiang Y (2019) Construction of Ultrathin Nitrogen-Doped Porous Carbon Nanospheres Coated With Polyaniline Nanorods for Asymmetric Supercapacitors. Front. Chem. 7:455. doi: 10.3389/fchem.2019.00455

INTRODUCTION

Carbon materials as the developing anodes have played pivotal roles in the energy storage area owing to its abundant sources, cost-effective, high chemical stability, and good conductivity (Gao and Fang, 2015; Benzigar et al., 2018). The excellent properties endow carbon materials (carbon nanotubes (CNT), activated carbon (AC) and graphene) with promising potential applications in the electric double-layer capacitance (EDLC) supercapacitors (Wu et al., 2017; Jiang et al., 2018). The electrochemical performances of the supercapacitors largely depend on characteristics of these adopted carbon materials, including morphologies, surface properties, specific surface

area, and porous channels (Peng et al., 2014; Liu et al., 2016; Goldfarb et al., 2017; Li et al., 2018; Yang et al., 2018). Therefore, carbon materials with accessible surface area as well as high electron transport efficiency are essential for preparing the carbon-based supercapacitors. The materials with hierarchical porous nanostructure are intensively investigated recently (Badwal et al., 2014; Xu et al., 2018), which could be the promising candidate to satisfy the multiple requirements for the supercapacitors.

Activated carbon is generally prepared by pyrolyzing versatile carbonaceous precursors with physical or chemical activation to introduce the hierarchical pores. However, when the surface area increases to 3,000 m^2 g^{-1}, its electric capacity is still low (100–140 F/g) in the organic electrolyte (Barbieri et al., 2005). The interplayed aspects indicate that the capacity depends on the pore size distribution, accessibility of the electrolyte and the electrical conductivity (Zhang H. et al., 2015). Therefore, numerous biomass-based carbon combining hierarchical pores and heteroatom doping have gained considerable attentions, resulting in pesudocapacitance and electrical double layer capacitance. Carbonization of natural biomass materials, including seaweeds (Kang et al., 2015), peanut shell (Ding et al., 2015), rice bran (Hou et al., 2014), plant leaves (Liu B. et al., 2017; Zhang et al., 2018; Zhao et al., 2018), fruit (Wu et al., 2014), and wheat flour (Wu et al., 2015; Yu et al., 2016), has been investigated. It is demonstrated as a feasible approach, which could result in a low cost and eco-friendly way to prepare hierarchical porous carbon electrodes.

Among all the kinds of the investigated biomass, wheat flour is considered as the most promising one. Wheat flour can be well dispersed in aqueous solution via magnetic stirring to form suspension because it contains starch (72–80%) and protein (8–10%). Thus, wheat flour is a green carbon source to prepare the hierarchical porous carbon. Chemical activation is a preferable approach to prepare the high performance porous carbon using the chemical agents (KOH, NaOH, $ZnCl_2$ and H_3PO_4) (Duan et al., 2016; Lei et al., 2016; Pang et al., 2016a,b; Goldfarb et al., 2017; Yang et al., 2019). The strong activation effect of KOH and NaOH can degrade the wheat flour into small molecular and lose a large proportion of carbon atoms, making the low yield of carbon materials (Wang and Liu, 2017). $ZnCl_2$ as a milder activation reagent can react with precursor by dehydrating and cross-linking along the temperature increase, creating hierarchical pores, high specific surface area and high yield.

Polyaniline (PANI) is considered as a good developing supercapacitor electrode due to its large pseudocapacitance, intrinsic redox states and simple synthesis (Yu et al., 2013a, 2014, 2017). However, because of the degradation of PANI electrodes in the process of repeated charging and discharging, the cycle life of PANI electrodes is usually poor (Liu et al., 2014). In order to overcome this shortcoming, combination of the well-ordered PANI nanostructure and carbon materials has been explored to prevent the collapse. Wang et al. reported that the ordered whiskerlike PANI/mesoporous carbon composites formed "V-type" channels which shorten the ion transport pathway and increase the contacted area for electrolyte (Wang et al., 2006). Liu et al. synthesized hierarchical graphene/PANI hollow microspheres hybrid electrode with supercapacitor capacitance of 446.2 F/g, which exhibits an outstanding long cycle life (Liu L. et al., 2017). Sulfur-encapsulated porous carbon nanospheres/polyaniline composites were synthesized to improve chemical stability and electronic conductivity (Li et al., 2016). However, these PANI-based binary composites exhibit single-scale pores, complex synthetic procedure, and high cost, which is not suitable for the high-performance-supercapacitor.

In this study, the one-step carbonization for wheat flour is employed by pyrolysis of urea and $ZnCl_2$ to prepare interconnected hierarchical porous N-doped carbon nanospheres (HPCN). **Figure 1** presents the approach for the fabrication of the HPCN/PANI composites by chemical oxidative polymerization. The highest specific capacitance of HPCN with surface area of 930 m^2/g is 168 F/g, and then PANI nanorods are vertically coated on the HPCN by chemical bonding interaction with nitrogen groups, providing the significant enhancement of supercapacitor performances. Moreover, this assembled asymmetric supercapacitor (ASC) combining HPCN and HPCN/PANI can work in 1 M H_2SO_4 electrolyte and its electrochemical performances are investigated in this paper.

EXPERIMENTAL SECTIONS

Synthesis of Hierarchical Porous Hpcn

HPCN were formed using wheat flour as renewable biomass resource through one-step carbonization. Typically, the waste wheat flour, urea and $ZnCl_2$ (1:1:2, w/w) were added to 50 mL distilled water with magnetic stirring, followed by carbonization at 700–900°C for 1 h under N_2 flow. As-carbonized samples were stirred in 10% HCl and DI water successively for 15 h. After purification, the HPCN was dried under 80°C vacuum oven. The obtained products were termed as HPCN7, HPCN8, and HPCN9 standing for the pyrolysis temperature at 700, 800, and 900 °C, respectively.

Fabrication of HPCN/PANI

The HPCN (100 mg) were dispersed in 1 M H_2SO_4 solution containing aniline monomers (AN, 45.65 μL) by strong stirring. 40 mL 1 M H_2SO_4 of ammonium persulfate (APS, 114.12 mg, [AN]/[APS] = 1:1) solution was rapidly added with stirring for more than 5 min. The oxidative reaction was conducted at −5°C overnight, and the obtained composites were filtered, rinsed with DI water and overnight dried at 50°C. The content of PANI is 26.21% in HPCN7/PANI, 29.34% in HPCN8/PANI and 32.05% in HPCN9/PANI, respectively.

Material Characterization

The composites were conducted with a field-emission scanning electron microscope (FESEM, Zeiss Sigma), a transmission electron microscope (TEM, TECNAI G^2 S-TWIN), X-ray diffraction (XRD, Bruker D8-A25, λ = 1.5405 Å, Cu Kα radiation, 10-50°), Raman spectra (LabRam-1B, 632.8 nm laser), X-ray photoelectron spectroscopy (XPS, PHI 5000C ESCA) and ASAP 3000.

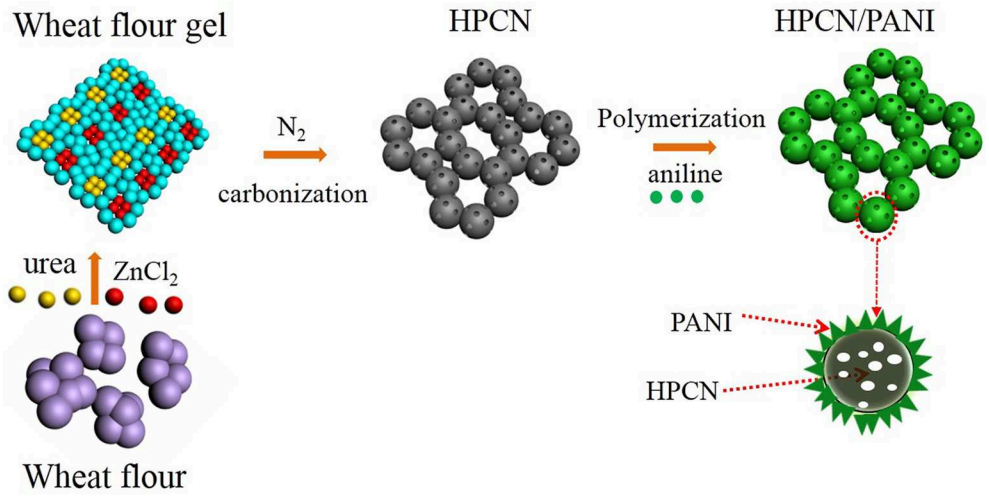

FIGURE 1 | Schematic illustration of fabricating HPCN/PANI composites.

Electrochemical Measurements

The mixture was blended with ratio of 90/5/5 for as-prepared samples/carbon black/ polytetrafluoroethylene. The uniform paste was coated on a titanium mesh (1 cm in diameter) as working electrode. The HPCN and HPCN/PANI were tested in three-electrode cell. The asymmetric supercapacitors were fabricated with negative electrode of HPCN9 and positive electrode of HPCN9/PANI. The filter paper were placed between two electrodes to be the separator. The mass of active materials deposited on Ti mesh was approximated to be 2.0 mg. Electrochemical performances of electrodes were conducted with an electrochemical workstation of CHI 660D in electrolyte of 1 M H_2SO_4 aqueous.

According to the GCD plots, the specific capacitance of the HPCN and HPAN/PANI electrodes can be calculated depending on equation (1):

$$C_{sp} = \frac{I\Delta t}{m\Delta V} \tag{1}$$

where I (A) is the current, Δt (s) stands for the time required for full discharge, m (g) is the weight of the electrodes, and ΔV (V) is the voltage difference. In order to keep the charge balance, the mass ratio of positive and negative electrode was calculated using the following formula (2):

$$\frac{m_+}{m_-} = \frac{C_- V_-}{C_+ V_+} \tag{2}$$

The specific capacitance (C_{asy}), energy density (E, Wh/kg) and power density (P, W/kg) of ASC device were obtained by the following equations:

$$C_{asy} = \frac{I\Delta t}{M\Delta V} \tag{3}$$

$$\mathrm{E} = \frac{C_{asy}\Delta V^2}{2 \times 3.6} \tag{4}$$

$$\mathrm{P} = 3600 \times \frac{E}{\Delta t} \tag{5}$$

where M ($M = m_+ + m_-$) is the total mass of electrode materials.

RESULTS AND DISCUSSION

The morphologies of HPCN7, HPCN8, and HPCN9 (carbonized at 700, 800 and 900°C) indicate that the samples consist of a large amount of uniformly interconnected carbon nanospheres (**Figures 2A–C**). The diameter of the HPCN7 (**Figure 2A**) is 70 nm, which is higher than that of HPCN8 (61 nm, **Figure 2B**) and that of HPCN9 (50 nm, **Figure 2C**) because carbonization temperature increases from 700 to 900°C. In this chemical activation process, $ZnCl_2$ as dehydrating agent can promote the condensation reaction of wheat flour, reduce the gasification of carbon atoms and lead to high carbon yields (>35%). $ZnCl_2$ is also as an effective activation-graphitization agent that promotes aromatic condensation reactions at high temperature due to its Lewis acid nature and introduce the porous structure to improve the surface area. The nanospheres are interconnected to form the porous network. This structure has benefit for fast electrode/electrolyte interface kinetics.

The porous contour of the HPCN can be used as a buffer boost for expansion and shrinking of PANI nanorods. PANI nanorods are vertically deposited on the HPCN7, HPCN8, and HPCN9 to improve the specific capacitance, as shown in **Figures 2D–F**. Compared to HPCN9/PANI (**Figure 2F**), there are obvious denser and longer PANI nanorods stacked on HPCN7/PANI (∼50 nm, **Figure 2D**) and HPCN8/PANI (∼40 nm, **Figure 2E**) than those in HPCN9/PANI. This shows that the thicknesses of the PANI layers of HPCN7/PANI and HPCN8/PANI are higher than that of the HPCN9/PANI. This may be due to the HPCN7 and HPCN8 with more nitrogen-groups and higher specific surface area to

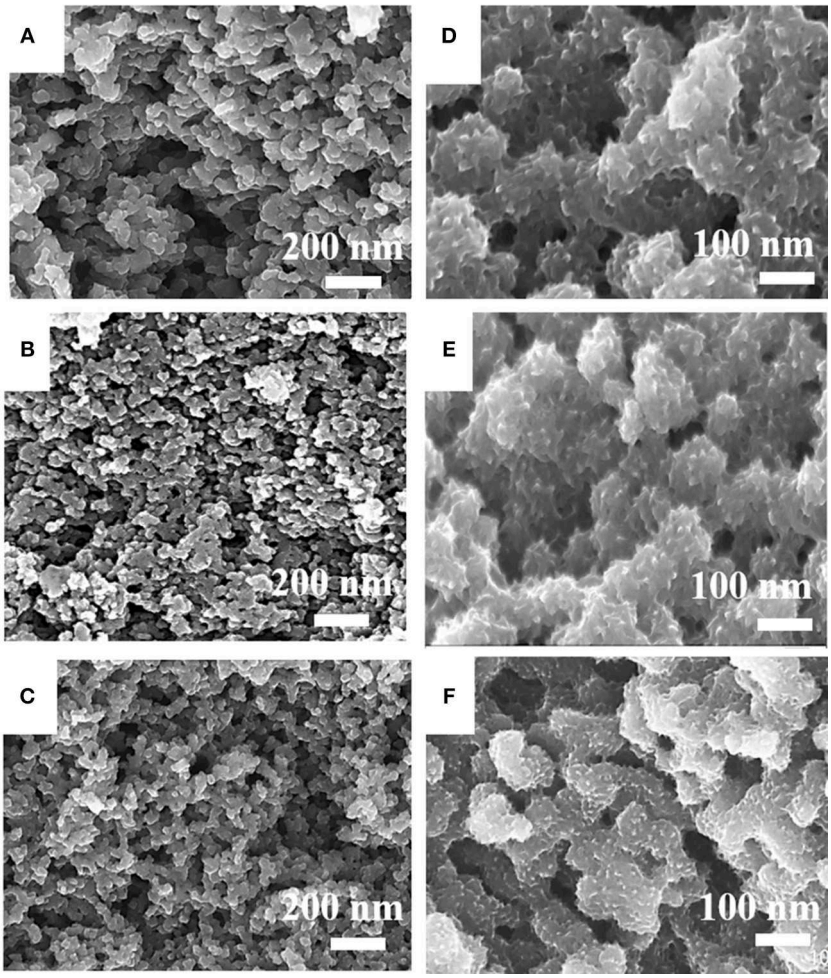

FIGURE 2 | FESEM images of HPCN7 **(A)**, HPCN8 **(B)**, and HPCN9 **(C)**, HPCN7/PANI **(D)**, HPCN8/PANI **(E)** and HPCN9/PANI **(F)**.

be bonded with much more aniline monomers to form the PANI nanorods.

The above analysis shows that HPCN9/PANI has thinner PANI layer. The average diameter of carbon nanospheres in HPCN9 is 50 nm. Their thin carbonaceous walls are connected to form the reticular morphology (**Figure 3A**). Plenty of nanopores can be observed in the HPCN9. The thickness of these carbonaceous walls (**Figure 3B**) is about 3 nm equal to 6–8th layer of graphene. For the sample HPCN9/PANI (**Figure 3C**), the PANI nanorods are grown on the porous carbon nanospheres, maintaining the interconnected network structure. **Figure 3D** presents that the diameter and the length of the PANI nanorods are about 5–10 and 15–17 nm, respectively. The well-ordered and much smaller sized PANI in HPCN9/PANI can largely short the diffusion pathway by enhancing utilization of the active materials, improving the electrochemical performances.

Figure 4A shows XRD profiles of the HPCN and HPCN/PANI composites. As-prepared HPCN7, HPCN8, and HPCN9 all show two characteristic diffraction peaks (002) and (101) at around 24° and 44°, respectively. The (002) diffraction with broad width and low intensity of (101) plane indicate the amorphous carbon structure (Yu et al., 2016). Three crystalline peaks located at $2\theta = 14.8°$, 25.2°, and 20.3° for the three-HPCN/PANI composites are assigned to be the crystal planes of (011), (200), and (020) for emeraldine salt polyaniline, indicating the periodicity of the perpendicular and the parallel of the polymer chains, respectively, (Yu et al., 2013a).

The Raman spectra of HPCN7, HPCN8, and HPCN9 (**Figure 4B**) exhibit the strong D-peak at 1,344 cm^{-1}, representing disordered carbon confirmed with XRD results (Kudin et al., 2008). G-band at 1,597 cm^{-1} indicates graphitic carbon with vibration of sp^2 C. The value of I_D/I_G for HPCN7, HPCN8, and HPCN9 is 1.04, 1.03, and 1.01, respectively. It indicates that the HPCN9 has relatively higher graphitized degree, offering good electric conductivity. There are other additional four characterization peaks for HPCN7/PANI, HPCN8/PANI, and HPCN9/PANI. The peak at 1,175 and 1,482 cm^{-1} is assigned to in-plane C-H bending and C = N stretching of quinoid ring, respectively. At 1356 and 1,593 cm^{-1}, the peaks indicate protonated C-N stretching vibration and C-C

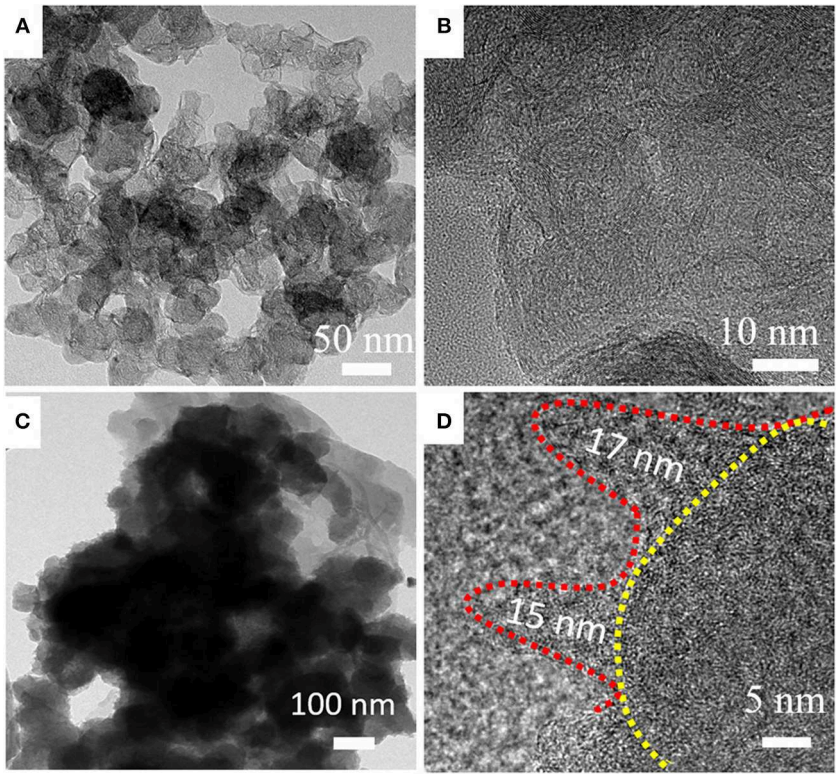

FIGURE 3 | Different magnification for TEM images of HPCN9 **(A,B)** and HPCN9/PANI **(C,D)**.

stretching of benzenoid ring. It shows PANI nanorods in the emeraldine form (Yu et al., 2013a,b; Chen et al., 2016; Zheng et al., 2016).

The XPS spectra demonstrate the fact that the nitrogen atoms exist in the HPCN9 and HPCN9/PANI in **Figure 4C** observed the C, N, and O 1s peaks. The deconvoluted C 1s peaks of HPCN9 reveal 284.7 eV of the sp^2 C=C bond of graphitic carbon and 285.8 eV of sp^3 C-C/C-H bonds while the one at 287.1 eV attributes to C=O/N-C=N bonds (**Figure S1a**). The concentration of nitrogen species is 2.4 at.% and 6.7 at.% for HPCN9 and HPCN9/PANI, respectively (**Tables S1, S2**). The N 1s spectra (**Figures S1b,c**) of HPCN9 are deconvoluted into three bands: 401.2, 399.8 and 398.6 eV, which is corresponding to quaternary N, pyrrole N and pyridine N, respectively (Li et al., 2015; Wang et al., 2015). It indicates the O/N functional groups originated form wheat flour and urea during the carbonization process. For HPCN9/PANI, three peaks centered at 401.3, 399.6, and 398.2 eV indicate the positively charged nitrogen atoms ($-NH^+=$), benzenoid amine (-NH-) and quinoid amine (-N=) in the deconvoluted N 1s spectra (**Figure S1d**), respectively (Yu et al., 2013a; Zhang Y. et al., 2015; Wang and Liu, 2017).

Figure 4D is the N_2 adsorption/desorption isotherms of the HPCN and HPCN/PANI. It can be seen that the isotherms of HPCN and HPCN/PANI are I/IV type adsorption/desorption. At the relative low pressure, there is a fast and distinct adsorption, while it shows slight hysteresis loop at P/P_0 of 0.3–1.0. This suggests that HPCN and HPCN/PANI contains micropores and mesopores. In addition, the increment in adsorption quantity at P/P_0 of 1.0 is caused by the small amount of macropores. The specific surface area (**Figure S2**) follow the trend: HPCN9 (978 m^2/g) > HPCN8 (965 m^2/g) > HPCN7 (930 m^2/g). HPCN9/PANI has superior surface area of 639 m^2/g to HPCN7/PANI (580 m^2/g) and HPCN8/PANI (602 m^2/g), which is higher than the reported carbon materials and PANI hybrids (Liu L. et al., 2017; Yu et al., 2017), promising to achieve favorable capacitor performance. The decreased pore volumes and specific surface area suffer from pore blockage after coating PANI nanorods by the *in-situ* polymerization, while the average pore diameter of HPCN9/PANI is still 1.0 nm (inset in **Figure 3D**).

The electrochemical characterizations of the HPCN and HPCN/PANI electrodes are demonstrated by CV curves, GCD and EIS in a three-electrode setup based on the −0.2–0.8 V. **Figure 5A** presents the nearly rectangular CV curves of HPCN9 electrode with scanning rate of 5–200 mV/s. There is a slight distortion because of the interconnected hierarchical porous nanospheres and nitrogen atoms doping from urea, indicating the good rate performance. It exhibits the electrochemical double layer capacitive features. The CV curve of HPCN9 possesses the higher integrated areas than those of HPCN7 and HPCN8 at 100 mV/s (**Figure 5B**), revealing the higher charge storage capabilities of HPCN9. Therefore, the hierarchical porous HPCN can be the good scaffold for the PANI nanorods loading. The enhanced area of CV curves is attributed to

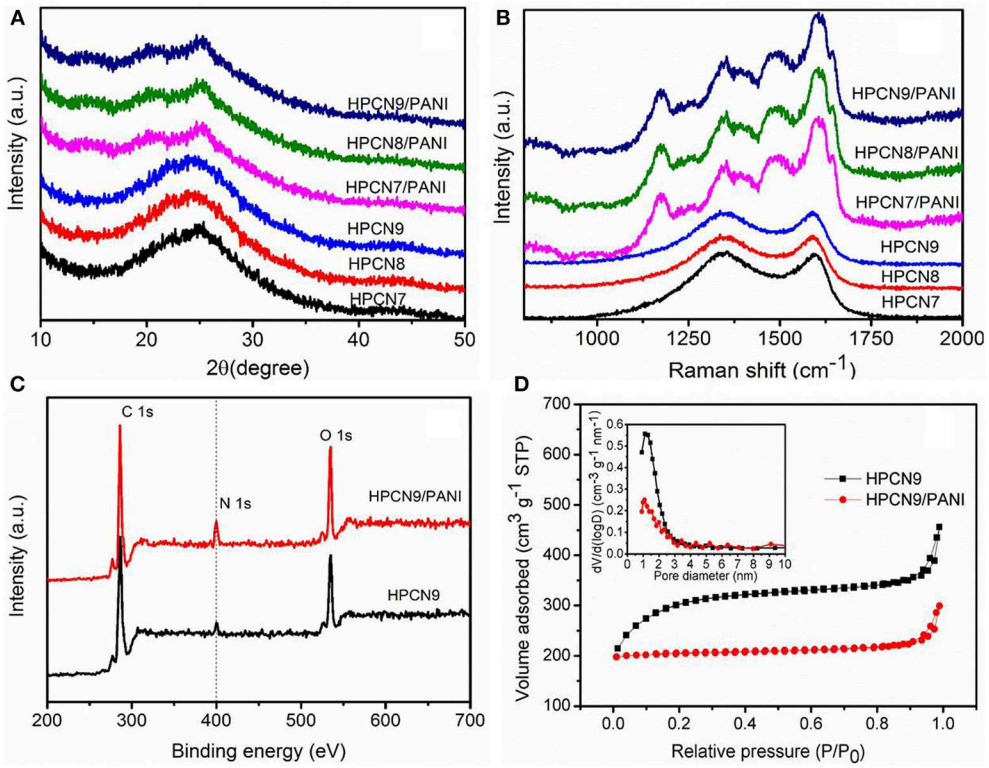

FIGURE 4 | (A) XRD patterns of HPCN7, HPCN8, HPCN9, HPCN7/PANI, HPCN8/PANI, and HPCN9/PANI composites. **(B)** Raman spectra for all the samples. XPS spectra **(C)** and N_2 sorption isotherm **(D)** (inset: pore size distribution) of HPCN9 and HPCN9/PANI.

the well-ordered porous HPCN/PANI structure. Two new pairs of intense peaks in HPCN7/PANI, HPCN8/PANI, and HPCN9/PANI are assigned to the redox reactions of PANI, implying the main chain change of PANI as semiconducting leucoemeraldine/conducting polaronic emeraldine and faradaic transformation of emeraldine/pernigraniline, respectively (Yu et al., 2013b). The HPCN9/PANI shows the higher specific capacitance than HPCN7/PANI and HPCN8/PANI based on the areas of the CV curves, consistent with the GCD plots (**Figure 5C**). Different from the symmetric triangle plot for HPCN, there are voltage plateau and longer discharge time in the GCD plots of HPCN/PANI at 1 A/g, suggesting the pseudocapacitive characteristics. Obviously, the HPCN9/PANI possesses the optimal capacitive performance owing to the longer discharge time. Therefore, capacity performance of electrodes increases with the addition of PANI nanorods confirming by the GCD and CV tests. The maximum specific capacitance (C_{sp}) of HPCN9, HPCN8, and HPCN7 obtained in **Figure 5D** is 168 F/g, 133 F/g, and 152 F/g, superior to the capacitance of previous published biomass-carbon electrodes (Zhang H. et al., 2015; Zhang Y. et al., 2015; Lei et al., 2016; Pang et al., 2016a,b). The HPCN9 shows the interconnected porous structure to help reducing the diffusion pathway of electrolyte ions and providing low-resistance to enhanced capability performances. The calculated C_{sp} of HPCN9/PANI, HPCN8/PANI, and HPCN7/PANI (**Figure 5D**) at 1 A/g is 783 F/g, 751 F/g and 710 F/g, respectively. **Table 1** is the comparison of specific capacitances of HPCN/PANI and previously reported carbon/PANI composites. The exceptional capacitance mainly arises from the synergic effect of pseudocapacitance and double-layer capacitance, due to the well-ordered PANI nanorods on the interconnected porous network structure. The nanometer size of PANI with "V-type" channels facilitates the large accessible surface area between electrolyte and active species for fast faradaic reactions and shorten diffusion pathway to ensure the effective utilization of PANI nanorods.

Figure 6A shows the Nyquist plots for HPCN and HPCN/PANI electrodes. HPCN7/PANI, HPCN8/PANI, and HPCN9/PANI electrodes exhibit small charge transfer resistance (R_{ct}) corresponding to equivalent circuit (**Figure S3**), which is 0.75, 0.68, and 0.51 Ω, respectively, higher than that of HPCN7 (0.42 Ω), HPCN8 (0.32 Ω), and HPCN9 (0.17 Ω), due to the PANI nanorods grown on the porous carbon nanospheres. The decreased R_{ct} from HPCN7/PANI to HPCN9/PANI is attributed to the increased electrode/electrolyte interface area, facilitating the fast redox reactions in the as-prepared electrodes. Moreover, the almost straight line at low frequency of HPCN9/PANI plot shows ideal capacitive characteristic, indicating to the good rate performance. Apart from the high specific capacitance and small resistances, the HPCN, and HPCN/PANI electrodes also exhibit good cycling durability (**Figure 6B**). HPCN electrodes exhibits outstanding cycling behavior with losing

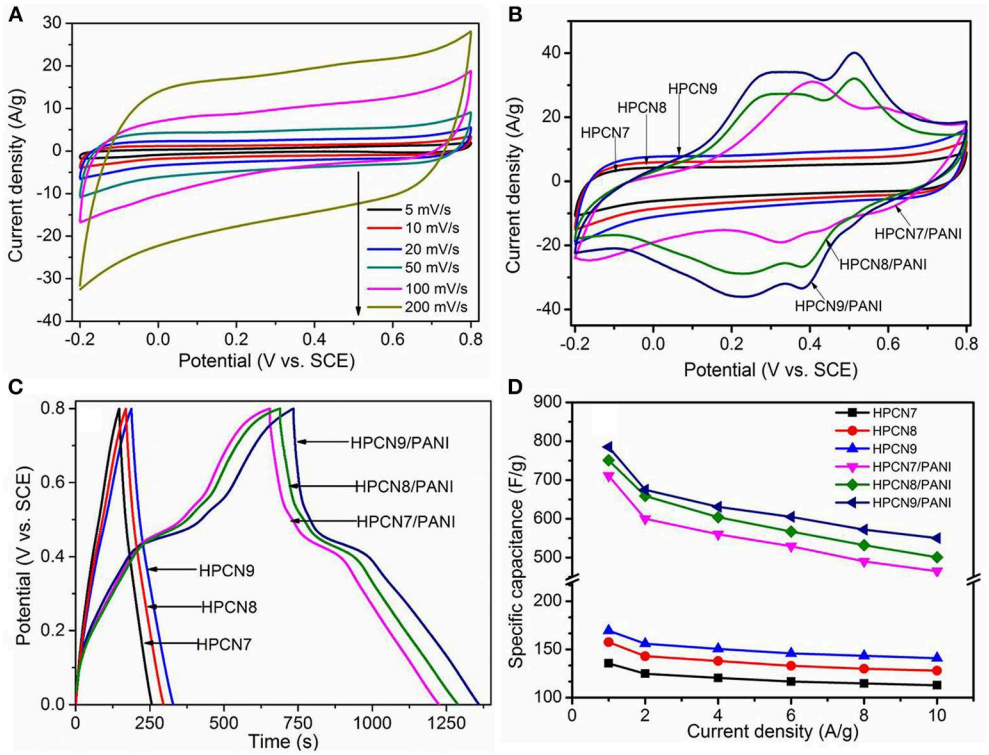

FIGURE 5 | CV curves **(A)** of HPCN9 at various scan rates. Supercapacitor behavior of all samples. **(B,C)** and **(D)** shows compared CV curves, GCD response and change in specific capacitance *vs.* current density of HPCN7, HPCN8, HPCN9, HPCN7/PANI, HPCN8/PANI, and HPCN9/PANI composites.

TABLE 1 | Comparison of the performances for hybrid PANI electrodes in aqueous electrolyte.

Materials	C_{sp} (F/g)	Weight (mg)	Current density	System	Cycle life	References
PANI/CNT	403.3	NA	1 A/g	3-electrode GCD	NA	Wu et al., 2017
Grapheme/PANI	446.2	NA	5 mV/s	2-electrode CV	88.7% (5,000 cycles at 2 A/g)	Liu L. et al., 2017
$MnFe_2O_4$/graphene/PANI	241	1.3	0.5mA/cm^2	3-electrode GCD	NA	Sankar and Selvan, 2015
Porous grapheme/PANI film	740	0.82	0.5 A/g	3-electrode GCD	87% (1,000 cycles at 10A/g)	Wang et al., 2015
Kenaf-carbon/PANI	628	2	0.1 A/g	3-electrode GCD	89.2% (1,000 cycles at 0.1A/g)	Lu et al., 2016
N-Graphene/PANI	514.3	7.4	1 A/g	3-electrode GCD	87.1% (1,000 cycles at 10 A/g)	Zou et al., 2018
Macroporous carbon/PANI	662	~2.5	1 A/g	3-electrode GCD	83% (7,000 cycles at 2 A/g)	Li et al., 2015
MoS_2/rGO/PANI	570	4-5	1 A/g	3-electrode GCD	78.6% (500 cycles at 1 A/g)	Bai et al., 2018
HPCN9/PANI	783	~2.0	1 A/g	3-electrode GCD	89.3% (5,000 cycles at 1 A/g)	This work

5% of initial capacitance over 5,000 cycles. HPCN9/PANI electrode remains 698 F/g and holds 89.3% of initial value after 5,000 cycles, while HPCN7/PANI and HPCN8/PANI show the capacitance retention of 85.1 and 86.5%, respectively. The fast capacitance decay may be caused by the collapse and swelling of PANI structure because of the doping/dedoping of electrolyte ions.

Furthermore, the HPCN9//HPCN9/PANI asymmetric supercapacitor (ASC) was fabricated by sandwiching a H_2SO_4/filter paper as the separator between negative (HPCN9) and positive electrode (HPCN9/PANI) (**Figure 7A**). The voltage window of HPCN9//HPCN9/PANI ASC device is 1.6 V. CV curves of HPCN9//HPCN9/PANI ASC device (**Figure 7B**) maintain the good roughly rectangular shape at 200 mV/s. The GCD curves (**Figure 7C**) exhibit a slight non-linearity and almost symmetric characteristic especially at the low current density for ASC device, indicating the contribution of the redox reaction from PANI. The equivalent series resistance (ESR) of ASC device is 1.4 Ω (**Figure S4**), indicating a small contact resistance. The C_{sp} of HPCN9//HPCN9/PANI asymmetric supercapacitor is 81.2 F/g at 1 A/g (**Figure 7D**), and remains 69.5% retention at 8 A/g.

To examine the long-term cycling stability of HPCN9//HPCN9/PANI ASC, GCD tests are measured to

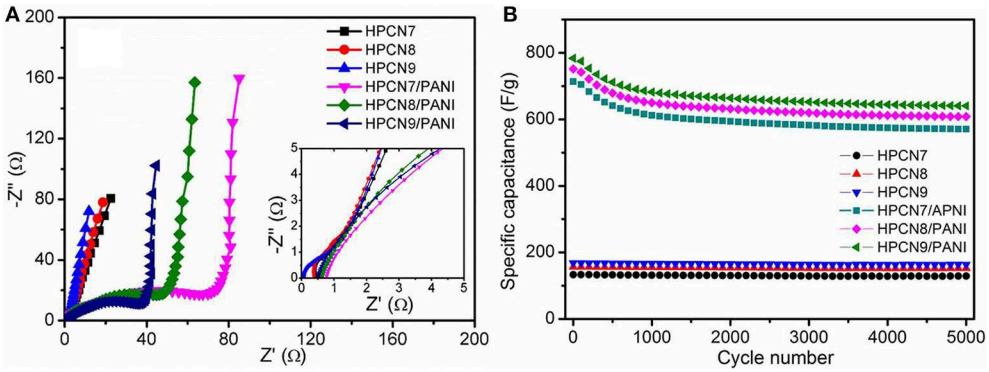

FIGURE 6 | Impedance spectra of HPCN and HPCN/PANI electrodes measured from 10^5 Hz^{-} 10^{-2} Hz **(A)** (inset: high frequency region). Capacitance retention of HPCN and HPCN/PANI electrodes over 5,000 cycles at 1 A/g **(B)**.

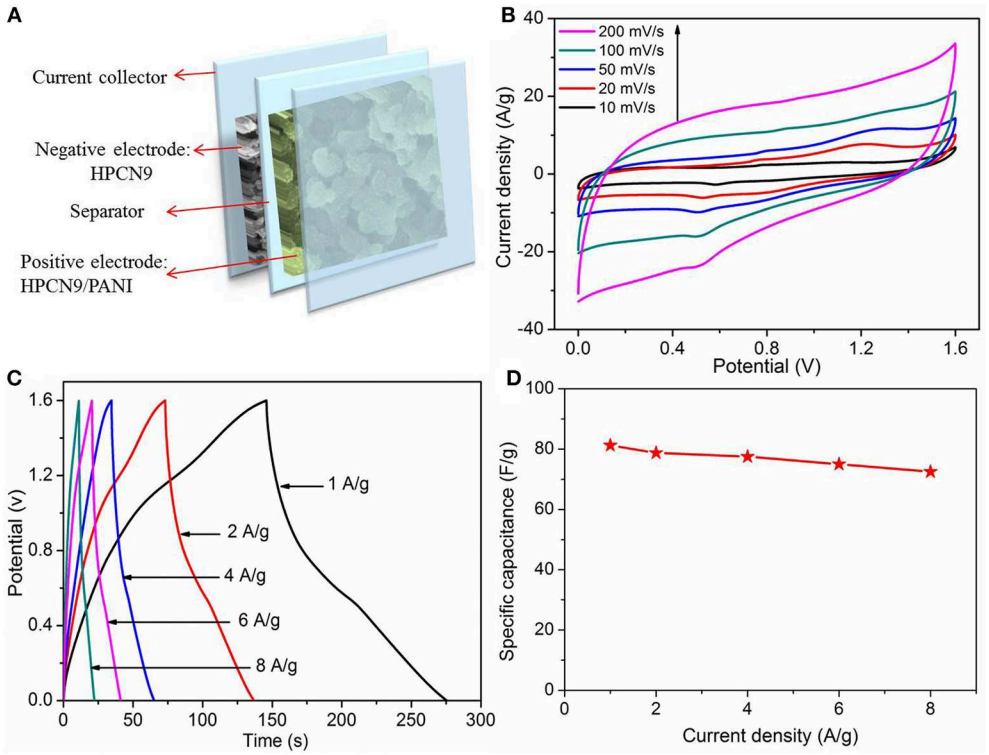

FIGURE 7 | Schematic illustration of HPCN9//HPCN9/PANI asymmetric device **(A)**. CV profiles of HPCN9//HPCN9/PANI ASC device at various scan rates **(B)**. GCD profiles of HPCN9//HPCN9/PANI ASC device **(C)**. Specific capacitance of HPCN9//HPCN9/PANI ASC device vs. current densities **(D)**.

the change of specific capacitance at 1 A/g (**Figure 8a**). HPCN9//HPCN9/PANI ASC shows 88.4% of initial capacitance after 10,000 cycling, lower than that of honeycomb-like porous carbon (HPC)//HPC/PANI (91.6% retention after 5,000 cycles) (Yu et al., 2016), due to the mechanical degradation of PANI in the acid electrolyte. However, the value is higher than graphene/PANI//graphene/RuO_2 ASC (30% decay over 2500 cycles) (Zhang et al., 2011) and activated graphene//PANI/MnO_2/carbon cloth ASC (30% loss of initial value after 5,000 cycles) (Zhao et al., 2015). **Figure 8b** displays the Ragone plot of HPCN9//HPCN9/PANI ASC, which has the highest energy density of 31.2 Wh/kg at 860 W/kg and retains that value of 25.1 Wh/kg at 6.88 kW/kg. As far as authors know, the results are higher than recently reported AC//AC fiber/PANI (20 Wh/kg, 2.1 kW/kg) (Salinas-Torres et al., 2013), AC//SiC-N-MnO_2 (30.06 Wh/kg, 0.11 kW/kg) (Kim and Kim, 2014), mesoporous carbon/PANI (23.8 Wh/kg, 0.21 kW/kg) (Cai et al., 2010), AC/CNT//graphene/MnO_2/CNT (27 Wh/kg, 7.8 kW/kg) (Cheng et al., 2013), graphene//MnO_2 (25.2 Wh/kg, 0.1 kW/kg) (Cao et al., 2013), and MnO_2/graphene// grapheme

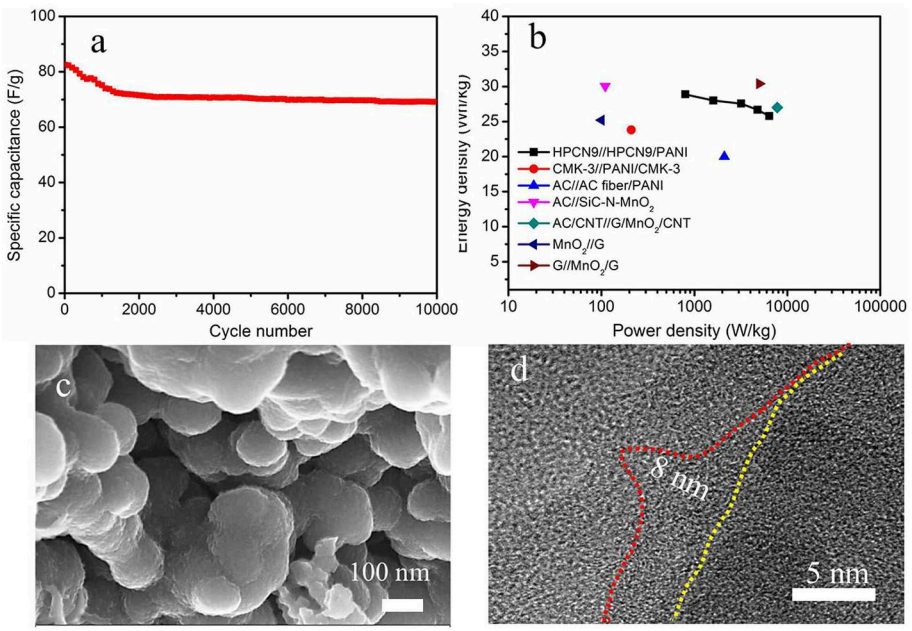

FIGURE 8 | (a) Cycling performance after 10,000 cycles and **(b)** Ragone plots for HPCN9//HPCN9/PANI ASC device and other devices in the literatures. **(c)** SEM image and **(d)** high-resolution TEM image of HPCN9/PANI in ASC device after 10,000 cycling.

(30.4 Wh/kg, 5 kW/kg) (Wu et al., 2010). Furthermore, the morphology of ASC device is investigated after 10,000 cycles. The nanospheres of HPCN9 (**Figure S5**) still stack with each other and form a porous network structure after 10,000 cycles. Obviously, HPCN9/PANI (**Figure 8c**) remains well-constructed porous network structure with advantage for high efficient ion diffusion. The length of PANI nanorods decreases to be ~8 nm owing to the degration during the long cycling process (**Figure 8d**). The excellent electrochemical performances of HPCN9//HPCN9/PANI ASC arise from the unique structure of well-ordered PANI nanorods grown on the hierarchical interconnected porous HPCN. Nitrogen heteroatom in HPCN enhance the surface wettability and active sites for electrolyte ions. The micropores in HPCN9 can offer high available interfacial areas; the mesopores make ions with high mobility to drift into the internal regions by efficient diffusion channels, while the interconnected network provides the macropores as the ion-buffering reservoirs, contributing to the excellent rate capacity. Moreover, the nanoscale PANI with high pseudocapacitance enhances supercapacitor performances of the integrated asymmetric device. Therefore, the synergistic effect of PANI and HPCN results in high electrochemical performances.

CONCLUSIONS

In summary, the interconnected hierarchical porous N-doped HPCN with high conductivity is successfully synthesized in this paper, starting from the easy accessible raw materials, such as sustainable wheat flour, urea and $ZnCl_2$. The prepared HPCN exhibits high specific surface area of 930 m^2/g with rational micro-mesopore distribution, which also delivers a specific capacitance of 168 F/g with remarkable stability (5% decay of initial value over 5,000 cycles). The well-ordered PANI nanorods deposited on HPCN9 displays high specific capacitance of 783 F/g. As-fabricated HPCN9//HPCN9/PANI ASC device delivers specific capacitance of 81.2 F/g, maximum energy density and power density, and 11.6% loss of original capacitance over 10,000 cycles. This work will provide a possibility of sustainable biomass materials to be the supercapacitor electrodes using the facile and low-cost process in the modern society.

DATA AVAILABILITY

All datasets generated for this study are included in the manuscript/**Supplementary Files**.

AUTHOR CONTRIBUTIONS

PY designed the work and wrote the paper. QW performance the experiments. LZ polished the english of this manuscript. YJ was responsible for the drafting.

FUNDING

This work was funded by the National Natural Science Foundation of China (No. 51802124 and No. 51702287) and Jiangsu Province (BK 20180626) and the Fundamental Research Funds for the Central Universities (JUSRP11858).

ACKNOWLEDGMENTS

The authors would like to thank the Engineering Research Center of Internet of Things Technology Applications Ministry of Education for kind support.

SUPPLEMENTARY MATERIAL

The Supplementary Material for this article can be found online at: https://www.frontiersin.org/articles/10.3389/fchem.2019.00455/full#supplementary-material

REFERENCES

Badwal, S. P., Giddey, S. S., Munnings, C., Bhatt, A. I., and Hollenkamp, A. F. (2014). Emerging electrochemical energy conversion and storage technologies. *Front. Chem.* 2, :79. doi: 10.3389/fchem.2014.00079

Bai, L. Z., Wang, Y. H., Cheng, S. S., Li, F., Zhang, Z. Y., and Liu, Y. Q. (2018). Synthesis and electrochemical performance of molybdenum disulfide-reduced graphene oxide-polyaniline ternary composites for supercapacitors. *Front. Chem.* 6, :218. doi: 10.3389/fchem.2018.00218

Barbieri, O., Hahn, M., Herzog, A., and Kötz, R. (2005). Capacitance limits of high surface area activated carbons for double layer capacitors. *Carbon* 43, 1303–1310. doi: 10.1016/j.carbon.2005.01.001

Benzigar, M. R., Talapaneni, S. N., Joseph, S., Ramadass, K., Singh, G., Scaranto, J., et al. (2018). Recent advances in functionalized micro and mesoporous carbon materials: synthesis and applications. *Chem. Soc. Rev.* 47, 2680–2721. doi: 10.1039/c7cs00787f

Cai, J. J., Kong, L. B., Zhang, J., Luo, Y. C., and Kang, L. (2010). A novel polyaniline/mesoporous carbon nano-composite electrode for asymmetric supercapacitor. *Chin. Chem. Lett.* 21, 1509–1512. doi: 10.1016/j.cclet.2010.07.003

Cao, J., Wang, Y., Zhou, Y., Ouyang, J. H., Jia, D., and Guo, L. (2013). High voltage asymmetric supercapacitor based on MnO_2 and graphene electrodes. *J. Electroanal. Chem.* 689, 201–206. doi: 10.1016/j.jelechem.2012.10.024

Chen, H., Yu, P., Zhang, Z., Teng, F., Zheng, L., Hu, K., et al. (2016). Ultrasensitive self-powered solar-blind deep-ultraviolet photodetector based on all-solid-state polyaniline/MgZnO bilayer. *Small* 12, 5809–5816. doi: 10.1002/smll.201601913

Cheng, Y., Zhang, H., Lu, S., Varanasi, C. V., and Liu, J. (2013). Flexible asymmetric supercapacitors with high energy and high power density in aqueous electrolytes. *Nanoscale* 5, 1067–1073. doi: 10.1039/C2NR33136E

Ding, J., Wang, H. L., Li, Z., Cui, K., Karpuzov, D., Tan, X. H., et al. (2015). Peanut shell hybrid sodium ion capacitor with extreme energy-power rivals lithium ion capacitors. *Energy Environ. Sci.* 8, 941–955. doi: 10.1039/c4ee02986k

Duan, B., Gao, X., Yao, X., Fang, Y., Huang, L., Zhou, J., et al. (2016). Unique elastic N-doped carbon nanofibrous microspheres with hierarchical porosity derived from renewable chitin for high rate supercapacitors. *Nano Energy* 27, 482–491. doi: 10.1016/j.nanoen.2016.07.034

Gao, N., and Fang, X. (2015). Synthesis and development of graphene–inorganic semiconductor nanocomposites. *Chem. Rev.* 115, 8294–8343. doi: 10.1021/cr400607y

Goldfarb, J. L., Dou, G., Salari, M., and Grinstaff, M. W. (2017). Biomass-based fuels and activated carbon electrode materials: an integrated approach to green energy systems. *ACS Sustainable Chem. Eng.* 5, 3046–3054. doi: 10.1021/acssuschemeng.6b02735

Hou, J., Cao, C., Ma, X., Idrees, F., Xu, B., Hao, X., et al. (2014). From rice bran to high energy density supercapacitors: a new route to control porous structure of 3D carbon. *Sci. Rep.* 4, :7260. doi: 10.1038/srep07260

Jiang, Y., Wu, Z., Jiang, L., Pan, Z., Yang, P., Tian, W., et al. (2018). Freestanding $CoSeO_3{\cdot}H_2O$ nanoribbon/carbon nanotube composite paper for 2.4 V high-voltage, flexible, solid-state supercapacitors. *Nanoscale* 10, 12003–12010. doi: 10.1039/C8NR02924E

Kang, D., Liu, Q., Gu, J., Su, Y., Zhang, W., and Zhang, D. (2015). "Egg-box"-assisted fabrication of porous carbon with small mesopores for high-rate electric double layer capacitors. *ACS Nano* 9, 11225–11233. doi: 10.1021/acsnano.5b04821

Kim, M., and Kim, J. (2014). Development of high power and energy density microsphere silicon carbide-MnO_2 nanoneedles and thermally oxidized activated carbon asymmetric electrochemical supercapacitors. *Phys. Chem. Chem. Phys.* 16, 11323–11336. doi: 10.1039/c4cp01141d

Kudin, K. N., Ozbas, B., Schniepp, H. C., Prud'homme, R. K., Aksay, I. A., and Car, R. (2008). Raman spectra of graphite oxide and functionalized graphene sheets. *Nano Lett.* 8, 36–41. doi: 10.1021/nl071822y

Lei, H., Chen, D., and Huo, J. (2016). Blowing and *in-situ* activation of carbonaceous "lather" from starch: preparation and potential application. *Mater. Des.* 92, 362–370. doi: 10.1016/j.matdes.2015.12.063

Li, J. P., Ren, Y. Q., Ren, Z. H., Wang, S. G., Qiu, Y. J., and Yu, J. (2015). Aligned polyaniline nanowires grown on the internal surface of macroporous carbon for supercapacitors. *J. Mater. Chem.* 3, 23307–23315. doi: 10.1039/c5ta05381a

Li, W., Zhang, B., Lin, R., Ho-Kimura, S., He, G., Zhou, X., et al. (2018). Battery electrodes: a dendritic nickel cobalt sulfide nanostructure for alkaline battery electrodes. *Adv. Funct. Mater.* 28, :1870154. doi: 10.1002/adfm.201870162

Li, X., Rao, M., and Li, W. (2016). Sulfur encapsulated in porous carbon nanospheres and coated with conductive polyaniline as cathode of lithium–sulfur battery. *J. Solid State Electrochem.* 20, 153–161. doi: 10.1007/s10008-015-3013-6

Liu, B., Liu, Y., Chen, H., Yang, M., and Li, H. (2017). Oxygen and nitrogen co-doped porous carbon nanosheets derived from Perilla frutescens for high volumetric performance supercapacitors. *J. Power Sources* 341, 309–317. doi: 10.1016/j.jpowsour.2016.12.022

Liu, L., Niu, Z., and Chen, J. (2016). Unconventional supercapacitors from nanocarbon-based electrode materials to device configurations. *Chem. Soc. Rev.* 45, 4340–4363. doi: 10.1039/c6cs00041j

Liu, L., Wang, Y., Meng, Q., and Cao, B. (2017). A novel hierarchical graphene/polyaniline hollow microsphere as electrode material for supercapacitor applications. *J. Mater. Sci.* 52, 7969–7983. doi: 10.1007/s10853-017-1000-2

Liu, T., Finn, L., Yu, M., Wang, H., Zhai, T., Lu, X., et al. (2014). Polyaniline and polypyrrole pseudocapacitor electrodes with excellent cycling stability. *Nano Lett.* 14, 2522–2527. doi: 10.1021/nl500255v

Lu, X., Hu, Y., Wang, L., Guo, Q., Chen, S., Chen, S., et al. (2016). Macroporous carbon/nitrogen-doped carbon nanotubes/polyaniline nanocomposites and their spplication in supercapacitors. *Electrochim. Acta* 189, 158–165. doi: 10.1016/j.electacta.2015.12.099

Pang, L., Zou, B., Han, X., Cao, L., Wang, W., and Guo, Y. (2016a). One-step synthesis of high-performance porous carbon from corn starch for supercapacitor. *Mater. Lett.* 184, 88–91. doi: 10.1016/j.matlet.2016.07.147

Pang, L., Zou, B., Zou, Y., Han, X., Cao, L., Wang, W., et al. (2016b). A new route for the fabrication of corn starch-based porous carbon as electrochemical supercapacitor electrode material. *Colloids Surf. A Physicochem. Eng. Asp.* 504, 26–33. doi: 10.1016/j.colsurfa.2016.05.049

Peng, L., Hu, L., and Fang, X. (2014). Energy harvesting for nanostructured self-powered photodetectors. *Adv. Funct. Mater.* 24, 2591–2610. doi: 10.1002/adfm.201303367

Salinas-Torres, D., Sieben, J. M., Lozano-Castell,ó, D., Cazorla-Amorós, D., and Morallón, E. (2013). Asymmetric hybrid capacitors based on activated carbon and activated carbon fibre–PANI electrodes. *Electrochim. Acta* 89, 326–333. doi: 10.1016/j.electacta.2012.11.039

Sankar, K. V., and Selvan, R. K. (2015). The ternary $MnFe_2O_4$/graphene/polyaniline hybrid composite as negative electrode for supercapacitors. *J. Power Sources* 275, 399–407. doi: 10.1016/j.jpowsour.2014.10.183

Wang, C., and Liu, T. (2017). Nori-based N, O, S, Cl co-doped carbon materials by chemical activation of $ZnCl_2$ for supercapacitor. *J. Alloys Compd.* 696, 42–50. doi: 10.1016/j.jallcom.2016.11.206

Wang, S., Ma, L., Gan, M., Fu, S., Dai, W., Zhou, T., et al. (2015). Free-standing 3D graphene/polyaniline composite film electrodes for

high-performance supercapacitors. *J. Power Sources* 299, 347–355. doi: 10.1016/j.jpowsour.2015.09.018

Wang, Y. G., Li, H. Q., and Xia, Y. Y. (2006). Ordered whiskerlike polyaniline grown on the surface of mesoporous carbon and its electrochemical capacitance performance. *Adv. Mater.* 18, 2619–2623. doi: 10.1002/adma.200600445

Wu, G., Tan, P., Wang, D., Li, Z., Peng, L., Hu, Y., et al. (2017). High-performance supercapacitors based on electrochemical-induced vertical-aligned carbon nanotubes and polyaniline nanocomposite electrodes. *Sci. Rep.* 7:43676. doi: 10.1038/srep43676

Wu, X., Jiang, L., Long, C., and Fan, Z. (2015). From flour to honeycomb-like carbon foam: carbon makes room for high energy density supercapacitors. *Nano Energy* 13, 527–536. doi: 10.1016/j.nanoen.2015.03.013

Wu, X. L., Wen, T., Guo, H. L., Yang, S., XiangkeWang and Xu, A. W. (2014). Biomass-derived multifunctional magnetite carbon aerogel nanocomposites for recyclable sequestration of ionizable aromatic organic pollutants. *ACS Nano* 245, 210–216. doi: 10.1016/j.cej.2014.02.032

Wu, Z. S., Ren, W., Wang, D. W., Li, F., Liu, B., and Cheng, H. M. (2010). High-energy MnO2 nanowire/graphene and graphene asymmetric electrochemical capacitors. *ACS Nano* 4, :5835–5842. doi: 10.1021/nn101754k

Xu, X., Zuo, Y., Cai, S., Tao, X., Zhang, Z., Zhou, X., et al. (2018). Three-dimensional helical inorganic thermoelectric generators and photodetectors for stretchable and wearable electronic devices. *J. Mater. Chem. C* 6, 4866–4872. doi: 10.1039/c8tc01183d

Yang, H., Ye, S., Zhou, J., and Liang, T. (2019). Biomass-derived porous carbon materials for supercapacitor. *Front. Chem.* 7, :274. doi: 10.3389/fchem.2019.00274

Yang, P., Wu, Z., Jiang, Y., Pan, Z., Tian, W., Jiang, L., et al. (2018). Fractal nanodendrites: fractal $(NixCo1–x)_9Se_8$ nanodendrite arrays with highly exposed (011) surface for wearable, all-solid-state supercapacitor. *Adv. Energy Mater.* 8, :1870116. doi: 10.1002/aenm.201870116

Yu, P., Li, Y., Yu, X., Zhao, X., Wu, L., and Zhang, Q. (2013a). Polyaniline nanowire arrays aligned on nitrogen-doped carbon fabric for high-performance flexible supercapacitors. *Langmuir* 29, 12051–12058. doi: 10.1021/la402404a

Yu, P., Zhao, X., Huang, Z., Li, Y., and Zhang, Q. (2014). Free-standing three-dimensional graphene and polyaniline nanowire arrays hybrid foams for high-performance flexible and lightweight supercapacitors. *J. Mater. Chem.* 2, 14413–14420. doi: 10.1039/C4TA02721C

Yu, P., Zhao, X., Li, Y., and Zhang, Q. (2017). Controllable growth of polyaniline nanowire arrays on hierarchical macro/mesoporous graphene foams for high-performance flexible supercapacitors. *Appl. Surf. Sci.* 393, 37–45. doi: 10.1016/j.apsusc.2016.09.119

Yu, P. P., Li, Y. Z., Zhao, X., Wu, L. H., and Zhang, Q. H. (2013b). *In situ* growth of ordered polyaniline nanowires on surfactant stabilized exfoliated graphene as high-performance supercapacitor electrodes. *Synth. Met.* 185, 89–95. doi: 10.1016/j.synthmet.2013.10.010

Yu, P. P., Zhang, Z. M., Zheng, L. X., Teng, F., Hu, L. F., and Fang, X. S. (2016). A novel sustainable flour ferived hierarchical nitrogen-doped porous carbon/polyaniline electrode for advanced asymmetric supercapacitors. *Adv. Energy Mater.* 6, :1601111. doi: 10.1002/Aenm.201601111

Zhang, H., Zhang, X., and Ma, Y. (2015). Enhanced capacitance supercapacitor electrodes from porous carbons with high mesoporous volume. *Electrochim. Acta* 184, 347–355. doi: 10.1016/j.electacta.2015.10.089

Zhang, J., Jiang, J., Li, H., and Zhao, X. S. (2011). A high-performance asymmetric supercapacitor fabricated with graphene-based electrodes. *Energy Environ. Sci.* 4, 4009–4015. doi: 10.1039/C1EE01354H

Zhang, Y., Jia, M., Gao, H., Yu, J., Wang, L., Zou, Y., et al. (2015). Porous hollow carbon spheres: facile fabrication and excellent supercapacitive properties. *Electrochim. Acta* 184, 32–39. doi: 10.1016/j.electacta.2015.10.042

Zhang, Y., Li, X., Dong, P., Wu, G., Xiao, J., Zeng, X., et al. (2018). Honeycomb-like hard carbon derived from pine pollen as high-performance anode material for sodium-ion battery. *ACS Appl. Mater. Interfaces*. 49, 42796–42803. doi: 10.1021/acsami.8b13160

Zhao, C., Huang, Y., Zhao, C., Shao, X., and Zhu, Z. (2018). Rose-derived 3D carbon nanosheets for high cyclability and extended voltage supercapacitors. *Electrochim. Acta* 291, 287–296. doi: 10.1016/j.electacta.2018.09.136

Zhao, X., Chen, C., Huang, Z., Jin, L., Zhang, J., Li, Y., et al. (2015). Rational design of polyaniline-MnO_2-carbon cloth ternary hybrids as electrodes for supercapacitors. *RSC Adv.* (5), 66311–66317.

Zheng, L., Yu, P., Hu, K., Teng, F., Chen, H., and Fang, X. (2016). Scalable-production, self-powered TiO_2 Nanowell-Organic Hybrid UV Photodetectors with Tunable Performances. *ACS Appl. Mater. Interfaces* 8, 33924–33932. doi: 10.1021/acsami.6b11012

Zou, Y., Zhang, Z., Zhong, W., and Yang, W. (2018). Hydrothermal direct synthesis of polyaniline, graphene/polyaniline and N-doped graphene/polyaniline hydrogels for high performance flexible supercapacitors. *J. Mater. Chem.* 6, 9245–9256. doi: 10.1039/c8ta01366g

Conflict of Interest Statement: The authors declare that the research was conducted in the absence of any commercial or financial relationships that could be construed as a potential conflict of interest.

frontiers in Chemistry

ORIGINAL RESEARCH
published: 23 July 2019
doi: 10.3389/fchem.2019.00521

Highly Ordered Mesoporous $NiCo_2O_4$ as a High Performance Anode Material for Li-Ion Batteries

Qilong Ren[1†], Guangyu Wu[2†], Weinan Xing[2*], Jiangang Han[2], Pingping Li[2], Bo Li[3*], Junye Cheng[4], Shuilin Wu[4], Rujia Zou[1] and Junqing Hu[1*]*

[1] State Key Laboratory for Modification of Chemical Fibers and Polymer Materials, College of Materials Science and Engineering, Donghua University, Shanghai, China, [2] College of Biology and the Environment, Nanjing Forestry University, Nanjing, China, [3] Department of Vascular Surgery, Shanghai Ninth People's Hospital, Shanghai JiaoTong University School of Medicine, Shanghai, China, [4] Center of Super-Diamond and Advanced Films, Department of Materials Science and Engineering, City University of Hong Kong, Hong Kong, China

OPEN ACCESS

Edited by:
Min Zeng,
Lanzhou Institute of Chemical Physics (CAS), China

Reviewed by:
Hui Yang,
Jiangxi University of Science and Technology, China
Ming Ma,
Shanghai Institute of Ceramics (CAS), China

***Correspondence:**
Guangyu Wu
gywuchem@163.com
Weinan Xing
xingweinan@126.com
Bo Li
boli@shsmu.edu.cn
Junqing Hu
hu.junqing@dhu.edu.cn

[†]These authors have contributed equally to this work

Specialty section:
This article was submitted to Electrochemistry, a section of the journal Frontiers in Chemistry

Received: *20 June 2019*
Accepted: *08 July 2019*
Published: *23 July 2019*

Citation:
Ren Q, Wu G, Xing W, Han J, Li P, Li B, Cheng J, Wu S, Zou R and Hu J (2019) Highly Ordered Mesoporous $NiCo_2O_4$ as a High Performance Anode Material for Li-Ion Batteries. Front. Chem. 7:521. doi: 10.3389/fchem.2019.00521

The controlled synthesis of highly ordered mesoporous structure has attracted considerable attention in the field of electrochemistry because of its high specific surface area which can contribute the transportation of ions. Herein, a general nano-casting approach is proposed for synthesizing highly ordered mesoporous $NiCo_2O_4$ microspheres. The as-synthesized mesoporous $NiCo_2O_4$ microsphere materials with high Brunner-Emmett-Teller (BET) surface area (~97.77 m^2g^{-1}) and uniform pore size distribution around 4 nm exhibited a high initial discharge capacity of ~1,467 $mAhg^{-1}$, a good rate capability as well as cycling stability. The superior electrochemical performance was mainly because of the highly porous nature of $NiCo_2O_4$, which rendered volume expansion during the process of cycling and shortened lithium-ions transport pathways. These properties showcase the inherent potential for use of highly ordered mesoporous $NiCo_2O_4$ microspheres as a potential anode material for lithium-ion batteries in the future.

Keywords: highly ordered, mesoporous, $NiCo_2O_4$, lithium-ion batteries, nano-casting

INTRODUCTION

Lithium-ion batteries (Yoo et al., 2008; Pan et al., 2013) have been proven to be viable alternatives to traditional energy storage devices and are vital tools when coupled with emerging renewable energy sources (Lewis and Nocera, 2006; Song, 2006; Chheda et al., 2007) (i.e., wind, solar, *etc.*). However, current energy demands outpace what is commercial systems are capable of, leading to the development of next-generation lithium-ion batteries (Liu et al., 2012; Lu et al., 2018; Shen et al., 2018). Particularly, the electrode is vital for optimal electrochemical performance (Toupin et al., 2004; Jiang et al., 2012; Wang et al., 2012; Yang et al., 2019a); however, conventional anode materials (Courtel et al., 2011; Chen et al., 2013; Chang et al., 2014) such as graphite have low theoretical specific capacities (372 mAh g^{-1}) and fail to satisfy energy storage demands. Consequently, transition metal oxides (TMOs) (Yuan et al., 2014; Tabassum et al., 2018) have been proposed as viable alternatives, attributed to high energy densities, which result in capacities more than double of those observed with graphite. However, this capacity relies on the morphology and structure of the TMO, which can suffer from undesired volume expansion and collapse of the structure as the battery cycles, leading to catastrophic failure.

Recently, space designed nanostructures have been acknowledged as an effective strategy to remit the volume expansion as well as shorten the lithium-ion transport pathways by providing a larger specific surface area, including implementation of a porous network (Wen et al., 2007; Lou et al., 2008; Shen et al., 2012, 2014; Yuan et al., 2012; Qie et al., 2013; Yang et al., 2019b), mesopores structures. For example, mesoporous Co_3O_4 (Li et al., 2008), NiO (Yin et al., 2018), $NiCo_2O_4$ (Li et al., 2018), and SnO_2 (Han et al., 2019) have been fabricated and have shown good electrochemical performance. However, limited attention has been focused to study ternary systems such as $NiCo_2O_4$ despite a higher electrical conductivity and specific capacity owing to its enhanced chemical kinetics. Inspired by ammonium hydrogen carbonate-assisted solvothermal route to prepare $Ni_{0.33}Co_{0.67}CO_3$ microspheres (Li et al., 2013), they led to a recent breakthrough technique to form mesoporous microspheres, we present a modified structure design containing ordered mesopores to further improve the electrochemical performance of $NiCo_2O_4$.

Herein, we developed a template-assisted method to synthesize novel $NiCo_2O_4$ microspheres containing highly ordered mesoporous structures and nanoparticles to effectively alleviate the huge volume expansion and enhance the electrical conductivity. The synthesis process is schematically shown in **Figure 1**. Firstly, mesoporous silica (KIT-6) is synthesized as a template by a typical approach which is illustrated in the experiment section in detail. Then the template is immersed in the mixed solution of $Ni(NO_3)_2$ and $Co(NO_3)_2$ to introduce the Ni^{2+} and Co^{2+} to be filled into KIT-6. After a subsequent calcination step at 450°C under N_2 atmosphere, the $NiCo_2O_4$@KIT-6 is successfully prepared. Finally, NaOH solution is utilized to remove the template of KIT-6 in the $NiCo_2O_4$@KIT-6 and obtain mesoporous $NiCo_2O_4$ microspheres. When acted as an anode material for Li-ion batteries, mesoporous $NiCo_2O_4$ microsphere electrode exhibits the superior electrochemical performance, whose stable specific capacity was 430 $mAhg^{-1}$ after 100 cycles, which is better than that of the non-porous $NiCo_2O_4$ (270 $mAhg^{-1}$ after 100 cycles). The improved lithium storage performance mainly benefits from the rationally designed mesoporous structures of $NiCo_2O_4$. We believe that this versatile strategy could be extended to more ternary TMO materials for the development of high property electrode in LIBs.

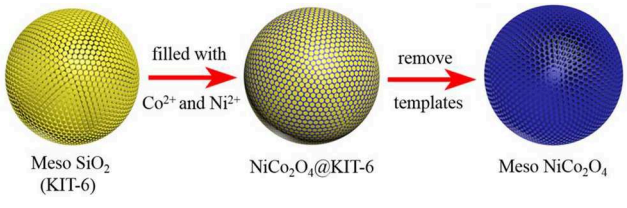

FIGURE 1 | Schematic illustration of the preparation for mesoporous $NiCo_2O_4$ microspheres.

EXPERIMENTAL SECTION

Materials

All chemicals (analytical reagent grade) used in this work, including polyethylene oxide-polypropylene oxide-polyethylene oxide (PEO-PPO-PEO, P123, MW = 5.8 K), hydrochloric acid, n-butanol, tetraethyl orthosilicate (TEOS), $Co(NO_3)_2{\bullet}6H_2O$, $Ni(NO_3)_2{\bullet}6H_2O$ and ethanol were purchased from Sigma-Aldrich.

Material Synthesis

Synthesis of Mesoporous SiO_2 (KIT-6)

The typical synthetic process was as follows (Zhou et al., 2018): 4.75 g of P123 were dissolved in a mixed solution containing 163 mL of deionized (DI) water and 7.5 ml of concentrated hydrochloric acid under stirring at 35°C. Once the P123 was fully dissolved, 4.53 g of n-butanol were added. After 1 h, TEOS (9.675 g) were added into the above mixed solution. The solution was then stirred for an additional 24 h at 35°C, followed by another 24 h incubation at 35°C. Cooling the mixed solution to room temperature, the precipitates could be collected by centrifugation for 3 times and moved to a vacuum oven at 90°C for 12 h. Then, after calcining the collected deposit at 550°C for 6 h, white mesoporous SiO_2 was obtained.

Synthesis of Mesoporous $NiCo_2O_4$ Microspheres

In a simple process, 0.4 g of KIT-6 were added to a solution containing 4 ml of 1 M $Co(NO_3)_2{\cdot}6H_2O$ and 2 ml of 1 M $Ni(NO_3)_2{\cdot}6H_2O$ in ethanol under stirring for 1.5 h at room temperature. Then, the solution was heated at 70°C until the ethanol was completely evaporated, and the solid was calcined at 200°C for 4 h. Immediately following, 2 mL of 1 M $Co(NO_3)_2{\cdot}6H_2O$ and 1 mL of $Ni(NO_3)_2{\cdot}6H_2O$ in ethanol were added following the previous steps and an additional calcination 450°C for 6 h. To obtain mesoporous $NiCo_2O_4$ microspheres, the powder was immersed in a 2 M NaOH solution to etch away the KIT-6 templates. Then, the samples were collected by centrifugation, washed for 3 times and moved to a vacuum oven at 60°C for 12 h. As a control, conventional $NiCo_2O_4$ microspheres were produced through the above-mentioned process without KIT-6 templates.

Materials Characterization

The mesoporous $NiCo_2O_4$ microspheres were characterized by using a PANalytical X' Pert X-ray diffractometer (Holland), with Cu-Kα radiation at 40 kV and 40 mA, selected-area electron diffraction (SAED), scanning electron microscope (SEM, S-4800) and transmission electron microscope (TEM, JEM-2100F). The N_2 adsorption/desorption isotherms were used to calculate the specific surface area and Barrett-Joyner-Halenda (BJH) equation was used to calculate the pore size distribution and average pore diameter.

RESULTS AND DISCUSSION

The mesoporous $NiCo_2O_4$ microspheres were prepared via nano-casting, with the crystalline structure and phase purity

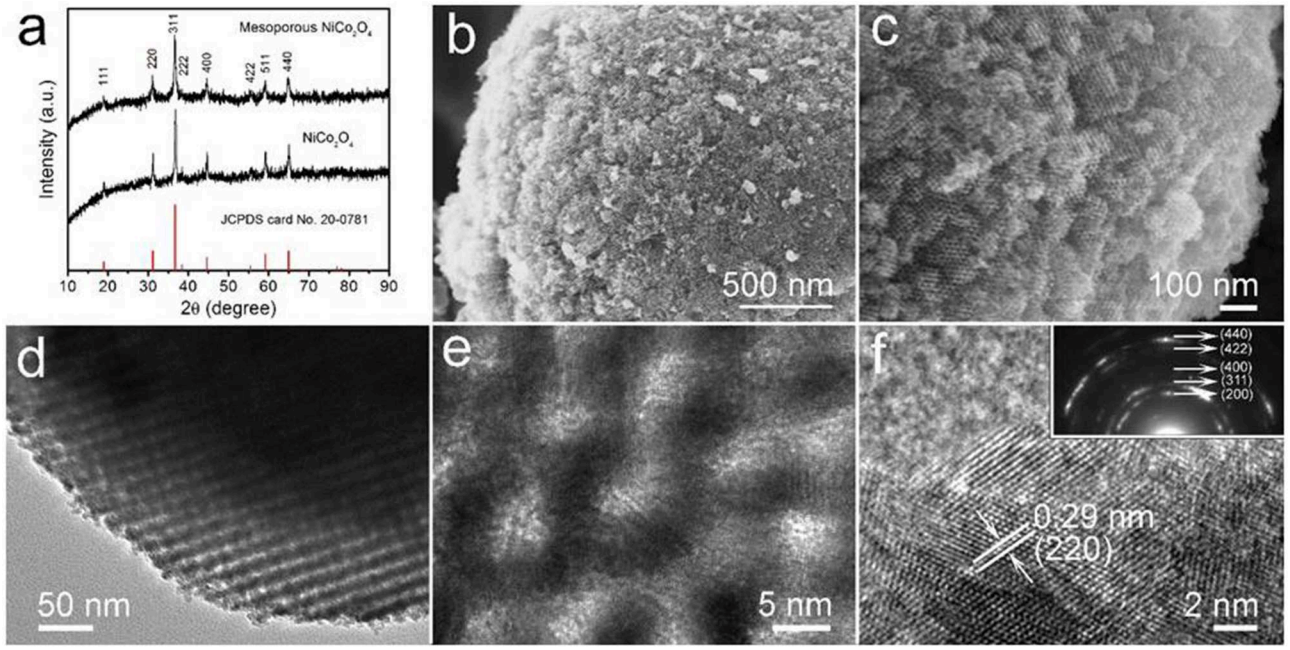

FIGURE 2 | (a) XRD patterns of mesoporous and non-porous $NiCo_2O_4$. **(b,c)** high magnification SEM images of mesoporous $NiCo_2O_4$. **(d)** TEM image and **(e,f)** high-resolution TEM image of mesoporous $NiCo_2O_4$. Inset in **(f)** shows the corresponding SAED pattern.

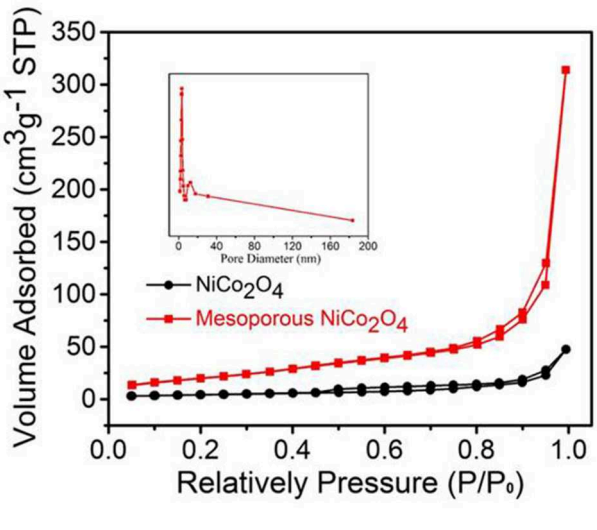

FIGURE 3 | Nitrogen adsorption-desorption isotherm and the corresponding pore size distribution of ordinary $NiCo_2O_4$ and mesoporous $NiCo_2O_4$.

characterized by X-ray diffraction (XRD). **Figure 2a** compares the diffraction patterns of both mesoporous and non-porous $NiCo_2O_4$ microspheres, showing eight obvious peaks at 2θ values of 18.9, 31.1, 36.7, 38.4, 44.6, 55.4, 59.1, and 64.9 for the (111), (220), (311), (222), (400), (422), (511), and (440) planes, respectively, which consist with the cubic spinel $NiCo_2O_4$ (JCPDS No.20-0781)without any apparent impurities.

The morphology and structure of obtained $NiCo_2O_4$are elucidated by SEM and TEM, as shown in **Figures 2b,c**, the surface morphology of the mesoporous microspheres, when compared to nonporous structures (**Figure S1**), is significantly rougher with highly ordered, uniform pores. This suggests that the polymeric precursor was fully injected within the KIT-6 microspheres, allowing the continuity of the mesoporous structure in subsequent deposition reactions. The highly ordered pores of the $NiCo_2O_4$ microspheres are clearly revealed with a pore size of ∼4 nm as shown by high-resolution TEM in **Figures 2d,e**. Additionally, in **Figure 2f**, the measured interplanar distance was found to be 0.29 nm, which aligns well with the (220) planes of spinel $NiCo_2O_4$. It is worth noting that well-defined diffraction rings were presented by the SAED pattern (Inset in **Figure 2f**), which correspond to the (440), (422), (400), (311), and (200) planes. The polycrystalline diffraction rings are in accordance with the result from the XRD pattern.

The pore diameter distribution and specific surface area of mesoporous $NiCo_2O_4$ samples were determined via N_2 adsorption-desorption measurements. The result of specific surface area was calculated from the isotherms (**Figure 3**) was 97.77 m^2g^{-1} for mesoporous $NiCo_2O_4$ microspheres, while the non-porous $NiCo_2O_4$ microspheres were 26.63 m^2g^{-1}. Additionally, the mesoporous structure was further analyzed by pore diameter distribution in the inset of **Figure 3**. $NiCo_2O_4$ microspheres displayed a pore volume (0.494 cm^3g^{-1}) with an average pore diameter of 3.416 nm. Ascribed to this special microsphere structure, the mesoporous structure could shorten the diffusion paths for lithium ions and provided buffering space to adapt

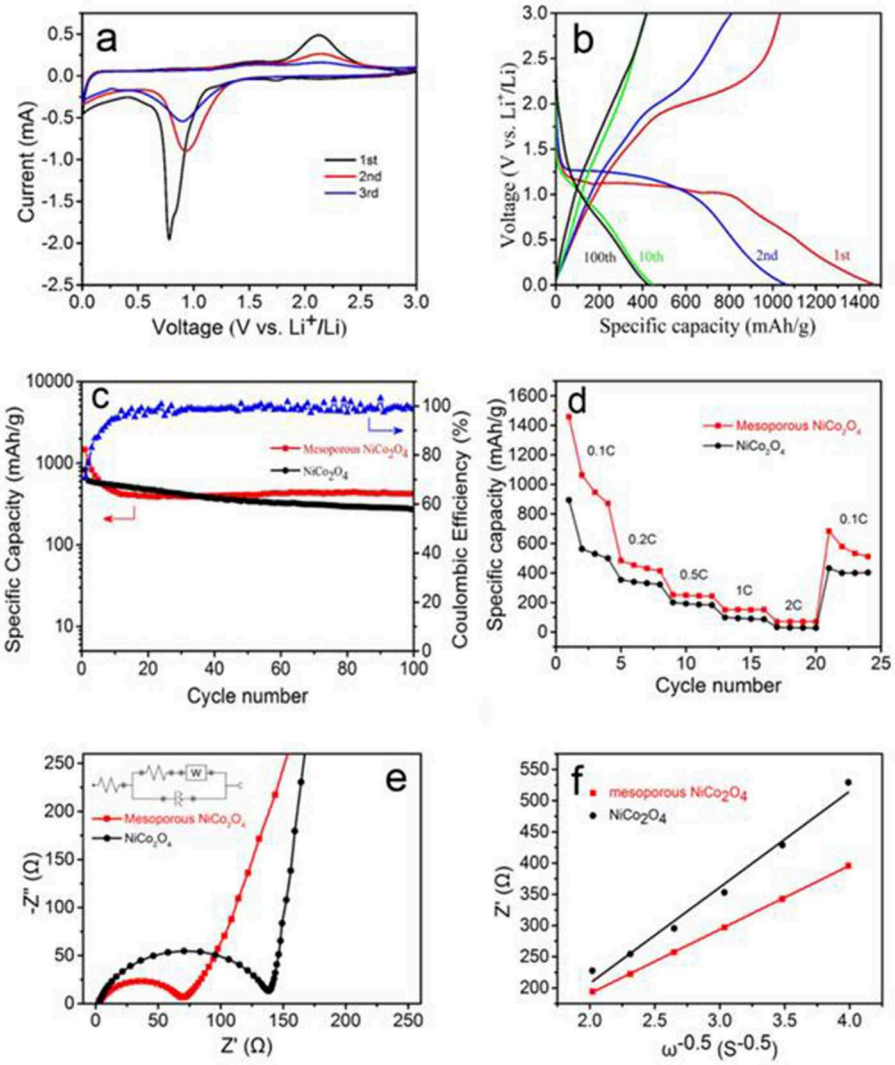

FIGURE 4 | First three consecutive CV curves of mesoporous $NiCo_2O_4$ **(a)**, galvanostatic discharge and charge profiles for 1st, 2nd,10th, 100th cycles of mesoporous $NiCo_2O_4$ **(b)** at the current densities of 100 mA.g^{-1}, cycling performance of ordinary $NiCo_2O_4$ and mesoporous $NiCo_2O_4$ at the current densities of 100 mAh.g^{-1} **(c)**, rate performances for ordinary $NiCo_2O_4$ and mesoporous $NiCo_2O_4$ at various current densities **(d)**. EIS pattern of ordinary $NiCo_2O_4$ and mesoporous $NiCo_2O_4$ **(e)**. The typical plots for Z' vs. $\omega^{-0.5}$ for the mesoporous $NiCo_2O_4$ **(f)**.

the volume expansion during the process of Li^+ insertion and extraction.

To confirm whether the mesoporous $NiCo_2O_4$ microspheres would be applicable as the anode materials in lithium-ion batteries, the as-prepared products were further investigated using cyclic voltammetry (CV), where **Figure 4a** exhibits the first three cycles of the mesoporous $NiCo_2O_4$ microspheres. In the 1st cycle, one dominant peak at 0.8 V could be assigned to the decomposition and reduction of Ni and Co ions. Meanwhile, the anodic peaks at approximately 2.1 V could be owing to the oxidation reaction of metallic Ni and Co to NiO and CoO. In subsequent tests, the cathodic peak broadened and shifted to 1.0 V. According to the analysis of the CV curves and previous literature reports, the Li reactions for mesoporous $NiCo_2O_4$ materials are as follows:

$$NiCo_2O_4 + 8Li^+ + 8e^- = Ni + 2Co + 4Li_2O \quad (1)$$

$$Ni + Li_2O = NiO + 2Li^+ + 2e^- \quad (2)$$

$$2Co + 2Li_2O = 2CoO + 4Li^+ + 4e^- \quad (3)$$

$$2CoO + 2/3Li_2O = 2/3Co_3O_4 + 4/3Li^+ + 4/3e^- \quad (4)$$

Galvanostatic tests were executed to ensure the influence of highly ordered mesoporous $NiCo_2O_4$ samples on the specific capacity values and capacity retention. The 1st, 2nd, 10th, and 100th cycles of the galvanostatic charge and discharge curves for mesoporous samples, at a current of 100 mA.g^{-1}, are shown

in **Figure 4b**. A long voltage plateau was showed in the initial discharge curve between 0.7 and 1.2 V, corresponding to the strong reduction peak that appeared during the first cathodic CV scan. The initial charge capacity for the mesoporous $NiCo_2O_4$ microspheres was ∼1467 $mAhg^{-1}$, which is markedly higher than the non-porous $NiCo_2O_4$ microspheres (∼820 $mAhg^{-1}$, **Figure S2**); however, this decreased to 1,060 $mAhg^{-1}$ after the 2nd discharge. The irreversible capacity increase during the 1st charge may be due to the generation of a solid electrolyte interface (SEI) layer.

A comparison of the specific capacity values obtained for non-porous $NiCo_2O_4$ and mesoporous $NiCo_2O_4$ over 100 cycles plotted is shown in **Figure 4c**. The non-porous $NiCo_2O_4$ suffers the most severe capacity fading with capacity values decreasing to 270 $mAhg^{-1}$ after 100 cycles, while the capacity retention was improved for mesoporous $NiCo_2O_4$ microspheres, obtaining capacity values of 430 $mAhg^{-1}$ after 100 cycles. The significant increase in the capacities for mesoporous $NiCo_2O_4$ compared to ordinary $NiCo_2O_4$ is attributed to the inherent properties of the mesoporous structure. Nevertheless, the final capacity is relatively low compared to the initial capacity, which may be attributed to the aperture being too small to relieve the expansion of the active material completely (Bhaway et al., 2017). For conversion-mode materials, the mesoporous $NiCo_2O_4$ provides particularly high buffering space, to adapt the large volume expansion during the process of Li^+ insertion/extraction and shorten the diffusion paths for lithium ions due to the interconnected architectures (**Figure S3**). Moreover, the coulombic efficiency for mesoporous $NiCo_2O_4$ over 100 cycles is also shown in **Figure 4c**. The initial coulombic efficiency is quite low (∼70%); however, the efficiency remains >95% after the 10th cycle. The rate performance of ordinary $NiCo_2O_4$ microspheres and mesoporous $NiCo_2O_4$ microspheres at various current densities were then compared in **Figure 4d**. The mesoporous $NiCo_2O_4$ microsphere electrode exhibits high initial discharge capacity and the capacity was recession with the increase of current density. However, the mesoporous $NiCo_2O_4$ microsphere electrode exhibited a higher capacity and rate of lithium-ion storage than the non-porous $NiCo_2O_4$ microsphere electrode.

To further investigate the mechanism for the improved electrochemical performance of the mesoporous $NiCo_2O_4$ microsphere, electrochemical impedance measurements (**Figure 4e**) and a fitting process (**Figure S4**) were measured containing the mesoporous $NiCo_2O_4$ electrode and ordinary $NiCo_2O_4$. As shown in **Figure 4e**, a semicircle and a straight line were acquired in the high frequency part and low frequency part, respectively. The intersection point from the curve in the high frequency part is on behalf of the electrolyte resistance. Moreover, the high frequency semicircle corresponds to the charge transfer resistance and the low frequency region with an inclined line represents the process of Li-ion diffusion. The initial value for charge transfer resistance is 66 Ω, which is far less than the ordinary $NiCo_2O_4$ (134 Ω, **Table S1**), which could be related to the more effective ion and electron transfer in the interface of electrolyte and active material, so that the cell has improved electrode reaction kinetics and a better cell cycling results.

TABLE 1 | Warburg factor (σ) and diffusion coefficient (D_{Li}^+) of sample ordinary $NiCo_2O_4$ and mesoporous $NiCo_2O_4$.

Materials	σ(Ω $s^{-0.5}$)	D_{Li}^+ (cm^2s^{-1})
Ordinary $NiCo_2O_4$	153.78	1.64×10^{-12}
Mesoporous $NiCo_2O_4$	102.48	2.46×10^{-12}

Moreover, the diffusion coefficient of the lithium ions (D_{Li}^+) can be confirmed in accordance with the following equation:

$$D_{Li^+} = \frac{0.5R^2T^2}{A^2F^4c^2\sigma_\omega^2}$$

Where R = gas constant, T = absolute temperature, A = surface area of the electrode, F = Faraday constant, c = concentration of Li+ in the material, and σ = Warburg factor obeying the following relationship:

$$Z_{Re} = R_S + R_{ct} + \sigma\omega^{-0.5}$$

Where Z_{Re} is the real part of impedance, thus ω is the angular frequency at low frequency. The linear relationship of Z_{Re} and $\omega^{-0.5}$ is shown in **Figure 4f**, with the slope of the fitted straight line indicating the value of σ. **Table 1** revealed the calculated values of σ and D_{Li}^+, where it can be clearly seen that the mesoporous $NiCo_2O_4$ exhibits a higher value of D_{Li}^+ than nonporous $NiCo_2O_4$.

CONCLUSION

Highly ordered mesoporous $NiCo_2O_4$ microspheres with a honeycomb-like structure, were synthesized via a nano-casting method. The mesoporous $NiCo_2O_4$ electrode possesses a high initial discharge capacity of ∼1,467 $mAh.g^{-1}$ at 100 mAg^{-1} and it exhibited both a high surface area and good rate capability. Such high electrochemical performance is due to its excellent surface area of mesoporous $NiCo_2O_4$ and the rapid ion transport in the electrolyte/electrode interface. This work may open a new sight in the synthesis of excellent Li-storage electrode materials and show an application in a promising candidate for Li-ion batteries.

DATA AVAILABILITY

The raw data supporting the conclusions of this manuscript will be made available by the authors, without undue reservation, to any qualified researcher. Requests to access the datasets should be directed to hu.junqing@dhu.edu.cn.

AUTHOR CONTRIBUTIONS

GW, BL, and JHu designed the project. QR, WX, JHa, PL, JC, SW, and RZ carried out the experiment and performed the experimental data analysis. QR, GW, and WX wrote the paper. BL revised the manuscript. All authors contributed to discussion of the results.

FUNDING

This work was financially supported by the National Key Research and Development of China (2017YFC0505803), the National Natural Science Foundation of China (41471191), Qing Lan Project of Jiangsu Province (Qinglan2016-15), Priority Academic Program Development of Jiangsu Higher Education Institutions (PAPD), and the Fundamental Research Funds for the Central Universities (grant no. CUSF-DH-D-2017044).

SUPPLEMENTARY MATERIAL

The Supplementary Material for this article can be found online at: https://www.frontiersin.org/articles/10.3389/fchem.2019.00521/full#supplementary-material

REFERENCES

Bhaway, S. M., Qiang, Z., Xia, Y., Xia, X., Lee, B., Yager, K. G., et al. (2017). Operando grazing incidence small-angle X-ray scattering/X-ray diffraction of model ordered mesoporous lithium-ion battery anodes. *ACS Nano* 11, 1443–1454. doi: 10.1021/acsnano.6b06708

Chang, J., Huang, X., Zhou, G., Cui, S., Hallac, P. B., Jiang, J., et al. (2014). Multilayered Si nanoparticle/reduced graphene oxide hybrid as a high-performance lithium-ion battery anode. *Adv. Mater.* 26, 758–764. doi: 10.1002/adma.201302757

Chen, Z., Belharouak, I., Sun, Y. K., and Amine, K. (2013). Titanium-based anode materials for safe lithium-ion batteries. *Adv. Funct. Mater.* 23, 959–969. doi: 10.1002/adfm.201200698

Chheda, J. N., Huber, G. W., and Dumesic, J. A. (2007). Liquid-phase catalytic processing of biomass-derived oxygenated hydrocarbons to fuels and chemicals. *Angew. Chem. Int. Ed.* 46, 7164–7183. doi: 10.1002/anie.200604274

Courtel, F. M., Duncan, H., Abu-Lebdeh, Y., and Davidson, I. J. (2011). High capacity anode materials for Li-ion batteries based on spinel metal oxides AMn_2O_4 (A = Co, Ni, and Zn). *J. Mater. Chem.* 21, 10206–10218. doi: 10.1039/C0JM04465B

Han, N., Wang, Y., Deng, J., Zhou, J., Wu, Y., Yang, H., et al. (2019). Self-templated synthesis of hierarchical mesoporous SnO_2 nanosheets for selective CO_2 reduction. *J. Mater. Chem. A* 7, 1267–1272. doi: 10.1039/C8TA10959A

Jiang, J., Li, Y., Liu, J., Huang, X., Yuan, C., and Lou, X. W. (2012). Recent advances in metal oxide-based electrode architecture design for electrochemical energy storage. *Adv. Mater.* 24, 5166–5180. doi: 10.1002/adma.201202146

Lewis, N. S., and Nocera, D. G. (2006). Powering the planet: chemical challenges in solar energy utilization. *Proc. Natl. Acad. Sci. U. S. A.* 103, 15729–15735. doi: 10.1073/pnas.0603395103

Li, J., Xiong, S., Liu, Y., Ju, Z., and Qian, Y. (2013). High electrochemical performance of monodisperse $NiCo_2O_4$ mesoporous microspheres as an anode material for li-ion batteries. *ACS Appl. Mater. Interfaces* 5, 981–988. doi: 10.1021/am3026294

Li, W., Zhang, B., Lin, R., Ho-Kimura, S., He, G., and Zhou, X., et al (2018). A dendritic nickel cobalt sulfide nanostructure for alkaline battery electrodes. *Adv. Funct. Mater.* 28:1705937. doi: 10.1002/adfm.201705937

Li, Y., Tan, B., and Wu, Y. (2008). Mesoporous Co_3O_4 nanowire arrays for lithium ion batteries with high capacity and rate capability. *Nano Lett.* 8, 265–270. doi: 10.1021/nl0725906

Liu, N., Wu, H., McDowell, M. T., Yao, Y., Wang, C., and Cui, Y. (2012). A yolk-shell design for stabilized and scalable li-ion battery alloy anodes. *Nano Lett.* 12, 3315–3321. doi: 10.1021/nl3014814

Lou, X. W., Deng, D., Lee, J. Y., and Archer, L. A. (2008). Thermal formation of mesoporous single-crystal Co3O4 nano-needles and their lithium storage properties. *J. Mater. Chem.* 18, 4397–4401. doi: 10.1039/B810093D

Lu, Y., Yu, L., and Lou, X. W. (2018). Nanostructured conversion-type anode materials for advanced lithium-ion batteries. *Chem* 4, 972–996. doi: 10.1016/j.chempr.2018.01.003

Pan, H., Hu, Y.-S., and Chen, L. (2013). Room-temperature stationary sodium-ion batteries for large-scale electric energy storage. *Energy Environ. Sci.* 6, 2338–2360. doi: 10.1039/C3EE40847G

Qie, L., Chen, W., Xu, H., Xiong, X., Jiang, Y., Zou, F., et al. (2013). Synthesis of functionalized 3D hierarchical porous carbon for high-performance supercapacitors. *Energy Environ. Sci.* 6, 2497–2504. doi: 10.1039/C3EE41638K

Shen, L., Che, Q., Li, H., and Zhang, X. (2014). Mesoporous $NiCo_2O_4$ nanowire arrays grown on carbon textiles as binder-free flexible electrodes for energy storage. *Adv. Funct. Mater.* 24, 2630–2637. doi: 10.1002/adfm.201303138

Shen, L., Zhang, X., Uchaker, E., Yuan, C., and Cao, G. (2012). $Li_4Ti_5O_{12}$ nanoparticles embedded in a mesoporous carbon matrix as a superior anode material for high rate lithium ion batteries. *Adv. Energy Mater.* 2, 691–698. doi: 10.1002/aenm.201100720

Shen, X., Liu, H., Cheng, X. B., Yan, C., and Huang, J. Q. (2018). Beyond lithium ion batteries: higher energy density battery systems based on lithium metal anodes. *Energy Storage Mater.* 12, 161–175. doi: 10.1016/j.ensm.2017.12.002

Song, C. (2006). Global challenges and strategies for control, conversion and utilization of CO_2 for sustainable development involving energy, catalysis, adsorption and chemical processing. *Catalysis Today* 115, 2–32. doi: 10.1016/j.cattod.2006.02.029

Tabassum, H., Zou, R., Mahmood, A., Liang, Z., Wang, Q., Zhang, H., et al. (2018). A universal strategy for hollow metal oxide nanoparticles encapsulated into B/N co-doped graphitic nanotubes as high-performance lithium-ion battery anodes. *Adv. Mater.* 30:1705441. doi: 10.1002/adma.201705441

Toupin, M., Brousse, T., and Bélanger, D. (2004). Charge storage mechanism of MnO_2 electrode used in aqueous electrochemical capacitor. *Chem. Mater.* 16, 3184–3190. doi: 10.1021/cm049649j

Wang, G., Zhang, L., and Zhang, J. (2012). A review of electrode materials for electrochemical supercapacitors. *Chem. Soc. Rev.* 41, 797–828. doi: 10.1039/C1CS15060J

Wen, Z., Wang, Q., Zhang, Q., and Li, J. (2007). *In situ* growth of mesoporous SnO_2 on multiwalled carbon nanotubes: a novel composite with porous-tube structure as anode for lithium batteries. *Adv. Funct. Mater.* 17, 2772–2778. doi: 10.1002/adfm.200600739

Yang, H., Ye, S., Wang, Y., Zhou, J., Jia, J., Chen, J., et al. (2019a). Scalable production of hierarchical n-doping porous carbon@cu composite fiber based on rapid gelling strategy for high-performance supercapacitor. *J. Alloys Compd.* 792, 976–982. doi: 10.1016/j.jallcom.2019.04.138

Yang, H., Ye, S., Zhou, J., and Liang, T. (2019b). Biomass-derived porous carbon materials for supercapacitor. *Front. Chem.* 7:274. doi: 10.3389/fchem.2019.00274

Yin, X., Chen, H., Zhi, C., Sun, W., Lv, L.-P., and Wang, Y. (2018). Functionalized graphene quantum dot modification of yolk-shell NiO microspheres for superior lithium storage. *Small* 14:1800589. doi: 10.1002/smll.201800589

Yoo, E., Kim, J., Hosono, E., Zhou, H.-S., Kudo, T., and Honma, I. (2008). Large Reversible Li storage of graphene nanosheet families for use in rechargeable lithium ion batteries. *Nano Lett.* 8, 2277–2282. doi: 10.1021/nl800957b

Yuan, C., Li, J., Hou, L., Zhang, X., Shen, L., and Lou, X. W. (2012). Ultrathin mesoporous $NiCo_2O_4$ nanosheets supported on ni foam as

advanced electrodes for supercapacitors. *Adv. Funct. Mater.* 22, 4592–4597. doi: 10.1002/adfm.201200994

Yuan, C., Wu, H. B., Xie, Y., and Lou, X. W. (2014). Mixed transition-metal oxides: design, synthesis, and energy-related applications. *Angew. Chem. Int. Ed.* 53, 1488–1504. doi: 10.1002/anie.201303971

Zhou, B., Li, C., Qi, N., Jiang, M., Wang, B., and Chen. Z. (2018). Pore structure of mesoporous silica (KIT-6) synthesized at different temperatures using positron as a nondestructive probe. *Appl. Surf. Sci.* 450, 31–37. doi: 10.1016/j.apsusc.2018.03.223

Conflict of Interest Statement: The authors declare that the research was conducted in the absence of any commercial or financial relationships that could be construed as a potential conflict of interest.

frontiers in Chemistry

CORRECTION
published: 28 August 2019
doi: 10.3389/fchem.2019.00600

Corrigendum: Highly Ordered Mesoporous $NiCo_2O_4$ as a High Performance Anode Material for Li-Ion Batteries

Qilong Ren[1†], Guangyu Wu[2†], Weinan Xing[2*], Jiangang Han[2], Pingping Li[2], Bo Li[3*], Junye Cheng[4], Shuilin Wu[4], Rujia Zou[1] and Junqing Hu[1*]*

[1] State Key Laboratory for Modification of Chemical Fibers and Polymer Materials, College of Materials Science and Engineering, Donghua University, Shanghai, China, [2] College of Biology and the Environment, Nanjing Forestry University, Nanjing, China, [3] Department of Vascular Surgery, Shanghai Ninth People's Hospital, Shanghai JiaoTong University School of Medicine, Shanghai, China, [4] Center of Super-Diamond and Advanced Films, Department of Materials Science and Engineering, City University of Hong Kong, Hong Kong, China

Keywords: highly ordered, mesoporous, $NiCo_2O_4$, lithium-ion batteries, nano-casting

OPEN ACCESS

Approved by:
Frontiers Editorial Office, Frontiers Media SA, Switzerland

***Correspondence:**
Guangyu Wu
gywuchem@163.com
Weinan Xing
xingweinan@126.com
Bo Li
boli@shsmu.edu.cn
Junqing Hu
hu.junqing@dhu.edu.cn

[†]These authors have contributed equally to this work

Specialty section:
This article was submitted to Electrochemistry, a section of the journal Frontiers in Chemistry

Received: *13 August 2019*
Accepted: *14 August 2019*
Published: *28 August 2019*

Citation:
Ren Q, Wu G, Xing W, Han J, Li P, Li B, Cheng J, Wu S, Zou R and Hu J (2019) Corrigendum: Highly Ordered Mesoporous $NiCo_2O_4$ as a High Performance Anode Material for Li-Ion Batteries. Front. Chem. 7:600. doi: 10.3389/fchem.2019.00600

A Corrigendum on

Highly Ordered Mesoporous $NiCo_2O_4$ as a High Performance Anode Material for Li-Ion Batteries

by Ren, Q., Wu, G., Xing, W., Han, J., Li, P., Li, B., et al. (2019). Front. Chem. 7:521. doi: 10.3389/fchem.2019.00521

In the original article, the author order list was incorrectly showed as Guangyu Wu[1*†], Qilong Ren[2†], Weinan Xing[2*], Jiangang Han[2], Pingping Li[2], Bo Li[3*], Junye Cheng[4], Shuilin Wu[4], Rujia Zou[1], Junqing Hu[1*]. The correct author order's list is Qilong Ren[1†], Guangyu Wu[2*†], Weinan Xing[2*], Jiangang Han[2], Pingping Li[2], Bo Li[3*], Junye Cheng[4], Shuilin Wu[4], Rujia Zou[1], Junqing Hu[1*].

In the published article, reflecting the above correction, there was an error with affiliations "1" and "2". Instead of appearing as "1 College of Biology and the Environment, Nanjing Forestry University, Nanjing, China" and "2 State Key Laboratory for Modification of Chemical Fibers and Polymer Materials, College of Materials Science and Engineering, Donghua University, Shanghai, China," they should be reversed to appear as "1 State Key Laboratory for Modification of Chemical Fibers and Polymer Materials, College of Materials Science and Engineering, Donghua University, Shanghai, China" and "2 College of Biology and the Environment, Nanjing Forestry University, Nanjing, China".

Furthermore, there was an error in affiliation "4". Instead of "Department of Materials Science and Engineering, Center of Super-Diamond and Advanced Films, City University of Hong Kong, Hong Kong, China," it should be "Center of Super-Diamond and Advanced Films, Department of Materials Science and Engineering, City University of Hong Kong, Hong Kong, China".

The authors apologize for this error and state that this does not change the scientific conclusions of the article in any way. The original article has been updated.

frontiers in Chemistry

ORIGINAL RESEARCH
published: 02 August 2019
doi: 10.3389/fchem.2019.00544

Liquid Phase Exfoliated Hexagonal Boron Nitride/Graphene Heterostructure Based Electrode Toward Asymmetric Supercapacitor Application

Xuan Zheng[1], Guangjin Wang[2,3], Fei Huang[4], Hai Liu[3], Chunli Gong[3], Sheng Wen[3], Yuanqiang Hu[3], Genwen Zheng[3] and Dongchu Chen[2]**

[1] Hubei Provincial Key Laboratory of Green Materials for Light Industry, School of Materials and Chemical Engineering, Hubei University of Technology, Wuhan, China, [2] School of Materials Science and Energy Engineering, Foshan University, Foshan, China, [3] College of Chemistry and Materials Science, Hubei Engineering University, Xiaogan, China, [4] Key Laboratory of Functional Foods, Ministry of Agriculture, Guangdong Key Laboratory of Agricultural Products Processing, Sericultural & Agri-Food Research Institute Guangdong Academy of Agricultural Sciences, Guangzhou, China

OPEN ACCESS

Edited by:
Wenyao Li,
Shanghai University of Engineering Sciences, China

Reviewed by:
Shijie Li,
Zhejiang Ocean University, China
Jiajun Wang,
Tianjin University, China

***Correspondence:**
Guangjin Wang
wgj501@163.com
Dongchu Chen
Chendc@fosu.edu.cn

Specialty section:
This article was submitted to Electrochemistry, a section of the journal Frontiers in Chemistry

Received: *20 June 2019*
Accepted: *16 July 2019*
Published: *02 August 2019*

Citation:
Zheng X, Wang G, Huang F, Liu H, Gong C, Wen S, Hu Y, Zheng G and Chen D (2019) Liquid Phase Exfoliated Hexagonal Boron Nitride/Graphene Heterostructure Based Electrode Toward Asymmetric Supercapacitor Application. Front. Chem. 7:544. doi: 10.3389/fchem.2019.00544

In this paper, owing to the electrostatic interaction between graphene and h-BN, a facile liquid phase exfoliation method was carried out to fabricate h-BN/graphene based van der Waals heterostructure nanocomposites without additional chemical cross-linkers. The physicochemical properties of as-prepared composites were characterized by several electron microscopic and spectroscopic measurements. The h-BN/graphene heterostructure composites were employed to use as the anodes of asymmetric supercapacitor, and exhibited exceptional capacitive performance due to their synergistic effects. It is expected that the as-prepared h-BN/graphene materials can boost scalable heterostructure electrodes in supercapacitors, and our liquid phase exfoliation method can be used for the construction of the other energy storage and electronics.

Keywords: heterostructure, h-BN, graphene, asymmetric supercapacitor, liquid phase exfoliation

INTRODUCTION

Graphene, as one of the most important representative of 2D nanomaterials, has been a research hotspot in recent years (Kong et al., 2017). It has special Dirac electronic properties (Loan et al., 2014), high carrier migration rate (Morozov et al., 2008), excellent thermal conductivity and mechanical properties (Balandin et al., 2008; Kong et al., 2017), and also been favored by the industry, academia and research institutes. Nevertheless, graphene is a zero band gap material, and its conducting and valence band interlace at the Dirac point. Therefore, the major dilemma to promote the application of graphene in electronic devices is the expansion of band gap. To process with this challenge, researchers have come up with many techniques to expand the bandgap of graphene, including the preparation of graphene nanoribbons (Jiao et al., 2009; Wang and Dai, 2010), nanomesh (Jingwei et al., 2010), and the chemical modification (Li et al., 2011). However, physical etching or chemical reaction would inevitably lead impurities into the boundary or surface of graphene, and greatly reduce the carrier mobility of grapheme (Liao et al., 2014).

Hexagonal Boron Nitride (h-BN) is defined as "white graphene" or "graphene-like" Boron Nitride, with an approximate honeycomb lattice formed by sp2 hybridization and a band gap of 5.9 eV (Wang et al., 2016). Because of its broad band gap, h-BN can be applied in prospects of spintronics, energy storage and composite materials. Because the h-BN and graphene have a rare low mismatched lattice constant, researchers have also revealed new features that the h-BN/graphene heterostructure can regulate the intrinsic electronic structure (Tran et al., 2016). Compared with the single-layer graphene, the carrier mobility (140,000 cm^2/Vs) of the h-BN/graphene heterostructure film prepared by chemical vapor deposition method is 3.5 times higher than that of the single-layer graphene film (40,000 cm^2/Vs) (Wang et al., 2013). Besides, the h-BN/graphene heterostructure was proved to have great potential value for application in energy storage devices, like Li-ion battery (Pomerantseva and Gogotsi, 2017; Wu et al., 2017; Li et al., 2018). Researchers also added the h-BN/Graphene heterostructure material into PVA fiber, greatly enhancing the mechanical properties of the composite fiber and increasing the conductivity to 3 S/m, so as to obtain the high-strength conductive composite fiber (Boland et al., 2016). Thus, combining graphene with other 2D materials (such as h-BN) to form heterostructure is bound to greatly expand the research scope of this field like a "snowball."

At present, large-scale preparation of high-quality h-BN/graphene heterostructure materials is still a recognized problem. From the preparation methods for h-BN/graphene heterostructure, it can be divided into two main modes: one is to grow graphene and h-BN on the substrate surface through CVD (chemical vapor deposition) method, and then transfer and mechanical superposition; the other is to directly use CVD method to grow graphene on substrate and then continue to grow h-BN on the surface of graphene, while this method needs to investigate the lattice mismatch problem. It is noted that the CVD method can ensure integrality of h-BN/graphene heterostructure, but the reaction condition is extremely harsh (usually requires high temperature vacuum environment), the heterostructure size is limited and the cost is high, so it's insufficient to meet the needs of practical application. Therefore, an effective preparation method is urgently needed to make up for the shortcomings of the CVD method to prepare the h-BN/graphene heterostructure materials.

As our best knowledge, liquid phase exfoliation method has been rarely carried out to prepare h-BN/graphene heterostructure. Nevertheless, some investigators have attempted to use this chemical method to create heterostructures, like graphene-black phosphorous-graphene sandwich heterostructure (Sun et al., 2015), metal oxide heterostructures (Xu et al., 2016, 2019; Mahmood et al., 2018; Wan et al., 2018), and (layered double hydroxide) LDH/rGO heterostructure (Ge et al., 2016) which are served as the electrodes in energy storage component. Compared with the heterostructure prepared by CVD method, the liquid phase exfoliation process is simpler and cheaper, and has a broader development prospect.

In this paper, we used the glycerol/urea system in graphene and h-BN exfoliation. The smaller h-BN nanosheets were attached on bigger graphene through ultrasonic assistant. Based on a certain amount of space size differences, the phenomenon of reunification in h-BN or graphene can be effectively prevented under the action of electrostatic force. Furthermore, the h-BN/graphene heterostructure system prepared in this work can be stably dispersed in organic solution, and the system can maintain long-term stability. Moreover, the h-BN/graphene heterostructure materials with different mass ratios in application of supercapacitors is studied in detail. As a result, the h-BN/graphene heterostructure materials show the maximum capacitance of 134 F/g and good cycling stability (96 % of the initial capacitance after 10,000 cycles at 10 A/g). Meanwhile, the assembled asymmertic supercapacitor (ASc) exhibits maximum energy density of 2.05 Wh/kg at high power density of 1998.5 W/kg.

EXPERIMENTAL SECTION

Materials Preparation

Graphite powder (300 mesh, purity>95%, XFNANO Materials) or h-BN powder (1 um, purity>98%, Sigma-Aldrich) were dissolved in the urea/glycerol (molar ratio = 2:1) dispersion. After that, 200 mL of the graphite or h-BN dispersion were transferred to a 800 mL flat bottom beaker, under which graphite or h-BN powder were exfoliated and dispersed through mechanical stirring at 800 rpm for 24 h. Then, the obtained products were evenly transferred to a 50 ml centrifuge tube, then centrifuged for 25 min at 5,000 rpm. The top half of the centrifuged graphite or h-BN dispersion were collected and re-dispersed in DMF, followed by filtration and ultrasonic washing with large amounts of DMF and ethanol, and drying in vacuum oven at 60°C. The yield of graphene or h-BN was decided by taking off the mass of the residual solid (Zheng et al., 2018).

The graphene/DMF and h-BN/DMF dispersion solution were mixed together with a certain mass ratio (the mass content ratio of graphene and h-BN was 1:2, 1:1, 2:1, respectively). The resulting mixed solution was ultrasonic for 30 min, then stirred at room temperature for 24 h and centrifuged at 1,000 rpm for 30 min. The upper liquid was discarded, and the solid precipitation was finally obtained, namely, h-BN/grapheme (BN/G) heterostructure materials.

Characterization

Transmission electron microscopy (TEM) and high resolution transmission electron microscopy (HRTEM) images were obtained using a JEM-2001F (JEOL, 200 kV primary beam) equipped with a Gatan CCD camera. The morphology of the samples was observed by using S-4800 (Hitachi, accelerating voltage of 25 KV) cold field emission scanning electron microscope (FESEM). The crystal structure of heterostructure was analyzed by D8 Advance X-ray diffraction systems (Bruker, $\lambda = 0.154056$ nm). Raman spectra of the samples were tested by an InVia (Renishaw, UK) spectrometer to reflect the composition equipped by a 633 nm laser. The thickness of all samples was also analyzed by MFP-3D-SA AFM (AsylumResearch, USA) using a tapping mode at a scan rate of 1 Hz.

Electrode Preparation and Electrochemical Tests

The BN/G working electrodes were prepared by mixing 90 wt.% active material (BN/G heterostructure materials) and 10 wt.% polyvinylidene fluoride (PVDF) in NMP solvent to form a slurry. Then the slurry was coated onto a clean Ni mesh (current collector) and dried in a vacuum oven at 60 °C for 24 h. The counter electrode was the activated carbon (AC, SSA = 1,800(±100) m^2/g, purity>94.2%, XFNANO Materials). The counter electrodes were prepared via the same method as the above working electrodes. The loading mass of each electrode was about 0.15 mg/cm^2. Microporous polypropylene and 2 M KOH solution were used as the separator and electrolyte, respectively.

The electrochemical performance of samples was measured on the CHI660E (Chenhua, China) electrochemical workstation. Cyclic voltammetry (CV) tests were carried out at the scan rate of 10∼200 mV/s. Galvanostatic charge-discharge (GCD) tests were performed at various current densities from 0.5 to 10 A/g. Electrochemical impedance spectroscopy (EIS) was employed in a frequency from 0.01 Hz to 100 kHz at an amplitude of 5 mV. All the related electrochemical tests were performed at room temperature. Specific capacity of the BN/G in two-electrode was calculated from Equations (1) and (2) (Wang et al., 2014):

$$C = \frac{\int I_1 dV}{\mathrm{sm}\Delta \mathrm{V}} \quad (1)$$

$$C = \frac{\mathrm{I_2 t}}{\mathrm{m}\Delta \mathrm{V}} \quad (2)$$

Where I represents the discharged current (A), s is the scanning rate (V/s), Δt and ΔV are the discharged time (s) and the voltage drop upon discharging, respectively, and m is the mass of the electroactive materials (g). The energy density (E, Wh/kg) and the power density (P, W/kg) of the BN/G//AC were calculated based on the following Equations (3) and (4) (Balogun et al., 2016):

$$E = 0.5CV^2/3.6 \quad (3)$$

$$P = \frac{E \times 3600}{t} \quad (4)$$

Where C represents specific capacity of the capacitor (F/g) calculated according to Equation (2), Δt and ΔV are the discharged time (s) and the voltage drop upon discharging, respectively.

RESULTS AND DISCUSSION

Figure 1 illustrates the preparation of the BN/G heterostructure. The graphene/DMF and h-BN/DMF dilute solution were added into the flat bottom beaker, respectively. Then the mixture was stirred to force the exfoliated h-BN nanosheets entering into the graphene layers to form heterostructure through π-π accumulation. Firstly, the morphology and structure of as-prepared graphene were characterized to verify the effectiveness of glycerol/urea liquid phase exfoliation system. In this work, due to the effectiveness of the exfoliation system, graphene/DMF dispersion solution was randomly diluted to a certain concentration to observe its micromorphology through TEM. As shown in **Figure 2a**, the graphene exhibited a dispersive lamellar distribution under a low magnification, whilst the unique wavy lattice fringes of graphene were further observed in the high magnification (**Figure 2b**). and these small lattice fringe is peculiar to the crystal of graphene material. At the same time, dotted impurities can be observed, which is most likely due to the non-covalently modified π-π accumulation effect formed by the interaction of urea or solvent with graphene in the glycerol/urea system (Chen et al., 2018). The selective fast fourier transform (FFT) analysis of the partial amplification of graphene in **Figure 2b** revealed the unique hexagonal pattern of electron diffraction in the few-layer of graphene. This result can clearly show the successful exfoliation of graphite (Paton et al., 2014).

In order to further observe the graphene prepared by the glycerol/urea system mentioned above, the graphene/DMF dispersion samples were analyzed with the SEM morphology. **Figure S1a** was the dispersion diagram of graphene after exfoliation, comparative measurements on scale bar of 1 um suggested that the size of graphene was close to 6 um. In addition, according to the morphology at high magnification (**Figure S1b**), the edges of graphene sheets were corrugated, and there were obvious upwarp, verifing the successful exfoliation of graphite.

We also used AFM to conduct random sample analysis of the exfoliated graphene, which was compared with the sampling method of TEM: the sample to be tested was dripped with pipette gun to the newly prepared mica film after vacuum dust removal. It can be observed the 2D morphology of typical graphene in the tapping mode from **Figure S2**. The size of the graphene lamella

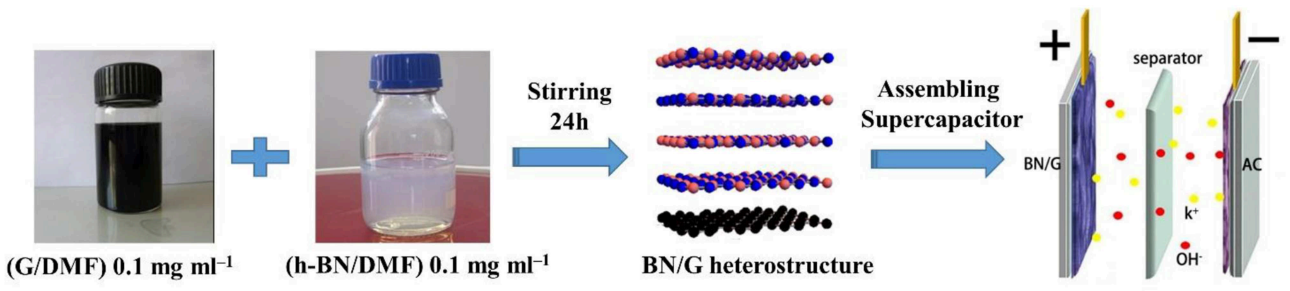

FIGURE 1 | Schematic illustration for the preparation of the BN/G heterostructure.

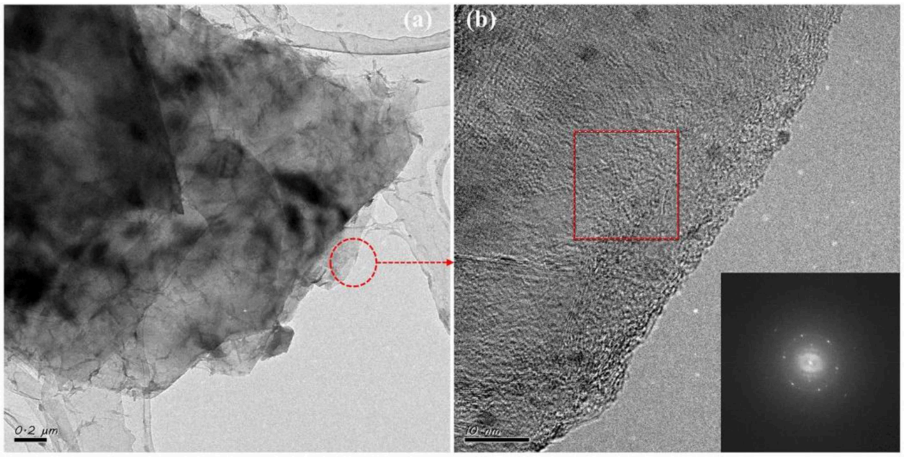

FIGURE 2 | The TEM **(a)** and HRTEM **(b)** images of graphene, the inset is fast fourier transform (FFT) image.

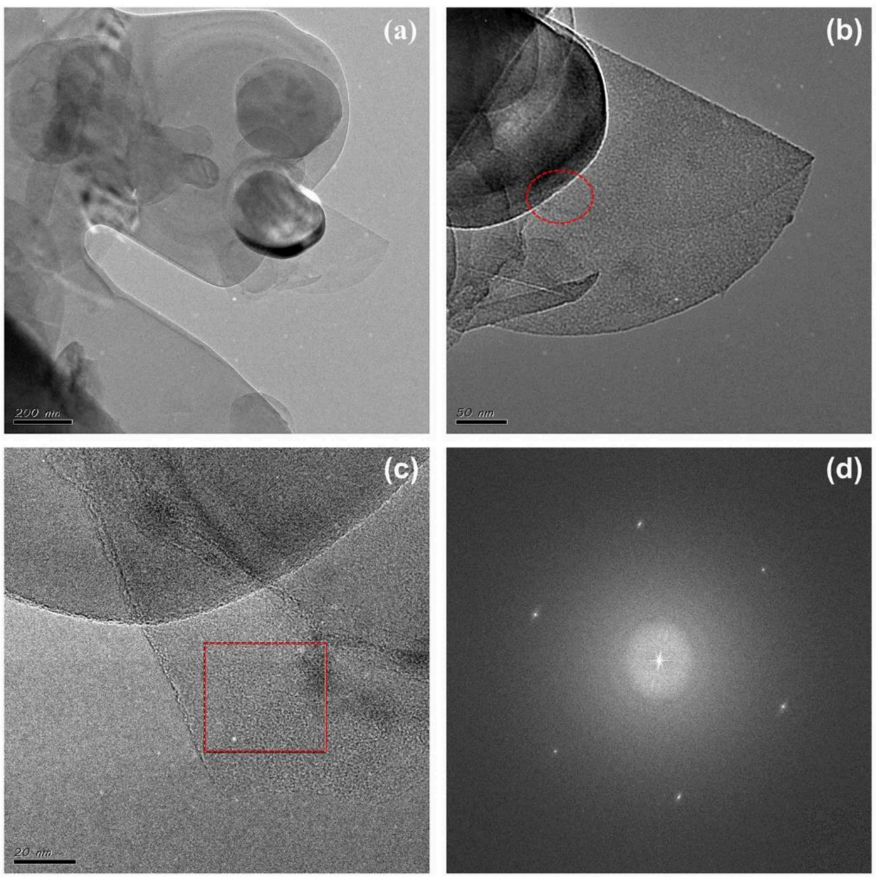

FIGURE 3 | The TEM **(a–c)** and FFT **(d)** images of h-BN nanosheets.

was also more than 5 um, which as similar with the observed size of TEM and SEM. Based on the theoretical thickness of graphene (0.34 nm), the thickness of two adjacent areas in view of **Figure S2** is about 0.68 nm (Pattammattel and Kumar, 2015). This value indicated that the as-prepared graphene was close to double-layer, showing the exfoliated graphene by glycerol/urea system was few-layer.

To test the universality of glycerol/urea in the above system, we used the same process to treat other 2D material, such as h-BN, and also obtained h-BN/DMF dispersion solution.

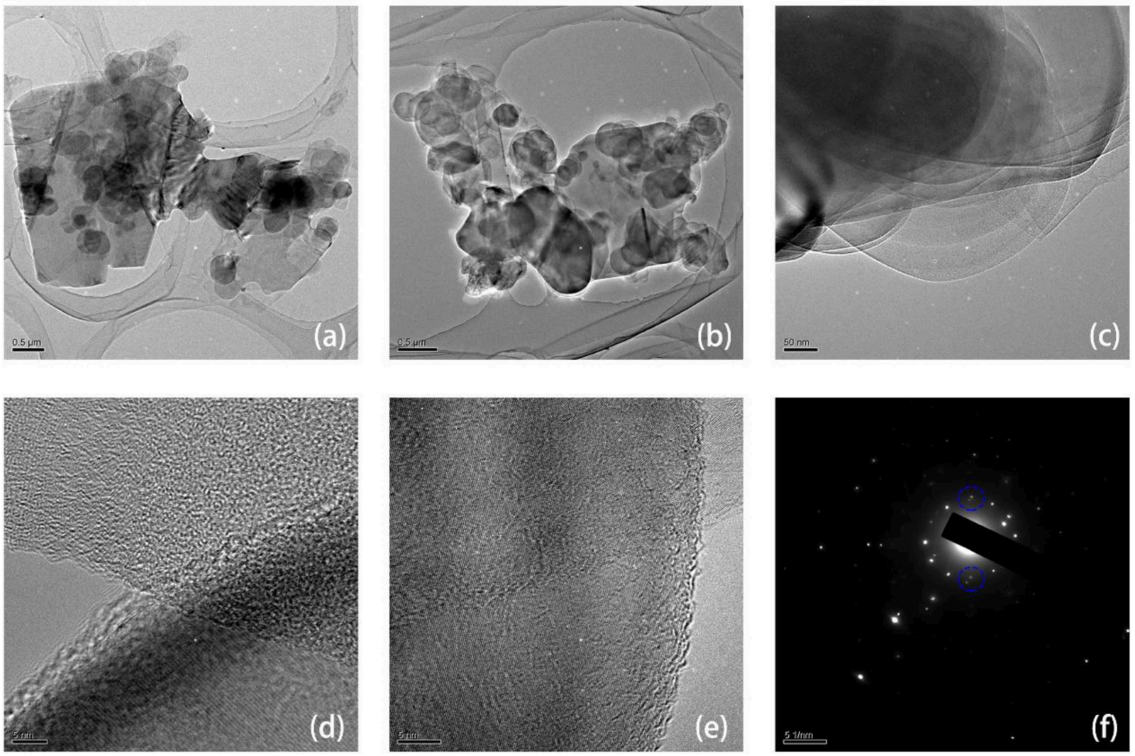

FIGURE 4 | The TEM **(a–e)** and selected area electron diffraction (SAED) **(f)** images of h-BN/graphene heterostructure.

Then the h-BN samples were observed by TEM. As shown in **Figure 3**, it can be seen that the h-BN nanosheets were stacked on top of each other, and their sizes were below 1 um, much smaller than the size of graphene. From the HRTEM images (**Figures 3b,c**), it can be preliminarily concluded that h-BN powders were exfoliated into nanosheets. Combined with the FFT image in **Figure 3d**, the obtained h-BN lamination belongs to few-layer, which also proves the availability of glycerol/urea system (Varrla et al., 2015).

Figure S3 is the SEM images of h-BN nanosheets. The white hexagonal circular lamella in **Figure S3b** is h-BN nanosheet with a size of <1 um, which is consistent with the intuitive size of TEM photographs. **Figure S3c** shows that h-BN nanosheet have obvious vertical stratification, indicating that h-BN raw powder is peeled into h-BN nanosheet. **Figure S4** shows the AFM diagram of h-BN sample, the thickness of the two adjacent white crystals is about 0.7 nm, which is in line with the theoretical value of the double-layer h-BN nanosheet (Kim et al., 2011; Tran et al., 2016).

To understand the crystal structure characteristics of the as-prepared BN/G heterostructure samples, XRD analysis was performed in **Figure S5**. It can be concluded that the graphene has extremely sharp diffraction peak at 26.5°, and h-BN has obvious diffraction peak at 26.7°, which is mainly reflected by the relatively small layer spacing difference between h-BN and graphene. The (002) crystal faces of graphene and h-BN still show no obvious deviation, implying that the formation of heterostructure is only a physical stacking process.

Figure S6 shows the typical Raman absorption peaks of h-BN/graphene, h-BN and graphene, such as D peak (∼1,331 cm^{-1}) and G peak (∼1,578 cm^{-1}), which are shown in Graphene and BN/G, respectively, demonstrating the presence of graphene in BN/G heterostructure. Due to the strong photoluminescence background of h-BN, the photoluminescence background shown in the BN/G region can be attributed to the defect states of h-BN, including defects along grain boundaries (Li et al., 2012). The heterostructure of BN/G was determined by HRTEM and SAED. **Figures 4a,b** depicted two BN/G heterostructure regions, in which the larger graphene sheet was covered by the smaller h-BN nanosheets. This structure size is in accordance with the previous TEM results of h-BN and graphene. The HRTEM image in **Figures 4c–e** further proved a certain difference between exfoliated h-BN and graphene on the interface edge of the BN/G heterostructure, and the lattice fringe of the two structures was particularly obvious. **Figure 4f** is the SAED result of lattice fringe corresponding to BN/G heterostructure. From its diffraction pattern, a set of clear hexagonal diffraction spots can be observed. The close view of the area indicated by the blue circle shows two separate diffraction points along the radial direction. These two points correspond to (100) plane diffraction of h-BN and graphene, respectively. The calculated plane spacing of the two points was 2.13 and 2.06 Å, which were in good agreement with the (100) crystal plane spacing values obtained by the XRD tests. The AFM height of BN/G heterostructure on mica substrate is shown in **Figure S7**. The h-BN is small in size and

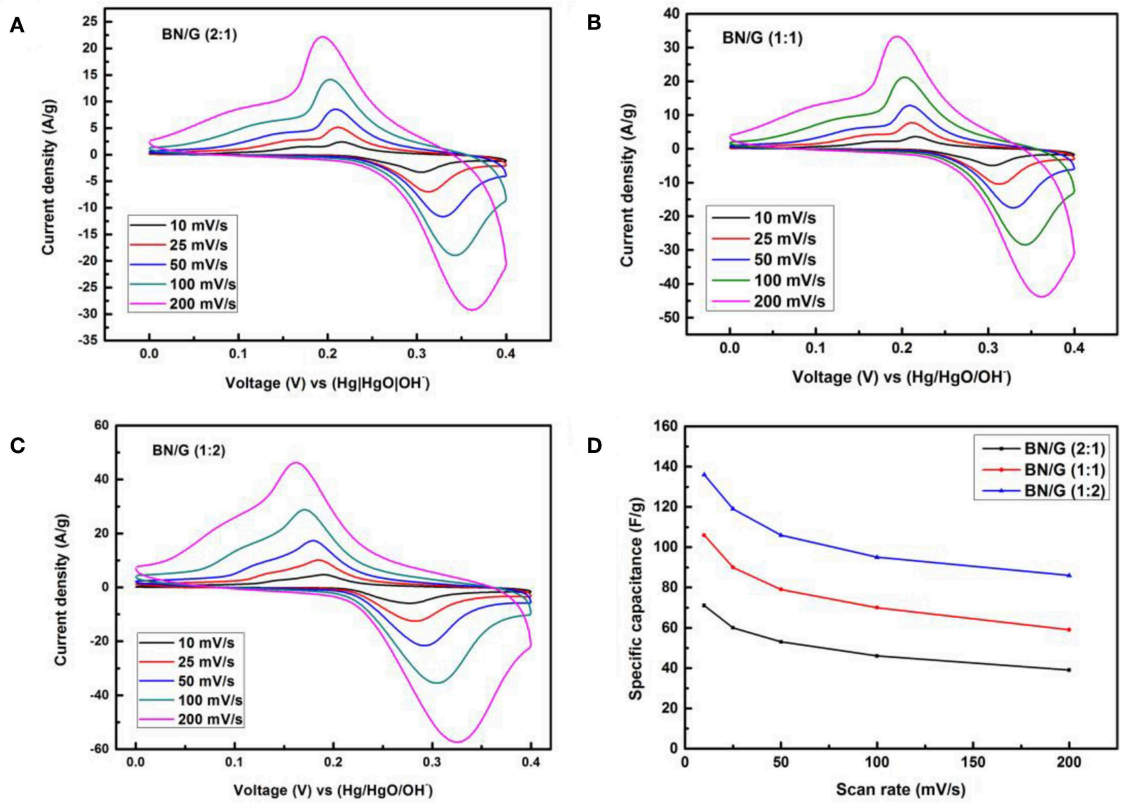

FIGURE 5 | CVs of all BN/G at different scan rates **(A–C)** and **(D)** tendency of the specific capacitance of three BN/G samples at scan rates of 10–200 mV/s.

stacked on top of the graphene layers in different thicknesses. However, the average thickness of graphene is larger than that of the previous graphene sheet, attributing to the alternating superposition of h-BN and graphene in the heterostructural materials (Yang et al., 2013a).

Inhibiting the stack of graphene is the key factor to realize high the performance of the electrochemical capacitor based on graphene materials. As for rGO, the capacitance is significantly reduced when re-stacking between graphene sheets, mainly due to the irreversible stacking of single rGO sheet during the reduction and drying process (Yang et al., 2013b). We expect that the h-BN nanosheet in the BN/G can be used as an effective electrolyte channel to increase the overall electroactive surface area (**Figure 1**). It is hoped that charges can be stored in graphene or h-BN electrodes through electrostatic interaction, adsorption and desorption of interface ions (**Figure S8**). Since graphene can be assumed as a zero-gap semiconductor with Fermi energy level located at Dirac point, the presence of B and N in h-BN makes it form h-BN/graphene superlattice above the Fermi energy level (Ge et al., 2016; Lee et al., 2016). Therefore, we prepared BN/G with different mass loads of h-BN and studied the potential application of h-BN as a 2D structural carrier and electrolyte channel in graphene-based membrane.

Figures 5A–C show the CV curves of three mass ratios BN/G measured by the two-electrode method at different scanning rates (10 ∼200 mV/s) in 2 M KOH. As illustrated in **Figures 5A–C**, we can notice the prominent redox peak, which ascribing to the change of oxidation state of N atoms by electrolyte insertion. **Figure 5D** is the change of capacitance with the increase of scan rates, the CV curve still shows a larger redox peak even when scan rate increases to 200 mV/s, this is because the Fermi level of BN/G electrode materials reached a higher potential compared to the redox potential of electrolyte, electrons transferred from the electrode to the interface of the electrolyte. Since h-BN is usually used as dielectric material, its capacitance is very low, while the capacitance of BN/G is relatively large, it possibly attributed to BN/G heterostructure shortening the ion transport path and increasing the specific surface area for charge storage.

However, due to the differences in the contributions of h-BN and graphene to the overall capacitance in BN/G, the accumulation of h-BN multilayer and the increase of Faraday resistance may be the reason for the lower capacitance of BN/G(2:1; 1:1). It is found that the graphene is inserted into the interlayer space of h-BN to play the role of interval layering, preventing the re-stacking of h-BN nanosheets. Therefore, the charge storage mechanism in BN/G may be caused by the synergistic effect of graphene and h-BN. **Figures 6A–C** shows the charge and discharge curves of BN/G samples with different mass ratios at different current densities. The specific capacitance value is calculated according to the above Equation (2). Compared

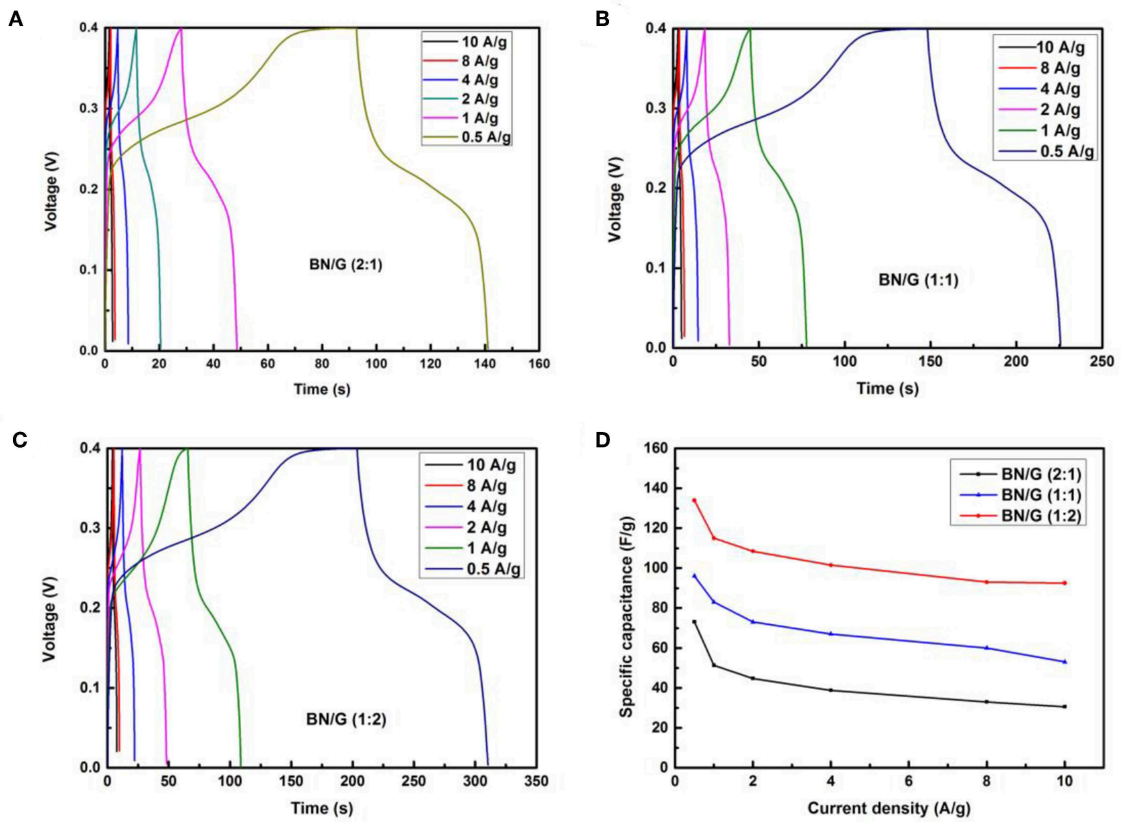

FIGURE 6 | Galvanostatic charge–discharge curves for all BN/G at different current densities: **(A)** BN/G(2:1), **(B)** BN/G(1:1), **(C)** BN/G(1:2), and **(D)** specific capacitance of all BN/G as a function of discharge current.

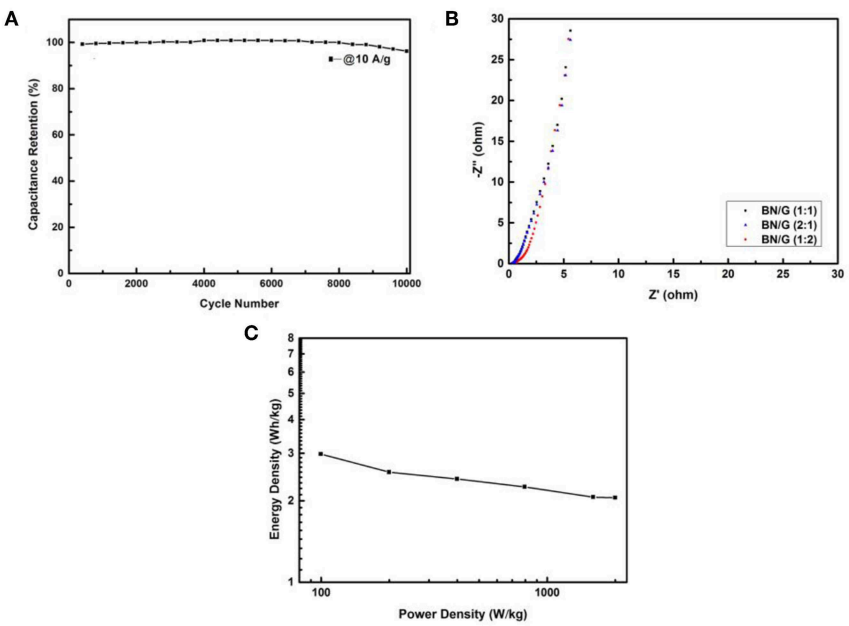

FIGURE 7 | Cyclic performances of the BN/G (1:2) after 10,000 cycles at 10 A/g **(A)**, Nyquist plots of all BN/G **(B)**, Ragone plots of the BN/G (1:2) **(C)**.

with BN/G(2:1) and BN/G(1:1), the discharge time of BN:G(1:2) is longer at the same current density. Furthermore, BN:G(1:2) has a specific capacitance of 134 F/g when the current density is 0.5 A/g. By contrast, BN/G(2:1) and BN/G(1:1) have specific capacitance of 71 and 106 F/g, respectively, at the same current density.

The variation trend of BN/G samples with different mass ratios is shown in **Figure 6D**. Driven by the increase of current density, the capacitance of BN/G declined, but it tended to be flat at current densities ranged from 2 to 10 A/g, indicating the BN/G heterostructural materials have good rate performance. When the current density is increased to 10 A/g, the capacitance retentions of BN/G(2:1), BN/G(1:1), and BN/G(1:2) are 55, 56, and 69 %, respectively. These capacitance retentions match well with the trend calculated by the CV method in **Figure 5D**, and the optimal ratio is BN:G = 1:2.

BN:G(1:2) was further taken as a representative to study its cycle stability for charging and discharging 10,000 times under the current density of 10 A/g. **Figure 7A** shows that after 10,000 times of rapid charge and discharge tests, BN:G(1:2) electrode has only 4% loss, exhibiting its excellent electrochemical stability. This is because h-BN has extremely high chemical and thermal stability, providing synergies with high electrochemical stability when it exists in conductive graphene systems (Kumar et al., 2015). **Figure 7B** shows the AC impedance diagram of BN/G samples with different mass ratios. The lattice in the figure shows that the BN/G sample exhibits excellent capacitive characteristics, especially the approximate vertical line in the lower frequency range. And the charge transfer resistances (Rct) of BN/G(2:1), BN/G(1:1), and BN/G(2:1) are small, and the equivalent series resistance (ESRs) is 6.7, 6.0, and 5.3 Ω, respectively. The results can be concluded that h-BN in heterostructure creates electrolyte channel, and as an effective ion channel to boost and expedite diffusion of electrolyte ions such as K^+ and OH^- (Hu et al., 2014).

Toward studying the electrochemical properties of our assembled BN/G//AC ASc, we further reflected its power density and energy density. **Figure 7C** showed the power-energy density relation curve of BN/G(1:2). The calculated values of the energy density and power density of BN/G(1:2) were obtained according to Equations (3) and (4). It can be seen from **Figure 7C** that the energy density of BN/G(1:2)//AC attenuates very little with the increase of power density. Even at the power density of 1998.5 W/kg, its energy density still retains at 2.05 Wh/kg, showing the bright prospects for the application of h-BN/grahene-based supercapacitors.

CONCLUSIONS

In summary, we reported a well-constructed heterostructure materials, in which the h-BN nanosheets were assembled with graphene through electrostatic interaction based on solution method. This scalable stacked heterostructure are well-aligned in vertical, but the layers are randomly stacked in horizontal. The synthesis method adopted in this work has extensive use, low cost and facile process, which can be applied to other 2D materials. Meanwhile, we further developed BN/G heterogstructure electrode material, and explored the feasibility of BN/G heterostructure electrode material in the application of asymmertic supercapacitors. The incorporation of h-BN not only constructs the electrolyte channel for the graphene layer, but also improves the electrochemical performance. Moreover, the assembled BN/G//AC ASc exhibits maximum energy density of 2.05 Wh/kg at high power density of 1998.5 W/kg, and excellent long cycling stability with 96% of initial specific capacitance after 10,000 cycles at 10 A/g, indicating its promising application in energy storage component.

DATA AVAILABILITY

The raw data supporting the conclusions of this manuscript will be made available by the authors, without undue reservation, to any qualified researcher.

AUTHOR CONTRIBUTIONS

XZ, GW, FH, HL, and CG were responsible for all the experiments and the analysis of data. FH, SW, YH, GZ, and DC were responsible for the drafting. All authors contributed equally to the final writing of the paper.

FUNDING

This work was supported by the National Natural Science Foundation of China (No. 21802037) and the Natural Science Foundation of Hubei Province (No. 2018CFB669).

SUPPLEMENTARY MATERIAL

The Supplementary Material for this article can be found online at: https://www.frontiersin.org/articles/10.3389/fchem.2019.00544/full#supplementary-material

REFERENCES

Balandin, A. A., Ghosh, S., Bao, W., Calizo, I., Teweldebrhan, D., Miao, F., et al. (2008). Superior thermal conductivity of single-layer graphene. *Nano Lett.* 8, 902–907. doi: 10.1021/nl0731872

Balogun, M. S., Zeng, Y., Qiu, W., Luo, Y., Onasanya, A., Olaniyi, T. K., et al. (2016). Three-dimensional nickel nitride (Ni 3 N) nanosheets: free standing and flexible electrodes for lithium ion batteries and supercapacitors. *J. Mater. Chem. A* 4, 9844–9849. doi: 10.1039/C6TA02492K

Boland, C. S., Barwich, S., Khan, U., and Coleman, J. N. (2016). High stiffness nano-composite fibres from polyvinylalcohol filled with graphene and boron nitride. *Carbon* 99, 280–288. doi: 10.1016/j.carbon.2015.12.023

Chen, J., Shi, W., Gao, Z., Wang, T., Wang, S., Dong, L., et al. (2018). Facile preparation of pristine graphene using urea/glycerol as efficient stripping agents. *Nano Res.* 11, 820–830. doi: 10.1007/s12274-017-1691-3

Ge, X., Gu, C., Yin, Z., Wang, X., Tu, J., and Li, J. (2016). Periodic stacking of 2D charged sheets: self-assembled superlattice of Ni–Al layered double

hydroxide (LDH) and reduced graphene oxide. *Nano Energy* 20, 185–193. doi: 10.1016/j.nanoen.2015.12.020

Hu, S., Lozada-Hidalgo, M., Wang, F., Mishchenko, A., Schedin, F., Nair, R., et al. (2014). Proton transport through one-atom-thick crystals. *Nature* 516, 227–230. doi: 10.1038/nature14015

Jiao, L., Zhang, L., Wang, X., Diankov, G., and Dai, H. (2009). Narrow graphene nanoribbons from carbon nanotubes. *Nature* 458, 877–880. doi: 10.1038/nature07919

Jingwei, B., Xing, Z., Shan, J., Yu, H., and Xiangfeng, D. (2010). Graphene nanomesh. *Nat. Nanotechnol.* 5, 190–194. doi: 10.1038/nnano.2010.8

Kim, K. K., Hsu, A., Jia, X., Kim, S. M., Shi, Y., Hofmann, M., et al. (2011). Synthesis of monolayer hexagonal boron nitride on Cu foil using chemical vapor deposition. *Nano Lett.* 12, 161–166. doi: 10.1021/nl203249a

Kong, X., Liu, Q., Zhang, C., Peng, Z., and Chen, Q. (2017). Elemental two-dimensional nanosheets beyond graphene. *Chem. Soc. Rev.* 46, 2127–2157. doi: 10.1039/C6CS00937A

Kumar, R., Gopalakrishnan, K., Ahmad, I., and Rao, C. (2015). BN-graphene composites generated by covalent cross-linking with organic linkers. *Adv. Funct. Mater.* 25, 5910–5917. doi: 10.1002/adfm.201502166

Lee, M., Wallbank, J. R., Gallagher, P., Watanabe, K., Taniguchi, T., Fal'Ko, V. I., et al. (2016). Ballistic miniband conduction in a graphene superlattice. *Science* 353, 1526–1529. doi: 10.1126/science.aaf1095

Li, B., Zhou, L., Wu, D., Peng, H., Yan, K., Zhou, Y., et al. (2011). Photochemical chlorination of graphene. *Acs Nano* 5, 5957–5961. doi: 10.1021/nn201731t

Li, W., Zhang, B., Lin, R., Ho-Kimura, S., He, G., Zhou, X., et al. (2018). A dendritic nickel cobalt sulfide nanostructure for alkaline battery electrodes. *Adv. Funct. Mater.* 28:1705937. doi: 10.1002/adfm.201705937

Li, X., Wu, X., Zeng, X. C., and Yang, J. (2012). Band-gap engineering via tailored line defects in boron-nitride nanoribbons, sheets, and nanotubes. *Acs Nano* 6, 4104–4112. doi: 10.1021/nn300495t

Liao, L., Peng, H., and Liu, Z. (2014). Chemistry makes graphene beyond graphene. *J. Am. Chem. Soc.* 136, 12194–12200. doi: 10.1021/ja5048297

Loan, P. T. K., Zhang, W., Lin, C. T., Wei, K. H., Li, L. J., Chen, C. H., et al. (2014). Graphene/MoS_2 heterostructures for ultrasensitive detection of DNA hybridisation. *Adv. Mater.* 26, 4838–4844. doi: 10.1002/adma.201401084

Mahmood, N., De Castro, I. A., Pramoda, K., Khoshmanesh, K., Bhargava, S. K., and Kalantar-Zadeh, K. (2018). Atomically thin two-dimensional metal oxide nanosheets and their heterostructures for energy storage. *Energy Storage Mater.* 16, 455–480. doi: 10.1016/j.ensm.2018.10.013

Morozov, S. V., Novoselov, K. S., Katsnelson, M. I., Schedin, F., Elias, D. C., Jaszczak, J. A., et al. (2008). Giant intrinsic carrier mobilities in graphene and its bilayer. *Phys. Rev. Lett.* 100:016602. doi: 10.1103/PhysRevLett.100.016602

Paton, K. R., Varrla, E., Backes, C., Smith, R. J., Khan, U., O'Neill, A., et al. (2014). Scalable production of large quantities of defect-free few-layer graphene by shear exfoliation in liquids. *Nat. Mater.* 13, 624–630. doi: 10.1038/nmat3944

Pattammattel, A., and Kumar, C. V. (2015). Kitchen chemistry 101: multigram production of high quality biographene in a blender with edible proteins. *Adv. Funct. Mater.* 25, 7088–7098. doi: 10.1002/adfm.201503247

Pomerantseva, E., and Gogotsi, Y. (2017). Two-dimensional heterostructures for energy storage. *Nat. Energy* 2:17089. doi: 10.1038/nenergy.2017.89

Sun, J., Lee, H. W., Pasta, M., Yuan, H., Zheng, G., Sun, Y., et al. (2015). A phosphorene-graphene hybrid material as a high-capacity anode for sodium-ion batteries. *Nat. Nanotechnol.* 10, 980–985. doi: 10.1038/nnano.2015.194

Tran, T. T., Bray, K., Ford, M. J., Toth, M., and Aharonovich, I. (2016). Quantum emission from hexagonal boron nitride monolayers. *Nat. Nanotechnol.* 11, 37–41. doi: 10.1038/nnano.2015.242

Varrla, E., Backes, C., Paton, K. R., Harvey, A., Gholamvand, Z., McCauley, J., et al. (2015). Large-scale production of size-controlled MoS_2 nanosheets by shear exfoliation. *Chem. Mater.* 27, 1129–1139. doi: 10.1021/cm5044864

Wan, C., Jiao, Y., Liang, D., Wu, Y., and Li, J. (2018). A geologic architecture system-inspired micro-/nano-heterostructure design for high-performance energy storage. *Adv. Energy Mater.* 8:1802388. doi: 10.1002/aenm.201802388

Wang, E., Lu, X., Ding, S., Yao, W., Yan, M., Wan, G., et al. (2016). Gaps induced by inversion symmetry breaking and second-generation Dirac cones in graphene/hexagonal boron nitride. *Nat. Phys.* 12, 1111–1115. doi: 10.1038/nphys3856

Wang, J., Zhao, R., Liu, Z., and Liu, Z. (2013). Widely tunable carrier mobility of boron nitride-embedded graphene. *Small* 9, 1373–1378. doi: 10.1002/smll.201202978

Wang, X., and Dai, H. (2010). Etching and narrowing of graphene from the edges. *Nat. Chem.* 2, 661–665. doi: 10.1038/nchem.719

Wang, X., Lu, X., Liu, B., Chen, D., Tong, Y., and Shen, G. (2014). Flexible energy-storage devices: design consideration and recent progress. *Adv. Mater.* 26, 4763–4782. doi: 10.1002/adma.201400910

Wu, Z., Zheng, Y., Zheng, S., Wang, S., Sun, C., Parvez, K., et al. (2017). Stacked-layer heterostructure films of 2D thiophene nanosheets and graphene for high-rate all-solid-state pseudocapacitors with enhanced volumetric capacitance. *Adv. Mater.* 29:1602960. doi: 10.1002/adma.201602960

Xu, K., Li, S., Yang, J., Xu, H., and Hu, J. (2016). Hierarchical MnO_2 nanosheets on electrospun $NiCo_2O_4$ nanotubes as electrode materials for high rate capability and excellent cycling stability supercapacitors. *J. Alloys Compounds* 678, 120–125. doi: 10.1016/j.jallcom.2016.03.255

Xu, K., Shen, Y., Zhang, K., Yang, F., Li, S., and Hu, J. (2019). Hierarchical assembly of manganese dioxide nanosheets on one-dimensional titanium nitride nanofibers for high-performance supercapacitors. *J. Colloid Interface Sci.* 552, 712–718. doi: 10.1016/j.jcis.2019.05.093

Yang, W., Chen, G., Shi, Z., Liu, C., Zhang, L., Xie, G., et al. (2013a). Epitaxial growth of single-domain graphene on hexagonal boron nitride. *Nat. Mater.* 12, 792–797. doi: 10.1038/nmat3695

Yang, X., Cheng, C., Wang, Y., Qiu, L., and Li, D. (2013b). Liquid-mediated dense integration of graphene materials for compact capacitive energy storage. *Science* 341, 534–537. doi: 10.1126/science.1239089

Zheng, X., Wang, S., Xiong, C., and Hu, G. (2018). *In situ* growth of 1T-MoS_2 on liquid-exfoliated graphene: a unique graphene-like heterostructure for superior lithium storage. *Carbon* 133, 162–169. doi: 10.1016/j.carbon.2018.03.028

Conflict of Interest Statement: The authors declare that the research was conducted in the absence of any commercial or financial relationships that could be construed as a potential conflict of interest.

frontiers in Chemistry

ORIGINAL RESEARCH
published: 04 September 2019
doi: 10.3389/fchem.2019.00595

Facile Synthesis of Novel $V_{0.13}Mo_{0.87}O_{2.935}$ Nanowires With High-Rate Supercapacitive Performance

Haishun Jiang[1], Wenjing Sun[1], Wenyao Li[1], Zhe Wang[1], Xiying Zhou[1]*, Zexing Wu[2] and Jinbo Bai[3]**

[1] School of Material Engineering, Shanghai University of Engineering Science, Shanghai, China, [2] College of Chemistry and Molecular Engineering, Qingdao University of Science and Technology, Qingdao, China, [3] Laboratoire Mécanique des Sols, Structures et Matériaux, CNRS UMR 8579, Ecole Centrale Supelec, Université Paris Saclay, Châtenay-Malabry, France

Binary metal oxides composed of molybdenum–vanadium oxides are promising candidates for supercapacitors. Here, we report the synthesis of one-dimensional $V_{0.13}Mo_{0.87}O_{2.935}$ nanowires through a facile one-step hydrothermal method. This nanowire presented a high specific capacitance of 394.6 F g^{-1} (1 mV s^{-1}) as an electrode applied to the supercapacitor. Importantly, this electrode showed a perfect rate capability of 91.5% (2 to 10 A g^{-1}) and a continuous verified outstanding cyclic voltammetry of 97.6% after 10,000 cycles. These superior electrochemical properties make the synthesized $V_{0.13}Mo_{0.87}O_{2.935}$ nanowires a prospective candidate for high-performance supercapacitors.

Keywords: molybdenum–vanadium oxides, nanowires, hydrothermal, high rate, supercapacitors

OPEN ACCESS

Edited by:
Elizabeth J. Podlaha, Clarkson University, United States

Reviewed by:
Dipankar Roy, Clarkson University, United States
John Zhanhu Guo, University of Tennessee, Knoxville, United States

***Correspondence:**
Wenyao Li
liwenyao314@gmail.com
Xiying Zhou
zhouxiying@sues.edu.cn
Jinbo Bai
jinbo.bai@centralesupelec.fr

Specialty section:
This article was submitted to Electrochemistry, a section of the journal Frontiers in Chemistry

Received: *30 May 2019*
Accepted: *12 August 2019*
Published: *04 September 2019*

Citation:
Jiang H, Sun W, Li W, Wang Z, Zhou X, Wu Z and Bai J (2019) Facile Synthesis of Novel $V_{0.13}Mo_{0.87}O_{2.935}$ Nanowires With High-Rate Supercapacitive Performance. Front. Chem. 7:595. doi: 10.3389/fchem.2019.00595

INTRODUCTION

Due to overconsumption of non-renewable resources and the growing threat of global warming, reliable and clean energy supplies, such as the secondary battery and supercapacitor (SC) science and technology, are in urgent need of a breakthrough (Liu et al., 2016; Salanne et al., 2016; Liu M. et al., 2018; Liang et al., 2019). SCs are becoming more appealing than ever because of their rapid recharge capabilities, high power density, and durable life cycles (Salanne et al., 2016; Du et al., 2018; Kirubasankar et al., 2018; Ho and Lin, 2019; Le et al., 2019; Ma et al., 2019; Yang L. et al., 2019). It is well-established that three main electrode materials include conducting polymer, transition metal oxide, and carbon materials (Jabeen et al., 2016a,b; Chen et al., 2017; Li et al., 2018; Idrees et al., 2019). In this regard, transition metal oxides can increase the efficiency and improve the specific capacitances compared to conducting polymers and carbon materials (Yang et al., 2015; Fu et al., 2016; Qin et al., 2016a,b; Meng et al., 2017; An and Cheng, 2018). Unfortunately, it has either insufficient electrochemical stability or low conductivity, which still greatly hampers their widespread applications in SCs (Jiang et al., 2012). Therefore, an innovative material that can be applied as a significant electrode material in the field of SCs is still needed.

In the last few years, binary metal oxides with stoichiometric or even nonstoichiometric composition such as $NiCo_2O_4$ (Ma et al., 2016), $NiFe_2O_4$ (Yu et al., 2014), and $MnCo_2O_{4.5}$ (Hu et al., 2019) have achieved efficient energy storage. It stems from its defect–effect mechanisms (Ellis et al., 2007; Wang et al., 2017) or possible jump processes (Hu et al., 2012; Li et al., 2018; Yang Y. et al., 2019) that provided the needed efficient electron conductivity. Also, the electrochemical

behavior of these binary metal oxides is different to simple metal oxides attributed to their composition, including the species and ratios of elements. In particular, binary metal oxides based on molybdenum oxides or vanadium oxides are also regarded as a potential candidate for SCs. Many binary metals–molybdenum oxides, such as $NiMoO_4$ (Cheng et al., 2015), a-$MnMoO_4$ (Purushothaman et al., 2012), $CoMoO_4 \bullet 0.9H_2O$ (Liu et al., 2014), and $NiMoO_4$ (Mehrez et al., 2019), and binary metal–vanadium oxides, such as β-$Na_{0.33}V_2O_5$ (Hong Trang et al., 2014), Li_3VO_4 (Iwama et al., 2016), and $BiVO_4$ (Patil et al., 2016; Guo et al., 2019), have been prepared for high-performance SCs. Despite the tremendous efforts that have been made on the electrode materials for these binary metal oxides, researchers continue to explore the performance of the electrode material for sustainable, low-cost, and clean energy storage and conversion technologies. Especially, binary metal oxides composed of molybdenum–vanadium oxide are also expected to be of favorable potential as SCs. However, such reports are rare.

Herein, we report a simple preparation of one-dimensional $V_{0.13}Mo_{0.87}O_{2.935}$ nanowires through a one-step hydrothermal method. This nanowire electrode exhibits a high specific capacitance of 394.6 F g^{-1} (1 mV s^{-1}) as an electrode material in SC. Additionally, this electrode showed a rate capability of 91.5% (2 to 10 A g^{-1}) and an outstanding cycle stability (97.6% after 10,000 cycles). Therefore, one-dimensional $V_{0.13}Mo_{0.87}O_{2.935}$ nanowires have been prepared and applied as a high-performance SC electrode material.

EXPERIMENTAL

Preparation

Firstly, the molybdenum powder (Mo, 0.192 g, 2 mmol) was mixed with 37 ml of deionized H_2O and 3 ml of hydrogen peroxide at room temperature and then continuous stirred till the solution became light yellow. After that, 0.088 g of ammonium vanadate (NH_4VO_3, 0.75 mmol) was added to the solution until the solid powder was completely dissolved. Then, the resulting solution was decanted into a Teflon reaction kettle and heated in oven at 200°C for 48 h. After cooling to room temperature, the obtained crude products were treated with 2 M nitric acid. Finally, the nanowires were collected through washing with distilled H_2O till neutral and then dried under air at 60°C for 18 h.

Material Characterizations

The X-ray diffractometer (XRD; with Cu-Kα radiation) presented the structure and phase of one-dimensional $V_{0.13}Mo_{0.87}O_{2.935}$ nanowires. The nanowires' morphological feature was studied by a scanning electron microscope (SEM; S-4800) and a transmission electron microscope (TEM; JEM-2100F). Compositions of the samples were tested by X-ray photoelectron spectroscopy (Thermo ESCALAB 250XI). An automated nitrogen adsorption analyzer (ASAP 2020, Micromeritics, America) presented N_2 adsorption–desorption isotherm under the 77 K conditions.

Electrochemical Characterizations

Electrochemistry performances were tested in three electrode systems with 1 M Na_2SO_4 electrolyte using Autolab potentiostat (PGSTAT302N). A saturated calomel electrode (SCE) was used as the reference electrode and a platinum (Pt) foil was used as the counter electrode. The working electrode was a mixture of one-dimensional $V_{0.13}Mo_{0.87}O_{2.935}$ nanowires, acetylene black, and polyvinylidene fluoride (PVDF) according to a certain mass ratio (80:15:5) in a few *N*-methyl pyrrolidinone (NMP). After the mixture was stirred for 24 h, the formed slurry was dripped on graphite paper and then vacuum dried at 60°C for 15 h. Cyclic voltammetry (CV) measurement was carried out in a voltage range of 0–1.0 V at different sweeping rates (1, 5, 10, 25, 50, 75, and 100 mV s^{-1}), and galvanostatic charge–discharge (GCD) was tested at different current densities (2, 4, 6, 8, and 10 A g^{-1}). EIS data are obtained at a frequency from 10^{-2} to 10^5 Hz with an AC amplitude of 5 mV.

RESULTS AND DISCUSSIONS

In the present work, the phase for one-dimensional $V_{0.13}Mo_{0.87}O_{2.935}$ nanowire was first characterized. The XRD spectrum for the prepared product is indicated in **Figure 1** in that all diffraction peaks matched a hexagonal phase of one-dimensional $V_{0.13}Mo_{0.87}O_{2.935}$ nanowires (JCPDS card No. 48-0766). No characteristic peaks from impurity have been detected, suggesting that the pure one-dimensional $V_{0.13}Mo_{0.87}O_{2.935}$ nanowires were prepared. Furthermore, the diffraction peaks were sharp and intense, showing their high degree of crystallinity.

The SEM image in **Figure 2a** depicts the typical morphology of the one-dimensional $V_{0.13}Mo_{0.87}O_{2.935}$ nanowires, which consists of a number of uniform nanowires with an edge length of more than 10 μm. For more detail, the samples were examined by TEM as indicated in **Figure 2b** in that the diameters of the

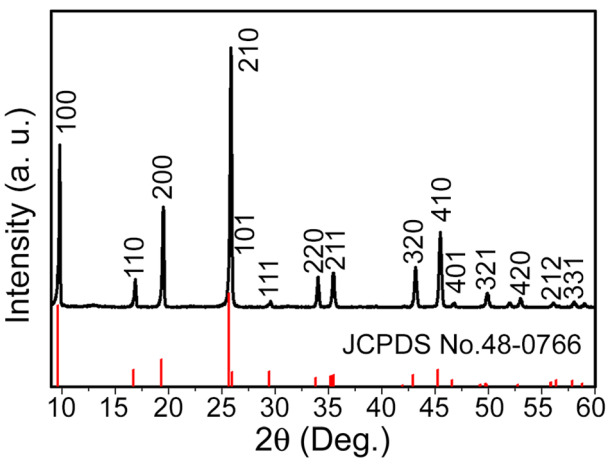

FIGURE 1 | XRD spectrum of the one-dimensional $V_{0.13}Mo_{0.87}O_{2.935}$ nanowires.

nanowires are 20–30 nm with uniform nanostructures. The HR-TEM image is indicated in **Figure 2c**; those one-dimensional $V_{0.13}Mo_{0.87}O_{2.935}$ nanowires have a similar crystal structure and no amorphous phase on the surface. It could be deduced from the lattice fringes that the lattice spacing is 0.26 nm, agreeing to the (220) plane of one-dimensional $V_{0.13}Mo_{0.87}O_{2.935}$ nanowires. In further studying the details, the brighter spots in the FFT pattern (illustration in **Figure 2c**) pointed out an excellent crystal. Besides, **Figure 2d** confirmed that the lattice spacing of 0.26 nm in **Figure 2c** belongs to the (220) plane. These results closely matched the data obtained from the XRD analysis, further confirming the crystal structure of $V_{0.13}Mo_{0.87}O_{2.935}$ nanowires.

The X-ray photoelectron spectroscopy (XPS) shows that the one-dimensional $V_{0.13}Mo_{0.87}O_{2.935}$ nanowires are composed of three elements: V, Mo, and O (**Figure S1** of the Supporting Information). The XPS peak of V 2p in **Figure 3A** was determined to be a peak of V $2p_{3/2}$ of 517.1 eV, and the V $2p_{1/2}$ peak of V^{5+} was not included because the low mole percentage of vanadium in the compound was the smallest (Geert et al., 2004; Liu X. et al., 2018). **Figure 3B** shows the Mo 3d spectrum composed of two peaks, the Mo $3d_{3/2}$ from the peak at 236.0 eV indicates Mo^{6+}, and another peak at 232.9 eV could be due to the superposition of Mo $3d_{5/2}$ and Mo $3d_{3/2}$, which indicates Mo^{6+} and Mo^{5+} (Bica de Moraes et al., 2004). Meanwhile, in **Figure 3C**, the XPS peak of the O 1s was observed at 530.8 eV. In addition, the existence of Mo^{5+} was ascribed to the oxygen anion vacancy in the framework of the compound structure, so that molybdenum is only coordinated by five oxygen species.

The one-dimensional $V_{0.13}Mo_{0.87}O_{2.935}$ nanowires were further investigated by the N_2 adsorption–desorption isotherms

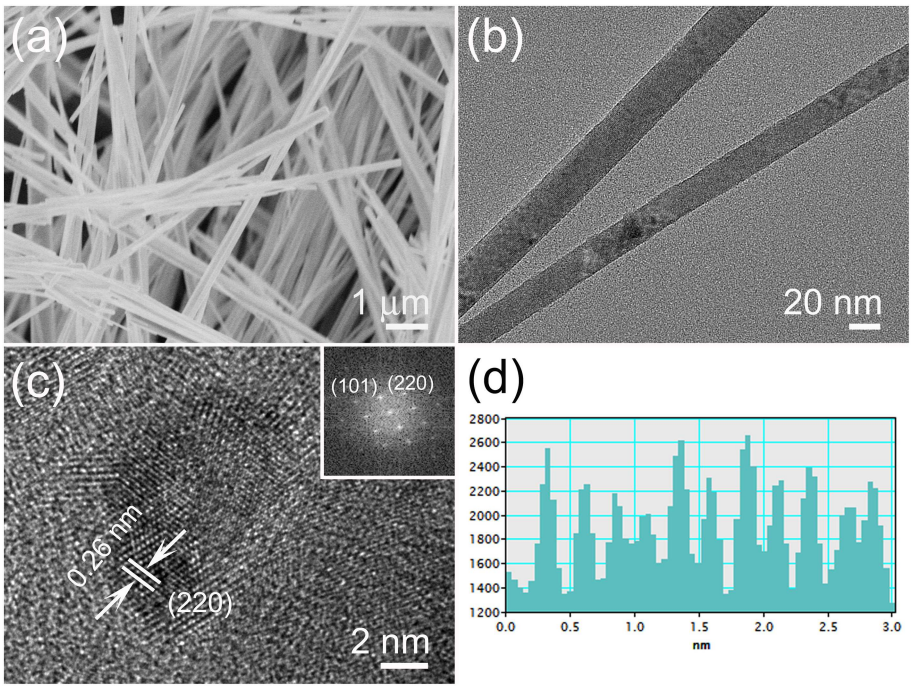

FIGURE 2 | (a) SEM, **(b)** TEM, and **(c)** HR-TEM images of the one-dimensional $V_{0.13}Mo_{0.87}O_{2.935}$ nanowires; the illustration shows the FFT pattern and **(d)** the corresponding lattice spacing obtained from **(c)**.

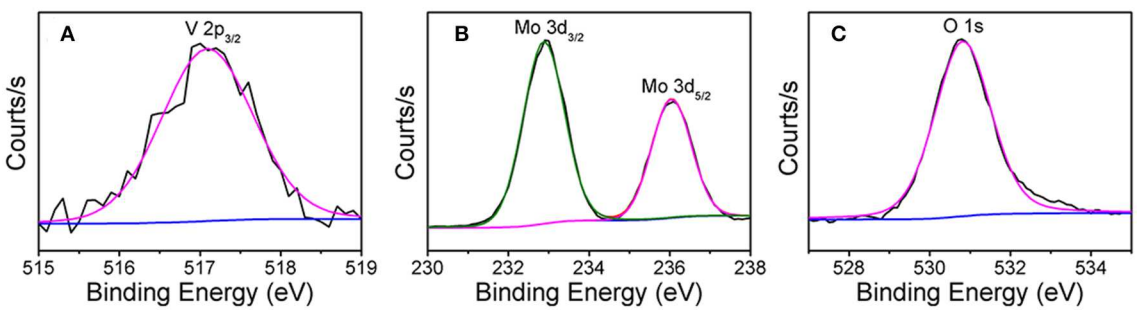

FIGURE 3 | XPS spectra of **(A)** V 2p, **(B)** Mo 3d, and **(C)** O 1s electrons in $V_{0.13}Mo_{0.87}O_{2.935}$ nanowires.

as indicated in **Figure 4**. According to IUPAC, the N_2 adsorption–desorption isotherms of the $V_{0.13}Mo_{0.87}O_{2.935}$ nanowires are a typical type IV adsorption isotherm with the H3 hysteresis loop, exhibiting a mesoporous structure with slit-shaped pores. The BET-specific surface area and pore diameters (illustration in **Figure 4**) of the $V_{0.13}Mo_{0.87}O_{2.935}$ nanowires are about 54.2 m^2 g^{-1} and 80 nm, respectively, which may be attributed to the assembly of the nanowires in space. This porous structure contributes to the diffusion of electrolyte ions and transport during the charge and discharge process of the SC electrodes (Hou et al., 2018, 2019).

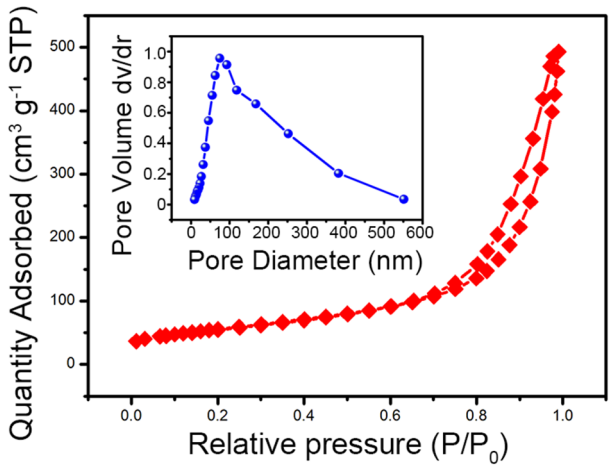

FIGURE 4 | The N_2 adsorption–desorption isotherm and pore size distributions (illustration) of the one-dimensional $V_{0.13}Mo_{0.87}O_{2.935}$ nanowires.

The as-prepared one-dimensional $V_{0.13}Mo_{0.87}O_{2.935}$ nanowires were applied to SC electrode materials. **Figure 5A** depicts the CV curves tested in the voltage from 0 to 1.0 V. Approximate rectangle-shaped and symmetrical CV curves were viewed without redox peaks, showing an EDLC-dominated capacitance behavior of the one-dimensional $V_{0.13}Mo_{0.87}O_{2.935}$ nanowires (Hung et al., 2011; Lokhande et al., 2011; Pujari et al., 2016). Besides, the specific capacitance (**Table S1** of the Supporting Information) of one-dimensional $V_{0.13}Mo_{0.87}O_{2.935}$ nanowires was very high and was 394.6 F g^{-1} at 1 mV s^{-1}. Notably, it can be seen that the CV curve mostly remains in an approximately rectangle-like shape with a sweeping rate between 1 and 100 mV s^{-1}, which confirmed good electrochemical reversibility and outstanding high-energy storage performance; the CV plot tilt increases with increasing scan rates owing to the fact that the electrons do not migrate from the inside of the material to the surface of the electrode in time. **Figure 5B** shows the GCD curves of the one-dimensional $V_{0.13}Mo_{0.87}O_{2.935}$ nanowire electrode at different current densities. It displayed

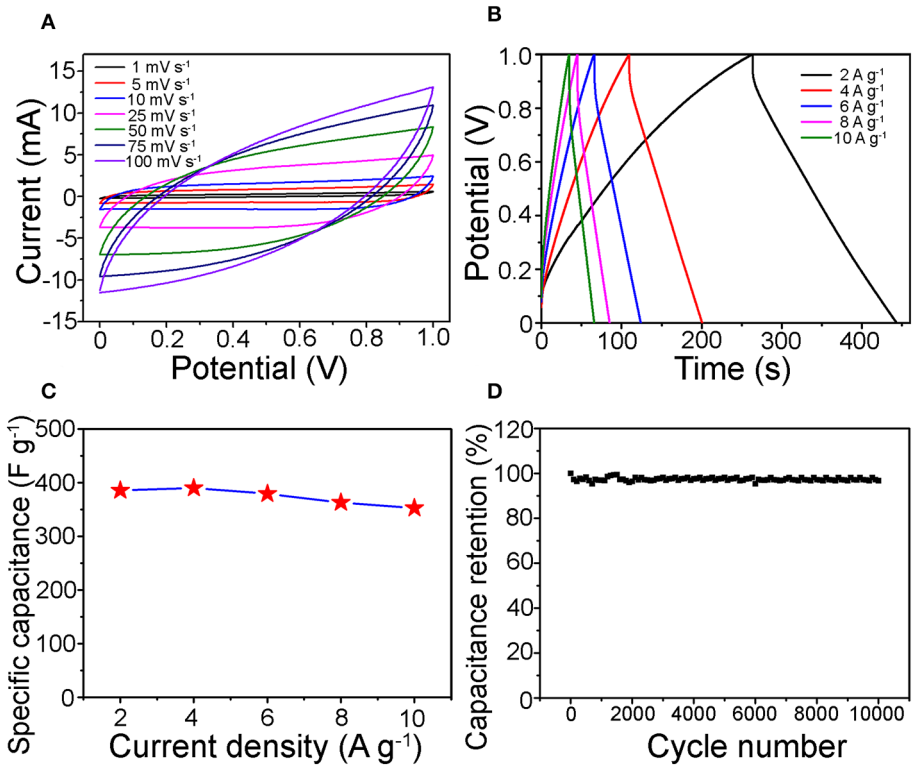

FIGURE 5 | (A) CV and **(B)** GCD curves of the one-dimensional $V_{0.13}Mo_{0.87}O_{2.935}$ nanowire electrodes on different sweeping rates and current densities, respectively. **(C)** Rate performance and **(D)** cycle stability of the $V_{0.13}Mo_{0.87}O_{2.935}$ nanowire electrodes, in 1 M Na_2SO_4 electrolyte.

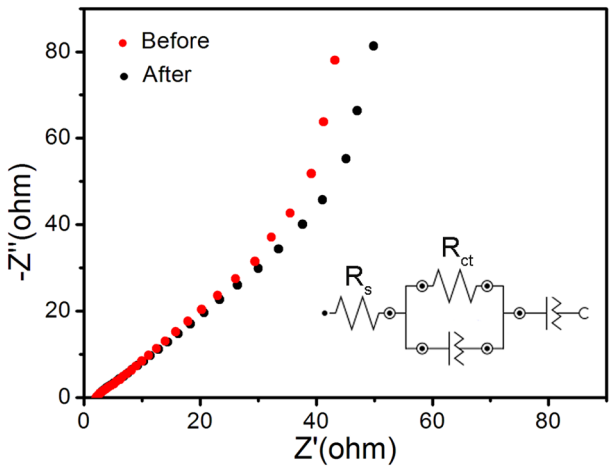

FIGURE 6 | Nyquist plot before and after 10,000 cycles of the one-dimensional $V_{0.13}Mo_{0.87}O_{2.935}$ nanowire electrodes, with the inset showing the corresponding equivalent circuit.

proximate central symmetry voltage profiles, which were consistent compared to the CV results, pointing to the one-dimensional $V_{0.13}Mo_{0.87}O_{2.935}$ nanowires having an excellent reversibility across the whole potential region. Furthermore, one-dimensional $V_{0.13}Mo_{0.87}O_{2.935}$ nanowire electrodes presented high specific capacitances from 385.2 to 352.5 F g^{-1} while discharge current density was enhanced to 2, 4, 6, 8, and 10 A g^{-1} (**Table S2** of the Supporting Information). Compared with other binary metal oxide electrodes, one-dimensional $V_{0.13}Mo_{0.87}O_{2.935}$ nanowire electrodes also indicated a strengthened specific capacitance as reported in the literature, such as $CoMoO_4$ (384 F g^{-1}) (Li et al., 2018), $BiVO_4$ (116.3 F g^{-1}) (Patil et al., 2016), and $MnMoO_4$ (168.32 F g^{-1}) (Veerasubramani et al., 2014).

The specific capacitances of the $V_{0.13}Mo_{0.87}O_{2.935}$ electrodes with different current densities are indicated in **Figure 5C**. It maintained a remarkable rate performance of 91.5% from 2 to 10 A g^{-1}. This result may be attributed to the active materials to form porous channels through intertwined networks, enabling efficient electrolyte transport and accessibility of active sites (Jiang et al., 2011). Therefore, it is possible to maintain a high specific capacitance even at higher current densities. **Figure 5D** indicates the long-term cycle stability of the one-dimensional $V_{0.13}Mo_{0.87}O_{2.935}$ nanowire electrode, which was tested through CV tests repeating 10,000 cycles at 50 mV s^{-1}. It can be observed that its specific capacitance retention showed outstanding stability, with the increase in some cycles fluctuating only a little. After 10,000 cycles, the retention rate value was found to be 97.6% of the initial value.

The $V_{0.13}Mo_{0.87}O_{2.935}$ electrodes were subjected to electrochemical impedance spectroscopy (EIS) to explore relevant charge transfer resistance. **Figure 6** shows the Nyquist plot before and after 10,000 cycles of the one-dimensional $V_{0.13}Mo_{0.87}O_{2.935}$ nanowire electrodes. The inset shows the corresponding equivalent circuit by its corresponding fitting curve (**Figure S2** in Supporting Information), which was fitted by an equivalent circuit consisting of a bulk solution resistance R_s, a charge-transfer R_{ct}, and constant phase element (CPE). The R_s values of the one-dimensional $V_{0.13}Mo_{0.87}O_{2.935}$ nanowire electrode before and after 10,000 cycles are 2.02 and 2.10 Ω, respectively. Also, the value of R_{ct} was connected with charge transfer after 10,000 cycles and is only slightly higher than before (68.6 vs. 50.1 Ω), manifesting superior conductivity and stability of the one-dimensional $V_{0.13}Mo_{0.87}O_{2.935}$ nanowire microstructure owing to good ion conductivity of the interface between electrolyte and electrodes.

CONCLUSIONS

In summary, one-dimensional $V_{0.13}Mo_{0.87}O_{2.935}$ nanowires were synthesized under a facile one-step hydrothermal condition. For application in a SC electrode, it was found to present a high specific capacitance of 394.6 F g^{-1} (1 mV s^{-1}). Besides, this electrode showed a perfect rate capability of 91.5% at the current density that was enhanced five times and outstanding long-term cyclic stability (97.6% after 10,000 cycles). This study offers a common preparation method of binary molybdenum–vanadium oxide used in SCs with a superior electrochemical property.

DATA AVAILABILITY

All datasets generated for this study are included in the manuscript/**Supplementary Files**.

AUTHOR CONTRIBUTIONS

WL conceived and designed the experiments. HJ, WS, and ZWa performed the experiments and analyzed the data. HJ and WS wrote and revised the manuscript. WL, ZWu, XZ, and JB discussed and supervised the whole project. All the authors revised and checked draft.

FUNDING

The research was supported by the National Natural Science Foundation of China (51602193), Shanghai Chen Guang project (16CG63), the Fundamental Research Funds for the Central Universities (WD1817002) and the Talent Program of Shanghai University of Engineering Science, the Natural Science Foundation of Shandong Province of China (ZR2019BB002), and Shanghai University of Engineering Science Innovation Fund (18KY0503).

SUPPLEMENTARY MATERIAL

The Supplementary Material for this article can be found online at: https://www.frontiersin.org/articles/10.3389/fchem.2019.00595/full#supplementary-material

REFERENCES

An, T., and Cheng, W. (2018). Recent progress in stretchable supercapacitors. *J. Mater. Chem. A* 6, 15478–15494. doi: 10.1039/C8TA03988G

Bica de Moraes, M. A., Trasferetti, B. C., Rouxinol, F. P., Landers, R., Durrant, S. F., Scarmínio, J., et al. (2004). Molybdenum oxide thin films obtained by the hot-filament metal oxide deposition technique. *Chem. Mater.* 16, 513–520. doi: 10.1021/cm034551a

Chen, X., Paul, R., and Dai, L. (2017). Carbon-based supercapacitors for efficient energy storage. *Natl. Sci. Rev.* 4, 453–489. doi: 10.1093/nsr/nwx009

Cheng, D., Yang, Y., Xie, J., Fang, C., Zhang, G., and Xiong, J. (2015). Hierarchical $NiCo_2O_4$ @$NiWO_4$ core-shell hybrid nanowire/nanosheet arrays for high-performance pseudocapacitors. *J. Mater. Chem. A* 3, 14348–14357. doi: 10.1039/C5TA03455H

Du, W., Wang, X., Zhan, J., Sun, X., Kang, L., Jiang, F., et al. (2018). Biological cell template synthesis of nitrogen-doped porous hollow carbon spheres/MnO_2 composites for high-performance asymmetric supercapacitors. *Electrochim. Acta* 296, 907–915. doi: 10.1016/j.electacta.2018.11.074

Ellis, B., Subramanya Herle, P., Rho, Y.-H., Nazar, L. F., Dunlap, R., Perry, L. K., et al. (2007). Nanostructured materials for lithium-ion batteries: surface conductivity vs. bulk ion/electron transport. *Faraday Discuss.* 134, 119–141. doi: 10.1039/B602698B

Fu, W., Wang, Y., Han, W., Zhang, Z., Zha, H., and Xie, E. (2016). Construction of hierarchical $ZnCo_2O_4$@Ni_xCo_{2x} $(OH)_{6x}$ core/shell nanowire arrays for high-performance supercapacitors. *J. Mater. Chem. A* 4, 173–182. doi: 10.1039/C5TA07965A

Geert, S., Depla, D., Poelman, H., Marin, G. B., and De Gryse, R. (2004). Determination of the V2p XPS binding energies for different vanadium oxidation states (V^{5+} to V^{0+}). *J. Electron Spectrosc. Relat. Phenom.* 135, 167–175. doi: 10.1016/j.elspec.2004.03.004

Guo, Z., Li, R., Zhu, X., Fu, Q., Liang, G., Chen, Y., et al. (2019). Nanosheet-based $Nb_{12}O_{29}$ hierarchical microspheres for enhanced lithium storage. *Chem. Commun.* 55, 2493–2496. doi: 10.1039/C8CC09924C

Ho, K.-C., and Lin, L.-Y. (2019). A review of electrode materials based on core–shell nanostructures for electrochemical supercapacitors. *J. Mater. Chem. A* 7, 3516–3530. doi: 10.1039/C8TA11599K

Hong Trang, N. T., Lingappan, N., Shakir, I., and Kang, D. J. (2014). Growth of single-crystalline β-$Na_{0.33}V_2O_5$ nanowires on conducting substrate: a binder-free electrode for energy storage devices. *J. Power Sources* 251, 237–242. doi: 10.1016/j.jpowsour.2013.11.041

Hou, C., Tai, Z., Zhao, L., Zhai, Y., Hou, Y., Fan, Y., et al. (2018). High performance MnO@C microcages with a hierarchical structure and tunable carbon shell for efficient and durable lithium storage. *J. Mat. Chem. A* 6, 9723–9736. doi: 10.1039/C8TA02863J

Hou, C., Wang, J., Du, W., Wang, J., Du, Y., Liu, C., et al. (2019). One-pot synthesized molybdenum dioxide–molybdenum carbide heterostructures coupled with 3D holey carbon nanosheets for highly efficient and ultrastable cycling lithium-ion storage. *J. Mat. Chem. A* 7, 13460–13472. doi: 10.1039/C9TA03551F

Hu, L., Wu, L., Liao, M., Hu, X., and Fang, X. (2012). Electrical transport properties of large, individual $NiCo_2O_4$ nanoplates. *Adv. Funct. Mater.* 22, 998–1004. doi: 10.1002/adfm.201102155

Hu, X., Nan, H., Liu, M., Liu, S., An, T., and Tian, H. (2019). Battery-like $MnCo_2O_4$ electrode materials combined with active carbon for hybrid supercapacitors. *Electrochim. Acta* 306, 599–609. doi: 10.1016/j.electacta.2019.03.166

Hung, C., Hung, J., Lin, P., and Tseng, T. (2011). Electrophoretic fabrication and characterizations of manganese oxide/carbon nanotube nanocomposite pseudocapacitors. *J. Electrochem. Soc.* 158, A942–A947. doi: 10.1149/1.3601862

Idrees, M., Batool, S., Kong, J., Zhuang, Q., Liu, H., Shao, Q., et al. (2019). Polyborosilazane derived ceramics—Nitrogen sulfur dual doped graphene nanocomposite anode for enhanced lithium ion batteries. *Electrochim. Acta* 296, 925–937. doi: 10.1016/j.electacta.2018.11.088

Iwama, E., Kawabata, N., Nishio, N., Kisu, K., Miyamoto, J., Naoi, W., et al. (2016). Enhanced electrochemical performance of ultracentrifugation-derived nc-Li_3VO_4/MWCNT composites for hybrid supercapacitors. *ACS Nano* 10, 5398–5404. doi: 10.1021/acsnano.6b01617

Jabeen, N., Xia, Q., Savilov, S. V., Aldoshin, S. M., Yu, Y., and Xia, H. (2016a). Enhanced pseudocapacitive performance of α-MnO_2 by cation preinsertion. *ACS Appl. Mater. Inter.* 8, 33732–33740. doi: 10.1021/acsami.6b12518

Jabeen, N., Xia, Q., Yang, M., and Xia, H. (2016b). Unique core–shell nanorod arrays with polyaniline deposited into mesoporous $NiCo_2O_4$ support for high-performance supercapacitor electrodes. *ACS Appl. Mater. Inter.* 8, 6093–6100. doi: 10.1021/acsami.6b00207

Jiang, H., Zhao, T., Ma, J., Yan, C., and Li, C. (2011). Ultrafine manganese dioxidenanowire network for high-performance supercapacitors. *Chem. Commun.* 47, 1264–1266. doi: 10.1039/C0CC04134C

Jiang, J., Li, Y., Liu, J., Huang, X., Yuan, C., and Lou, X. W. (2012). Recent advances in metal oxide-based electrode architecture design for electrochemical energy storage. *Adv. Mater.* 24, 5166–5180. doi: 10.1002/adma.201202146

Kirubasankar, B., Murugadoss, V., Lin, J., Ding, T., Dong, M., Liu, H., et al. (2018). *In situ*, grown nickel selenide on graphene nanohybrid electrodes for high energy density asymmetric supercapacitors. *Nanoscale* 10, 20414–20425. doi: 10.1039/C8NR06345A

Le, K., Wang, Z., Wang, F., Wang, Q., Shao, Q., Murugadoss, V., et al. (2019). Sandwich-like NiCo layered double hydroxides/reduced graphene oxide nanocomposite cathode for high energy density asymmetric supercapacitors. *Dalton Transact.* 175, 16–20. doi: 10.1039/C9DT00615J

Li, W., Wang, X., Hu, Y., Sun, L., Gao, C., Zhang, C., et al. (2018). Hydrothermal synthesized of $CoMoO_4$ microspheres as excellent electrode material for supercapacitor. *Nanoscale Res. Lett.* 13:120. doi: 10.1186/s11671-018-2540-3

Liang, C., Li, C., He, Y., Li, G., Yu, Y., Lou, Y., et al. (2019). Use of hyperaccumulator to enrich metal ions for supercapacitor. *Adv. Electron. Mater.* 5:1900094. doi: 10.1002/aelm.201900094

Liu, M., Meng, Q., Yang, Z., Zhao, X., and Liu, T. (2018). Ultra-long-term cycling stability of an integrated carbon–sulfur membrane with dual shuttle-inhibiting layers of graphene "nets" and a porous carbon skin. *Chem. Commun.* 54, 5090–5093. doi: 10.1039/C8CC01889H

Liu, M., Yang, Z., Sun, H., Lai, C., Zhao, X., Peng, H., et al. (2016). A hybrid carbon aerogel with both aligned and interconnected pores as interlayer for high-performance lithium–sulfur batteries. *Nano Res.* 9, 3735–3746. doi: 10.1007/s12274-016-1244-1

Liu, M.-C., Kong, L.-B., Kang, L., Li, X., Walsh, F. C., Xing, M., et al. (2014). Synthesis and characterization of $M_3V_2O_8$ (M = Ni or Co) based nanostructures: a new family of high performance pseudocapacitive materials. *J. Mater. Chem. A* 2, 4919–4926. doi: 10.1039/c4ta00582a

Liu, X., Wang, J., and Yang, G. (2018). *In situ* growth of the $Ni_3V_2O_8$@PANI composite electrode for flexible and transparent symmetric supercapacitors. *ACS Appl. Mater. Inter.* 10, 20688–20695. doi: 10.1021/acsami.8b04609

Lokhande, C., Dubal, D., and Joo, O. (2011). Metal oxide thin film based supercapacitors. *Curr. Appl. Phys.* 11, 255–270. doi: 10.1016/j.cap.2010.12.001

Ma, F.-X., Yu, L., Xu, C.-Y., and Lou, X. W. (David). (2016). Self-supported formation of hierarchical NiCo2O4 tetragonal microtubes with enhanced electrochemical properties. *Energy Environ. Sci.* 9, 862–866. doi: 10.1039/C5EE03772G

Ma, Y., Hou, C., Zhang, H., Zhang, Q., Liu, H., and Wu, S. (2019). Three-dimensional core–shell Fe_3O_4/polyaniline coaxial heterogeneous nanonets: preparation and high performance supercapacitor electrodes. *Electrochim. Acta* 315, 114–123. doi: 10.1016/j.electacta.2019.05.073

Mehrez, J. A.-A., Owusu, K. A., Chen, Q., Li, L., Hamwi, K., Luo, W., et al. (2019). Hierarchical $MnCo_2O_4$@$NiMoO_4$ as free-standing core–shell nanowire arrays with synergistic effect for enhanced supercapacitor performance. *Inorg. Chem. Front.* 6, 857–865. doi: 10.1039/C8QI01420E

Meng, Q., Cai, K., Chen, Y., and Chen, L. (2017). Research progress on conducting polymer based supercapacitor electrode materials. *Nano Energy* 36, 268–285. doi: 10.1016/j.nanoen.2017.04.040

Patil, S. S., Dubal, D. P., Deonikar, V. G., Tamboli, M. S., Ambekar, J. D., Gomez-Romero, P., et al. (2016). Fern-like rGO/$BiVO_4$ hybrid nanostructures for high-energy symmetric supercapacitor. *ACS Appl. Mater. Inter.* 8, 31602–31610. doi: 10.1021/acsami.6b08165

Pujari, R., Lokhande, V., Kumbhar, V., Chodankar, N., and Lokhande, C. (2016). Hexagonal microrods architectured MoO3 thin film for supercapacitor application. *J. Mater. Sci.* 27, 3312–3317. doi: 10.1007/s10854-015-4160-3

Purushothaman, K. K., Cuba, M., and Muralidharan, G. (2012). Supercapacitor behavior of α-$MnMoO_4$ nanorods on different electrolytes. *Mater. Res. Bull.* 47, 3348–3351. doi: 10.1016/j.materresbull.2012.07.027

Qin, T., Liu, B., Wen, Y., Wang, Z., Jiang, X., Wan, Z., et al. (2016a). Freestanding flexible graphene foams@polypyrrole@MnO_2 electrodes for high-performance supercapacitors. *J. Mater. Chem. A* 4, 9196–9203. doi: 10.1039/C6TA02835G

Qin, T., Wan, Z., Wang, Z., Wen, Y., Liu, M., Peng, S., et al. (2016b). 3D flexible O/N Co-doped graphene foams for supercapacitor electrodes with high volumetric and areal capacitances. *J. Power Sources* 336, 455–464. doi: 10.1016/j.jpowsour.2016.11.003

Salanne, M., Rotenberg, B., Naoi, K., Kaneko, K., Taberna, P.-L., Grey, C. P., et al. (2016). Efficient storage mechanisms for building better supercapacitors. *Nat. Energy* 1:16070. doi: 10.1038/nenergy.2016.70

Veerasubramani, G. K., Krishnamoorthy, K., Sivaprakasam, R., and Kim, S. J. (2014). Sonochemical synthesis, characterization, and electrochemical properties of $MnMoO_4$ nanorods for supercapacitor applications. *Mater. Chem. Phys.* 147, 836–842. doi: 10.1016/j.matchemphys.2014.06.028

Wang, G., Yang, Y., Han, D., and Li, Y. (2017). Oxygen defective metal oxides for energy conversion and storage. *Nano Today* 13, 23–39. doi: 10.1016/j.nantod.2017.02.009

Yang, J., Yu, C., Fan, X., Zhao, C., and Qiu, J. (2015). Ultrafast self-assembly of graphene oxide-induced monolithic NiCo-carbonate hydroxide nanowire architectures with a superior volumetric capacitance for supercapacitors. *Adv. Funct. Mater.* 25, 2109–2116. doi: 10.1002/adfm.201404019

Yang, L., Shi, M., Jaing, J., Liu, Y., Yang, C., Liu, H., et al. (2019). Heterogeneous interface induced formation of balsam pear-like PPy for high performance supercapacitors. *Mater. Lett.* 244, 27–30. doi: 10.1016/j.matlet.2019.02.064

Yang, Y., Li, S., Huang, W., Shangguan, H., Engelbrekt, C., Duan, S., et al. (2019). Effective synthetic strategy of $Zn_{0.76}Co_{0.24}S$ encapsulated in stabilized N-doped carbon nanoarchitecture toward ultra-long-life hybrid supercapacitors. *J. Mat. Chem. A* 7, 14670–14680. doi: 10.1039/C9TA03575C

Yu, Z.-Y., Chen, L.-F., and Yu, S.-H. (2014). Growth of NiFe2O4 nanoparticles on carbon cloth for high performance flexible supercapacitors. *J. Mater. Chem. A* 2, 10889–10894. doi: 10.1039/c4ta00492b

Conflict of Interest Statement: The authors declare that the research was conducted in the absence of any commercial or financial relationships that could be construed as a potential conflict of interest.

frontiers in Materials

ORIGINAL RESEARCH
published: 04 September 2019
doi: 10.3389/fmats.2019.00208

Fabrication and Electrochemical Performance of Al-Doped ZnO Nanosheets on Graphene-Based Flexible Substrates

Qi Yu[1]*, *Ping Rong*[1], *Shuai Ren*[1], *Liyun Jiang*[2] and *Yapeng Li*[1]

[1] School of Materials Science and Engineering, Institute of Graphene at Shaanxi Key Laboratory of Catalysis, Shaanxi University of Technology, Hanzhong, China, [2] School of Physics and Telecommunication Engineering, Shaanxi University of Technology, Hanzhong, China

In this work, Al-doped ZnO (AZO) nanosheets (NSs) were successfully synthesized on graphene-coated polyethylene terephthalate (GPET) flexible substrate via hydrothermal method. Studies have indicated that with the addition of Al^{3+}, the nanostructure of ZnO gradually grows from nanorods (NRs) to NSs, and the (100), (002), and (101) diffraction peak strength of ZnO that grows perpendicularly to the substrate along the c-axis weakened. The mechanism of hydrothermal growth of AZO/GPET was also studied. The electrochemical properties of the samples were investigated by cyclic voltammetry (CV) and electrochemical impedance spectroscopy (EIS), and it was concluded that AZO NSs grown on GPET substrates has better capacitance performance than undoped ZnO NRs.

Keywords: ZnO, Al-doped, hydrothermal method, graphene-based flexible substrates, electrochemical performance

OPEN ACCESS

Edited by:
Wenyao Li,
Shanghai University of Engineering Sciences, China

Reviewed by:
Xuenian Chen,
Henan Normal University, China
Jun Li,
Tsinghua University, China

***Correspondence:**
Qi Yu
kukukoko2004@163.com

Specialty section:
This article was submitted to Energy Materials, a section of the journal Frontiers in Materials

Received: *22 June 2019*
Accepted: *12 August 2019*
Published: *04 September 2019*

Citation:
Yu Q, Rong P, Ren S, Jiang L and Li Y (2019) Fabrication and Electrochemical Performance of Al-Doped ZnO Nanosheets on Graphene-Based Flexible Substrates. Front. Mater. 6:208. doi: 10.3389/fmats.2019.00208

INTRODUCTION

Up to now, energy reserves and environmental contamination are still the focus of extensive attention, especially the problems of air pollution, water pollution, global warming, and renewable energy, which are closely linked with our lives. In order to solve these problems, batteries and supercapacitors have become research hotspots of electrochemical energy storage systems. Among them, supercapacitor (SC), is of great attention in the fields of automobiles (Cao and Emadi, 2011; Biplab et al., 2017), wind power systems (Abbey and Joos, 2007), solar cells (Narayanan et al., 2015; Xu et al., 2015), and so on, because of its great power density, lack of required maintenance, wide operating temperature range, green environmental protection, long cycling life, etc. (Zhao et al., 2011). In addition to those, SCs can provide high power pulses in a short period of time compared to conventional capacitors or storage batteries. SCs, for example, are often used for intelligent start-stop control systems (lightweight hybrid power system), which are particularly prominent in plug-in hybrid electric vehicles (Cao and Emadi, 2011). Due to the different energy storage mechanism, SCs can be divided into electric double-layer capacitors (EDLCs) and faraday pseudo-capacitors. The former generates and stores energy by adsorption of a pure electrostatic charge on the electrode surface and the latter uses redox reaction to store electrical energy in an electrochemical manner (Liu et al., 2014). The properties of SCs are closely related to the electrode materials used, and examples of materials used in current research are: carbon materials

(Salinas-Torres et al., 2019), metal oxides (Wu et al., 2018) and conductive polymers. Of all electrode materials, carbon materials with high specific surface area and low internal resistance receive more attention, including activated carbon fibers (Ren et al., 2013), carbon aerogel (Liu et al., 2018), carbon nanotubes (Futaba et al., 2006), activated carbon (Wang et al., 2014; Isabel et al., 2016), porous carbon (Yang et al., 2019), and graphene (Zhang et al., 2016; Ren et al., 2018).

The theoretical specific capacity of semiconductor oxides such as ZnO, SnO_2, and TiO_2 is 2,3 times that of graphite, which has attracted enormous attention. Among them, ZnO, as a n-type semiconductor, has tremendous senses for the fields of chemicals, electronics, and optics owing to its superior properties [i.e., a large exciton binding energy (60 meV) and a wide bandgap of about 3.3 eV at room temperature] (Klingshirn, 2010). In addition, as the electrode material of supercapacitor, ZnO has been paid more and more attention because of its advantages of high chemical stability and thermal stability, low cost, environment friendly, and easy doping. However, ZnO has the disadvantages of poor conductivity and large volume effect in the process of charging and discharging, which affects the practical application of ZnO as an electrode material. Graphene, a two-dimensional carbon nanomaterial with zero bandgap, is attracted much attention that as a prospective candidate electrode material for EDLCs due to its high carrier mobility, great chemical resistance, large surface area, high conductivity, and transparency (Han et al., 2014; Ren et al., 2018). However, the presence of Van der Waals makes graphene easy to reunite, thus reducing the specific surface area and specific capacity of graphene. Therefore, ZnO and graphene materials composite and doped, can achieve the complementary advantages of material properties.

Bhirud et al. prepared N-doped ZnO/graphene (NZO/GR) by *situ* wet chemical method and studied their electrochemical properties. It was observed, the specific capacitance of NZO/GR was 555 Fg^{-1}, which was 529 Fg^{-1} and 20% higher than pure ZnO/GR (Bhirud et al., 2015). Cu/ZnO doped graphene nanocomposites was investigated by Jacob et al. (2018). Electrochemical analysis showed that the material has a specific capacity of 630 $mAhg^{-1}$ and retains around 95% of this capacity after 100 cycles. Faraji and Ani (2014) reviewed the application of microwave-assisted metal oxide thin film electrodes in supercapacitors. And they noted that ZnO/GR composites have high specific capacitance and good reversible charge-discharge performance. Many previous studies have used the hummer method to prepare graphene to prepare ZnO/graphene nanoparticles (Wang et al., 2011; Bu and Huang, 2015; Zhang et al., 2015). Therefore, it is necessary to explore the preparation of ZnO nanofilms based on transparent conductive flexible graphene-coated polyethylene terephthalate (GPET) substrates.

In this paper, ZnO nanosheets (NSs) with different Al doped concentration on GPET substrates were fabricated by a simple-green hydrothermal method, and their electrochemical properties were studied. The effect of adding different concentrations of Al on electrochemical properties of ZnO composite nanostructures was compared.

EXPERIMENTAL

Synthesis of ZnO Nanosheets

The Al-doped ZnO (AZO) NSs with different concentrations were prepared on GPET substrates. The ZnO seed layer (about 30 nm thickness) was sputtered by radio frequency magnetron sputtering on the surface of GPET substrates, which used acetone (10 min), methanol (10 min), and deionized (DI) water to clean in turn by ultrasonic cleaning machines. In the hydrothermal growth process of AZO NSs, zinc nitrate hexahydrate ($Zn(NO_3)_2{\cdot}6H_2O$), and hexamethylenetetramine ($C_6H_{12}N_4$) were mixed in DI water to prepare precursor solutions (30 ml). Then added aluminum oxide (Al_2O_3) as dopant to the solutions with the concentration of 0.1 and 0.05 mol/L, and kept stirring for 30 min under mild magnets. The precursor solutions were transferred to a Teflon-lined stainless-steel autoclave, and then the GPET substrates were immersed in it. After that, the autoclave was sealed and put into an oven, and heated at a temperature of 95°C for 6 h. The products on the substrates were washed with DI water and dried naturally at room temperature.

Structural Characteristics

Field emission scanning electron microscope (FESEM, by FEI Magellan 400) and X-ray diffraction (XRD, by Rigaku D/MAX-Ultima with Cu Kα radiation) were used to characterize the microscopic morphology and crystal structure of the samples, respectively.

Electrochemical Measurement

The cyclic voltammetry (CV) and electrochemical impedance spectroscopy (EIS) of the samples have used electrochemical workstation (CHI760E) to test. AZO NSs on GPET substrates as a working electrode, Ag/AgCl as a reference electrode, and platinum foil as counter electrode comprise the three-electrode test system. 1 mol/L Na_2SO_4 solution be used as electrolyte in this process of electrochemical measurement.

RESULTS AND DISCUSSION

The SEM and XRD images of ZnO with different Al doped concentration (doping concentrations of 0, 0.05, and 0.1 mol/L) prepared on GPET substrates are seen in **Figure 1**. As shown in **Figure 1A**, in the case of the undoped Al elements, ZnO has a vertically arranged NR structure with hexagon of its top and a uniformly dense cover on the surface of GPET substrate, suggesting that undoped ZnO has a good degree of orientation. With the addition of Al elements, the structure of ZnO is gradually changed from NR to NS, which clearly observed in **Figures 1B,C**. It is not difficult to see that AZO NSs, with its smooth surface, still grow perpendicularly to the GPET substrate and are connected together to form a network structure. Compared with the ZnO NRs, the conductivity of obtained electrodes of the AZO NSs can be improved due to the fact that the AZO NSs array can develope the branched network. And the pseudo-capacitance of ZnO nanostructure may improve its capacitance value and thus obtain an excellent

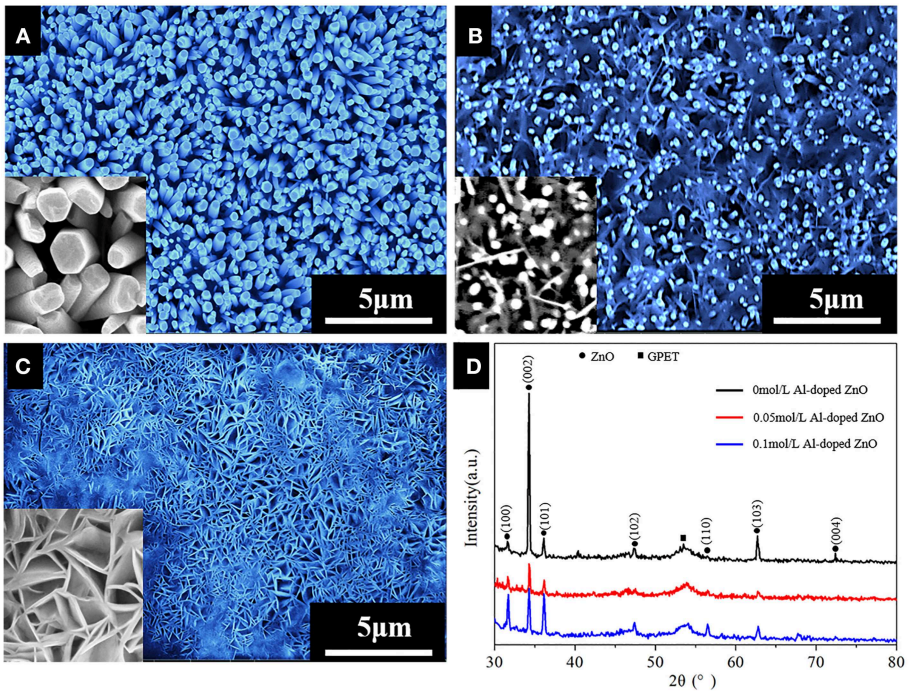

FIGURE 1 | (A–C) FE-SEM image of Al-doped ZnO nanostructure grown on GPET substrate at different Al doped concentration: **(A)** 0 mol/L; **(B)** 0.05 mol/L; **(C)** 0.1 mol/L; **(D)** XRD spectra of all samples. The inset in **(A–C)** correspond high-magnification images.

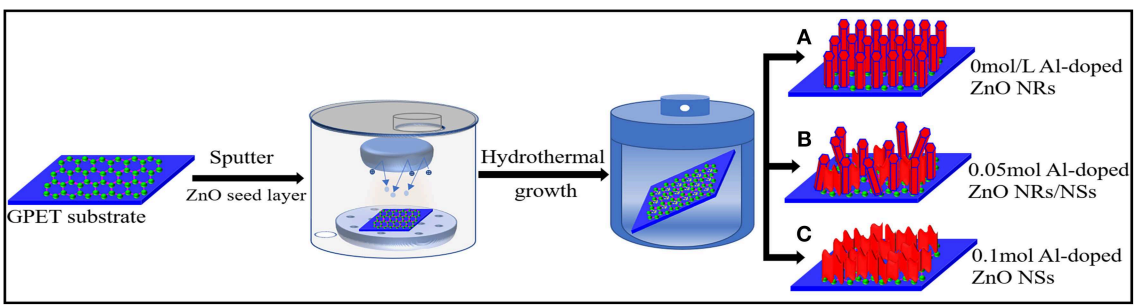

FIGURE 2 | Schematic diagram of hydrothermal growth mechanism of ZnO nanostructures.

electrochemical property (Zhang et al., 2015). As can be seen from the XRD image (**Figure 1D**), except for the characteristic peaks belonging to graphene and GPET substrate appearing at 26° and 54°, the other peaks are the diffraction peaks of ZnO, which are basically in agreement with the standard PDF card (JCPDS 89-1397) of ZnO. Moreover, the (002) diffraction peak strength is higher than (100) and (101), which indicates that AZO grow preferentially perpendicular to the substrate along the c-axis. The doping of Al generates stress during crystallization, and the crystal structure of ZnO changes accordingly. Further, the intensity of the diffraction peaks of (002) may become weak due to the incorporation of Al elements.

Schematic diagram of hydrothermal growth mechanism of ZnO NSs in **Figure 2** revealed that incorporation of Al inhibits the growth of ZnO NRs, thereby forming AZO NSs. The ZnO crystal has a (0001) plane and a (0001) plane, that is, a Zn positive polar surface and an O negative polar surface and six non-polar surfaces. Al_2O_3 dissolved in the solution to produce complexing ions, and the positive polar surface (0001) of the ZnO lattice is more likely to adsorb the Al $(OH)_4^-$ complexing ions with negative charges, which can hinder the growth of ZnO along the [0001] direction. The growth of NRs was inhibited along c-axis, which promoted the lateral growth of ZnO, and then formed ZnO NSs (**Figure 2C**; Koh et al., 2004). The main chemical reactions occurring in the solution during the formation of the ZnO NSs

were involved in the following Equations (1) and (4):

$$C_6H_{12}N_4 + 10H_2O \rightleftharpoons 6HCHO + 4NH_3{\cdot}H_2O \quad (1)$$

$$Zn^{2+} + NH_3{\cdot}H_2O \rightleftharpoons Zn(NH_3)_4^{2+} \quad (2)$$

$$Zn(NH_3)_4^{2+} + OH^- \rightleftharpoons ZnO + NH_3H_2O \quad (3)$$

$$Al + 4OH^- \rightleftharpoons Al(OH)_4^- \quad (4)$$

In order to study the effects of different concentrations of Al doping on the electrochemical characteristics of ZnO nanostructures, the CV curves of three different samples were analyzed under a potential range of −0.8 to 0.9 V at scanning rates of 100 mV/s.

The CV curves, which has been clearly observed by **Figure 3A**, revealed that redox peaks of 0.1 mol/L AZO NSs can be significant observed, which indicated that the synthesized active substances are beneficial for rapid redox reactions (Pu et al., 2014). Comparing the integrated area of the samples on the current-potential axis (**Figure 3A**), it is well-known that the integrated area of the 0.1 mol/L AZO NSs is larger, indicating that the 0.1 mol/L AZO NSs has a stronger charge storage capacity. Further study on the of different scanning rates of 5, 10, 20, 30, 50, and 100 mV/s on the electrochemical characteristics of 0.1 mol/L AZO NSs nanostructures (**Figure 3B**), and the results showed that the electrical current density increases with the increases of scan rates, which confirmed that 0.1 mol/L AZO NSs nanomaterials have excellent scanning ability.

The Nyquist plots of AZO/GPET electrodes are shown in **Figure 4**. The impedance curves of all obtained samples consisted of high frequency zones (shown as semicircle), which reflects the charge transfer resistance (R_{ct}) of the electrode, and low frequency zones (shown as slash),

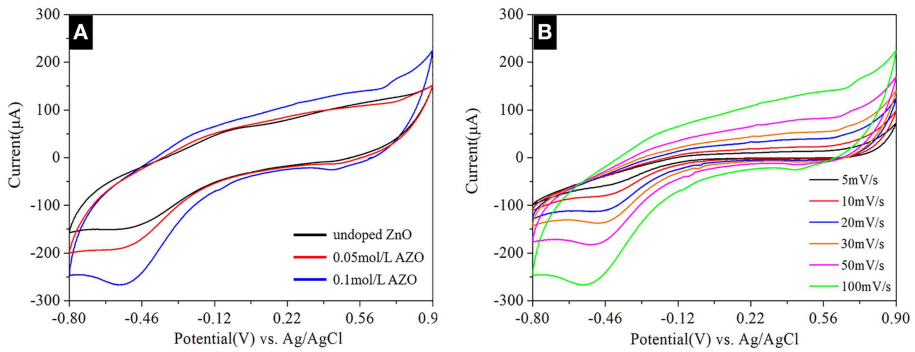

FIGURE 3 | (A) CV curves of all samples at a scan rate of 50 mV/s. **(B)** CV curves of 0.1 mol/L AZO nanostructures grown on GPET substrates with different scan rates in the range of 5–100 mV/s.

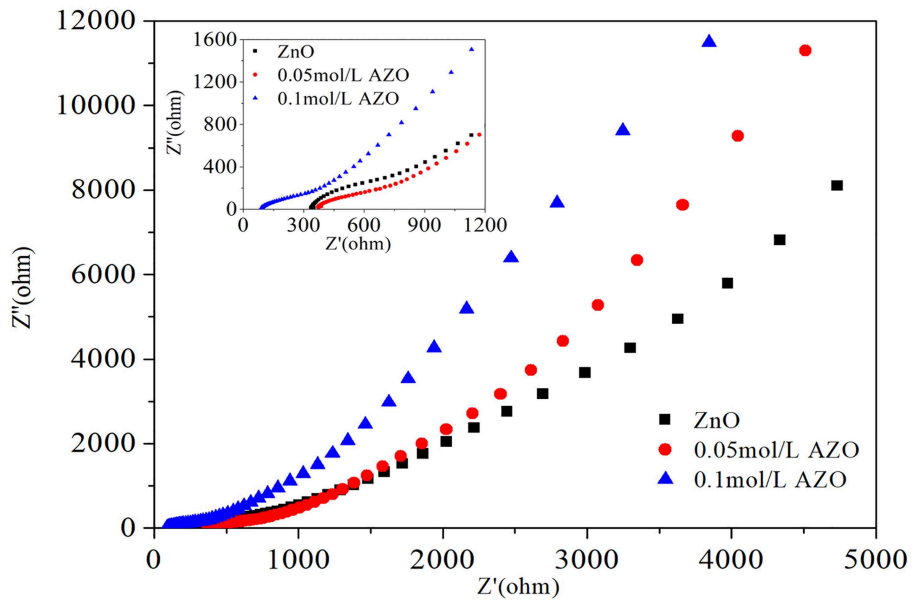

FIGURE 4 | Nyquist plots of 0 mol/L ZnO, 0.05 mol/L AZO, and 0.1 mol/L AZO. Inset is the enlarged high frequency zones.

which mirrors the diffusion resistance of the ions of the electrode. The semicircular diameter of the high-frequency zone is basically the same, indicating that the addition of Al does not enhance the charge transfer ability of ZnO/GPET electrode. In the low frequency zones the diffusion rate of electrode is proportional to the slope of impedance curve. The diffusion rate of AZO/GPET electrode is significantly greater than that of ZnO/GPET electrode, which indicated that AZO/GPET electrode has better electrochemical properties.

CONCLUSIONS

In summary, AZO NSs, which are evenly grown perpendicular to the GPET substrate, were successfully prepared using hydrothermal method assisted by ion sputtering. The structure, microscopic morphology and growth mechanism of the samples were analyzed, and it was concluded that the incorporation of Al^{3+} inhibited the growth of ZnO NRs, but promoted the formation of ZnO NSs, and weakened the characteristic diffraction peak intensity of ZnO growing perpendicular to the substrate along the c-axis. The electrochemical performance test of the samples concluded that the AZO NSs have better electrochemical performance than the undoped ZnO NRs, which have broad application prospects in the field of capacitors.

DATA AVAILABILITY

All datasets generated for this study are included in the manuscript/supplementary files.

AUTHOR CONTRIBUTIONS

QY contributed to the research and result analysis and discussion. SR, PR, YL, and LJ assisted in the synthesis and analysis of the materials. All authors contributed to the general discussion.

FUNDING

This work was financially supported by the National Natural Science Foundation of China (Grant no. 51502166), Scientific Research Program Funded by Shaanxi Provincial Department (Grant no. 17JK0130), and the Industrial Field of Key Research and Development Plan of Shaanxi Province (Grant no. 2018GY-040).

REFERENCES

Abbey, C., and Joos, G. (2007). Supercapacitor energy storage for wind energy applications. *IEEE Trans. Ind. Appl.* 43, 769–776. doi: 10.1109/TIA.2007.895768

Bhirud, A., Sathaye, S., Waichal, R., Park, C. J, and Kale, B. (2015). *In situ* preparation of N– ZnO/graphene nanocomposites: excellent candidate as a photocatalyst for enhanced solar hydrogen generation and high performance supercapacitor electrode. *J. Mater. Chem. A* 3, 17050–17063. doi: 10.1039/C5TA03955J

Biplab, K. D., Ankita, H., and Jisoo, K. (2017). Recent development and challenges of multifunctional structural supercapacitors for automotive industries. *Int. J. Energ. Res.* 41, 1397–1411. doi: 10.1002/er.3707

Bu, I. Y. Y., and Huang, R. (2015). One-pot synthesis of ZnO/reduced graphene oxide nanocomposite for supercapacitor applications. *Mat. Sci. Semicon. Proc.* 31, 131–138. doi: 10.1016/j.mssp.2014.11.037

Cao, J., and Emadi, A. (2011). A new battery/ultracapacitor hybrid energy storage system for electric, hybrid, and plug-in hybrid electric vehicles. *IEEE Trans. Power Electr.* 27, 122–132. doi: 10.1109/TPEL.2011.2151206

Faraji, S., and Ani, F. N. (2014). Microwave-assisted synthesis of metal oxide/hydroxide composite electrodes for high power supercapacitors – a review. *J. Power Sources* 263, 338–360. doi: 10.1016/j.jpowsour.2014.03.144

Futaba, D. N., Hata, K., Yamada, T., Hiraoka, T., Hayamizu, Y., Kakudate, Y., et al. (2006). Shape-engineerable and highly densely packed single-walled carbon nanotubes and their application as super-capacitor electrodes. *Nat. Mater.* 5, 987–994. doi: 10.1038/nmat1782

Han, W. J., Ren, L., Gong, L. J., Qi, X., Liu, Y. D., Yang, L. W., et al. (2014). Self-assembled three- dimensional graphene-based aerogel with embedded multifarious functional nanoparticles and its excellent photoelectrochemical activities. *ACS Sustain. Chem. Eng.* 2, 741–748. doi: 10.1021/sc400417u

Isabel, P. P., David, S. T., Ramiro, R. R., Emilia, M., and Diego, C. A. (2016). Design of activated carbon/activated carbon asymmetric capacitors. *Front. Mater.* 3:16. doi: 10.3389/fmats.2016.00016

Jacob, L., Prasanna, K., Vengatesan, M. R., Santhoshkumar, P., Lee, C. W., and Mittal, V. (2018). Binary Cu/ZnO decorated graphene nanocomposites as an efficient anode for lithium ion batteries. *J. Ind. Eng. Chem.* 59, 108–114.doi: 10.1016/j.jiec.2017.10.012

Klingshirn, C. (2010). The luminescence of ZnO under high one- and two-quantum excitation. *Scripta Mater.* 71, 547–556. doi: 10.1002/pssb.2220710216

Koh, Y. W., Ming, L., Tan, C. K., Yong, L. F., and Loh, K. P. (2004). Self-assembly and selected area growth of zinc oxide nanorods on any surface promoted by an aluminum precoat. *J. Phys. Chem. B* 108, 11419–11425. doi: 10.1021/jp049134f

Liu, W. J., Kao, T. W., Dai, Y. M., and Jehng, J. (2014). M. Ni-based nanocomposites supported on graphene nano sheet (GNS) for supercapacitor applications. *J. Solid State Electrochem.* 18, 18189–18196. doi: 10.1007/s10008-013-2263-4

Liu, X., Sheng, G., Zhong, M., and Zhou, X. (2018). Hybrid nanowires and nanoparticles of WO_3 in a carbon aerogel for supercapacitor applications. *Nanoscale* 10, 4209–4217. doi: 10.1039/C7NR07191D

Narayanan, R., Kumar, P. N., Deepa, M., and Srivastava, A. K. (2015). Combining energy conversion and storage: a solar powered supercapacitor. *Electrochim. Acta* 178, 113–126. doi: 10.1016/j.electacta.2015.07.121

Pu, J., Wang, Z., Wu, K., Yu, N., and Sheng, E. (2014). Co_9S_8 nanotubes arrays supported on nickel foam for high-performance supercapacitors. *Phys. Chem. Chem. Phys.* 16, 16785–16791. doi: 10.1039/C3CP54192D

Ren, J., Li, L., Chen, C., Chen, X., Cai, Z., Qiu, L., et al. (2013). Twisting carbon nanotube fibers for both wire-shaped micro-supercapacitor and micro-battery. *Adv. Mater.* 25, 1155–1159. doi: 10.1002/adma.201203445

Ren, S., Rong, P., and Yu, Q. (2018). Preparations, properties and applications of graphene in functional devices: a concise review. *Ceram. Int.* 44, 11940–11955. doi: 10.1016/j.ceramint.2018.04.089

Salinas-Torres, D., Ruiz-Rosas, R., Morallón, E., and Cazorla-Amorós, D. (2019). Strategies to enhance the performance of electrochemical capacitors based on carbon materials. *Front. Mater.* 6:115. doi: 10.3389/fmats.2019.00115

Wang, G., Wang, H., Lu, X., Ling, Y., Yu, M., Zhai, T., et al. (2014). Solid-state supercapacitor based on activated carbon cloths exhibits excellent rate capability. *Adv. Mater.* 26, 2676–2682. doi: 10.1002/adma.201304756

Wang, J., Zan, G., Li, Z. S., Wang, B., Yan, Y. X., Liu, Q., et al. (2011). Green synthesis of graphene nanosheets/ZnO composites and electrochemical properties. *J. Solid State Chem.* 184, 1421–1427. doi: 10.1016/j.jssc.2011.03.006

Wu, C., Chen, L., Lou, X., Ding, M., and Jia, C. (2018). Fabrication of cobalt-nickel-zinc ternary oxide nanosheet and applications for supercapacitor electrode. *Front. Chem.* 6:597. doi: 10.3389/fchem.2018.00597

Xu, X., Li, S., Zhang, H., Shen, Y., Zakeeruddin, S. M., Graetzel, M., et al. (2015). A power pack based on organometallic perovskite solar cell and supercapacitor. *ACS Nano* 9, 1782–1787. doi: 10.1021/nn506651m

Yang, H., Ye, S., Zhou, J., and Liang, T. (2019). Biomass-derived porous carbon materials for supercapacitor. *Front Chem.* 7:274. doi: 10.3389/fchem.2019.00274

Zhang, Y., Zou, Q., Hsu, H. S., Raina, S., Xu, Y., and Kang, J. B. (2016). Morphology effect of vertical graphene on the high performance of supercapacitor electrode. *ACS Appl. Mater. Inter*. 8, 7363–7369. doi: 10.1021/acsami.5b12652

Zhang, Z., Ren, L., Han, W. J., Meng, L., Wei, X., and Qi, X. (2015). One-pot electrodeposition synthesis of ZnO/graphene composite and its use as binder-free electrode for supercapacitor. *Ceram. Int*. 41, 4374–4380. doi: 10.1016/j.ceramint.2014.11.127

Zhao, X., Sánchez, B. M., Dobson, P. J., and Grant, P. S. (2011). The role of nanomaterials in redox-based supercapacitors for next generation energy storage devices. *Nanoscale* 3, 839–855. doi: 10.1039/c0nr00594k

Conflict of Interest Statement: The authors declare that the research was conducted in the absence of any commercial or financial relationships that could be construed as a potential conflict of interest.

frontiers in Chemistry

MINI REVIEW
published: 01 October 2019
doi: 10.3389/fchem.2019.00660

Three-Dimensional Graphene-Based Composite Hydrogel Materials for Flexible Supercapacitor Electrodes

Enping Lai, Xinxia Yue, Wan'e Ning, Jiwei Huang, Xinlong Ling and Haitao Lin**

Guangxi Key Laboratory of Green Processing of Sugar Resources, College of Biological and Chemical Engineering, Guangxi University of Science and Technology, Liuzhou, China

Three-dimensional (3D) graphene-based hydrogels have attracted great interest for applying in supercapcacitors electrodes, owing to their intriguing properties that combine the structural interconnectivities and the outstanding properties of graphene. However, the pristine graphene hydrogel can not satisfy the high-performance demands, especial in high specific capacitance. Consequently, novel graphene-based composite hydrogels with increased electrochemical properties have been developed. In this mini review, a brief summary of recent progress in the research of the three-dimensional graphene-based composite hydrogel for flexible supercapacitors electrodes materials is presented. The latest progress in the graphene-based composite hydrogel consisting of graphene/metal, graphene/polymer, and atoms doped graphene is discussed. Furthermore, future perspectives and challenges in graphene-based composite hydrogel for supercapacitor electrodes are also expressed.

Keywords: flexible supercapacitor, electrode materials, grahpene-based hydrogel, three-dimensional architecture, composite materials

OPEN ACCESS

Edited by:
Wenyao Li,
Shanghai University of Engineering Sciences, China

Reviewed by:
Shijie Li,
Zhejiang Ocean University, China
Chengyi Hou,
Donghua University, China

****Correspondence:***
Enping Lai
nemodhu@163.com
Haitao Lin
lhthost@163.com

Specialty section:
This article was submitted to Electrochemistry, a section of the journal Frontiers in Chemistry

Received: *15 August 2019*
Accepted: *17 September 2019*
Published: *01 October 2019*

Citation:
Lai E, Yue X, Ning W, Huang J, Ling X and Lin H (2019) Three-Dimensional Graphene-Based Composite Hydrogel Materials for Flexible Supercapacitor Electrodes. Front. Chem. 7:660. doi: 10.3389/fchem.2019.00660

INTRODUCTION

In recent years, supercapacitors have been attracted intensive investigation for sustainable energy application, because of their advantages in excellent power density and high charge/discharge rates (Li et al., 2018). With the rapid growth of wearable electronics, flexible supercapacitors that can work under consecutive bending or stretching are urgently needed. However, it remains a great challenge to obtain supercapacitors with excellent electrochemical performance and good flexibility. Since the supercapacitors mainly consist of two electrodes and a separated membrane, the electrodes are often considered to be a key factor (Xu et al., 2018). Thus, it is critically important to develop innovative materials for flexible supercapacitor electrodes.

As a unique two-dimensional (2D) carbon material, graphene has gained tremendous attention in various application aspects due to its fast-charged carrier mobility, excellent conductivity and largely tunable surface area (Sattar, 2019). Based on the extraordinary physico-chemical properties, graphene and its functionalized derivatives (graphene oxide, GO) can be applied in supercapacitors as the electrode materials. Previous studies have demonstrated that the supercapacitors based on graphene can possess excellent specific capacitance (Horn et al., 2019). Unfortunately, the restacking or irreversible agglomeration of graphene sheets can suppress the high conductivity and decrease accessible surface area, which limit the improvement of capacitive performance. To tackle these challenges, three-dimensional (3D) graphene-based architectures including foam, hydrogels, sponges are developed.

Among various 3D macroscopic structures, graphene hydrogels consist of interconnected porous networks with large specific surface areas have received particular attention (Lu et al., 2017). These hydrogels provide multidimensional ion/electron transport pathways with the intrinsic properties of graphene, which makes them promising candidates for supercapacitor electrodes. Great achievements of supercapacitors based on graphene hydrogels have been obtained, while the pristine graphene hydrogel cannot meet the requirements in practical application (Ma et al., 2018). Functional materials or dopants such as metal oxides or hydroxide, conducting polymers, and so on have been introduced to the graphene hydrogels to further improve the electrochemical performance. In this mini-review, a brief retrospect on graphene-based composite hydrogel materials for flexible supercapacitor electrodes will be provided.

GRAPHENE-BASED COMPOSITE HYDROGEL ELECTRODE MATERIALS

Graphene-Metal Composite Hydrogels Electrode Materials

Usually, metal oxides or hydroxides exhibit high pseudo-capacitance mainly due to their faradic reaction beyond formation of electrical double-layers in the charge-discharge processes. Thus, metal oxides or hydroxides including MnO_2, $Ni(OH)_2$, and etc. have been widely incorporated into graphene to form composite materials to obtain enhanced performance.

Researches have been focused on coupling MnO_2 with other materials (Xu et al., 2019) for supercapacitor electrodes, and different structures of MnO_2 have also been incorporated in graphene hydrogel. Zhang et al. (2016) prepared micro-nanostructured pompon-like MnO_2/graphene hydrogel composites, and the hydrogel with a MnO_2 content of 50% displayed a good capacitive behavior (445.7 F/g at 0.5 A/g). Tran et al. (2017) synthesized graphene/α-MnO_2 nanowire hydrogel with a high specific capacitance (397 F/g) at 1.0 A/g. Meng et al. (2018) designed a glucose and ammonia reduction system to synthesize δ-MnO_2/graphene hydrogel with a capacity of 200.6 F/g.

As a transition metal hydroxide, $Ni(OH)_2$ have been commonly used. In view of the structure, the $Ni(OH)_2$ nanoplate (Mao et al., 2016) and nanoflower structure (Wang et al., 2016) have been designed to form 3D graphene-based frameworks, and the capacitance can be achieve to 782 F/g at 0.2 A/g and 1,632 F/g at 1 A/g, respectively. Recently, Li et al. (2019) coupled $Ni(OH)_2$ nanosheets with nitrogen-enriched graphene hydrogel, which featured a specific capacitance of 896 F/g at 0.5 A/g.

Besides, in consideration of the advantage of Co and Ni, the strategy of combining Ni with Co was developed. Hwang et al. (2018) embedded Ni-Co hydroxide nanoneedles in graphene hydrogel, and the nanocomposite exhibited a specific capacitance of 544 C/g at 2 A/g. Tiruneh et al. (2018) designed a binder-free hybrid graphene hydrogel with nickel cobalt sulfide embedded, which can exhibit a capacity of about 1,000 F/g at 0.75 A/g with outstanding stability.

In addition, as one of the most promising nanomaterials, TiO_2 has also been focused. Liu et al. (2017) obtained rice-like TiO_2/graphene composite hydrogel, and the interaction between TiO_2 nanoparticles and graphene hydrogel can endow the composite hydrogel with superior physicochemical properties, resulting in an excellent capacity of 372.3 F/g at 0.2 A/g. In addition, to realize synergic effect of organic and inorganic materials, Zhang et al. (2018b) synthesized RuO_2/graphene hydrogel, and then adsorbed 1,4-naphthoquinone (NQ) molecules onto the hydrogel to form an hybrid graphene hydrogel, and the hydrogel containing ∼14.6% RuO_2 also can show a superior specific capacitance of 450.8 F/g.

Graphene-Polymer Composite Hydrogels Electrode Materials

Conductive polymers with the reverse doping-dedoping behavior have been extensively incorporated into 3D graphene hydrogels to fabricate high-performance electrodes. One of the successful conducting polymers is polyaniline (PANI), which has good environmental stability and high pseudocapcacitance. Various types of PANI including nanorods and nanowires have been used to form graphene/PANI composite hydrogel, and these hydrogels can show improved specific capacitance (Chen et al., 2017; Xu et al., 2017). To retain the essential features of the native hydrogel, the thin PANI layer wrapped on the graphene hydrogel by Gao et al. (2016) using an electrodeposition method, and the hydrogel displayed a good specific capacitance (710 F/g at 2 A/g). In addition, the hydrogel structure and the preparation temperature are also important. Wu et al. (2016) found that the phase-separated structure can produce much channels for electrolyte diffusion in PANI/graphene hydrogel, leading to a specific capacitance as high as 783 F/g at 27.3 A/g. Zou et al. (2018b) used *m*-phenylenediamine (*m*PD) to preserve the conjugated structure of PANI, and the composite hydrogel showed an improved capacity of 514.3 F/g. They also developed double-crosslinked network functionalized graphene/PANI hydrogel with high specific capacitance and mechanical strength (Zou et al., 2018a). For the preparation temperature, Ates et al. (2018) showed that the high capacitance can be kept at ∼99% of its pristine value for the hydrogel prepared at 25°C, in comparison of that at 0°C.

Due to the ultrahigh theoretical capacitance and mechanical flexibility, polypyrrole (PPy) has also attracted considerable attention. Wu and Lian (2017) synthesized graphene/PPy hydrogel with a specific capacitance of 363 F/cm^3 at 1.0 mA/cm^3 using hydroquinone as a functionalized molecule. Since the ion transportation may be restricted by the compact morphology of PPy/graphene composite, the strategy of PPy wrapped graphene was developed. Pattananuwat and Aht-ong (2017) controlled nanoporous structure for PPy coated on graphene hydrogel surface with aiding of the surfactant, and a high specific capacitance (640.8 F/g at 1 A/g) can be achieved. They also used poly(3,4-ethylenedioxythiophene) (PEDOT) with PPy to form the synergistic effect, and the resultant hydrogel exhibited a specific capcacitance of 342 F/g at 0.5 A/g (Pattananuwat and Aht-ong, 2016). Recently, a hybrid PPy/rGO hydrogel *in-situ*

electropolymerization preparation of PPy on the outside layer of graphene was reported by Zhang et al. (2019), and the specific capacitance is 340 F/g at 1 A/g.

Except for PANI and PPy, biopolymer such as lignosulfonate that a derivate of lignin can be regarded as a candidate for electrode material due to its electroactive components. Xiong et al. (2016) prepared lignosulfonate/graphene hydrogel with a maximum capacity of 549.5 F/g at 1 A/g. Li et al. (2017a) also reported lignosulfonate functionalized graphene hydrogels, which can present a specific capacitance of 432 F/g. These renewable composite hydrogels exhibit great potential in supercapacitor as electrodes materials.

Doped Graphene Composite Hydrogels Electrode Materials

As known, chemical doping is an effective strategy to modify the intrinsic properties of the materials. For graphene materials, nitrogen doping has been found to be an important method to provide graphene composite with high capacitance (Jin et al., 2019). For example, Liao et al. (2016) used urea and a small amount of ammonia to prepare N-doped graphene hydrogel, and the different N-types in graphene can resulted in an excellent specific capacitance (387.2 F/g at 1 A/g). Except for urea and ammonia, other materials containing N also have been used. Jiang et al. (2016) designed N-doped graphene hydrogel with a good specific capacitance (167.7 F/g at 1 A/g) by using carbohydrazide. Liu et al. (2016) used ammonium bicarbonate to prepared porous N-doped graphene hydrogel, and the hydrogel with high N content (10.8 at%) showed a high specific capacitance of 194.4 F/g. Gao et al. (2019) synthetized nitrogen-doped graphene-based hydrogels with concentrated sulfuric acid and o-phenylenediamine (oPDA), and the optimal hydrogel showed specific capacitance about 519.8 F/g.

Compared to single-atom doping, multiple doping can exhibit a synergetic effect and further improve the capacitive behavior of the materials. Typically, nitrogen and sulfur can be doped into graphene concurrently. After co-doping, the pseudo capacitance of the graphene will be increase, because of the redox faradic reactions existed at nitrogen-containing groups and sulf-containing species. Tran et al. (2016) outlined that N and S co-doped graphene hydrogel with holy defect can show a wonderful specific capacitance of 538 F/g at 0.5 mV/s, and the electrochemical property of the hydrogel can be modulated by the level of N and S doping. Li et al. (2017b) synthesized N/S co-doped graphene hydrogels with hierarchical pores, which can demonstrate a very good specific capacitance (251 F/g at 0.5 A/g) surprisingly. Zhang et al. (2018a) developed a one-step method to synthesize N/S co-doped graphene hydrogel, and the as-prepared hydrogel can show a capacity of 1,063 C/g at 1 A/g. Kong et al. (2018) constructed N,S-codoped graphene hydrogel with 3D hole, and the abundant in-plane pores leading to an outstanding specific capacitance of 320.0 F/g at 1 A/g.

CONCLUDING REMARKS

In this work, the recent advances in three-dimensional graphene-based composite hydrogel were reviewed in term of their use as flexible supercapacitors electrode materials. As can be seen, much effort has been devoted in the field of 3D graphene-based composite hydrogel electrode materials. A variety of materials including metals, polymers, dopants have been reported to construct high performance graphene-based composite hydrogel, and the excellent capacitive behavior of the typical composite hydrogel can be achieved (**Table 1**). Nevertheless, a massive effort is still needed before real practical applications become possible. For one, the exhibited capacitance values of the hydrogel still need to be further enhanced. In particular, large scale production of graphene-based composite hydrogel with high capacitance and quality is still a challenge. More importantly, for industry-level applications, technical movements should focus on more cost-effective and straightforward approaches for the fabrication of 3D graphene-based composite hydrogel rather than the design of complicated nanomaterials. It is believed that continuous breakthroughs in the graphene-based composite hydrogel will be made with the further research and development in this exciting field, and the hydrogel can play a great role in flexible capacitive devices in the near future.

TABLE 1 | Characteristics of typical graphene-based composite hydrogel for supercapacitor electrodes.

Composite component	Method	Capacitance	Testing conditions	References
α-MnO2 nanowire	Hydrothermal	397 F g^{-1}	1.0 A g^{-1}, two-electrode	Tran et al., 2017
$Ni(OH)_2$ nanosheet	Hydrothermal	896 F g^{-1}	0.5 A g^{-1}, three-electrode	Li et al., 2019
Ni-Co hydroxide nanoneedles	Chemical reduction and hydrothermal	544 C g^{-1}	2 A g^{-1}, three-electrode	Hwang et al., 2018
TiO_2 nanoparticles	Hydrothermal	372.3 F g^{-1}	0.2 A g^{-1}, three-electrode	Liu et al., 2017
PANI	Hydrothermal and eletrodeposition	710 F g^{-1}	2 A g^{-1}, three-electrode	Gao et al., 2016
PPy	Chemical reaction	363 F cm^{-3}	1.0 mA cm^{-3}, two-electrode	Wu and Lian, 2017
Lignosulfonate	Hydrothermal	549.5 F g^{-1}	1 A g^{-1}, three-electrode	Xiong et al., 2016
N dopant	Hydrothermal	387.2 F g^{-1}	1 A g^{-1}, three-electrode	Liao et al., 2016
N/S co-dopant	Hydrothermal	1,063 C g^{-1}	1 A g^{-1}, three-electrode	Zhang et al., 2018a

AUTHOR CONTRIBUTIONS

All authors listed have made a substantial, direct and intellectual contribution to the work, and approved it for publication.

FUNDING

This work was supported by the Natural Science Foundation of Guangxi Province (No. 2018GXNSFBA281084) and the Middle-aged and Young Teachers Basic Ability Promotion Project of Guangxi (No.2019KY0371).

REFERENCES

Ates, M., El-Kady, M., and Kaner, R. B. (2018). Three-dimensional design and fabrication of reduced graphene oxide/polyaniline composite hydrogel electrodes for high performance electrochemical supercapacitors. *Nanotechnology* 29:175402. doi: 10.1088/1361-6528/aaae44

Chen, J., Song, J., and Feng, X. (2017). Facile synthesis of graphene/polyaniline composite hydrogel for high-performance supercapacitor. *Polym. Bull.* 74, 27–37. doi: 10.1007/s00289-016-1695-2

Gao, S., Zhang, L., Qiao, Y., Dong, P., Shi, J., and Cao, S. (2016). Electrodeposition of polyaniline on three-dimensional graphene hydrogel as a binder-free supercapacitor electrode with high power and energy densities. *RSC Adv.* 6, 58854–58861. doi: 10.1039/C6RA06263F

Gao, X., Han, G., Song, H., Chang, Y., Xiao, Y., Zhang, Y., et al. (2019). Purified nitrogen-doped reduced graphene oxide hydrogels for high-performance supercapacitors. *J. Electroanal. Chem.* 834, 206–215. doi: 10.1016/j.jelechem.2019.01.004

Horn, M., Gupta, B., MacLeod, J., Liu, J., and Motta, N. (2019). Graphene-based supercapacitor electrodes: addressing challenges in mechanisms and materials. *Curr. Opin. Green Sust. Chem.* 17, 42–48. doi: 10.1016/j.cogsc.2019.03.004

Hwang, M., Kang, J., Seong, K., Kim, D. K., Jin, X., Antink, W. H., et al. (2018). Ni-Co hydroxide nanoneedles embedded in graphene hydrogel as a binder-free electrode for high-performance asymmetric supercapacitor. *Electrochim. Acta.* 270, 156–164. doi: 10.1016/j.electacta.2018.03.075

Jiang, M., Xing, L. B., Zhang, J. L., Hou, S. F., Zhou, J., Si, W., et al. (2016). Carbohydrazide-dependent reductant for preparing nitrogen-doped graphene hydrogels as electrode materials in supercapacitor. *Appl. Surf. Sci.* 368, 388–394. doi: 10.1016/j.apsusc.2016.02.009

Jin, Y., Meng, Y., Fan, W., Lu, H., Liu, T., and Wu, S. (2019). Free-standing macroporous nitrogen doped graphene film for high energy density supercapacitor. *Electrochim. Acta* 318, 865–874. doi: 10.1016/j.electacta.2019.06.107

Kong, W., Zhu, J., Zhang, M., Liu, Y., and Hu, J. (2018). Three-dimensional N- and S-codoped graphene hydrogel with in-plane pores for high performance supercapacitor. *Micropor. Mesopor. Mat.* 268, 260–267. doi: 10.1016/j.micromeso.2018.04.029

Li, F., Wang, X., and Sun, R. (2017a). A metal-free and flexible supercapacitor based on redox-active lignosulfonate functionalized graphene hydrogels. *J. Mater. Chem. A* 5, 20643–20650. doi: 10.1039/C7TA03789A

Li, J., Hao, H., Wang, J., Li, W., and Shen, W. (2019). Hydrogels that couple nitrogen-enriched graphene with Ni(OH)2 nanosheets for high-performance asymmetric supercapacitors. *J. Alloy. Compd.* 782, 516–524. doi: 10.1016/j.jallcom.2018.12.188

Li, J., Zhang, G., Fu, C., Deng, L., Sun, R., and Wong, C. P. (2017b). Facile preparation of nitrogen/sulfur co-doped and hierarchical porous graphene hydrogel for high-performance electrochemical capacitor. *J. Power Sources* 345, 146–155. doi: 10.1016/j.jpowsour.2017.02.011

Li, W., Zhang, B., Lin, R., Ho-Kimura, S., He, G., Zhou, X., et al. (2018). A dendritic nickel cobalt sulfide nanostructure for alkaline battery electrodes. *Adv. Funct. Mater.* 28, 1705937. doi: 10.1002/adfm.201705937

Liao, Y., Huang, Y., Shu, D., Zhong, Y., Hao, J., He, C., et al. (2016). Three-dimensional nitrogen-doped graphene hydrogels prepared via hydrothermal synthesis as high-performance supercapacitor materials. *Electrochim Acta* 194, 136–142. doi: 10.1016/j.electacta.2016.02.067

Liu, D., Fu, C., Zhang, N., Zhou, H., and Kuang, Y. (2016). Three-dimensional porous nitrogen doped graphene hydrogel for high energy density supercapacitors. *Electrochim. Acta* 213, 291–297. doi: 10.1016/j.electacta.2016.07.131

Liu, Y., Gao, T., Xiao, H., Guo, W., Sun, B., Pei, M., et al. (2017). One-pot synthesis of rice-like TiO_2/graphene hydrogels as advanced electrodes for supercapacitors and the resulting aerogels as high-efficiency dye adsorbents. *Electrochim. Acta* 229, 239–252. doi: 10.1016/j.electacta.2017.01.142

Lu, H., Zhang, S., Guo, L., and Li, W. (2017). Applications of graphene-based composite hydrogels: a review. *RSC Adv.* 7, 51008–51020. doi: 10.1039/C7RA09634H

Ma, H., Zhou, Q., Wu, M., Zhang, M., Yao, B., Gao, T., et al. (2018). Tailoring the oxygenated groups of graphene hydrogel for high-performance supercapacitors with large areal mass loadings. *J. Mater. Chem. A* 6, 6587–6594. doi: 10.1039/C7TA10843E

Mao, L., Guan, C., Huang, X., Ke, Q., Zhang, Y., and Wang., J. (2016). 3D graphene-nickel hydroxide hydrogel electrode for high-performance supercapacitor. *Electrochim. Acta* 196, 653–660. doi: 10.1016/j.electacta.2016.02.084

Meng, X., Lu, L., and Sun., C. (2018). Green synthesis of three-dimensional MnO_2/graphene hydrogel composites as a high-performance electrode material for supercapacitors. *ACS Appl. Mater. Interf.* 2018, 16474–16481. doi: 10.1021/acsami.8b02354

Pattananuwat, P., and Aht-ong, D. (2016). One-step method to fabricate the highly porous layer of poly (pyrrole/(3, 4-ethylenedioxythiophene)/) wrapped graphene hydrogel composite electrode for the flexibile supercapacitor. *Mater. Lett.* 184, 60–64. doi: 10.1016/j.matlet.2016.08.031

Pattananuwat, P., and Aht-ong, D. (2017). Controllable morphology of polypyrrole wrapped graphene hydrogel framework composites via cyclic voltammetry with aiding of poly (sodium 4-styrene sulfonate) for the flexible supercapacitor electrode. *Electrochim. Acta* 224, 149–160. doi: 10.1016/j.electacta.2016.12.036

Sattar, T. (2019). Current review on synthesis, composites and multifunctional properties of graphene. *Topics Curr. Chem.* 377:10. doi: 10.1007/s41061-019-0235-6

Tiruneh, S. N., Kang, B. K., Kwag, S. H., Lee, Y. H., Kim, M., and Yoon., D. H. (2018). Synergistically active $NiCo_2S_4$ nanoparticles coupled with holey defect graphene hydrogel for high-performance solid-state supercapacitors. *Chem-Eur. J.* 24, 3263–3270. doi: 10.1002/chem.201705445

Tran, N. Q., Kang, B. K., Woo, M. H., and Yoon, D. H. (2016). Enrichment of pyrrolic nitrogen by hole defects in nitrogen and sulfur co-doped graphene hydrogel for flexible supercapacitors. *ChemsusChem* 9, 2261–2268. doi: 10.1002/cssc.201600668

Tran, T. S., Tripathi, K. M., Kim, B. N., You, I. K., Park, B. J., Han, Y. H., et al. (2017). Three-dimensionally assembled graphene/α-MnO_2 nanowire hybrid hydrogels for high performance supercapacitors. *Mater. Res. Bull.* 96, 395–404. doi: 10.1016/j.materresbull.2017.04.012

Wang, R., Jayakumar, A., Xu, C., and Lee., J. M. (2016). $Ni(OH)_2$ nanoflowers/graphene hydrogels: a new assembly for supercapacitors. *ACS Sustainable Chem. Eng.* 4, 3736–3742. doi: 10.1021/acssuschemeng.6b00362

Wu, J., Zhang, Q., Zhou, A., Huang, Z., Bai, H., and Li, L. (2016). Phase-separated polyaniline/graphene composite electrodes for high-rate electrochemical supercapacitors. *Adv. Mater.* 28, 10211–10216. doi: 10.1002/adma.201601153

Wu, X., and Lian, M. (2017). Highly flexible solid-state supercapacitor based on graphene/polypyrrole hydrogel. *J Power Sources* 362, 184–191. doi: 10.1016/j.jpowsour.2017.07.042

Xiong, C., Zhong, W., Zou, Y., Luo, J., and Yang, W. (2016). Electroactive biopolymer/graphene hydrogels prepared for high-performance supercapacitor electrodes. *Electrochim. Acta* 211, 941–949. doi: 10.1016/j.electacta.2016.06.117

Xu, H., Liu, J., Chen, Y., Li, C. L., Tang, J., and Li, Q. (2017). Synthesis of three-dimensional nitrogen-doped graphene/polyaniline hydrogels for high performance supercapacitor application. *J. Mater. Sci-Mater. EL* 28, 10674–10683. doi: 10.1007/s10854-017-6842-5

Xu, K., Li, S., Yang, J., and Hu, J. (2018). Hierarchical hollow MnO_2 nanofibers with enhanced supercapacitor performance. *J. Colloid Interf. Sci.* 513, 448–454. doi: 10.1016/j.jcis.2017.11.052

Xu, K., Shen, Y., Zhang, K., Yang, F., Li, S., and Hu, J. (2019). Hierarchical assembly of manganese dioxide nanosheets on one-dimensional titanium nitride nanofibers for high-performance supercapacitors. *J. Colloid Interf. Sci.* 552, 712–718. doi: 10.1016/j.jcis.2019.05.093

Zhang, N., Fu, C., Liu, D., Li, Y., Zhou, H., and Kuang, Y. (2016). Three-dimensional pompon-like MnO_2/graphene hydrogel composite for supercapacitor. *Electrochim. Acta* 210, 804–811. doi: 10.1016/j.electacta.2016.06.004

Zhang, W., Chen, Z., Guo, X., Jin, K., Wang, Y. X., Li, L., et al. (2018a). N/S co-doped three-dimensional graphene hydrogel for high performance supercapacitor. *Electrochim. Acta* 278, 51–60. doi: 10.1016/j.electacta.2018.05.018

Zhang, X., Zhang, J., Chen, Y., Cheng, K., Yan, J., Zhu, K., et al. (2019). Freestanding 3D Polypyrrole@reduced graphene oxide hydrogels as binder-free electrode materials for flexible asymmetric supercapacitors. *J. Colloid Interf Sci.* 536, 291–299. doi: 10.1016/j.jcis.2018.10.044

Zhang, Z., Guo, B., Wang, X., Li, Z., Yang, Y., and Hu., Z. (2018b). Design and synthesis of an organic (naphthoquinone) and inorganic (RuO_2) hybrid graphene hydrogel composite for asymmetric supercapacitors. *New J. Chem.* 42, 14956–14964. doi: 10.1039/C8NJ01908H

Zou, Y., Liu, R., Zhong, W., and Yang, W. (2018a). Mechanically robust double-crosslinked network functionalized graphene/polyaniline stiff hydrogels for superior performance supercapacitors. *J. Mater. Chem. A* 6, 8568–8578. doi: 10.1039/C8TA00860D

Zou, Y., Zhang, Z., Zhong, W., and Yang, W. (2018b). Hydrothermal direct synthesis of polyaniline, graphene/polyaniline and N-doped graphene/polyaniline hydrogels for high performance flexible supercapacitors. *J. Mater. Chem. A* 6, 9245–9256. doi: 10.1039/C8TA01366G

Conflict of Interest: The authors declare that the research was conducted in the absence of any commercial or financial relationships that could be construed as a potential conflict of interest.

frontiers in Chemistry

MINI REVIEW
published: 02 October 2019
doi: 10.3389/fchem.2019.00640

Capacity Contribution Induced by Pseudo-Capacitance Adsorption Mechanism of Anode Carbonaceous Materials Applied in Potassium-ion Battery

Jiahao Liu[1†], *Ziqiang Xu*[1†], *Mengqiang Wu*[1*], *Yuesheng Wang*[2*] *and Zaghib Karim*[2*]

[1] School of Materials and Energy, University of Electronic Science and Technology of China, Chengdu, China, [2] Center of Excellence in Transportation Electrification and Energy Storage, Hydro-Québec, Varennes, QC, Canada

OPEN ACCESS

Edited by:
Min Zeng,
Lanzhou Institute of Chemical Physics (CAS), China

Reviewed by:
Dongliang Chao,
University of Adelaide, Australia
Chao Wang,
Massachusetts Institute of Technology, United States

***Correspondence:**
Mengqiang Wu
mwu@uestc.edu.cn
Yuesheng Wang
wang.yuesheng@ireq.ca
Zaghib Karim
Zaghib.Karim@hydro.qc.ca

[†]These authors have contributed equally to this work

Specialty section:
This article was submitted to Electrochemistry, a section of the journal Frontiers in Chemistry

Received: 08 July 2019
Accepted: 05 September 2019
Published: 02 October 2019

Citation:
Liu J, Xu Z, Wu M, Wang Y and Karim Z (2019) Capacity Contribution Induced by Pseudo-Capacitance Adsorption Mechanism of Anode Carbonaceous Materials Applied in Potassium-ion Battery. Front. Chem. 7:640. doi: 10.3389/fchem.2019.00640

The intrinsic bottleneck of graphite intercalation compound mechanism in potassium-ion batteries necessitates the exploitation of novel potassium storage strategies. Hence, utmost efforts have been made to efficiently utilize the extrinsic pseudo-capacitance, which offers facile routes by employing low-cost carbonaceous anodes to improve the performance of electrochemical kinetics, notably facilitating the rate and power characteristics for batteries. This mini-review investigates the methods to maximize the pseudo-capacitance contribution based on the size control and surface activation in recent papers. These methods employ the use of cyclic voltammetry for kinetics analysis, which allows the quantitative determination on the proportion of diffusion-dominated vs. pseudo-capacitance by verifying a representative pseudo-capacitive material of single-walled carbon nanotubes. Synergistically, additional schemes such as establishing matched binder–electrolyte systems are in favor of the ultimate purpose of high-performance industrialized potassium-ion batteries.

Keywords: potassium-ion batteries, carbonaceous anodes, pseudo-capacitance adsorption, surface doping activation, kinetic analysis

INTRODUCTION

Suffering from the geopolitical maldistribution of lithium resources, sodium-ion batteries (SIBs) and potassium-ion batteries (PIBs) reach a hotspot in view of wider resource reserves compared with lithium-ion batteries (LIBs) (2.09 wt% of K vs. 2.36 wt% of Na vs. 0.0017 wt% of Li) (Carmichael, 1989; Larcher and Tarascon, 2015). Significantly, the PIB system has the lowest negative potential (0.15 V below the Li/Li^+) (Komaba et al., 2015; Eftekhari et al., 2016; Wang et al., 2018a,b) and satisfactory electrochemical kinetics in ionic diffusion kinetics and conductivity theoretically (Okoshi et al., 2013, 2017; Komaba et al., 2015; Eftekhari et al., 2016; Su et al., 2016) in non-aqueous electrolytes, ascribed to low de-solvation due to its weak Lewis acid character (Okoshi et al., 2017; Lei et al., 2018). Similar to the behavior of LIBs in graphite (Wang, 2017), the intercalation mechanism of PIBs involves three potassiation stages, generating the KC_{36} in Stage III, KC_{24} in Stage II, and finally the KC_8 in Stage I (Jian et al., 2017) with 270 mA h g^{-1}, which is far more stable than SIBs (Wang et al., 2013; Zheng et al., 2017). Nevertheless, large Shannon ionic radius (K^+ = 1.38 Å, Na^+ = 1.02 Å, Li^+ = 0.76 Å) and atomic mass

(K = 39.10, Na = 22.99, Li = 6.94) (Shannon, 1976) have decreased the theoretical capacity and induced high volume expansion of 61% (Wen et al., 2015; Eftekhari et al., 2016; Zou et al., 2017). Although some strategies enter into consideration such as adopting expand graphite (An et al., 2018), implementing solvent co-intercalation (SCI) (Wang et al., 2013, 2019; David and Singh, 2014), and developing dual-carbon batteries (DCBs) (Carlin et al., 1996, 2010; Beltrop et al., 2017; Fan et al., 2017; Ji et al., 2017), essential kinetics deficiency is hard to surmount.

To address the irreversible expansion induced by equilibrium graphite, amorphous carbons come into the focused sight (Xing et al., 2017), which are admittedly classified as hard carbon (HC) and soft carbon (SC). HC is proven to have a prolonged cycling ability for its randomly oriented bend graphitic layers along the c axis without observed expansion after a thorough potassiation (Jian et al., 2016, 2017). On the contrary, SC is easily graphitized with turbostratic domains although far from the commercial graphite. SC presents obvious expansion to HC if undergoing complete potassiation (Luo et al., 2015a; Wang et al., 2017). Nonetheless, SC has a better rate performance than HC for more aligned domains (Jian et al., 2017), regarded as the reason for the better rate performance.

Pseudo-capacitance is the middle part of the battery and electrical double-layer capacitors (EDLCs) (Jiang and Liu, 2019) as shown in **Figure 1a**. In **Figure 1a**, Liu points out that the current generation of batteries depends on the Faradic electron transfer from the surface to the metal center based on the charge-compensating ions by intercalation or adsorption. In contrast, a pseudo-capacitor is different from EDLCs because it is not electrostatic-induced and the transfer process of surface electrons distinguishes the behavior from batteries. Pseudo-capacitance can be classified into two categories—intrinsic and extrinsic. The former (Chao et al., 2016) describes an inherent feature of specific materials such as RuO_2 and MnO_2, which is on the strength of Faradaic electron transfer. However, the latter emphasizes the technological means of low dimension, nanoscale size, and high surface area (Wang et al., 2007; Brezesinski et al., 2009; Muller et al., 2015; Cook et al., 2016) among a majority of materials, for instance, the single-walled carbon nanotube (SWCNT) with surface-enriched potassium ions in **Figure 1b** (Hersam, 2009; Kang et al., 2013), attributed to the regular hexagonal arrangement of carbon atoms on the surface. This non-Faradaic pathway provides a possibility to utilize inexpensive carbonaceous anodes (Gogotsi and Penner, 2018) if proper surface treatments such as activization, doping, and plasma processing have been undergone (Chao et al., 2018).

These surface-dominated anodes uptake and absorb potassium ions with fast reaction kinetics during the electrochemistry process, avoiding the hindrance in the intercalation mechanism, which is regarded as the primary cause for high rate property and large capacity of PIBs undergoing charging and discharging processes (Shin et al., 2011; Shao et al., 2013; Chen et al., 2016; Long et al., 2016). As a consequence, this mini-review analyzes the methods for distinguishing the proportion of capacity contribution and summarizes the application of pseudo-capacitance to PIBs very recently, aiming to design a practical performance improvement approach.

ANALYSES AND APPLICATIONS OF PSEUDO-CAPACITANCE

Generally, it is widely admitted that pseudo-capacitance is not a pure Faradaic progress but a rapid reversible surface redox reaction involved in EDLCs. The charge storage mechanism of complex PIBs behaviors is composed of two typical contribution progresses: surface-induced pseudo-capacitor process and diffusion-dominated process (Brezesinski et al., 2009; Wen et al., 2015; Xu et al., 2019b). Nonetheless, Faradaic and non-Faradaic reactions are electro indistinguishable for jointly contributing to the current parameter (Gogotsi and Penner, 2018). Most researchers employ cyclic voltammetry (CV) to determine the relative proportion of contribution from pseudo-capacitor and diffusion-dominated processes. The peak current is proportional to the square root of sweep rate describing the reversible diffusion-limited state (i-$v^{\frac{1}{2}}$), whereas it is proportional to the sweep rate (i-v) describing the capacitive state. A representative power law relationship between the current and scan rate reveals the charge storage mechanism in PIBs (Wang et al., 2007; Torsten et al., 2010; Veronica et al., 2013):

$$\mathrm{i} = \mathrm{a}v^{b}$$

where a and b are constants. The b value can be figured out by profiling the log(i)–log(v) curve. If $b = 0.5$, the Faradic diffusion is predominant; while $b = 1$, the pseudo-capacitance assumes the primary contribution (Sathiya et al., 2011; Lijun et al., 2014; Zou et al., 2017). Furthermore, as for a fixed sweep rate, the specific pseudo-capacitance contribution can be given in detail by the following formula (Torsten et al., 2010; Wang Y. et al., 2016):

$$\mathrm{i} = k_1 v + k_2 v^{\frac{1}{2}}$$

where the parameter $k_1 v$ represents the capacitive process while the $k_2 v^{\frac{1}{2}}$ is in favor of the diffusion process as stated earlier.

Furthermore, Marveh maintains that compared with the CV method, the step potential electrochemical spectroscopy (SPECS) has wider adaptive range with prominent advantages. In high sweep rates, SPECS presents precise characterization to depict the process of electrical double layer on the surface of electrodes (Forghani and Donne, 2018).

Recent works validate the validity of the pseudo-capacitance algorithm based on the surface-dominated pseudo-capacitance mechanism, which has been extensively applied in carbonaceous anodes in PIBs by constructing high surface area or activating.

Doping and activating are highly feasible methods that introduce abundant defects, expand specific surface area, and promote the conductivity, meanwhile adding charge storage for PIBs (Lijun et al., 2014; Share et al., 2016; Chen et al., 2017; Lei et al., 2018; Xu et al., 2018).

Nitrogen-doped strategy has a practical significance eliciting satisfying performance enhancements. According to the X-ray photoelectron spectroscopy (XPS) results, pyrrole nitrogen (N-5), pyridine nitrogen (N-6), and quaternary N (N-Q) are three N-doping forms presented in **Figure 2A**, where N-5 and N-6 possess high electrochemical activity and generate additional defects in the surface of the graphene layer, hence promoting the adsorption

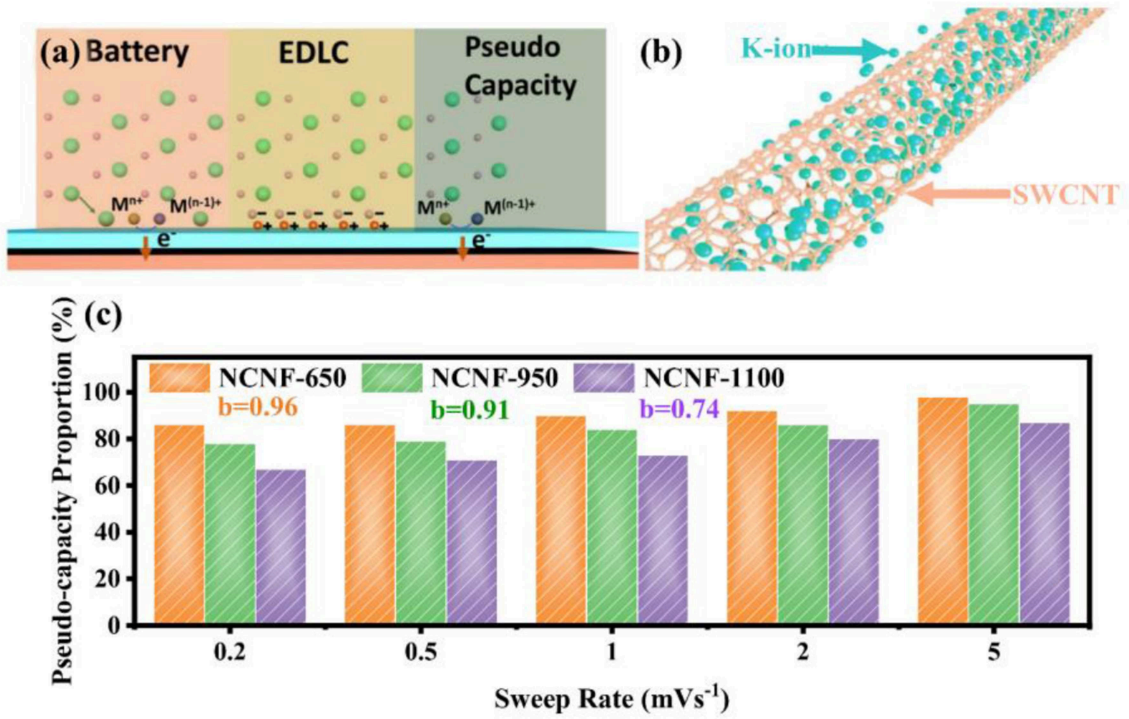

FIGURE 1 | (a) Surface processes among battery, EDLC and pseudo-capacitance. **(b)** Diagram of the surface-dominated procedure for SWCNT; with permission from Wiley. **(c)** Pseudo-capacity proportion of NCNF-650, NCNF-950 and NCNF-1100 with *b* value; with permission from Springer.

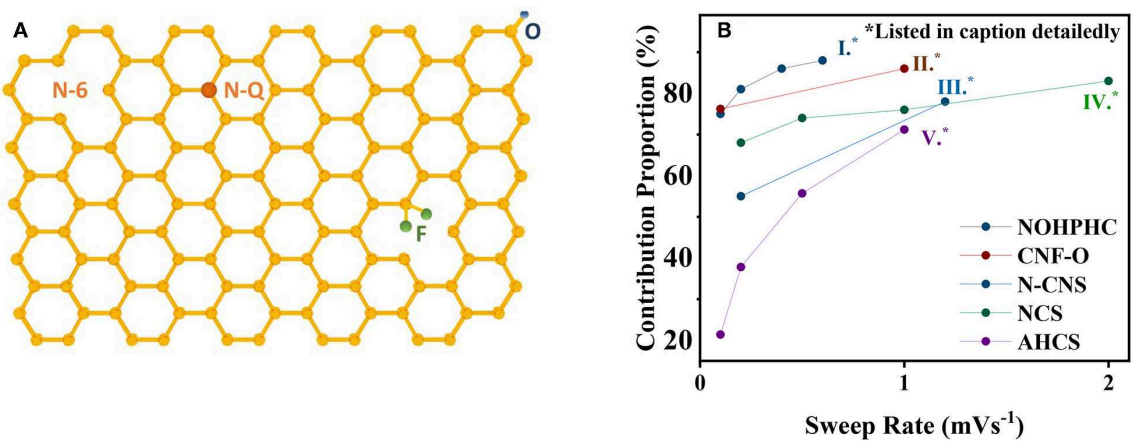

FIGURE 2 | (A) Surface defects induced by N-doping, O-doping and F-doping. **(B)** Relationship between pseudo-capacitance contribution proportion and sweep rate based on recent researches (I) (Yang et al., 2018), (II) (Adams et al., 2017), (III) (Lei et al., 2018), (IV) (Chen et al., 2017), (V) (Wang et al., 2018).

quantity of potassium ions, accelerating the kinetic process (Li et al., 2013; Wang et al., 2014; Xu et al., 2018). This differentiation of N forms is ascribed to their constructions of respective bonding electrons, resulting in different chemical activities. However, N-Q, located in the internal surface of graphene layer, bonding with three sp2 carbon atoms, is beneficial to improve electrical conductivity (Yang et al., 2018). Notably, N-6 is regarded as the most effective doping precursor because it replaces the carbon atom with a nitrogen atom at the defect or the edge of the graphite plane and occupies abundant active centers to adsorb potassium ions (Ma et al., 2012; Ding et al., 2014; Xie et al., 2017). Consistently, recent researches demonstrated that N-6 defects decreases with temperature increasing; meanwhile, the degree of graphitization rises, accompanied by the generation of N-Q. Xu concludes that among three temperature-controlled materials NCNF-650, NCNF-950, and NCNF-1100 derived from poly-pyrrole nanofibers, the pseudo-capacitance contribution of NCNF-650 occupies 90% at 1 mV s^{-1} for abundant N-6 defects, while the others occupy 73 and 84% at 1 mV s^{-1} as displayed in **Figure 1c** with their *b* value (Xu et al., 2018). The

b value increases with the temperature dropping, revealing the degree deepening of pseudo-capacity, in accordance with the quantity N-6 defects. Similar results are obtained in Xie's report; nonetheless, Xie indicates that enhancement of electrochemical performance is a comprehensive result associated with N-6 defects, electrical conductivity, and transfer resistance. Three sets of temperature-controlled experiments point out that PNCM-700 is equipped with the best comprehensive performance compared with PNCM-500 and PNCM-900. As for the function of defects, Clement states that the D-bond from the Raman spectrum is employed to describe the sp^3 defect distribution, which intensifies a six-fold rate performance to the un-doped material (Clement et al., 2015; Share et al., 2016). The prominent significance of N-doping is to spread out the interlayer spacing and provide huge specific surface area to promote the pseudo-capacitive effect.

Doping some other elements also achieves fair results. Oxidation functional groups on the carbon surface polishes up the wettability of carbon-based materials and advances the pseudo-capacitance behavior (Tarun et al., 2010; Shao et al., 2013; Wang X. et al., 2016; Wu et al., 2016; Xie et al., 2017; Wang et al., 2018). Adams reported that oxidation groups increase obviously on the surface capacitive storage while inducing the capacity reduction contributed by the intercalation mechanism. As a consequence, there is no significant enhancement to the total capacity (Adams et al., 2017). In addition, mixed-doping P and O doping (Ma et al., 2017) based on the triphenylphosphine precursor obtains a satisfactory capacity of 474 mA h g^{-1}, benefiting from expanding the interlayer spacing; N and F doping immensely adds the conductivity distinctly (Ju et al., 2016; Share et al., 2016; Adams et al., 2017).

Activated hollow carbon nanospheres (HCS) underwent HF etching from C@SiO2 nanospheres in Wang's work. Wang emphasizes on the sharp increase on the surface area from 481.4 to 757.8 m^2 g^{-1} after activating utilizing KOH as the activator. Capacitive contribution occupies 71.2% at a sweep rate of 1 mV s^{-1}, leading to 192.7 mA h g^{-1} at 2 A g^{-1} after 5,000 cycles with a retention of 99.5% (Wang et al., 2018). Aforesaid data support the rule that the pseudo-capacity contribution has the tendency of positive correlation with sweep rate as summarized in **Figure 2B**. This work claimed that activated hollow carbon expands the layer spacing of the carbon anode and shortens the diffusion distance of K-ions.

Nevertheless, surface-modified strategies, whether doping or activating, may give rise to the decrease of initial Coulombic efficiency (ICE) unsatisfactorily. Compensatory methods work well in LIBs and SIBs (Suo et al., 2017) to establish appropriate binder–electrolyte systems (BESs), which directly impact the formation of solid electrolyte interphase (SEI), especially the morphology features such as thickness, pore, and wrinkle. Tailored BESs shape the SEI into a smooth and thin layer, hence improving the transfer efficiency of ions on the phase interface (Xu et al., 2019a). Similarly, employing KFSI and KTFSI electrolyte (Eftekhari et al., 2016; Jin et al., 2016), adding electrolyte additives (Wu et al., 2017), selecting hydrophilic binders such as CMC, PANa, and SA (Komaba et al., 2015; Luo et al., 2015b; Jin et al., 2016; Xu et al., 2019a), and utilizing pre-potassiation technique (Yang et al., 2018) serve the same purpose for superb PIBs.

CONCLUSIONS AND PERSPECTIVES

PIBs with carbonaceous anodes provide the possibility for industrialization under controlled price. Facilely, surface modifications such as doping and activating obviously enhance the pseudo-capacitance contribution, speeding up the rate and power performance based on a rapid electrochemical kinetics.

This non-insertion charge storage (pseudo-capacitance absorption) integrates with both battery-type and capacitor-type characteristics, exhibiting distinct redox separation peaks including analogous linear capacitive voltage response. However, the relationship between capacitive and sweep rate is only authentic limited in a low and narrow sweep rate under the CV separation method. Precisely, the SPECS is suitable for a wider range of sweep rates, inducing detailed contribution information for each potential point (Forghani and Donne, 2018). In addition, matching binder–electrolyte with anodes accurately can synergistically promote specific capacity and rate properties, deriving high-performance PIBs.

AUTHOR CONTRIBUTIONS

All authors listed have made a substantial, direct and intellectual contribution to the work, and approved it for publication.

FUNDING

This work was supported by the Sichuan Science and Technology Program (Grant Nos. 2018GZ0006 and 2018GZ0134).

REFERENCES

Adams, R. A., Syu, J. M., Zhao, Y., Lo, C. T., Varma, A., and Pol, V. G. (2017). Binder-free N- and O-rich carbon nanofiber anodes for long cycle life K-ion batteries. *ACS Appl. Mater. Interfaces* 9, 17872–17881. doi: 10.1021/acsami.7b02476

An, Y., Fei, H., Zeng, G., Ci, L., Xi, B., Xiong, S., et al. (2018). Commercial expanded graphite as a low-cost, long-cycling life anode for potassium–ion batteries with conventional carbonate electrolyte. *J. Power Sources* 378, 66–72. doi: 10.1016/j.jpowsour.2017.12.033

Beltrop, K., Beuker, S., Heckmann, A., Winter, M., Placke, T. J. E., and Science, E. (2017). Alternative electrochemical energy storage: Potassium-based dual-graphite batteries. *Energy Environ. Sci.* 10, 2090–2094. doi: 10.1039/C7EE01535F

Brezesinski, T., Wang, J., Polleux, J., Dunn, B., and Tolbert, S. H. (2009). Templated nanocrystal-based porous TiO(2) films for next-generation electrochemical capacitors. *J. Am. Chem. Soc.* 131, 1802–1809. doi: 10.1021/ja8057309

Carlin, R. T., Fuller, J., Kuhn, W. K., Lysaght, M. J., and Trulove, P. C. (1996). Electrochemistry of room-temperature chloroaluminate molten salts

at graphitic and nongraphitic electrodes. *J. Appl. Electrochem.* 26, 1147–1160. doi: 10.1007/BF00243740

Carlin, R. T., Long, H. C. D., Fuller, J., and Trulove, P. C. (2010). ChemInform abstract: dual intercalating molten electrolyte batteries. *Cheminform* 25, L73–L76. doi: 10.1002/chin.199446010

Carmichael, R. S. (1989). *CRC Practical Handbook of Physical Properties of Rocks and Minerals*. Boca Raton, FL: CRC Press.

Chao, D., Ouyang, B., Liang, P., Huong, T. T. T., Jia, G., Huang, H., et al. (2018). C-plasma of hierarchical graphene survives SnS bundles for ultrastable and high volumetric Na-ion storage. *Adv. Mater.* 30:1804833. doi: 10.1002/adma.201804833

Chao, D., Zhu, C., Yang, P., Xia, X., Liu, J., Wang, J., et al. (2016). Array of nanosheets render ultrafast and high-capacity Na-ion storage by tunable pseudocapacitance. *Nat. Commun.* 7:12122. doi: 10.1038/ncomms12122

Chen, C., Wang, Z., Zhang, B., Miao, L., Cai, J., Peng, L., et al. (2017). Nitrogen-rich hard carbon as a highly durable anode for high-power potassium-ion batteries. *Energy Storage Mater.* 8, 161–168. doi: 10.1016/j.ensm.2017.05.010

Chen, C., Xu, H., Zhou, T., Guo, Z., Chen, L., Yan, M., et al. (2016). Integrated intercalation-based and interfacial sodium storage in graphene-wrapped porous $Li_4Ti_5O_{12}$ nanofibers composite aerogel. *Adv. Energy Mater.* 6:1600322. doi: 10.1002/aenm.201600322

Clement, B., Todd Wesley, S., Michelle, D., and Xiulei, J. J. N. L. (2015). New mechanistic insights on Na-ion storage in nongraphitizable carbon. *Nano Lett.* 15, 5888–5892. doi: 10.1021/acs.nanolett.5b01969

Cook, J. B., Kim, H. S., Yan, Y., Ko, J. S., Robbennolt, S., Dunn, B., et al. (2016). Mesoporous MoS_2 as a transition metal dichalcogenide exhibiting pseudocapacitive Li and Na-ion charge storage. *Adv. Energy Mater.* 6:1501937. doi: 10.1002/aenm.201501937

David, L., and Singh, G. (2014). Reduced graphene oxide paper electrode: opposing effect of thermal annealing on Li and Na cyclability. *J. Phys. Chem. C* 118, 28401–28408. doi: 10.1021/jp5080847

Ding, N., Huang, Z. H., Lv, R., Lu, Y., Wang, J., Shen, W., et al. (2014). Nitrogen-enriched electrospun porous carbon nanofiber networks as high-performance free-standing electrode materials. *J. Mater. Chem. A* 2, 19678–19684. doi: 10.1039/C4TA03868A

Eftekhari, A., Jian, Z., and Ji, X. (2016). Potassium secondary batteries. *ACS Appl. Mater. Interfaces* 9, 4404–4419. doi: 10.1021/acsami.6b07989

Fan, L., Liu, Q., Chen, S., Lin, K., Xu, Z., and Lu, B. J. S. (2017). Potassium-based dual ion battery with dual-graphite electrode. *Small* 13:1701011. doi: 10.1002/smll.201701011

Forghani, M., and Donne, S. W. (2018). Method comparison for deconvoluting capacitive and pseudo-capacitive contributions to electrochemical capacitor electrode behavior. *J. Electrochem. Soc.* 165, A664–A673. doi: 10.1149/2.0931803jes

Gogotsi, Y., and Penner, R. M. (2018). Energy storage in nanomaterials—Capacitive, pseudocapacitive, or battery-like? *Acs Nano* 12, 2081–2083. doi: 10.1021/acsnano.8b01914

Hersam, M. C. (2009). "Progress towards monodisperse single-walled carbon nanotubes," in *Nanoscience and Technology*, ed P. Rodgers (London: Macmillan Publishers Ltd.), 3–10. doi: 10.1142/9789814287005_0001

Ji, B., Fan, Z., Wu, N., and Tang, Y. (2017). A dual-carbon battery based on potassium-ion electrolyte. *Adv. Energy Mater.* 7:1700920. doi: 10.1002/aenm.201700920

Jian, Z., Hwang, S., Li, Z., Hernandez, A. S., Wang, X., Xing, Z., et al. (2017). Hard–soft composite carbon as a long-cycling and high-rate anode for potassium-ion batteries. *Adv. Funct. Mater.* 27:1700324. doi: 10.1002/adfm.201700324

Jian, Z., Xing, Z., Bommier, C., Li, Z., and Ji, X. (2016). Hard carbon microspheres: potassium-ion anode versus sodium-ion anode. *Adv. Energy Mater.* 6:1501874. doi: 10.1002/aenm.201501874

Jiang, Y., and Liu, J. (2019). Definitions of pseudocapacitive materials: a brief review. *Energy Environ. Sci.* 2, 30–37. doi: 10.1002/eem2.12028

Jin, Z., Zou, X., Zhu, Y., Xu, Y., and Wang, C. (2016). Electrochemical intercalation of potassium into graphite. *Adv. Funct. Mater.* 26, 8103–8110. doi: 10.1002/adfm.201602248

Ju, Z., Zhang, S., Xing, Z., Zhuang, Q., Qiang, Y., and Qian, Y. (2016). Direct synthesis of few-layer F-doped graphene foam and its lithium/potassium storage properties. *ACS Appl. Mater. Interfaces* 8, 20682–20690. doi: 10.1021/acsami.6b04763

Kang, J., Wen, J., Jayaram, S. H., Wang, X., and Chen, S. K. (2013). Electrochemical characterization and equivalent circuit modeling of single-walled carbon nanotube (SWCNT) coated electrodes. *J. Power Sources* 234, 208–216. doi: 10.1016/j.jpowsour.2013.01.058

Komaba, S., Hasegawa, T., Dahbi, M., and Kubota, K. (2015). Potassium intercalation into graphite to realize high-voltage/high-power potassium-ion batteries and potassium-ion capacitors. *Electrochem. Commun.* 60, 172–175. doi: 10.1016/j.elecom.2015.09.002

Larcher, D., and Tarascon, J. M. (2015). Towards greener and more sustainable batteries for electrical energy storage. *Nat. Chem.* 7, 19–29. doi: 10.1038/nchem.2085

Lei, L., Yu, C., Xie, Y., Peng, T., Li, Q., and Yan, C. (2018). Understanding of the ultrastable K-ion storage of carbonaceous anode. *Adv. Funct. Mater.* 28:1801989. doi: 10.1002/adfm.201801989

Li, Z., Xu, Z., Tan, X., Wang, H., Holt, C. M. B., Stephenson, T., et al. (2013). Mesoporous nitrogen-rich carbons derived from protein for ultra-high capacity battery anodes and supercapacitors. *Energy Environ. Sci.* 6, 871–878. doi: 10.1039/c2ee23599d

Lijun, F., Kun, T., Kepeng, S., Van Aken, P. A., Yu, Y., and Maier, J. (2014). Nitrogen doped porous carbon fibres as anode materials for sodium ion batteries with excellent rate performance. *Nanoscale* 6, 1384–1389. doi: 10.1039/C3NR05374A

Long, Q., Chen, W., Xiong, X., Hu, C., Feng, Z., Hu, P., et al. (2016). Sulfur-doped carbon with enlarged interlayer distance as a high-performance anode material for sodium-ion batteries. *Adv. Sci.* 2:1500195. doi: 10.1002/advs.201500195

Luo, W., Jian, Z., Xing, Z., Wang, W., Bommier, C., Lerner, M. M., et al. (2015a). Electrochemically expandable soft carbon as anodes for Na-ion batteries. *ACS Central Sci.* 1, 516–522. doi: 10.1021/acscentsci.5b00329

Luo, W., Wan, J., Ozdemir, B., Bao, W., Chen, Y., Dai, J., et al. (2015b). Potassium ion batteries with graphitic materials. *Nano Lett.* 15, 7671–7677. doi: 10.1021/acs.nanolett.5b03667

Ma, C., Shao, X., and Cao, D. (2012). Nitrogen-doped graphene nanosheets as anode materials for lithium ion batteries: a first-principles study. *J. Mater. Chem. A* 22, 8911–8915. doi: 10.1039/c2jm00166g

Ma, G., Huang, K., Ma, J. S., Ju, Z., Xing, Z., and Zhuang, Q. C. (2017). Phosphorus and oxygen dual-doped graphene as superior anode material for room-temperature potassium-ion batteries. *J. Mater. Chem. A* 5, 7854–7861. doi: 10.1039/C7TA01108C

Muller, G. A., Cook, J., Kim, H. S., Tolbert, S. H., and Dunn, B. J. N. L. (2015). High performance pseudocapacitor based on 2D layered metal chalcogenide nanocrystals. *Nano Lett.* 15, 1911–1917. doi: 10.1021/nl504764m

Okoshi, M., Yamada, Y., Komaba, S., Yamada, A., and Nakai, H. (2017). Theoretical analysis of interactions between potassium ions and organic electrolyte solvents: a comparison with lithium, sodium, and magnesium ions. *J. Electrochem. Soc.* 164, A54–A60. doi: 10.1149/2.0211702jes

Okoshi, M., Yamada, Y., Yamada, A., and Nakai, H. (2013). Theoretical analysis on de-solvation of lithium, sodium, and magnesium cations to organic electrolyte solvents. *J. Electrochem. Soc.* 160, A2160–A2165. doi: 10.1149/2.074311jes

Sathiya, M., Prakash, A. S., Ramesha, K., Tarascon, J. M., and Shukla, A. K. (2011). V2O5-anchored carbon nanotubes for enhanced electrochemical energy storage. *J. Am. Chem. Soc.* 133, 16291–16299. doi: 10.1021/ja207285b

Shannon, R. (1976). Revised effective ionic radii and systematic studies of interatomic distances in halides and chalcogenides. *Acta Crystallogr. Sect. A* 32, 751–767. doi: 10.1107/S0567739476001551

Shao, Y., Xiao, J., Wang, W., Engelhard, M., Chen, X., Nie, Z., et al. (2013). Surface-driven sodium ion energy storage in nanocellular carbon foams. *Nano Lett.* 13, 3909–3914. doi: 10.1021/nl401995a

Share, K., Cohn, A. P., Carter, R., Rogers, B., and Pint, C. L. (2016). Role of nitrogen doped graphene for improved high capacity potassium ion battery anodes. *Acs Nano* 10, 9738–9744. doi: 10.1021/acsnano.6b05998

Shin, J. Y., Samuelis, D., and Maier, J. (2011). Sustained lithium-storage performance of hierarchical, nanoporous anatase TiO_2 at high rates: emphasis on interfacial storage phenomena. *Adv. Funct. Mater.* 21, 3464–3472. doi: 10.1002/adfm.201002527

Su, D., Mcdonagh, A., Qiao, S. Z., and Wang, G. (2016). High-capacity aqueous potassium-ion batteries for large-scale energy storage. *Adv. Mater.* 29:1604007. doi: 10.1002/adma.201604007

Suo, L., Borodin, O., Wang, Y., Rong, X., Sun, W., Fan, X., et al. (2017). "Water-in-salt" electrolyte makes aqueous sodium-ion battery safe, green, and long-lasting. *Adv. Energy Mater.* 7:1701189. doi: 10.1002/aenm.201701189

Tarun, B., Aleks, A., Barbara, P., Veronica, B., and Fahlman, B. D. (2010). Enhanced electrochemical lithium storage by graphene nanoribbons. *J. Am. Chem. Soc.* 132, 12556–12558. doi: 10.1021/ja106162f

Torsten, B., John, W., Tolbert, S. H., and Bruce, D. (2010). Ordered mesoporous alpha-MoO_3 with iso-oriented nanocrystalline walls for thin-film pseudocapacitors. *Nat. Mater.* 9, 146–151. doi: 10.1038/nmat2612

Veronica, A., Jérémy, C., Lowe, M. A., Jong Woung, K., Pierre-Louis, T., Tolbert, S. H., et al. (2013). High-rate electrochemical energy storage through Li+ intercalation pseudocapacitance. *Nat. Mater.* 12, 518–522. doi: 10.1038/nmat3601

Wang, G., Xiong, X., Xie, D., Lin, Z., and Liu, M. (2018). Chemical activated hollow carbon nanospheres as a high-performance anode material for potassium ion batteries. *J. Mater. Chem. A* 6, 24317–24323. doi: 10.1039/C8TA09751H

Wang, J., Polleux, J., Lim, J., and Dunn, B. (2007). Pseudocapacitive contributions to electrochemical energy storage in TiO_2 (anatase) nanoparticles. *J. Phys. Chem. C* 111, 14925–14931. doi: 10.1021/jp074464w

Wang, L., Yang, J., Li, J., Chen, T., Chen, S., Wu, Z., et al. (2019). Graphite as a potassium ion battery anode in carbonate-based electrolyte and ether-based electrolyte. *J. Power Sources* 409, 24–30. doi: 10.1016/j.jpowsour.2018.10.092

Wang, X., Han, K., Qin, D., Li, Q., Wang, C., Niu, C., et al. (2017). Polycrystalline soft carbon semi-hollow microrods as anode for advanced K-ion full batteries. *Nanoscale* 9, 18216–18222. doi: 10.1039/C7NR06645G

Wang, X., Weng, Q., Liu, X., Wang, X., Tang, D. M., Tian, W., et al. (2014). Atomistic origins of high rate capability and capacity of N-doped graphene for lithium storage. *Nano Lett* 14, 1164–1171. doi: 10.1021/nl4038592

Wang, X., Xu, X., Niu, C., Meng, J., Huang, M., Liu, X., et al. (2016). Earth abundant Fe/Mn-based layered oxide interconnected nanowires for advanced K-ion full batteries. *Nano Lett.* 17, 544–550. doi: 10.1021/acs.nanolett.6b04611

Wang, Y. (2017). Practical challenges in employing graphene for lithium-ion batteries and beyond. *Small* 1:1700099. doi: 10.1002/smtd.201700099

Wang, Y., Ding, Y., Pan, L., Shi, Y., Yue, Z., Shi, Y., et al. (2016). Understanding the size-dependent sodium storage properties of $Na_2C_6O_6$-based organic electrodes for sodium-ion batteries. *Nano Lett.* 16, 3329–3334. doi: 10.1021/acs.nanolett.6b00954

Wang, Y., Feng, Z., Yang, S.-Z., Gagnon, C., Gariépy, V., Laul, D., et al. (2018a). Layered oxides-$LiNi_{1/3}Co_{1/3}Mn_{1/3}O_2$ as anode electrode for symmetric rechargeable lithium-ion batteries. *J. Power Sources* 378, 516–521. doi: 10.1016/j.jpowsour.2017.12.043

Wang, Y., Yang, S., You, Y., Feng, Z., Wen, Z., Gariepy, V., et al. (2018b). A high-capacity and long cycle life aqueous rechargeable lithium-ion battery with $FePO_4$ anode. *ACS Appl. Mater. Interfaces* 10, 7061–7068. doi: 10.1021/acsami.7b18058

Wang, Z., Selbach, S. M., and Grande, T. (2013). Van der Waals density functional study of the energetics of alkali metal intercalation in graphite. *RSC Adv.* 4, 4069–4079. doi: 10.1039/C3RA47187J

Wen, Y., He, K., Zhu, Y., Han, F., Xu, Y., Matsuda, I., et al. (2015). Expanded graphite as superior anode for sodium-ion batteries. *Nat. Commun.* 5:4033. doi: 10.1038/ncomms5033

Wu, L., Buchholz, D., Vaalma, C., Giffin, G. A., and Passerini, S. J. C. (2016). Apple biowaste-derived hard carbon as powerful anode material for Na-ion batteries. *ChemElectroChem* 3, 292–298. doi: 10.1002/celc.201500437

Wu, X., Leonard, D. P., and Ji, X. (2017). Emerging non-aqueous potassium-ion batteries: challenges and opportunities. *Chem. Mat.* 29, 5031–5042. doi: 10.1021/acs.chemmater.7b01764

Xie, Y., Chen, Y., Liu, L., Tao, P., Fan, M., Xu, N., et al. (2017). Ultra-high pyridinic N-doped porous carbon monolith enabling high-capacity K-ion battery anodes for both half-cell and full-cell applications. *Adv. Mater.* 29:1702268. doi: 10.1002/adma.201702268

Xing, Z., Qi, Y., Jian, Z., and Ji, X. (2017). Polynanocrystalline graphite: a new carbon anode with superior cycling performance for K-ion batteries. *ACS Appl. Mater. Interfaces* 9, 4343–4351. doi: 10.1021/acsami.6b06767

Xu, Y., Zhang, C., Zhou, M., Fu, Q., Zhao, C., Wu, M., et al. (2018). Highly nitrogen doped carbon nanofibers with superior rate capability and cyclability for potassium ion batteries. *Nat. Commun.* 9:1720. doi: 10.1038/s41467-018-04190-z

Xu, Z., Liu, J., Chen, C., Potapenko, H., and Wu, M. (2019a). Hydrophilic binder interface interactions inducing inadhesion and capacity collapse in sodium-ion battery. *J. Power Sources* 427, 62–69. doi: 10.1016/j.jpowsour.2019.04.063

Xu, Z., Wu, M., Chen, Z., Chen, C., Yang, J., Feng, T., et al. (2019b). Direct structure–performance comparison of all-carbon potassium and sodium ion capacitors. *Adv. Sci.* 6:1802272. doi: 10.1002/advs.201970075

Yang, J., Ju, Z., Jiang, Y., Xing, Z., Xi, B., Feng, J., et al. (2018). Enhanced capacity and rate capability of nitrogen/oxygen dual-doped hard carbon in capacitive potassium-ion storage. *Adv. Mater.* 30:1700104. doi: 10.1002/adma.201700104

Zheng, Y., Wang, Y., Lu, Y., Hu, Y.-S., and Li, J. (2017). A high-performance sodium-ion battery enhanced by macadamia shell derived hard carbon anode. *Nano Energy* 39, 489–498. doi: 10.1016/j.nanoen.2017.07.018

Zou, X., Xiong, P., Zhao, J., Hu, J., Liu, Z., and Xu, Y. (2017). Recent research progress in non-aqueous potassium-ion batteries. *Phys. Chem. Chem. Phys.* 19, 26495–26506. doi: 10.1039/C7CP03852F

Conflict of Interest: The authors declare that the research was conducted in the absence of any commercial or financial relationships that could be construed as a potential conflict of interest.

frontiers in Chemistry

ORIGINAL RESEARCH
published: 09 October 2019
doi: 10.3389/fchem.2019.00664

N-Propyl-N-Methylpyrrolidinium Difluoro(oxalato)borate as a Novel Electrolyte for High-Voltage Supercapacitor

*Weili Zhang, Fuming Zhang, Peng Zhang, Shuo Liang and Zhiqiang Shi**

Tianjin Key Laboratory of Advanced Fibers and Energy Storage, College of Materials Science and Engineering, Tianjin Polytechnic University, Tianjin, China

Development of high voltage electrolyte is one of the effective ways to improve the performance of supercapacitor. The new ionic liquid N-propyl-N-methylpyrrolidinium difluoro(oxalato)borate (Py_{13}DFOB) was designed and mixed with propylene carbonate (PC) as electrolyte for supercapacitor. The operating voltage of the new electrolyte system has been proven to be up to 3.0 V by a series of electrochemical techniques. Surprisingly, the new salt exhibits nearly symmetric capacitance contribution in the positive and negative electrodes, leading to a high capacitance value of 130 F g^{-1}. The energy and power density of EDLCs using Py_{13}DFOB in the PC electrolyte reach 39.06 Wh kg^{-1} (100 mA g^{-1}) and 8.03 kW kg^{-1} (5,000 mA g^{-1}), respectively, at the working voltage of 3.0 V, significantly exceeding the performance of commercial electrolyte tetraethylammonium tetrafluoroborate ($TEABF_4$). The results indicate that Py_{13}DFOB can be a promising electrolyte salt for supercapacitor.

Keywords: N-propyl-N-methylpyrrolidinium difluoro(oxalato)borate, supercapacitors, ionic liquid, electrolyte, high voltage

OPEN ACCESS

Edited by:
Yuanlong Shao,
King Abdullah University of Science and Technology, Saudi Arabia

Reviewed by:
Xingbin Yan,
Lanzhou Institute of Chemical Physics (CAS), China
Jun Jin,
Shanghai Institute of Ceramics (CAS), China

****Correspondence:***
Zhiqiang Shi
shizhiqiang@tjpu.edu.cn

Specialty section:
This article was submitted to Electrochemistry, a section of the journal Frontiers in Chemistry

Received: *12 July 2019*
Accepted: *18 September 2019*
Published: *09 October 2019*

Citation:
Zhang W, Zhang F, Zhang P, Liang S and Shi Z (2019) N-Propyl-N-Methylpyrrolidinium Difluoro(oxalato)borate as a Novel Electrolyte for High-Voltage Supercapacitor. Front. Chem. 7:664. doi: 10.3389/fchem.2019.00664

INTRODUCTION

Supercapacitors (SCs), a kind of electrochemical energy storage device with high power density, long cycle life, and excellent reliability, has been widely used in many fields such as hybrid electric vehicle and high-power output equipment. However, the low energy density is the main factor hindering their further applications (Wang et al., 2012; Simon et al., 2014). It can be obtained from the calculation formula of energy density that expanding the voltage window of the cell is the most effective way for achieving high energy supercapacitor (Li et al., 2007; Snook et al., 2011; Boukhalfa et al., 2012; Díaz et al., 2012; Kato et al., 2012; Okashy et al., 2013; Xiang et al., 2013; Borenstein et al., 2014, 2015; Choi et al., 2014; Kumar et al., 2016). As a matter of fact, the working voltage V depends to a great extent on the stability of the electrolyte. Unfortunately, tetraethylammonium tetrafluoroborate ($TEABF_4$) as the state-of-the-art electrolyte material can only withstand a working voltage of 2.5–2.7 V, which is usually limited by the oxidation and reduction stability of electrolyte ions.

Recently, Ionic liquids (ILs) have been intensively studied and viewed as potentially ideal electrolytes for increasing the operating voltage of EDLCs due to their relatively wide electrochemical stability (Ue et al., 2003; Zhu et al., 2007; Kim et al., 2014). In addition, ILs are

attracted to supercapacitors owing to several other excellent properties in terms of non-volatile, non-flammable, and high thermal stability. However, most ILs are trapped in their low ionic conductivity and high viscosity compared to aqueous electrolytes and even organic electrolytes. Considering this situation, mixing ILs with organic solvents is a promising alternative strategy to enlarge the working voltage without sacrificing the power density and cycle life of the EDLCs (Guerfi et al., 2010; Kühnel et al., 2011). The introduction of organic solvent not only reduces the viscosity and increases the conductivity of the pure ionic liquid, but also maintains a large electrochemical stability window, which greatly improves the capacitive performance of the device.

The most conventional families of ionic liquids, which have been evaluated as the most prospective electrolytes for supercapacitors, are based on pyrrolidinium and imidazolium cations (Mousavi et al., 2016; Watanabe et al., 2017). In general, pyrrolidinium based ILs could deliver noticeably enhanced electrochemical stability than the ones based on imidazolium owing to its superior ability to resist oxidation and reduction, which are suitable for realizing novel symmetric supercapacitor with high working voltage (Lin et al., 2011; Brandt et al., 2013; Zhang et al., 2016; Martins et al., 2018). Moreover, the mixing of the ionic liquid with the organic solvent can substantially ignore the high viscosity of the pyrrolidinium-based ionic liquid. The choice of anions also has a great effect on the properties of the ionic liquid. Difluoro(oxalate)borate (DFOB) have received particular interest in recent years due to its high asymmetry compared to conventional anions, resulting in higher solubility of electrolyte salt in ester solvents. Also, the electron-withdrawing fluorine atom on DFOB leads to more delocalization charges, causing lower affinity of binding cation and higher conductivity of electrolyte salt. More importantly, DFOB possesses high electrochemical stability and non-corrosive to aluminum current collector, rendering it an ideal choice for high-voltage electrolytes (Lai et al., 2011; Allen et al., 2013; Tian et al., 2014; Wu et al., 2015). In this manuscript, we designed a new ionic liquid Py_{13}DFOB mixed with an organic solvent PC as electrolyte for supercapacitor. The physicochemical properties (conductivity, melting point, thermal stability, etc.) of the new electrolyte salt were characterized for the first time. Afterwards, we evaluated the performance of supercapacitors containing Py_{13}DFOB/PC electrolyte from the aspects of withstand voltage, cycle stability, energy density, power density, etc.

EXPERIMENTAL

Materials

N-Methyl pyrrole (>99%), 1-Bromopropane (>98%), acetonitrile (>99.5%) were obtained from Aldrich and used without further purification. The PC solvent (battery grade, extra dry <20 ppm of water) and Lithium difluoro(oxalato)borate (>99%) were purchased from Jiangsu Guotai Super Power New Materials Co. Ltd. (China). The prepared electrolyte salt (Py_{13}DFOB) was placed in a glove box filled with high pure argon (<1 ppm O_2 and <1 ppm H_2O), then dissolved in the PC with 1 mol L^{-1} concentration, added 3Å molecular sieves to remove trace moisture for 1 week. The final water content is <20 ppm testing by Karl Fischer titration method (Mettler-Toledo C20, Switzerland). The impurities of halide and alkali metal ions were <2 ppm confirmed by Inductive Coupled Plasma Emission Spectrometer (ICP) test.

The activated carbon electrodes were prepared by mixing 82% activated carbon (Kuraray YP-50), 10% carbon black (VXC72) as the conductor, 4% carboxymethylcellulose sodium (CMC), and 4% styrene butadiene rubber (SBR) as the binder. The mixture was stirred to a sticky state followed by coating on aluminum foils. The electrodes were punched into disks with a diameter of 18 mm, then dried under vacuum at 120°C for more than 12 h prior to be used. The mass of each electrode is about 6 mg and the thickness is ∼60 um (including 20 um aluminum foil).

Electrolyte Synthesis/Purification

N-Methyl pyrrole (8.11 g, 0.1 mol) and Lithium difluoro(oxalato)borate (14.38 g, 0.1 mol) were dissolved in 100 mL acetonitrile. To this solution, 1-Bromopropane (12.99 g, 0.1 mol) was added dropwise for 12 h. The crude products were obtained by filtration and rotary evaporation of the reaction solution and then purified by extraction with ethyl acetate/deionized water. Finally, the target product of high purity clear liquid was obtained after decoloring by activated carbon. The resulting electrolyte salts are dried for 48 h at 80°C and stored in a sealed container in a glove box with high pure argon (<1 ppm O_2 and <1 ppm H_2O).

Characterization and Measurements

^{1}H-NMR and ^{13}C-NMR spectra were performed on a Bruker AVANCE 400M spectrometer. Thermal gravimetric analysis was tested by a Netzsch thermogravimetric analyzer at a heating rate of 5°C min^{-1} from 20 to 600°C under nitrogen conditions. Differential scanning calorimetry (DSC) analysis was performed on a TA Instruments Q2000 differential scanning calorimeter at a heating rate of 10°C min^{-1} under nitrogen atmosphere. The relationship between conductivity and concentration of Py_{13}DFOB/PC was determined by using a conductivity meter (Mettler-Toledo S30, Switzerland). The viscosity of the electrolyte is tested by a viscosity testing device (A&D SV-10, Japan). Activated Carbon/Activated carbon symmetrical coin cells were prepared in an argon-filled glove box for electrochemical measurements of electrolytes. The galvanostatic charge/discharge tests (GCD) and cycling performance were tested at Arbin battery test system. Cyclic voltammetry (CV) was tested in the same range by Autolab electrochemical workstation (PGSTAT302N, Switzerland). The gravity specific capacitance of single electrode was obtained from equation $C_m = 2I\Delta t/m\Delta V$, in which I is the current value, Δt is the discharge time, ΔV is the potential difference between the end of the voltage drop and the end of the discharge, and m is the mass of the active material of single electrode. The energy density is calculated from the formula $E = 1/2C\Delta V^2$, where C is the specific discharge capacitance. The power density was calculated by the equation $P = I\Delta V/2m$.

RESULTS AND DISCUSSIONS

Chemical Structure and Physical Properties Characterization of Synthesized Sample

^{1}H NMR and ^{13}C NMR analysis were used to verify the purity of our synthesized sample. The results are as follows: ^{1}H NMR (D_2O) δ: 3.42∼3.34 (m,4H), 3.17∼3.13 (m,2H), 2.90 (s,3H), 2.12∼2.06 (m,4H), 1.74∼1.64 (m,2H), 0.87∼0.83 (t,3H), ^{13}C-NMR (D_2O): δ = 9.99, 16.75, 21.24, 47.97, 64.17, 65.71, 163.76 ppm, which confirm that Py_{13}-DFOB is synthesized successfully. The original NMR spectrum is shown in **Figure S1**.

The chemical structure and ionic size of the synthesized Py_{13}DFOB are shown in **Figure 1** and several basic physical properties (conductivity, viscosity, thermal stability, etc.) of the new electrolyte were summarized in **Table 1**. The phase transformation behavior of Py_{13}DFOB investigated by DSC is illustrated in **Figure 2A**. Py_{13}DFOB shows a low melting point value of 3.21°C, which is due to the unfavorable packing of ions and the decrease of lattice energy of IL materials caused by the highly spatial asymmetry of Py_{13}^{+} and the large Vander Waals volume of $DFOB^{-}$. TG analysis is used to observe the thermal stability of electrolytes. As can be seen in **Figure 2B**, Py_{13}DFOB is subjected to two-step degradation, where the initial degradation temperature of 290°C is considered to meet the thermal stability requirements of supercapacitors. The result is similar with the decomposition curve of the LiDFOB mentioned in the previous study (Allen et al., 2011).

Obviously, **Table 1** shows that the pure ionic liquid exhibits lower conductivity and higher viscosity than the organic electrolyte. Therefore, the mobility of the ions is enhanced by the addition of the organic solvent PC, thereby making it easier for the electrolyte to access the pores of the activated carbon. As shown in **Figure 3**, the maximum conductivity of Py_{13}DFOB/PC was observed to reach 14.5 mS cm^{-1} at 2.0 mol L^{-1}, and the conductivity drops sharply as the concentration exceeds or <2.0 mol L^{-1}. Besides, the addition of the solvent significantly reduces the viscosity of the pure ionic liquid, taking a 1 mol L^{-1} Py_{13}DFOB/PC as an example, the viscosity value of which is only 3.8% of the pure ionic liquid. It should be emphasized that 1 mol L^{-1} Py_{13}DFOB/PC was selected as the most preferred one to be applied later in the study based on the data in supporting documentation. Therefore, the electrochemical performance of the electrolyte applied to supercapacitors is not only determined by the conductivity, but viscosity is also a factor that cannot be ignored.

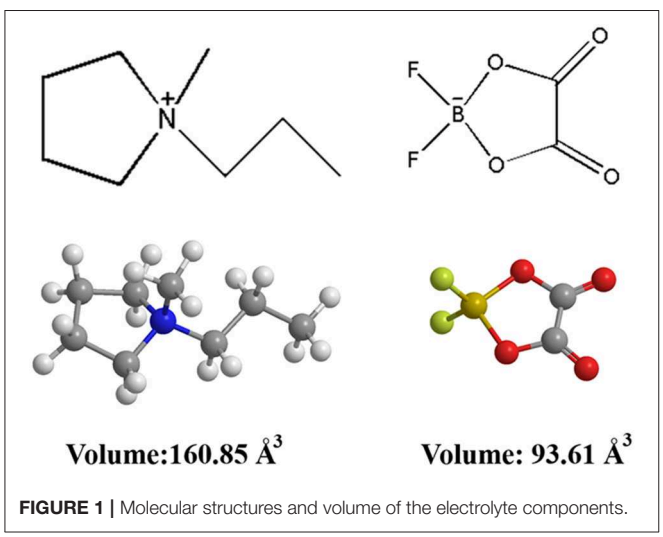

FIGURE 1 | Molecular structures and volume of the electrolyte components.

TABLE 1 | Physical characteristics of Py_{13}DFOB.

Electrolyte	Molecular weight (g/mol)	Viscosity (mPas)	Conductivity (mS cm^{-1})	Melting point (°C)	thermal-decomposition temperature (°C)
Py_{13}DFOB	263.81	105	2.2	3.21	306

Potential Window Opening: Stability of the Electrolytes

Compared with $TEABF_4$/PC, the supercapacitor using 1 mol L^{-1} Py_{13}DFOB/PC displayed higher energy density and power density under conventional working voltage (2.7 V) while maintaining excellent rate performance and long cycle stability (**Figure S3**). Further, the high voltage characteristics of the new

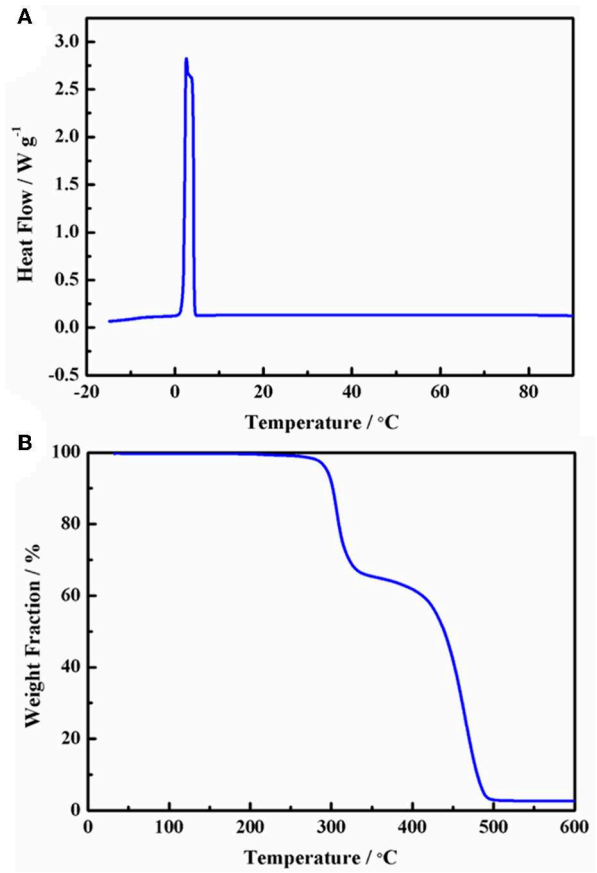

FIGURE 2 | DSC **(A)** and TGA **(B)** heating traces (5°C min^{-1}) of the Py_{13}DFOB.

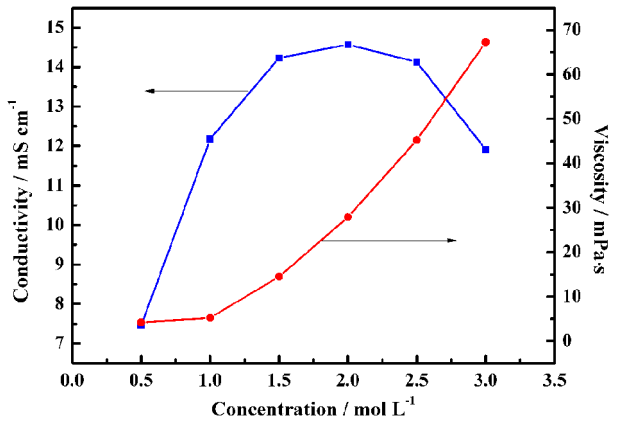

FIGURE 3 | Relationship between conductivity (viscosity) and concentration of Py_{13}DFOB/PC at 20°C.

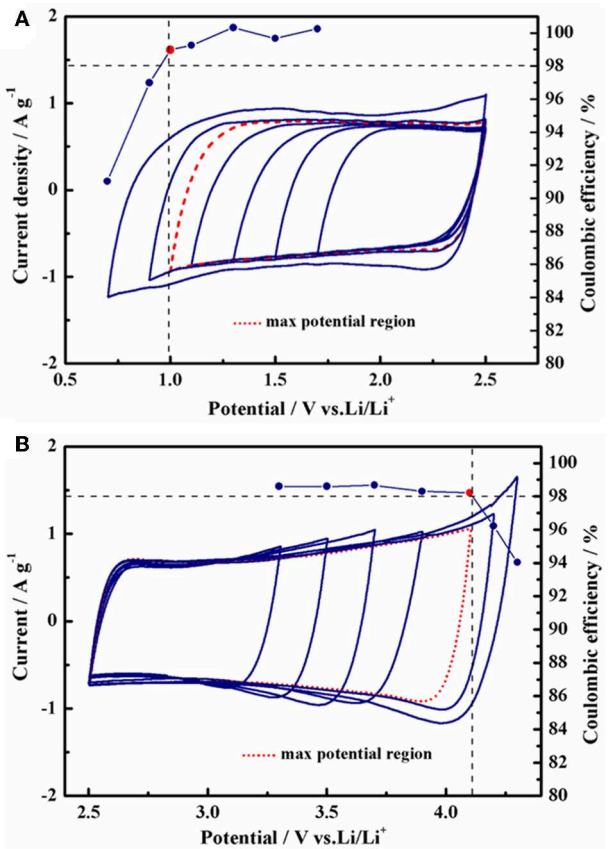

FIGURE 4 | Operating potential determination using cyclic voltammetry. Coulombic efficiency (right axis) of cells used in the determination of anodic/cathodic limits. **(A)** Negative, **(B)** positive scans in different windows of the half-cell using 1 mol L^{-1} Py_{13}DFOB/PC.

electrolyte system need to be clarified. Since the electrochemical window cannot directly reflect the working voltage of the full cell due to the difference in the structure of anions and cations, it is necessary to identify the real positive and negative stability limits of the new electrolyte in activated carbon electrodes (Fic et al., 2012). For this purpose, we initially evaluated the maximum operating voltage possible of 1 mol L^{-1} Py_{13}DFOB/PC via cyclic voltammetry investigations on three electrode cells with an AC-based working electrode, a largely oversized AC-based counter electrode with the same composition and a Li wire reference electrode. An efficiency threshold value of 98% was chosen, and further efficiency declines were considered to be a series of irreversible reactions involving electrolytes in the cell system. The obtained single cell electrochemical window limits are presented in **Figure 4**. With this condition, the positive and negative potential limits occur at +1.6 V vs. Li and −1.5 V vs. Li, respectively, resulting in a maximum operating voltage of 3.1 V.

We further measured the GCD curve of a symmetric full-cell at an operation voltage of 3.0 V while monitoring the capacitive behavior of positive and negative electrodes. It can be seen from **Figure 5** that the GCD curves exhibits superior capacitive behavior, and the nearly symmetric potential window of positive and negative electrodes shows that the capacitance contributions of $DFOB^-$ anion and Py_{13}^+ cation are almost the same. More importantly, the cutoff potential of the positive and negative electrodes vs. Li is within the safe potential range when the operating voltage of the full cell reaches 3.0 V.

In previous studies, mass balancing is currently the preferred method to make full use of the maximum working voltage of electrolyte, but it will have a negative impact on the specific capacitance of the full cell due to the extra increase in the mass of one of the electrodes (Weingarth et al., 2013; Van Aken et al., 2015; Hu et al., 2016). Besides, due to the change of ion transfer channel and electronic response time of high-quality electrode, resulting in inconsistent polarity of the two electrodes, thus affecting the cycle life of the cell. Excitingly, the Py_{13}DFOB/PC can almost fully exploit its maximum working potential window without requiring additional mass balance, eliminating the time consumption and technical problems of electrode matching, and harvesting higher energy density.

Electrochemical Study in EDLCs Configuration

To evaluate the withstand voltage of EDLCs configuration, the GCD curves of EDLCs based on 1 mol L^{-1} Py_{13}DFOB/PC operating at 500 mA g^{-1} under several applied voltages are shown in **Figure 6A**. The GCD curves maintain a typical triangular shape, and the variation of potential with time shows an approximate linear relationship as the voltage rising to 3.0 V, which demonstrates excellent electrochemical reversibility and stability of EDLCs. However, the charging curve shifts rather than overlaps, and the linearity and symmetry of the GCD curves gradually deteriorated when the voltage exceeds 3.0 V, indicating detrimental processes may be occurring between electrodes and electrolytes. We obtained the same result from the relationship between specific capacitance (**Figure 6B**), IR drop (**Figure 6C**) with voltage obtained from the GCD test in **Figure 6A**, that is, the abrupt change of the curve all occurs when the voltage

exceeds 3.0 V. The IR drop is closely related to the equivalent series resistance of the cell, reflecting the state of the working environment inside the EDLCs. When the voltage is raised from 3.0 to 3.5 V, the IR drop abruptly increases from 0.074 to 0.152 V, indicating some irreversible changes in the internal environment of the cell. The rate behavior under different voltages (2.7, 3.0, 3.2, 3.5 V) was given by the GCD test with a current density ranging from 100 to 10,000 mA g^{-1}. As shown in **Figure 6D**, the discharge capacitance of the cell decreases with increasing current density due to the rise in internal resistance (IR drop) caused by the kinetic limitation at the electrolyte/electrode interface. However, the cell with Py_{13}DFOB/PC still shows the most superior capacitance performance and rate performance at the working voltage of 3.0 V. In general, it is proved that the new electrolyte system can work stably at 3.0 V by electrochemical evaluation of single electrode and assembled supercapacitor.

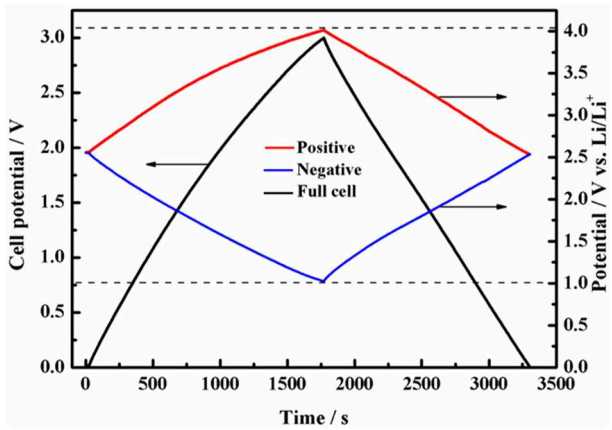

FIGURE 5 | Potential profiles of the positive and negative electrodes during galvanostatic charge/discharge of symmetric supercapacitor with 1 mol L^{-1} Py_{13}DFOB/PC.

Next, we evaluated the electrochemical performance of EDLCs containing Py_{13}DFOB/PC at 3.0 V operating voltage. **Figure 7A** showed the CV curves of the cell at different scan rates. The rectangular shape of the CV curves is deteriorated with the increase of the scan rate, but a good rectangular shape is still maintained at the high scan rate, demonstrating the outstanding transfer characteristic of the electrolyte ion. Similarly, GCD curves (**Figure 7B**) exhibit good linearity, symmetry, and negligible instantaneous

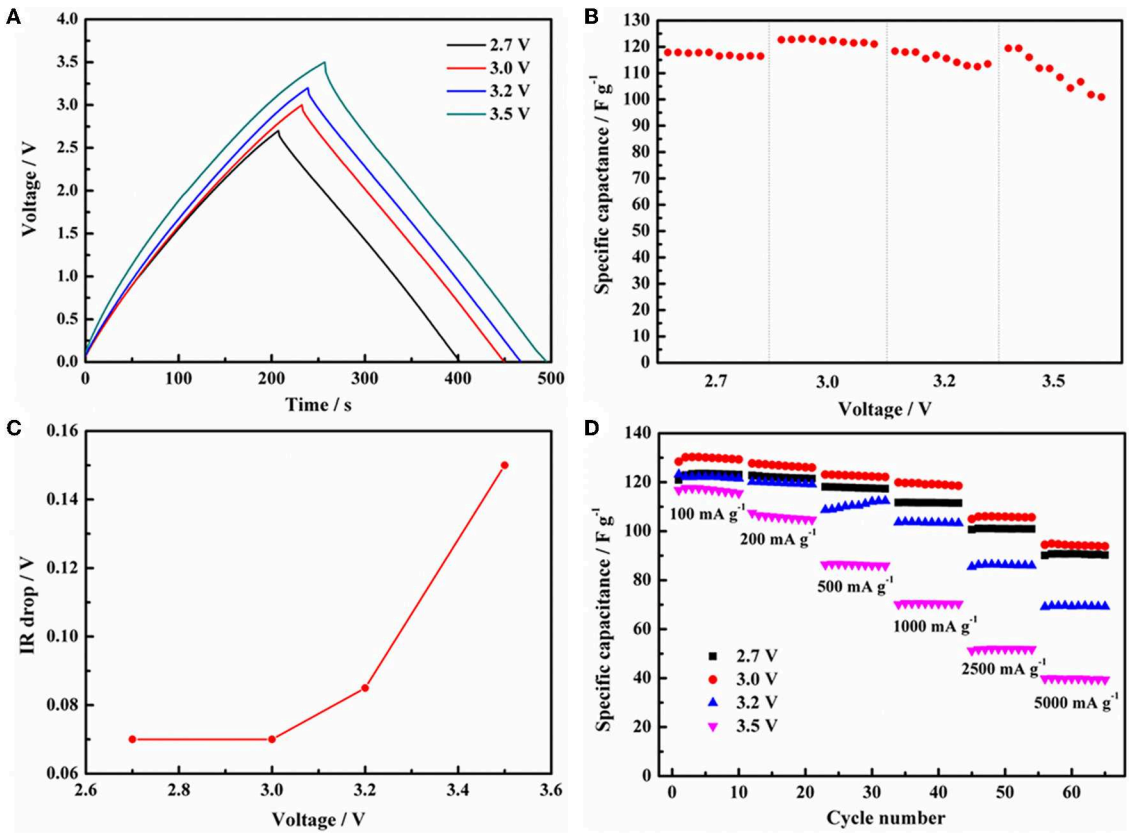

FIGURE 6 | (A) GCD curves of the EDLCs with 1 mol L^{-1} Py_{13}DFOB/PC at current density of 500 mA g^{-1} with different voltage ranges. **(B)** Specific capacitance and **(C)** IR drop vs. voltage obtained from **(A)** charge-discharge curves. **(D)** The charge/discharge rates performance of EDLCs with 1.0 mol L^{-1} Py_{13}DFOB/PC under different voltage ranges.

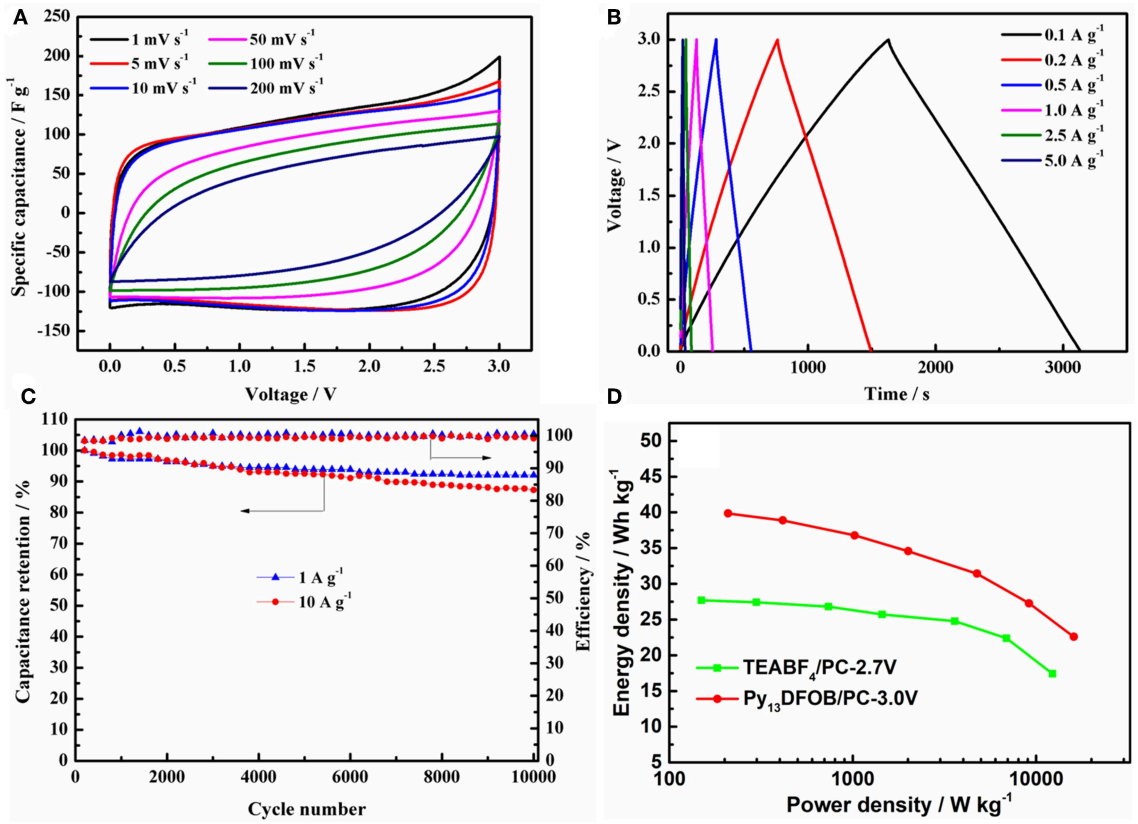

FIGURE 7 | (A) GCD curves at different current densities **(B)** CV curves at different scan rates **(C)** cycle performance at current density of 1 A g^{-1} and 10 A g^{-1} under 3.0 V of the EDLCs using 1.0 mol L^{-1} Py_{13}DFOB/PC. **(D)** Ragone plots of the EDLCs with two electrolytes.

voltage drop at different current densities, indicating superior double-layer characteristics. The specific capacitance obtained from the discharge time of the GCD curves can reach a high value of 130 F/g at a current density of 100 mA g^{-1} and still maintain 96 F g^{-1} at 5,000 mA g^{-1} under a working voltage of 3.0 V, which was about 78% of its initial capacitance.

With the aim to determine whether Py_{13}DFOB/PC can operate steadily for a long time under the working voltage of 3.0 V, the charge-discharge performance of 10,000 cycles were recorded at current density of 1 and 10 A g^{-1}. **Figure 7C** conveys a clear message that Py_{13}DFOB/PC presents excellent long cycle performance at different current densities, delivering capacity retention of 92% at 1 A g^{-1} and 87% at 10 A g^{-1} after 10,000 cycles with nearly 100% coulombic efficiency, confirming the long-term electrochemical stability of Py_{13}DFOB /PC at high working voltage.

Ragone plots (energy density vs. power density) has been widely used to evaluate the overall performance of a supercapacitor device. From the results summarized in **Figure 7D**, Py_{13}DFOB/PC obtained a considerably higher energy density and power density than $TEABF_4$/PC at each current density due to the simultaneous increase in voltage and specific capacitance. It should be noted that the maximum energy density and power density of the supercapacitor based on Py_{13}DFOB /PC can reach 39.06 Wh kg^{-1} (100 mA g^{-1}) and 8.03 kW kg^{-1} (5,000 mA g^{-1}), respectively, when the voltage goes up to 3.0 V.

CONCLUSION

In this work, we successfully synthesized a novel ionic liquid Py_{13}DFOB as electrolyte salt for supercapacitor. The 1 mol L^{-1} solution formed by the mixture of Py_{13}-DFOB and PC shows the closely transport properties as the commercial electrolyte ($TEABF_4$/PC), which solves the problems of high viscosity and low conductivity of pure ionic liquids. More importantly, it is proved that Py_{13}DFOB/PC can exhibit outstanding capacitance behavior at high operating voltage of 3 V confirmed by several electrochemical testing techniques. Moreover, we found that the nearly symmetric capacity contributions of positive and negative electrodes convey a high specific capacitance value of 130 F g^{-1}. The energy density and power density of supercapacitor with Py_{13}DFOB can reach 39.06 Wh kg^{-1} (100 mA g^{-1}) and 8.03 kW kg^{-1} (5,000 mA g^{-1}), respectively. Based on these results, the new electrolyte

system is considered to be a promising electrolyte for high-voltage supercapacitor.

DATA AVAILABILITY STATEMENT

All datasets generated for this study are included in the manuscript/**Supplementary Files**.

AUTHOR CONTRIBUTIONS

All authors listed have made a substantial, direct and intellectual contribution to the work, and approved it for publication.

FUNDING

This work was supported by the National Science Foundation of China (51603147), Tianjin application foundation and advanced technology research plan project (15ZCZDGX00270, 14RCHZGX00859).

SUPPLEMENTARY MATERIAL

The Supplementary Material for this article can be found online at: https://www.frontiersin.org/articles/10.3389/fchem.2019.00664/full#supplementary-material

REFERENCES

Allen, J. L., Han, S.-D., Boyle, P. D., and Henderson, W. A. (2011). Crystal structure and physical properties of lithium difluoro(oxalato)borate (LiDFOB or LiBF2Ox). *J. Power Sources* 196, 9737–9742. doi: 10.1016/j.jpowsour.2011.07.065

Allen, J. L., McOwen, D. W., Delp, S. A., Fox, E. T., Dickmann, J. S., Han, S. D., et al. (2013). N-Alkyl-N-methylpyrrolidinium difluoro(oxalato)borate ionic liquids: physical/ electrochemical properties and Al corrosion. *J. Power Sources* 237, 104–111. doi: 10.1016/j.jpowsour.2013.02.086

Borenstein, A., Fleker, O., Luski, S., Benisvy, L., and Aurbach, D. (2014). Metal–organic complexes as redox candidates for carbon based pseudo-capacitors. *J. Mater. Chem. A* 2, 18132–18138. doi: 10.1039/C4TA04378B

Borenstein, A., Hershkovitz, S., Oz, A., Luski, S., Tsur, Y., and Aurbach, D. (2015). Use of 1,10-phenanthroline as an additive for high-performance supercapacitors. *J. Phys. Chem. C* 119, 12165–12173. doi: 10.1021/acs.jpcc.5b02335

Boukhalfa, S., Evanoff, K., and Yushin, G. (2012). Atomic layer deposition of vanadium oxide on carbon nanotubes for high-power supercapacitor electrodes. *Energy Environ. Sci.* 5, 6872–6879. doi: 10.1039/c2ee21110f

Brandt, A., Pohlmann, S., Varzi, A., Balducci, A., and Passerini, S. (2013). Ionic liquids in supercapacitors. *MRS Bull.* 38, 554–559. doi: 10.1557/mrs.2013.151

Choi, K. M., Jeong, H. M., Park, J. H., Zhang, Y., and Kang, J. K. (2014). Supercapacitors of nanocrystalline metal–organic frameworks. *ACS Nano* 8, 7451–7457. doi: 10.1021/nn5027092

Díaz, R., Orcajo, M. G., Botas, J. A., Calleja, G., and Palma, J. (2012). Co8-MOF-5 as electrode for supercapacitors. *Mater. Lett.* 68, 126–128. doi: 10.1016/j.matlet.2011.10.046

Fic, K., Lota, G., Meller, M., and Frackowiak, E. (2012). Novel insight into neutral medium as electrolyte for high-voltage supercapacitors. *Energy Environ. Sci.* 5, 5842–5850. doi: 10.1039/C1EE02262H

Guerfi, A., Dontigny, M., Charest, P., Petitclerc, M., Lagacé, M., Vijh, A., et al. (2010). Improved electrolytes for li-ion batteries: mixtures of ionic liquid and organic electrolyte with enhanced safety and electrochemical performance. *J. Power Sources* 195, 845–852. doi: 10.1016/j.jpowsour.2009.08.056

Hu, L. T., Guo, D. Q., Feng, G., Li, H. Q., and Zhai, T. Y. (2016). Asymmetric behavior of positive and negative electrodes in carbon/carbon supercapacitors and its underlying mechanism. *J. Phys. Chem. C* 120, 24675–24681. doi: 10.1021/acs.jpcc.6b09898

Kato, F., Kikuchi, A., Okuyama, T., Oyaizu, K., and Nishide, H. (2012). Nitroxide radicals as highly reactive redox mediators in dye-sensitized solar cells. *Angew. Chem. Int. Ed. Engl.* 51, 10177–10180. doi: 10.1002/anie.201205036

Kim, J. K., Ahn, J. H., and Jacobsson, P. (2014). Influence of temperature on ionic liquid-based gel polymer electrolyte prepared by electrospun fibrous membrane. *Electrochim. Acta* 116, 321–325. doi: 10.1016/j.electacta.2013.11.061

Kühnel, R. S., Böckenfeld, N., Passerini, S., Winter, M., and Balducci, A. (2011). Mixtures of ionic liquid and organic carbonate as electrolyte with improved safety and performance for rechargeable lithium batteries. *Electrochim. Acta* 56, 4092–4099. doi: 10.1016/j.electacta.2011.01.116

Kumar, V., Borenstein, A., Markovsky, B., Aurbach, D., Gedanken, A., and Porat, Z. (2016). Activated carbon modified with carbon nanodots as novel electrode material for supercapacitors. *J. Phys. Chem. C* 120, 13406–13413. doi: 10.1021/acs.jpcc.6b04045

Lai, Y. Q., Chen, X. J., Zhang, Z. A., Li, Z., and Liu, Y. X. (2011). Tetraethylammonium difluoro(oxalato)borate as electrolyte salt for electrochemical double-layer capacitors. *Electrochim. Acta* 56, 6426–6430. doi: 10.1016/j.electacta.2011.04.136

Li, W. R., Chen, D. H., Li, Z., Shi, Y. F., Wan, Y., Wang, G., et al. (2007). Nitrogen-containing carbon spheres with very large uniform mesopores: the superior electrode materials for EDLC in organic electrolyte. *Carbon* 45, 1757–1763. doi: 10.1016/j.carbon.2007.05.004

Lin, R. Y., Taberna, P. L., Fantini, S., Presser, V., Pérez, C. R., Malbosc, F., et al. (2011). Capacitive energy storage from−50 to 100°C using an ionic liquid electrolyte. *J. Phys. Chem. Lett.* 2, 2396–2401. doi: 10.1021/jz201065t

Martins, V. L., Rennie, A. J. R., Sanchez-Ramirez, N., Torresi, R. M., and Hall, P. J. (2018). Improved performance of ionic liquid supercapacitors by using tetracyanoborate anions. *ChemElectroChem* 5, 598–604. doi: 10.1002/celc.201701164

Mousavi, M. P. S., Wilson, B. E., Sadra, K., Anderson, E. L., He, S. Y., Bühlmann, P., et al. (2016). Ionic liquids as electrolytes for electrochemical double-layer capacitors: structures that optimize specific energy Interfaces. *ACS Appl. Mater.* 8, 3396–3406. doi: 10.1021/acsami.5b11353

Okashy, S., Noked, M., Zimrin, T., and Aurbach, D. (2013). The study of activated Carbon/CNT/MoO3 electrodes for aqueous pseudo-capacitors. *J. Electrochem. Soc.* 160, 1282–1285. doi: 10.1149/2.084309jes

Simon, P., Gogotsi, Y., and Dunn, B. (2014). Where do batteries end and supercapacitors begin? *Science* 343, 1210–1211. doi: 10.1126/science.1249625

Snook, G. A., Kao, P., and Best, A. S. (2011). Conducting-polymer-based supercapacitor devices and electrodes. *J. Power Sources* 196, 1–12. doi: 10.1016/j.jpowsour.2010.06.084

Tian, S. F., Qi, L., Yoshio, M., and Wang, H. Y. (2014). Tetramethylammonium difluoro(oxalato)borate dissolved in ethylene/propylene carbonates as electrolytes for electrochemical capacitors. *J. Power Sources* 256, 404–409. doi: 10.1016/j.jpowsour.2014.01.101

Ue, M., Takeda, M., Toriumi, A., Kominato, A., Hagiwara, R., and Ito, Y. (2003). Application of low-viscosity ionic liquid to the electrolyte of double-layer capacitors. *J. Electrochem. Soc.* 150, A499–A502. doi: 10.1149/1.1559069

Van Aken, K. L., Beidaghi, M., and Gogotsi, Y. (2015). Formulation of ionic-liquid electrolyte to expand the voltage window of supercapacitors. *Angew. Chem. Int. Ed.* 54, 4806–4809. doi: 10.1002/anie.201412257

Wang, G. P., Zhang, L., and Zhang, J. J. (2012). A review of electrode materials for electrochemical supercapacitors. *Chem. Soc. Rev.* 41, 797–828. doi: 10.1039/C1CS15060J

Watanabe, M., Thomas, M. L., Zhang, S. G., Ueno, K., Yasuda, T., and Dokko, K. (2017). Application of ionic liquids to energy storage and conversion materials and devices. *Chem. Rev.* 117, 7190–7239. doi: 10.1021/acs.chemrev.6b00504

Weingarth, D., Noh, H., Foelske-Schmitz, A., Wokaun, A., and Kötz, R. (2013). A reliable determination method of stability limits for electrochemical double layer capacitors. *Electrochim. Acta* 103, 119–124. doi: 10.1016/j.electacta.2013.04.057

Wu, F., Zhu, Q. Z., Chen, R. J., Chen, N., Chen, Y., and Li, L. (2015). Ionic liquid electrolytes with protective lithium difluoro(oxalate)borate for high voltage lithium-ion batteries. *Nano Energy* 13, 546–553. doi: 10.1016/j.nanoen.2015.03.042

Xiang, C. C., Li, M., Zhang, M. J., Manivannan, A., and Wu, N. Q. (2013). A reduced graphene oxide/Co3O4 composite for supercapacitor electrode. *J. Power Sources* 226, 65–70. doi: 10.1016/j.jpowsour.2012.10.064

Zhang, L., Tsay, K., Bock, C., and Zhang, J. J. (2016). Ionic liquids as electrolytes for non-aqueous solutions electrochemical supercapacitors in a temperature range of 20°C-80°C. *J. Power Sources* 324, 615–624. doi: 10.1016/j.jpowsour.2016.05.008

Zhu, Q., Song, Y., Zhu, X. F., and Wang, X. L. (2007). Ionic liquid-based electrolytes for capacitor applications. *J. Electroanal. Chem.* 601, 229–236. doi: 10.1016/j.jelechem.2006.11.016

Conflict of Interest: The authors declare that the research was conducted in the absence of any commercial or financial relationships that could be construed as a potential conflict of interest.

frontiers in Chemistry

ORIGINAL RESEARCH
published: 13 December 2019
doi: 10.3389/fchem.2019.00831

Hollow Co_3O_4@MnO_2 Cubic Derived From ZIF-67@Mn-ZIF as Electrode Materials for Supercapacitors

Jiani Xu[2], *Chaoting Xu*[2], *Yanhong Zhao*[2], *Jianghong Wu*[1,3]* *and Junqing Hu*[1]

[1] College of Health Science and Environmental Engineering, Shenzhen Technology University, Shenzhen, China, [2] State Key Laboratory for Modification of Chemical Fibers and Polymer Materials, College of Materials Science and Engineering, Donghua University, Shanghai, China, [3] College of Materials Science and Engineering, Changsha University of Science & Technology, Changsha, China

Hollow Co_3O_4@MnO_2 cubic nanomaterials are synthesized by ZIF-67@Mn-ZIF sacrificial precursor through a facile thermal treatment. As a kind of supercapacitor electrode material, it demonstrates high performances, such as specific capacitance of 413 F g^{-1} at the current density of 0.5 A g^{-1}; as the current densities raised from 0.5 to 10 A g^{-1} (20 times increasing), there is still ~41% retention of its initial capacitance. These satisfactory electrochemical properties should be put down to the hollow and porous structure and the relative higher BET surface area, which supplies more reactive sites for charge and discharge processes.

Keywords: metal-organic frameworks, ZIF-67, Mn-ZIF, Co_3O_4@MnO_2, supercapacitors

OPEN ACCESS

Edited by:
Min Zeng,
Lanzhou Institute of Chemical Physics (CAS), China

Reviewed by:
Shijie Li,
Zhejiang Ocean University, China
Hui Yang,
Jiangxi University of Science and Technology, China

***Correspondence:**
Jianghong Wu
wujianghong@sztu.edu.cn

Specialty section:
This article was submitted to Electrochemistry, a section of the journal Frontiers in Chemistry

Received: *27 October 2019*
Accepted: *14 November 2019*
Published: *13 December 2019*

Citation:
Xu J, Xu C, Zhao Y, Wu J and Hu J (2019) Hollow Co_3O_4@MnO_2 Cubic Derived From ZIF-67@Mn-ZIF as Electrode Materials for Supercapacitors. Front. Chem. 7:831. doi: 10.3389/fchem.2019.00831

INTRODUCTION

As a new and efficient energy storage device, supercapacitors qualified the benefits of high-power density, high security, long service life, and fast short time storage and release (El-Kady et al., 2016; Shao et al., 2018; Xu et al., 2018). As a result, supercapacitors attracted wide attention in the application on portable consumer electrical products and electric automobiles, and so on (Qu et al., 2016; Li et al., 2018). The performance of the used electrode materials is the main factor affecting the performance of supercapacitors. Currently, the most studied materials are carbon-based materials (Zhang and Zhao, 2009; Zhang et al., 2017), transition metal oxides (TMOs) (Liu et al., 2011; Li et al., 2014; Yu and Lou, 2018; Xu et al., 2019), and conductive polymer materials (Snook et al., 2011; Du et al., 2017). In recent years, metal-organic frameworks (MOFs) are developed as a new type of porous materials ascribed to their great specific surface area, porosity and regulatory pores, functional and special optical and electrical properties (Yue et al., 2015; Salunkhe et al., 2017). So they have great potential in the high-performance supercapacitor after thermal treatment as TMOs' sacrificial precursor.

Up to the present, numerous TMO nanomaterials have been synthesized as supercapacitor electrodes from many kinds of MOF precursors. For instance, high surface area Co_3O_4 nanoparticles have been obtained from the pyrolysis of ZIF-67 with an appreciable 190 F g^{-1} specific capacitance value at 5 A g^{-1} (Saraf et al., 2019), NiO architecture with porous structure was constructed by thermal treatment Ni-MOF under the air flow and demonstrated 324 F g^{-1} at 1 A g^{-1} (Han et al., 2017), and porous hollow α-Fe_2O_3 microboxes synthesized by using MOF as precursor and self-template can reach 380 F g^{-1} at 0.1 A g^{-1} as supercapacitor electrode

(Yu et al., 2019). Except for these single metal oxides, some mixed metal oxides, and metal oxide composites can also be obtained by MOF precursors. Chen and coworkers have fabricated porous small size $ZnCo_2O_4$ nanoparticles (<20 nm) from a mixed zinc and cobalt-MOF, which exhibited an unexpected specific capacitance of 451 F g^{-1} at 0.5 mV s^{-1} (Chen et al., 2015). Hierarchical NiO/ZnO double-shell hollow spheres are obtained by Li and coworkers through calcining the bimetallic organic frameworks, which delivered 497 F g^{-1} at current density of 1.3 A g^{-1} (Li et al., 2016). Xu and coworkers developed a Co_3O_4/ZnO nano-heterostructure *via* a solid-solid conversion process, the synthesized core-shell MOFs@MOFs were used as a template with cobalt and zinc as metal sources, which demonstrated 415 F g^{-1} specific capacitance value at 0.5 A g^{-1} (Xu et al., 2016). The mixed metal oxides and the metal oxide composites as electrodes exhibit superior electrochemical performance compared with single ones. Despite these achievements, there are still large spaces to explore other metal oxide composites based on MOF precursors.

Herein, we have prepared single ZIF-67 nanocrystals first, combined it with Mn-ZIF to form ZIF-67@Mn-ZIF composite, and finally obtained Co_3O_4@MnO_2 electrode material by thermal treatment. After evaluating the electrochemical performance of Co_3O_4@MnO_2 electrode, we found that it exhibited excellent electrochemical properties. When the current density is 0.5 A g^{-1}, the specific capacitance could achieve 413 F g^{-1}, with 20 times current density increasing, it kept 41% retention of initial capacitance and good long-term cycling stability, which is a very promising electrode for use in a supercapacitor.

EXPERIMENTAL

Preparation of ZIF-67

First, 1.455g $Co(NO_3)_2{\cdot}6H_2O$ and 1.642g 2-methylimidazole were separately dissolved in 40 ml methanol. Second, the two different solutions were mixed and vigorously stirred for 60 s and reacted for 24 h to complete reaction at room temperature after 24 h. Third, the purple precipitates in the bottom were collected by centrifugation with ethanol as washing solution for several times. The collected purple precipitates were dried at 80°C overnight in a vacuum drying chamber.

Preparation of ZIF-67@Mn-ZIF

First, 0.25 g $Mn(NO_3)_2{\cdot}6H_2O$ was dissolved in 50 ml ethanol. ZIF-67 obtained in the first step was well-dispersed in the above solution. Then, the mixture was transferred into a beaker flask after 20 min of continuous stirring, and the reaction temperature was 50°C and kept for 3 h in an oil bath.

Thermal Treatment of ZIF-67@Mn-ZIF Crystals

The obtained ZIF-67@Mn-ZIF crystals could be converted to Co_3O_4@MnO_2 nanomaterials through a thermal treatment in a tube furnace with air flow at 300°C for 0.5 h; the heating rate was controlled at 0.5°C·min^{-1}. As a contrast experiment, the single precursors (ZIF-67) were calcined under the same thermal conditions, and the final product is Co_3O_4 nanomaterial.

Material Characterizations

X-ray diffraction (XRD) patterns were measured by using monochromator Cu Kα radiation at a scanning rate of 2°•min^{-1} (PA-Nalytical X′Pert PRO). Binding energies were detected by the X-ray photoelectron spectroscopy (XPS; ESCALab250). The morphologies were obtained by scanning electron microscope (SEM) (Hitachi, SU-8000). The more detailed structures were investigated by transmission electron microscope (TEM) (JEOL, JEM-2100F), and the elements were detected by its equipped energy dispersive X-ray spectrometer (EDS). The BET surface area and pore size distribution are tested on Accelerated Surface Area & Porosimetry System (ASAP 2020, Micromeritics). XS analytical balance (Mettler Toledo; $\delta = 0.01$ mg) is used to weigh the mass of the electrode materials.

Electrochemical Characterizations

The electrochemical performances of the final products were accomplished by the AUTOLAB PGSTAT302N electrochemical workstation in a standard three-electrode test cell at ∼25°C with 1.0 M LiOH solution as electrolyte. The Ag/AgCl (3M KCl) electrode and platinum (Pt) plate (2.5 cm × 2.5 cm × 0.2 mm) directly served as the reference electrode and counter electrode, respectively. The fabricating processes of working electrode were as follows: Co_3O_4@MnO_2 materials (active electrode material, 80%) derived from ZIF-67@Mn-ZIF crystals were mixed with acetylene black (5%) and polyvinylidene difluoride (15%), which was mixed with appropriate volume N-methyl pyrrolidone solvent. The mixture was treated by ultrasonication to form a homogeneous slurry and dropped onto the graphite substrate current collector, the covered surface area is ∼1 × 1 cm^2, and then dried under vacuum condition at 120°C for 4 h to form the electrodes. For comparison, the Co_3O_4 materials prepared from single ZIF-67 crystals were also fabricated into electrode with the same processes.

The electrochemical performances of the fabricated electrodes were evaluated from the galvanostatic charge-discharge (GCD) and cyclic voltammetry (CV) measurements. The equation of $C = [(I \times \Delta t)/(m \times \Delta V)]$ is applied to calculate the specific capacitance values of Co_3O_4@MnO_2 and Co_3O_4 electrodes, where the I (A), Δt(s), ΔV (V), and m (g) represent the discharge current, the discharge time, the potential window, the mass of active materials in the electrodes, respectively.

RESULTS AND DISCUSSIONS

The synthesized products were analyzed by X-ray diffraction (XRD) first. The result is shown in **Figure 1a**. As can be seen from the obtained pattern, there are some strong diffraction peaks that appeared in $2\theta = 7.3°$, 10.4°, 12.8°, 14.8°, 16.5°, 18.1°, which can be confirmed with the sample ZIF-67 and highly consistent with reported literature (Qin et al., 2017). **Figures 1b,c** are the low to high magnification SEM images. The particles' morphology is uniform rhombic dodecahedral nanocrystals which were clearly

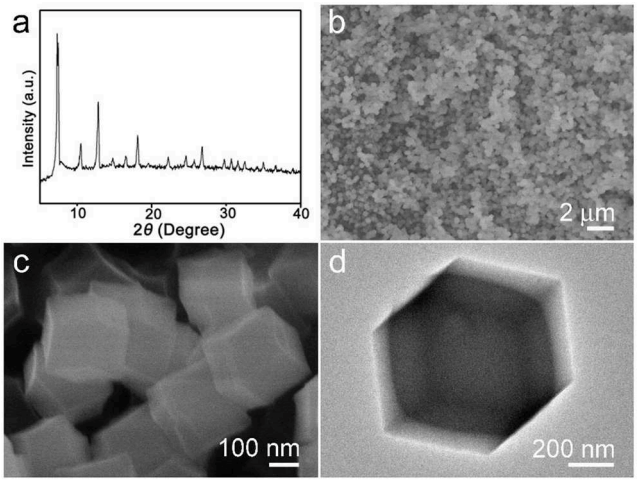

FIGURE 1 | (a) X-ray diffraction (XRD) pattern, **(b,c)** scanning electron microscope (SEM), and **(d)** transmission electron microscope (TEM) images of synthesized ZIF-67 sample.

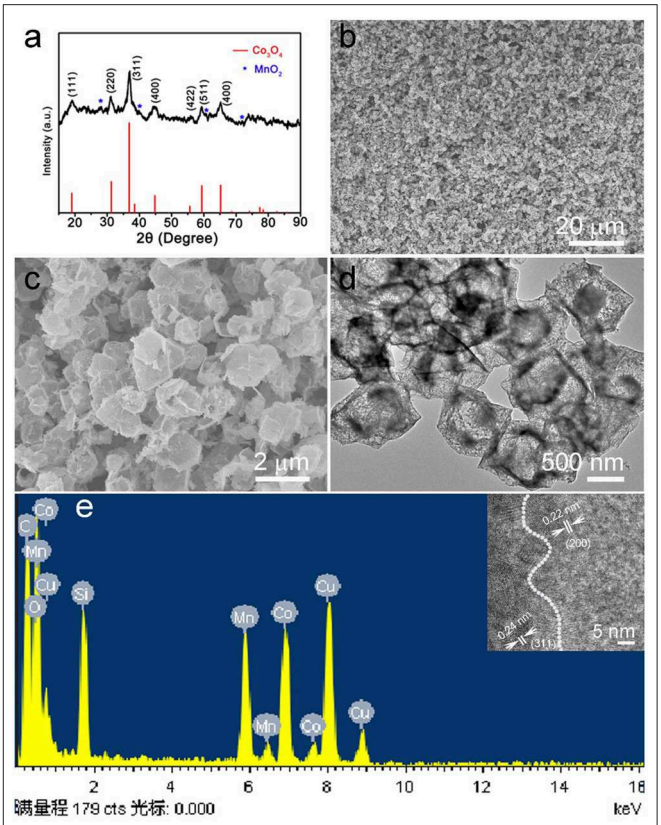

FIGURE 2 | (a) X-ray diffraction (XRD) pattern of the products after calcinating the ZIF-67@Mn-ZIF. **(b,c)** Low magnification and enlarged scanning electron microscope (SEM) images of the Co_3O_4@MnO_2. **(d)** Transmission electron microscope (TEM) image and corresponding **(e)** energy dispersive X-ray spectrometer (EDS) pattern of the Co_3O_4@MnO_2 products. Inset shows the HRTEM image of Co_3O_4@MnO_2.

monodispersed, with a diameter of about 300–500 nm. **Figure 1d** shows a single ZIF-67 nanocrystal with dodecahedron and solid construction. After thermal treatment, the structure collapsed (**Figure S1**).

The calcined ZIF-67@Mn-ZIF products were detected by XRD, and the result is shown in **Figure 2a**. The main diffraction peaks consisted of cubic phase Co_3O_4 (JCPDS card No. 074-2120), which is obtained by calcinating the ZIF-67 nanocrystal (**Figures S2, S3**). In addition, there are some other small peaks that also appeared in the pattern (marked with blue star), which could be MnO_2 formed by Mn-ZIF (the exact components were detected by XPS, which is detailed later). **Figure 2b** is a low-resolution SEM image of the obtained Co_3O_4@MnO_2 products, which indicated that the products can be synthesized in large scale. In the enlarged SEM image of **Figure 2c**, the diameter of obtained Co_3O_4@MnO_2 products increased to about 800 nm; interestingly, the obtained Co_3O_4@MnO_2 products are with hollow structure (**Figure 2d**), and the corresponding EDS result in **Figure 2e** is consistent with our designed concept. Co, Mn, and O elements are from Co_3O_4@MnO_2 products, the existence of Cu and C signals is because the TEM grid is made of Cu substrate and carbon membrane, while the peak of Si could be an impurity that brings in the sample preparation process. Inset shows the HRTEM image of the Co_3O_4@MnO_2, the *d-spacing* of 0.24 nm corresponding to the (311) lattice plane of the Co_3O_4 crystal, and the *d-spacing* of 0.22 nm corresponding to the (200) lattice plane of the MnO_2 crystal (JCPDS No. 12-0716).

The obtained calcinated products were further detected by XPS to confirm the metal oxidation states and the chemical compositions. **Figure 3A** is the survey spectrum of the products, which shows the core levels of Co 2p, Mn 2p, and O 1s, respectively. To get clearer information, the high-resolution XPS spectra analysis was carried out. The Co 2p's high-resolution XPS spectrum is shown in **Figure 3B**. The main two peaks centered at 780.3 and 796.2 eV can be appointed to the binding energies of 2p3/2 and 2p1/2 of Co(II), whereas the other two lower peaks centered at 786.1 and 802.5 eV can be appointed to the binding energies of 2p3/2 and 2p1/2 of Co(III). These results imply the Co_3O_4 phase in our sample and agreement with the XRD result (Yan et al., 2012; Li et al., 2013). **Figure 3C** is the high-resolution XPS spectrum extracted from Mn 2p. The main two peaks are centered at 641.1 and 652.7 eV; therefore, the spin-orbital splitting calculated is 11.6 eV. These results well refer to the electronic orbits of Mn 2p3/2 and 2p1/2, pointing to Mn(IV) state of the products (Sui et al., 2009). As can be seen from the high-resolution spectrum of O 1s in **Figure 3D**, there are two distinct components, except for the binding energy of 531.2 eV assigned to the oxygen atoms in the hydroxyl groups, the strong peak of 529.6 eV should belong to the oxygen atoms in the chemical compositions of Co_3O_4 and MnO_2 (Wei et al., 2008; Xia et al., 2010). These results further proved that the chemical component of as-fabricated products is Co_3O_4@MnO_2.

A typical IV type adsorption behavior was observed in the prepared Co_3O_4 and Co_3O_4@MnO_2 products by the N_2

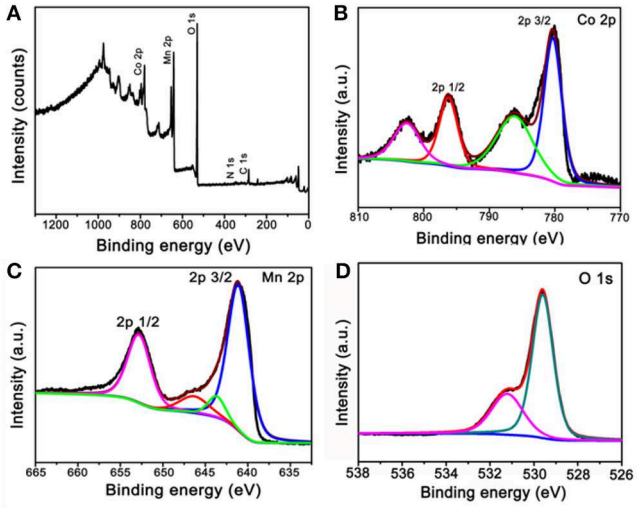

FIGURE 3 | X-ray photoelectron spectroscopy (XPS) spectra of the products after calcinating the ZIF-67@Mn-ZIF. **(A)** Survey XPS spectrum and **(B–D)** high-resolution XPS spectra of Co 2p, Mn 2p, and O 1s.

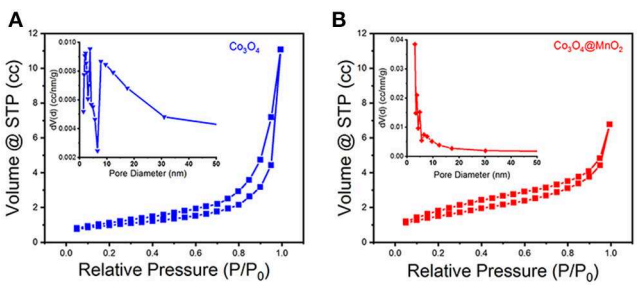

FIGURE 4 | N_2 adsorption-desorption isotherms of **(A)** Co_3O_4 and **(B)** Co_3O_4@MnO_2 products. Inset shows their corresponding pore size distributions.

adsorption-desorption isotherms (**Figures 4A,B**), which exhibit a mesoporous structure with slit type pores. The BET surface areas for the Co_3O_4 and Co_3O_4@MnO_2 are 72.214 and 148.407 m^2 g^{-1}, a high BET surface area might be beneficial for the electrons and ions' storage and shuttle in the electrode because it provides more active sites, hence could lead to enhanced electrochemical capacity (Jiang et al., 2012). From the corresponding pore size distributions of the inset image, it can be found that the pore sizes are concentrated in 3–10 nm for Co_3O_4 sample and 3–6 nm for Co_3O_4@MnO_2 sample. The porous structure is facilitating the electrolyte ion diffusion and transference in the course of charge and discharge processes.

The electrochemical properties of the Co_3O_4@MnO_2 electrode materials were evaluated, and the results are summarized and shown in **Figure 5**. Enclosed loops in **Figure 5A** show the electrode's CV performance at increasing scan rates from 1 to 100 mV s^{-1}, unlike the pseudocapacitance behavior of single Co_3O_4 nanocrystals (**Figure S4**). The shapes of the CV curves of Co_3O_4@MnO_2 indicate a typical electrical double layer capacitance (EDLC) behavior, and it retains well as the scan rate

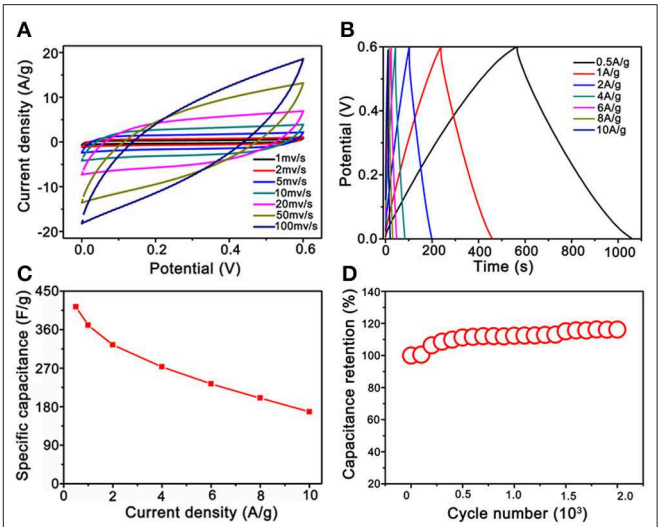

FIGURE 5 | Electrochemical test results of Co_3O_4@MnO_2 electrode. **(A)** Cyclic voltammetry (CV) curves at extending scan rates from 1 to 100 mV s^{-1}. **(B)** CD curves under extending current densities from 0.5 to 10 A g^{-1}. **(C)** Plot of the specific capacitance against different current densities. **(D)** Long-term cycling stability.

upscales to 20 mV s^{-1}, demonstrating its good rate capability (Wu et al., 2015). The EDLC behavior of Co_3O_4@MnO_2 ascribes to the MnO_2 outer layer (Li et al., 2012). The slight shape deformation was observed when the scan rate achieves 50 and 100 mV s^{-1}; this could be ascribed to the polarization phenomenon at high scan rate (Salanne et al., 2016). The GCD properties were evaluated at current densities from 0.5 A g^{-1} and extended to 10 A g^{-1} in the voltage range from 0 to 0.6 V vs. Ag/AgCl (3M KCl). In **Figure 5B**, it is clear to observe a series of good symmetric triangle shape GCD curves, revealing its good EDLC behavior; this result is consistent with CV performance. Under a series of current densities, that is, 0.5, 1, 2, 4, 6, 8, and 10 A g^{-1}, the specific capacitances were calculated to be 413, 370, 324, 273, 233, 200, and 168 F g^{-1}, respectively. On the contrary, single Co_3O_4 nanocrystal only delivers 187, 155, 108, 76, 57, and 45 F g^{-1} at 1, 2, 4, 6, 8, and 10 A g^{-1}, respectively (**Figure S5**). Obviously, the Co_3O_4@MnO_2 electrode presents better capacitance values than single Co_3O_4 electrode, the reason could be owing to the multicomponent and higher BET surface of Co_3O_4@MnO_2 electrode that endows the more charge storage (Jiang et al., 2012). Under the extending current densities from 0.5 to 10 A g^{-1}, the specific capacitance decreased from 413 to 168 F g^{-1}, retaining ~41% of its initial capacitance (shown in **Figure 5C**). While for single Co_3O_4 nanocrystal, the rate capability is only 25% from 1 to 10 A g^{-1} (187 vs. 45 F g^{-1}, **Figure S6**). After 2,000 times cycles of CV test at 20 mV s^{-1}, the capacitance retention remains at 110% (shown in **Figure 5D**), while only 80% of single Co_3O_4 nanocrystal (**Figure S7**), indicating a good stability of Co_3O_4@MnO_2 electrode. It is clear to conclude that the performance of Co_3O_4@MnO_2 in connection with capacitance retention and cycling ability is much improved compared with single Co_3O_4.

CONCLUSIONS

In conclusion, hollow Co_3O_4@MnO_2 cubic nanomaterials were synthesized by sacrificing the ZIF-67@Mn-ZIF precursor through an uncomplicated controlled thermal treatment. The porous structure and high BET surface area endow its excellent properties as supercapacitor electrode, it presented a high specific capacitance of 413 F g^{-1} (0.5 A g^{-1}) and showed a rate capability of 41% at the current density enhanced to 20 times with excellent stability, giving the impression that this hollow cubic nanomaterial possesses considerable potential as a supercapacitor electrode material.

DATA AVAILABILITY STATEMENT

The XRD datasets generated for this study can be found in the repository of ICDD, with the accession numbers of 74-2120 and 12-0716 in JCPDS card.

AUTHOR CONTRIBUTIONS

JW and JH conceived and designed the experiments. JX, YZ, and CX performed the experiments and analyzed the data. All authors revised and checked the draft.

FUNDING

This research was supported by the National Natural Science Foundation of China (51701022, 51972055), the Shenzhen Science and Technology Research Project (Grant No. JCYJ20180508152903208), and the Shenzhen Pengcheng Scholar Program.

SUPPLEMENTARY MATERIAL

The Supplementary Material for this article can be found online at: https://www.frontiersin.org/articles/10.3389/fchem.2019.00831/full#supplementary-material

REFERENCES

Chen, S., Xue, M., Li, Y. Q., Pan, Y., Zhu, L. K., Zhang, D. L., et al. (2015). Porous $ZnCo_2O_4$ nanoparticles derived from a new mixed-metal organic framework for supercapacitors. *Inorg. Chem. Front.* 2, 177–183. doi: 10.1039/C4QI00167B

Du, X., Zhang, Z., Liu, W., and Deng, Y. L. (2017). Nanocellulose-based conductive materials and their emerging applications in energy devices - A review. *Nano Energy* 35, 299–320. doi: 10.1016/j.nanoen.2017.04.001

El-Kady, M. F., Shao, Y., and Kaner, R. B. (2016). Graphene for batteries, supercapacitors and beyond. *Nat. Rev. Mater.* 1:16033. doi: 10.1038/natrevmats.2016.33

Han, Y., Zhang, S., Shen, N., Li, D. J., and Li, X. F. (2017). MOF-derived porous NiO nanoparticle architecture for high performance supercapacitors. *Mater. Lett.* 188, 1–4. doi: 10.1016/j.matlet.2016.09.051

Jiang, H., Sun, T., Li, C., and Ma, J. (2012). Hierarchical porous nanostructures assembled from ultrathin MnO_2 nanoflakes with enhanced supercapacitive performances. *J. Mater. Chem.* 22, 2751- 2756. doi: 10.1039/C1JM14732C

Li, G. C., Liu, P. F., Liu, R., Liu, M. M., Tao, K., Zhu, S. R., et al. (2016). MOF-derived hierarchical double-shelled NiO/ZnO hollow spheres for high-performance supercapacitors. *Dalton Trans.* 45, 13311–13316. doi: 10.1039/C6DT01791F

Li, W., Li, G., Sun, J., Zou, R., Xu, K., Sun, Y., et al. (2013). Hierarchical heterostructures of MnO_2 nanosheets or nanorods grown on Au-coated Co_3O_4 porous nanowalls for high-performance pseudocapacitance. *Nanoscale* 5, 2901–2908. doi: 10.1039/c3nr34140b

Li, W., Zhang, B., Lin, R., Ho-Kimura, S., He, G., Zhou, X., et al. (2018). A dendritic nickel cobalt sulfide nanostructure for alkaline battery electrodes. *Adv. Funct. Mater.* 28:1705937. doi: 10.1002/adfm.201705937

Li, W. Y., Liu, Q., Sun, Y. G., Sun, J. Q., Zou, R. J., Li, G., et al. (2012). MnO_2 ultralong nanowires with better electrical conductivity and enhanced supercapacitor performances. *J. Mater. Chem.* 22, 14864–14867. doi: 10.1039/c2jm33368f

Li, W. Y., Xu, K. B., An, L., Jiang, F. R., Zhou, X. Y., Yang, J. M., et al. (2014). Effect of temperature on the performance of ultrafine MnO_2 nanobelt supercapacitors. *J. Mater. Chem. A* 2, 1443–1447. doi: 10.1039/C3TA14182A

Liu, J., Jiang, J., Cheng, C., Li, H., Zhang, J., Gong, H., et al. (2011). Co_3O_4 Nanowire@MnO_2 ultrathin nanosheet core/shell arrays: a new class of high-performance pseudocapacitive materials. *Adv. Mater.* 23, 2076–2081. doi: 10.1002/adma.201100058

Qin, J. N., Wang, S. B., and Wang, X. C. (2017). Visible-light reduction CO_2 with dodecahedral zeolitic imidazolate framework ZIF-67 as an efficient co-catalyst. *Appl. Catal. B Environ.* 209, 476–482. doi: 10.1016/j.apcatb.2017.03.018

Qu, G., Cheng, J., Li, X., Yuan, D., Chen, P., Chen, X., et al. (2016). A fiber supercapacitor with high energy density based on hollow graphene/conducting polymer fiber electrode. *Adv. Mater.* 28, 3646–3652. doi: 10.1002/adma.201600689

Salanne, M., Rotenberg, B., Naoi, K., Kaneko, K., Taberna, P. L., Grey, C. P., et al. (2016). Efficient storage mechanisms for building better supercapacitors. *Nat. Energy* 1:16070. doi: 10.1038/nenergy.2016.70

Salunkhe, R. R., Kaneti, Y. V., and Yamauchi, Y. (2017). Metal-organic framework-derived nanoporous metal oxides toward supercapacitor applications: progress and prospects. *ACS Nano* 11, 5293–5308. doi: 10.1021/acsnano.7b02796

Saraf, M., Rajak, R., and Mobin, S. M. (2019). MOF derived high surface area enabled porous Co3O4 nanoparticles for supercapacitors. *ChemistrySelect* 4, 8142–8149. doi: 10.1002/slct.201901652

Shao, Y., El-Kady, M. F., Sun, J., Li, Y., Zhang, Q., Zhu, M., et al. (2018). Design and mechanisms of asymmetric supercapacitors. *Chem. Rev.* 118, 9233–9280. doi: 10.1021/acs.chemrev.8b00252

Snook, G. A., Kao, P., and Best, A. S. (2011). Conducting-polymer-based supercapacitor devices and electrodes. *J. Power Sources* 196, 1–12. doi: 10.1016/j.jpowsour.2010.06.084

Sui, N., Duan, Y. Z., Jiao, X. L., and Chen, D. R. (2009). Large-scale preparation and catalytic properties of one-dimensional alpha/beta-MnO_2 nanostructures. *J. Phys. Chem. C* 113, 8560–8565. doi: 10.1021/jp810452k

Wei, W. F., Cui, X. W., Chen, W. X., and Ivey, D. G. (2008). Phase-controlled synthesis of MnO_2 nanocrystals by anodic electrodeposition: implications for high-rate capability electrochemical supercapacitors. *J. Phys. Chem. C* 112, 15075–15083. doi: 10.1021/jp804044s

Wu, J., Ouyang, C., Dou, S., and Wang, S. (2015). Hybrid NiS/CoO mesoporous nanosheet arrays on Ni foam for high-rate supercapacitors. *Nanotechnology* 26:325401. doi: 10.1088/0957-4484/26/32/325401

Xia, H., Feng, J. K., Wang, H. L., Lai, M. O., and Lu, L. (2010). MnO_2 nanotube and nanowire arrays by electrochemical deposition for supercapacitors. *J. Power Sources* 195, 4410–4413. doi: 10.1016/j.jpowsour.2010.01.075

Xu, J., Liu, S. C., and Liu, Y. (2016). Co_3O_4/ZnO nanoheterostructure derived from core-shell ZIF-8@ZIF-67 for supercapacitors. *RSC Adv.* 6, 52137–52142. doi: 10.1039/C6RA07773K

Xu, K., Li, S., Yang, J., and Hu, J. (2018). Hierarchical hollow MnO_2 nanofibers with enhanced supercapacitor performance. *J. Colloid Interface Sci.* 513, 448–454. doi: 10.1016/j.jcis.2017.11.052

Xu, K., Shen, Y., Zhang, K., Yang, F., Li, S., and Hu, J. (2019). Hierarchical assembly of manganese dioxide nanosheets on one-dimensional titanium nitride nanofibers for high-performance supercapacitors. *J. Colloid Interface Sci.* 552, 712–718. doi: 10.1016/j.jcis.2019.05.093

Yan, N., Hu, L., Li, Y., Wang, Y., Zhong, H., Hu, X. Y., et al. (2012). Co_3O_4 nanocages for high-performance anode material in lithium-ion batteries. *J. Phys. Chem. C* 116, 7227–7235. doi: 10.1021/jp2126009

Yu, X. Y., and Lou, X. W. (2018). Mixed metal sulfides for electrochemical energy storage and conversion. *Adv. Energy Mater.* 8:1701592. doi: 10.1002/aenm.201701592

Yu, Z. Y., Zhang, X. Y., Wei, L., and Guo, X. (2019). MOF-derived porous hollow alpha-Fe_2O_3 microboxes modified by silver nanoclusters for enhanced pseudocapacitive storage. *Appl. Surf. Sci.* 463, 616–625. doi: 10.1016/j.apsusc.2018.08.262

Yue, Y., Fulvio, P. F., and Dai, S. (2015). Hierarchical metal-organic framework hybrids: perturbation-assisted nanofusion synthesis. *Acc. Chem. Res.* 48, 3044–3052. doi: 10.1021/acs.accounts.5b00349

Zhang, L. L., and Zhao, X. S. (2009). Carbon-based materials as supercapacitor electrodes. *Chem. Soc. Rev.* 38, 2520–2531. doi: 10.1039/b813846j

Zhang, W., Xu, C., Ma, C., Li, G., Wang, Y., Zhang, K., et al. (2017). Nitrogen-superdoped 3D graphene networks for high-performance supercapacitors. *Adv. Mater.* 29:1701677. doi: 10.1002/adma.201701677

Conflict of Interest: The authors declare that the research was conducted in the absence of any commercial or financial relationships that could be construed as a potential conflict of interest.

frontiers in Chemistry

ORIGINAL RESEARCH
published: 20 February 2020
doi: 10.3389/fchem.2020.00105

Nitrogen and Phosphorus Co-doped Porous Carbon for High-Performance Supercapacitors

Jiaming Zhou, Shewen Ye, Qinqin Zeng, Hui Yang, Jiahao Chen, Ziting Guo, Honghui Jiang and Karthikeyan Rajan**

School of Materials Science and Engineering, Jiangxi University of Science and Technology, Ganzhou, China

As one of the most promising fast energy storage devices, supercapacitor has been attracting intense attention for many emerging applications. However, how to enhance the electrochemical performance of electrode materials is still the main issue among various researches. In this paper, hierarchical porous carbons derived from *Eleocharis dulcis* has been prepared by chemical activation process with the aid of KOH at elevated temperature. Results show that the N, P co-doped porous carbon exhibits excellent electrochemical performance, it owns a specific capacitance of 340.2 F/g at 1 A/g, and obtains outstanding cycling stability of 96.9% of capacitance retention at 10 A/g after 5,000 cycles in a three-electrode system. Moreover, in the two-electrode system, the product still maintains a high specific capacitance of 227.2 F/g at 1 A/g, and achieves good electrochemical cycle stability (94.2% of capacitance retention at 10 A/g after 10,000 cycles); besides, its power/energy density are 3694.084 and 26.289 Wh/kg, respectively. Therefore, the combination of facile synthesis strategy and excellent electrochemical performance makes *Eleocharis dulcis*-based porous carbon as a promising electrode material for supercapacitor.

Keywords: biomass, porous carbon, supercapacitor, *Eleocharis dulcis*, N/P co-doped

OPEN ACCESS

Edited by:
Yuanlong Shao,
King Abdullah University of Science and Technology, Saudi Arabia

Reviewed by:
Bingjie Zhang,
Chapman University, United States
Shijie Li,
Zhejiang Ocean University, China

****Correspondence:***
Honghui Jiang
jhonghui@163.com
Karthikeyan Rajan
karthikeyan148@gmail.com

Specialty section:
This article was submitted to Electrochemistry, a section of the journal Frontiers in Chemistry

Received: *20 December 2019*
Accepted: *04 February 2020*
Published: *20 February 2020*

Citation:
Zhou J, Ye S, Zeng Q, Yang H, Chen J, Guo Z, Jiang H and Rajan K (2020) Nitrogen and Phosphorus Co-doped Porous Carbon for High-Performance Supercapacitors. Front. Chem. 8:105. doi: 10.3389/fchem.2020.00105

INTRODUCTION

Rapid development of global economy, the depletion of chemical fuels and the ever-worsening environment are intensified with the continuous growth of the population, which increases the demand for clean sustainable energy. Thence it requires the development of efficient and clean energy storage devices (Wang et al., 2016; Liu et al., 2017b; Yang et al., 2019). Among them, the traditional Lithium-ion batteries will generate quantum and form lithium dendrites under high-power operation, the supercapacitors have distinctive properties such as excellent power density, rapid charging and discharging speed and superior cycle stability, is considered the best substitute for lithium-ion batteries (Zhao et al., 2013; Shao et al., 2018; Li et al., 2019). Although supercapacitors exhibit excellent properties, low specific capacity and energy density (typically <10 Wh/kg) toward large scale commercial devices are still major constraints (Winter and Brodd, 2004; Liu et al., 2017b).

Electrode materials are the important constituent which affect the properties of supercapacitor. Traditionally, different allotropes of carbon materials are used as an electrode in energy storage applications. Among them, sustainable biomass derived carbons are individual class of materials, with the advantage of low-cost, abundant and sustainable in nature, excellent electrical conductivity

and specific surface area (SSA) (Pandolfo and Hollenkamp, 2006; Jiang et al., 2013; Titirici et al., 2015; Gong et al., 2017; He et al., 2018). Number of researchers have derived carbon from different biomass sources such as *Perilla frutescens* (Liu et al., 2017a), Rice straw (Liu et al., 2018), Peanut shells (Xiao et al., 2018), Buckwheat flour (Huang et al., 2019), Peach gum (Lin et al., 2019), and Bamboo (Zhang et al., 2018). By using KOH through chemical activation Cheng et al. (2016) have prepared flexible carbon fiber aerogel from natural cotton and achieved specific capacitance of 283 F/g at 1 A/g. Similarly, the graded porous carbon material derived from walnut shells resulted the capacitance of 462 F/g at 1 A/g (Wang et al., 2019). Besides, the specific surface area of carbon materials derived from seaweed microspheres show as high as 1337.9 m^2/g, the capacitance led to 309 F/g at 1 A/g, with the capacitance retention rate of 92% at 20 A/g with 10,000 cycles (Zhu et al., 2018). Therefore, it is necessary to reveal the relationship between different biomass sources and their relation to specific surface area and specific capacitance.

Due to their limited number of active sites on microporous carbon, it is important to investigate the improvement of electrical conductivity and electronegativity properties. In this work we have fabricated the nitrogen and phosphorus co-doped microporous derived carbon for supercapacitor application. The reason why biomass derived carbon materials can show excellent capacitance performance, is closely related to the incorporation of trace elements such as nitrogen and phosphorus into carbon materials in the carbonization process (Shen and Fan, 2013; Chen et al., 2014; Zhao et al., 2017). The presence of nitrogen in carbon materials is expected to improve the electron conductivity of the materials (Chen et al., 2013). Phosphorus contained materials could help to improve the electronegativity of carbon through the combination of lone pair electron nitrogen and carbon, thereby enhance the hydrophilicity of carbon materials. The nitrogen-containing groups on the surface are alkaline, which is conducive to ion adsorption (Shen and Fan, 2013). Nitrogen and phosphorus are belong to the same group in periodic table, however phosphorous possess higher electron-donor capacity, which is useful to achieve stable capacitive property (Zhao et al., 2017). Therefore, we believe that presence of nitrogen and phosphorus in carbon would greatly improve the capacitive performance.

China cultivates the largest quantities of *Eleocharis dulcis* (ED) in the world with the annual output of up to 1.75 million tons. *Eleocharis dulcis* is rich in trace elements such as nitrogen and phosphorous, and the phosphorus element is higher in root vegetables (Bao et al., 2018). Therefore, deriving carbon from *Eleocharis dulcis* without affecting the existing N and P elements could help to enhance the specific capacitance (Panja et al., 2015). In this work, we have derived the microporous activated carbon material from ED by chemical activation process and carbonized. To the results of N_2 adsorption-desorption isothermal analysis describes the highest, specific surface area of 2,454 m^2/g with the specific capacitance of 340.2 F/g at 1 A/g.

EXPERIMENTAL

Materials Synthesis

In general, ED were freeze-dried and grinded, after screening through a 70-mesh sieve, the obtained powders were mixed with certain amount of KOH solution, then dried at 80°C for 12 h. The as-prepared precursors were transferred into a tube furnace, after that, the powders were treated at an elevated temperature (800°C for 1 h) under N_2 atmosphere. The obtained carbon material was washed by 2 M HNO_3 to remove the impurities, subsequently, the final products were washed with deionized water several times, then dried at 60°C for 24 h. The samples treated with different KOH/ED mass ratio (1:1, 2:1, 3:1) were referred to referred to as NPC-1, NPC-2, and NPC-3, respectively.

Materials Characterization

Scanning electron microscope (SEM, ZEISS Sigma) and transmission electron microscope (TEM, JEOL, JEM-2010, Japan) are used to analyze the morphology and microstructure of the samples. The phase and results of the samples are analyzed by X-ray diffraction (XRD, Empyrean). Raman spectroscopy (excitation beam wavelength 532 nm) is used to analyze the graphitization degree of materials. The nitrogen adsorption and desorption isotherms and the specific surface area, pore diameter distribution and pore volume of the samples are measured by N_2 adsorption-desorption experiment (Micromeritics, ASAP 2010M, USA).

Electrochemical Measurements

All electrochemical measurements were performed at CHI760E electrochemical workstation (Chen Hua Shanghai). The electrochemical test used a standard three-electrode system, in which Hg/HgO is used as the reference electrode, Pt electrode was used as the counter electrode, the prepared NPCs were used as the working electrodes, and 6 M KOH aqueous solution as the electrolyte. The working electrodes were prepared according to the following procedure: 80 wt.% NPCs, 10 wt.% acetylene black, and 10 wt.% PVDF (binder) were thoroughly mixed in the N-methyl-2-pyrrolidone (NMP) solvent to obtain a uniform semi-fluid slurry; the prepared slurry was coated onto carbon cloth, and then dried in a vacuum oven at 60°C for 12 h. The coating mass of active material in each working electrode is about 2 mg/cm^2. The cyclic voltammetry and galvanostatic charge/discharge (GCD) curve had been performed at various scanning rate/current density, and the corresponding electrochemical impedance spectroscopy (EIS) was tested at an open circuit voltage (frequency range: 0.01–100 kHz, amplitude: 5 mV). The calculation details were provided in **Supplementary Material**.

RESULTS AND DISCUSSION

The scanning electron microscopy (SEM) analysis was used to analyze the morphological significance of synthesized carbon materials. **Figure 1** shows the low and high magnification images of NPC-3. The microstructure images reveal the presence

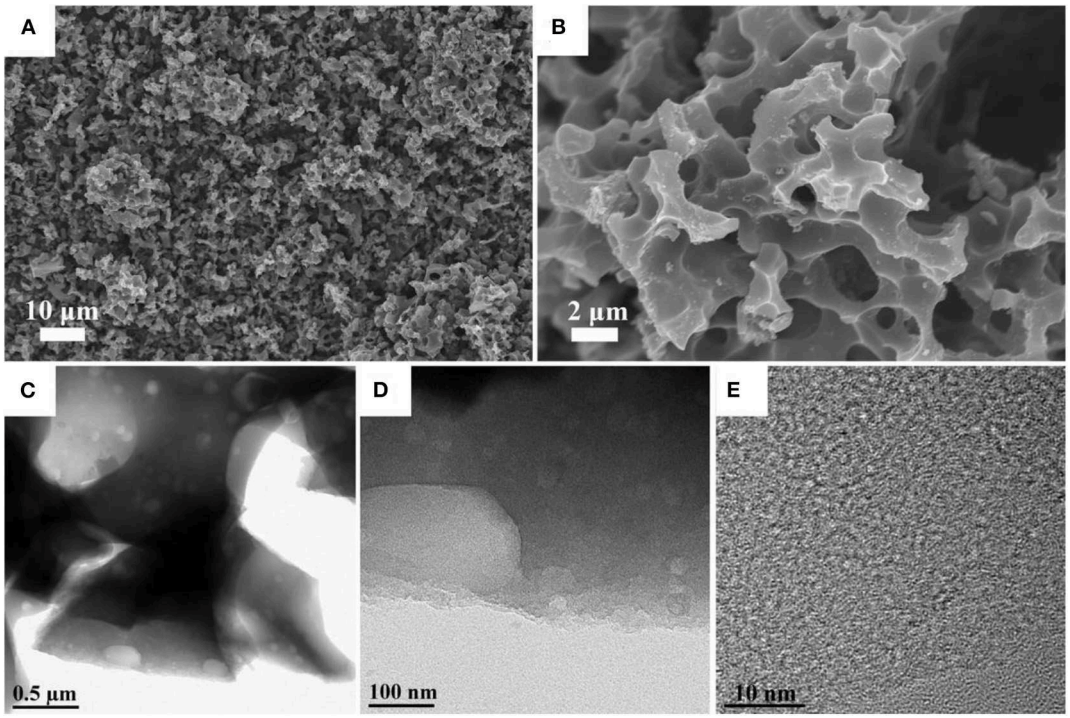

FIGURE 1 | (A,B) SEM images of the NPC-3. **(C,D)** TEM images of the NPC-3 under different magnifications. **(E)** HRTEM image of the NPC-3.

of large hierarchical porous on the derived carbon The diameter of these large pore structures varies from few to several micrometers, Compared with the NPC-1 (**Figures S2A,B**) and NPC-2 (**Figures S2C,D**), the NPC-3 has more uniform hole distribution with macropores structure. The structure of NPC-3 was further studied by TEM, according to the TEM results (**Figures 1C–E**), there are many randomly distributed mesopores, which connect with the macropores and form a hierarchical porous structure. It is well-stated that KOH activation leads to the formation of abundant micropores due to its corrosive nature (Bleda-Martínez et al., 2005; Guan et al., 2009), the reaction mechanism is described as follows:

$$KOH + C \leftrightarrow K + CO_2 + H_2O \quad (1)$$

The electrochemical performance of carbon-based materials are greatly depends upon its solid/electrolyte interface, and its porous structure (Salanne et al., 2016). The contribution of micropores and mesopores to the specific capacitance were not discussed in detail. Previous reports indicated that neither micropores nor mesopores influenced the energy/power density (Kim et al., 2013). Besides, Lei et al. found that hierarchical micropores with wider size distribution led to high energy storage, which provided a fast transportation pathway for ions (Lei et al., 2011). The nitrogen adsorption-desorption analysis was conducted for the synthesized carbon and the results are shown in **Table 1**. **Figures 2A,B** represents the N_2 adsorption-desorption isothermal and pore size distributions of NPC-1, NPC-2, and NPC-3. Results reveal that all samples are composed of type I and type IV isotherms. The sharp adsorption of N_2 at low relative pressure (0∼0.1) indicates the presence of micropores in the porous carbon structure. The hysteresis loops at higher relative pressure represents the presence of mesopores structure in NPC-3; the curve shape near high relative pressure region indicates there are small amount of macropores structure (Lv et al., 2012). The pore size distribution of the samples has been tested. As can be seen from **Table 1**, with the increase of KOH, the BET surface area (S_{BET}) and total pore volumes (V_{total}) of samples increased from 1,063 to 2,454 m^2/g and from 0.352 to 1.345 cm^3/g, respectively. The electrode material with high specific surface area can provide abundant electrochemical active sites and enhance the effective charge storage area between electrode and electrolyte, thus improving the performance of supercapacitor (Xu et al., 2018).

TABLE 1 | Adsorption parameters of different samples calculated from N_2 adsorption isotherms.

Samples	S_{BET} (m^2/g)	S_{micro} (m^2/g)	V_{micro} (cm^3/g)	V_{total} (cm^3/g)	$D_{Average}$ (nm)
NPC-1	1,063	889	0.302	0.352	0.415
NPC-2	1,708	1,455	0.596	0.729	0.545
NPC-3	2,454	1,522	0.650	1.345	0.852

Figure 3A shows the X-ray diffraction (XRD) pattern and Raman spectra (**Figure 3B**) of synthesized carbon samples

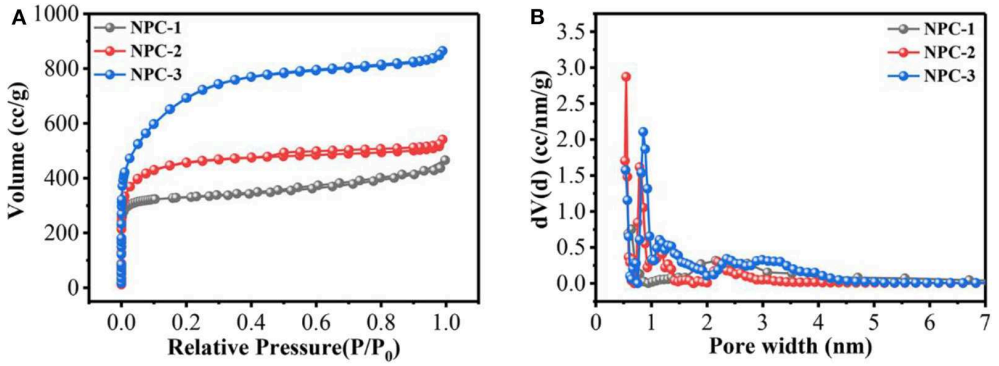

FIGURE 2 | (A) Nitrogen adsorption/desorption isotherms. **(B)** Pore size distribution curve of NPC.

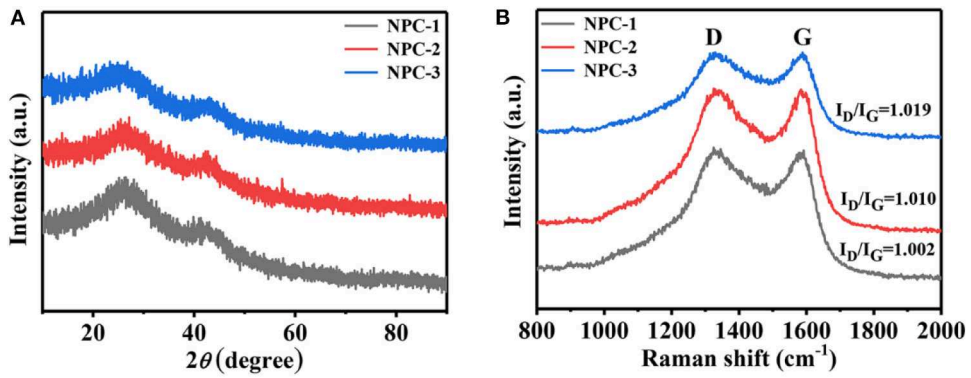

FIGURE 3 | (A) XRD patterns. **(B)** Raman spectrum.

derived from ED. The broad characteristic peaks at 25.9 and 43.1°C are corresponding to the (002) and (100) crystal planes of carbon materials, respectively (Wan et al., 2015). Increasing the mass ratio of KOH to ED leads to the broadening of diffraction peak (002) and (100). This indicates that the KOH can significantly affect the orderings of the crystal planes. Raman spectroscopy of **Figure 3B** describes the D-band (at 1,333 cm^{-1}) G-band (at 1,589 cm^{-1}). The D-band is attributed to disordered nature of graphitic planes and G-band ascribed to ordered planes due to sp^2 hybrid carbon stretching vibration. More importantly, I_D/I_G reflects the degree of graphitization of the material (Ferrari et al., 2006; Zhou et al., 2014), and the I_D/I_G of NPC-1, NPC-2, and NPC-3 are 1.019, 1.010, and 1.002, respectively. The result indicates that the higher KOH ratio inhibits the graphitization of the material, raises the disorder of the microstructure of the material. This is consistent with the XRD results.

The surface chemical properties of NPCs are investigated by X-ray photoelectron spectroscopy (XPS) measurements. The characteristic peak for C1s (∼284.60 eV), N1s (∼400.45 eV), O1s (∼532.64 eV), and P2p (∼134.40 eV) were observed in the spectrum (**Figure 4A**). The C1s spectra (**Figure 4B**) of the NPC-3 display three distinct characteristic peaks at 284.70, 286.03, and 288.82 eV, they are corresponding to different carbon functional groups of C-C or C=C, O-C-O, and O-C=O, respectively (Li et al., 2016). N1s spectra contains three peaks located at 399.67, 400.44, and 401.68 eV, corresponding to pyridinic-N, pyrrolic-N, and quaternary-N (**Figure 4C**). Pyridinic-N and pyrrolic-N species have positive charge, they can enhance the electron transfer at high current density, while quaternary-nitrogen can increase the conductivity of materials (Yang et al., 2019). In addition, **Figure 4D** shows a P2p spectrum with a peak value of 134.53 eV, representing P-O functional group. According to **Table 2**, the doping amount of P is about 0.18∼0.25%. P has a higher electron delivery capacity than N, which can significantly improve the charge storage and transport capacity of carbon materials. Therefore, N and P doping are beneficial to the electrochemical performance of supercapacitors. As we all know, the N content of NPCs decreases with the increase of KOH mass, while it won't affect the P content. Interested, O at% is negatively correlated with P at%, this should be attributed to the part of P atoms, which are directly bonded to C atoms, and do not bind the edges of the carbon lattice by P-O.

The electrochemical characterizations were carried out for the synthesized carbon materials as shown in **Figure 5**. All the samples are tested under 6 M KOH electrolyte through the three-electrode system. As shown in **Figure 5A**, all the CV curves of NPCs represent the quasi rectangular shape at 10 mV/s sweeping potential. This indicates that the charge can be reassembled

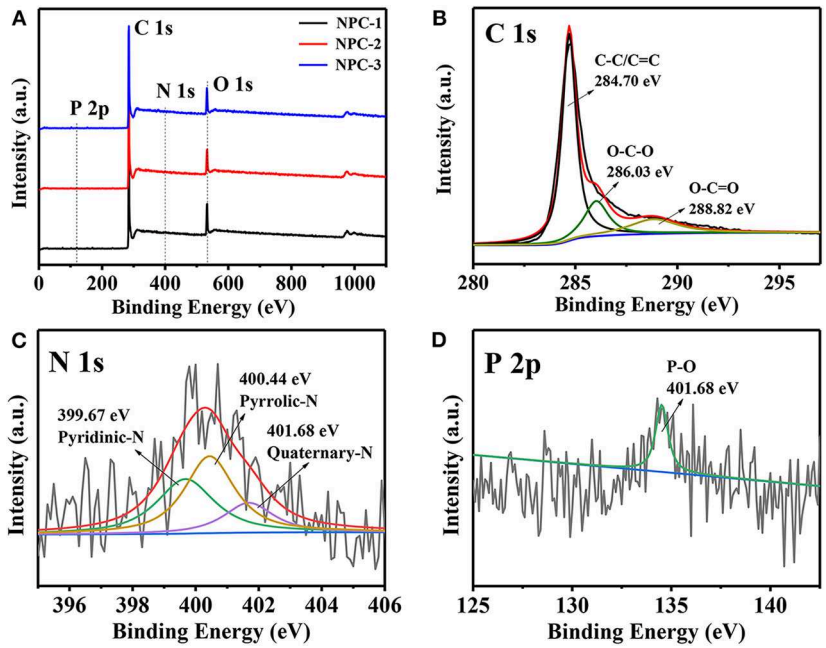

FIGURE 4 | (A) XPS survey spectra of NPCs. **(B)** C1s **(C)** N1s and **(D)** P2p XPS spectra of the NPC-3.

TABLE 2 | The contents of C, N, P and O in NPCs from XPS analysis.

Samples	C (at%)	N (at%)	O (at%)	P (at%)
NPC-1	87.43	1.24	11.08	0.25
NPC-2	87.96	1.07	10.68	0.29
NPC-3	85.98	0.95	12.89	0.18

quickly when the voltage is turned, it reveals the material has good rate capability and cycle performance (Xu et al., 2019). It can be seen that the CV curve of NPC-3 has the largest area which depicts the highest specific capacitance of, which represents 340.2 F/g at 1 A/g. **Figure 5C** shows the galvanostatic charge and discharge (GCD) curves of NPC-3 under different current densities. All curves show symmetrical triangular shape without any voltage drop, indicating that the material has good rate capability and cycle performance. However, the GCD curve is not strictly symmetric due to pseudocapacitive effect caused by the presence of N and P. **Figure 5B** plotted against capacitance with respect to different current densities. All the NPCs signify the decrease in its specific capacitance with respect to the increase in current density. Besides, the cycling stability of the NPC-3 has been resulted to 96.9% of the initial specific capacitance after 5,000 cycles at 10 A/g, this could be due to the 3D structure of carbon materials and the contribution of phosphorus and nitrogen functional groups, NPC-3 has good cycle stability.

In summary we summarize the reasons for the superior electrochemical performance of NPC-3: (1) The co-doped of N and P atoms produces more active sites, which leads to the increase of conductivity and electronegativity of porous carbon, increases the hydrophilicity of the material, and then increases the effective specific surface area, leading to the common effects of capacitance and pseudo capacitance (Chen et al., 2015). (2) The micropores in the hierarchical porous carbon can be used to store charge, and mesoporous and macropores materials can accelerate the migration rate of ions in electrolytes, improve multiplier performance and circle performance of the NPCs.

The NPCs have been assembled into symmetric supercapacitor to investigate their electrochemical performance. **Figure 6A** shows the NPC-3 cyclic voltammetry curves, which is approximately rectangular, indicating that the material has good capacitance performance. When the scanning speed reaches 100 mV/s, the curve slightly changes but still maintains the shape of rectangle, indicating that NPC-3 has good capacitance retention. Because of the NPCs' unique hierarchical porous structure and high specific surface area, the GCD curve (**Figure 6B**) presents the shape of a nearly symmetrical triangle, and its current density ranges from 0.5 to 50 A/g, representing highly reversible charge-discharge behavior. The capacitance reaches 227.2 F/g at 1 A/g. In addition, there is still a specific capacitance of 170.0 F/g at 10 A/g with high capacitance retention (73.9%) (**Figure 6C**). As recorded in **Figure 6D**, the capacitance of NPC-3 has been reduced after 10,000 cycles at 10 A/g, but it also can maintain 94.2% of the initial specific capacitance. It is well-known that power density/energy density is an important parameter to evaluate the quality of supercapacitors (Tang et al., 2015). Due to the incorporation of N and P elements and the design of graded porous structure, the power/energy density of NPCs is up to 3694.084 W/kg and 26.289 Wh/kg, respectively.

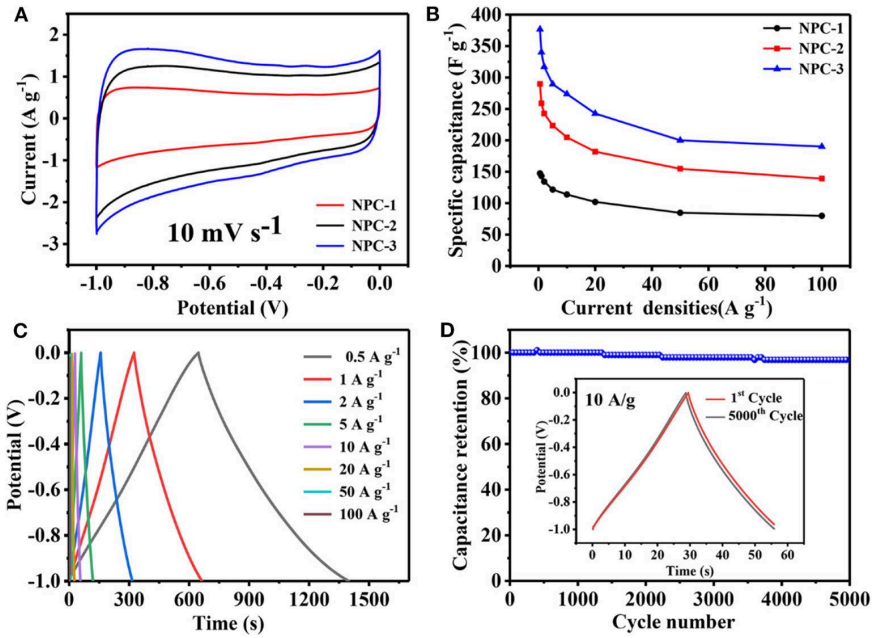

FIGURE 5 | (A) CV curves of PCs at10 mV/s. **(B)** GCD curves of NPC-3 at different current density. **(C)** Variation of specific capacitances vs. the current density of NPCs. **(D)** Cycling performance of NPC-3 at 10 A/g.

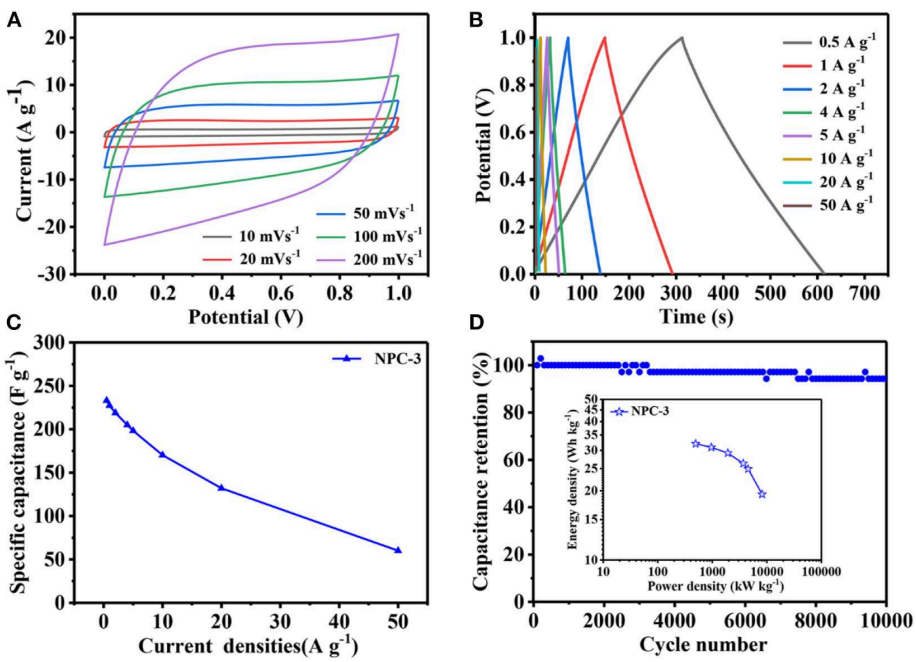

FIGURE 6 | (A) Electrochemical performance of NPC-3 tested in a two-electrode system. **(B)** GCD curves of NPC-3 at various current densities. **(C)** Specific capacitance of NPC-3 under variable current densities. **(D)** Cycling performance of NPC-3 at 10 A/g, the inset is Ragone plots before 10,000 cycles.

CONCLUSION

In this work, ED-derived porous carbon has been prepared through carbonization and activation at elevated temperature. The introducing of trace elements N and P influences the electron conductivity, ions adsorption and capacitive stability of the matrix, and endows the products with excellent electrochemical performance. Besides, the as-prepared samples show high specific

surface area because of the abundant hierarchical porous structure. In three-electrode testing system, NPC-3 exhibits a high specific capacitance (340 F/g at 1 A/g) and excellent rate capacity (190 F/g at 100 A/g). Furthermore, in two-electrode configuration, the corresponding materials also maintains superb electrochemical performance (227.2 F/g at 1 A/g and 170.0 F/g at 10 A/g). Its high energy/powder density (26.289 Wh/kg at a power density of 3694.084 W/kg) and good cycling stability ensure NPC holds great application promise for high-performance supercapacitor.

DATA AVAILABILITY STATEMENT

All datasets generated for this study are included in the article/**Supplementary Material**.

AUTHOR CONTRIBUTIONS

JZ and SY were responsible for literature searching and drafting. All authors contributed equally to the final writing of the paper.

FUNDING

This research was supported by National Natural Science Foundation of China (51702139) and Youth Science Foundation (20151BAB216007, GJJ150637, and 20161BAB216122).

SUPPLEMENTARY MATERIAL

The Supplementary Material for this article can be found online at: https://www.frontiersin.org/articles/10.3389/fchem.2020.00105/full#supplementary-material

REFERENCES

Bao, R., Chen, Z., Zhao, Z., Sun, X., Zhang, J., Hou, L., et al. (2018). Green and facile synthesis of nitrogen and phosphorus co-doped carbon quantum dots towards fluorescent ink and sensing applications. *Nanomaterials* 8:E386. doi: 10.3390/nano8060386

Bleda-Martínez, M. J., Maciá-Agulló, J. A., Lozano-Castelló, D., Morallon, E., Cazorla-Amorós, D., and Linares-Solano, A. (2005). Role of surface chemistry on electric double layer capacitance of carbon materials. *Carbon* 43, 2677–2684. doi: 10.1016/j.carbon.2005.05.027

Chen, H., Liu, D., Shen, Z., Bao, B., Zhao, S., and Wu, L. (2015). Functional biomass carbons with hierarchical porous structure for supercapacitor electrode materials. *Electrochim. Acta* 180, 241–251. doi: 10.1016/j.electacta.2015.08.133

Chen, H., Sun, F., Wang, J., Li, W., Qiao, W., Ling, L., et al. (2013). Nitrogen doping effects on the physical and chemical properties of mesoporous carbons. *J. Phys. Chem. C* 117, 8318–8328. doi: 10.1021/jp4017773

Chen, L. F., Huang, Z. H., Liang, H. W., Gao, H. L., and Yu, S. H. (2014). Three-dimensional heteroatom-doped carbon nanofiber networks derived from bacterial cellulose for supercapacitors. *Adv. Funct. Mater.* 24, 5104–5111. doi: 10.1002/adfm.201400590

Cheng, P., Li, T., Yu, H., Zhi, L., Liu, Z., and Lei, Z. (2016). Biomass-derived carbon fiber aerogel as a binder-free electrode for high-rate supercapacitors. *J. Phys. Chem. C* 120, 2079–2086. doi: 10.1021/acs.jpcc.5b11280

Ferrari, A. C., Meyer, J., Scardaci, V., Casiraghi, C., Lazzeri, M., Mauri, F., et al. (2006). Raman spectrum of graphene and graphene layers. *Phys. Rev. Lett.* 97:187401. doi: 10.1103/PhysRevLett.97.187401

Gong, Y., Li, D., Luo, C., Fu, Q., and Pan, C. (2017). Highly porous graphitic biomass carbon as advanced electrode materials for supercapacitors. *Green Chem.* 19, 4132–4140. doi: 10.1039/C7GC01681F

Guan, C., Wang, K., Yang, C., and Zhao, X. (2009). Characterization of a zeolite-templated carbon for H_2 storage application. *Micropor. Mesopor. Mater.* 118, 503–507. doi: 10.1016/j.micromeso.2008.09.029

He, Q., Liu, J., Liu, X., Li, G., Chen, D., Deng, P., et al. (2018). Fabrication of Amine-modified magnetite-electrochemically reduced graphene oxide nanocomposite modified glassy carbon electrode for sensitive dopamine determination. *Nanomaterials* 8:194. doi: 10.3390/nano8040194

Huang, J., Wu, J., Dai, F., and Li, C. M. (2019). 3D honeycomb-like carbon foam synthesized with biomass buckwheat flour for high-performance supercapacitor electrodes. *Chem. Commun.* 55, 9168–9171. doi: 10.1039/C9CC03039E

Jiang, H., Lee, P. S., and Li, C. (2013). 3D carbon based nanostructures for advanced supercapacitors. *Energy Environ. Sci.* 6, 41–53. doi: 10.1039/C2EE23284G

Kim, K., Choi, M., and Ryoo, R. (2013). Ethanol-based synthesis of hierarchically porous carbon using nanocrystalline beta zeolite template for high-rate electrical double layer capacitor. *Carbon* 60, 175–185. doi: 10.1016/j.carbon.2013.04.011

Lei, Z., Christov, N., Zhang, L. L., and Zhao, X. S. (2011). Mesoporous carbon nanospheres with an excellent electrocapacitive performance. *J. Mater. Chem.* 21, 2274–2281. doi: 10.1039/C0JM03322G

Li, B., Dai, F., Xiao, Q., Yang, L., Shen, J., Zhang, C., et al. (2016). Nitrogen-doped activated carbon for a high energy hybrid supercapacitor. *Energy Environ. Sci.* 9, 102–106. doi: 10.1039/C5EE03149D

Li, J., An, L., Li, H., Sun, J., Shuck, C., Wang, X., et al. (2019). Tunable stable operating potential window for high-voltage aqueous supercapacitors. *Nano Energy* 63:103848. doi: 10.1016/j.nanoen.2019.06.044

Lin, Y., Chen, Z., Yu, C., and Zhong, W. (2019). Heteroatom-doped sheet-like and hierarchical porous carbon based on natural biomass small molecule peach gum for high-performance supercapacitors. *ACS Sustain. Chem. Eng.* 7, 3389–3403. doi: 10.1021/acssuschemeng.8b05593

Liu, B., Liu, Y., Chen, H., Yang, M., and Li, H. (2017a). Oxygen and nitrogen co-doped porous carbon nanosheets derived from *Perilla frutescens* for high volumetric performance supercapacitors. *J. Power Sources* 341, 309–317. doi: 10.1016/j.jpowsour.2016.12.022

Liu, S., Zhao, Y., Zhang, B., Xia, H., Zhou, J., Xie, W., et al. (2018). Nano-micro carbon spheres anchored on porous carbon derived from dual-biomass as high rate performance supercapacitor electrodes. *J. Power Sources* 381, 116–126. doi: 10.1016/j.jpowsour.2018.02.014

Liu, T., Zhang, F., Song, Y., and Li, Y. (2017b). Revitalizing carbon supercapacitor electrodes with hierarchical porous structures. *J. Mater. Chem. A* 5, 17705–17733. doi: 10.1039/C7TA05646J

Lv, Y., Zhang, F., Dou, Y., Zhai, Y., Wang, J., Liu, H., et al. (2012). A comprehensive study on KOH activation of ordered mesoporous carbons and their supercapacitor application. *J. Mater. Chem.* 22, 93–99. doi: 10.1039/C1JM12742J

Pandolfo, A., and Hollenkamp, A. (2006). Carbon properties and their role in supercapacitors. *J. Power Sources* 157, 11–27. doi: 10.1016/j.jpowsour.2006.02.065

Panja, T., Bhattacharjya, D., and Yu, J.-S. (2015). Nitrogen and phosphorus co-doped cubic ordered mesoporous carbon as a supercapacitor electrode material with extraordinary cyclic stability. *J. Mater. Chem. A* 3, 18001–18009. doi: 10.1039/C5TA04169D

Salanne, M., Rotenberg, B., Naoi, K., Kaneko, K., Taberna, P. L., Grey, C. P., et al. (2016). Efficient storage mechanisms for building better supercapacitors. *Nat. Energy* 1:16070. doi: 10.1038/nenergy.2016.70

Shao, Y., El-Kady, M. F., Sun, J., Li, Y., Zhang, Q., Zhu, M., et al. (2018). Design and mechanisms of asymmetric supercapacitors. *Chem. Rev.* 118, 9233–9280. doi: 10.1021/acs.chemrev.8b00252

Shen, W., and Fan, W. (2013). Nitrogen-containing porous carbons: synthesis and application. *J. Mater. Chem. A* 1, 999–1013. doi: 10.1039/C2TA00028H

Tang, J., Salunkhe, R. R., Liu, J., Torad, N. L., Imura, M., Furukawa, S., et al. (2015). Thermal conversion of core–shell metal–organic frameworks: a new method

for selectively functionalized nanoporous hybrid carbon. *J. Am. Chem. Soc.* 137, 1572–1580. doi: 10.1021/ja511539a

Titirici, M.-M., White, R. J., Brun, N., Budarin, V. L., Su, D. S., del Monte, F., et al. (2015). Sustainable carbon materials. *Chem. Soc. Rev.* 44, 250–290. doi: 10.1039/C4CS00232F

Wan, C., Lu, Y., Jiao, Y., Jin, C., Sun, Q., and Li, J. (2015). Fabrication of hydrophobic, electrically conductive and flame-resistant carbon aerogels by pyrolysis of regenerated cellulose aerogels. *Carbohydr. Polym.* 118, 115–118. doi: 10.1016/j.carbpol.2014.11.010

Wang, Q., Yan, J., and Fan, Z. (2016). Carbon materials for high volumetric performance supercapacitors: design, progress, challenges and opportunities. *Energy Environ. Sci.* 9, 729–762. doi: 10.1039/C5EE03109E

Wang, Y., Jiang, H., Ye, S., Zhou, J., Chen, J., Zeng, Q., et al. (2019). N-doped porous carbon derived from walnut shells with enhanced electrochemical performance for supercapacitor. *Funct. Mater. Lett.* doi: 10.1142/S1793604719500425

Winter, M., and Brodd, R. J. (2004). What are batteries, fuel cells, and supercapacitors? *Chem. Rev.* 104, 4245–4269. doi: 10.1021/cr020730k

Xiao, Z., Chen, W., Liu, K., Cui, P., and Zhan, D. (2018). Porous biomass carbon derived from peanut shells as electrode materials with enhanced electrochemical performance for supercapacitors. *Int. J. Electrochem. Sci.* 13, 5370–5381. doi: 10.20964/2018.06.54

Xu, K., Li, S., Yang, J., and Hu, J. (2018). Hierarchical hollow MnO_2 nanofibers with enhanced supercapacitor performance. *J. Colloid Interface Sci.* 513, 448–454. doi: 10.1016/j.jcis.2017.11.052

Xu, K., Shen, Y., Zhang, K., Yang, F., Li, S., and Hu, J. (2019). Hierarchical assembly of manganese dioxide nanosheets on one-dimensional titanium nitride nanofibers for high-performance supercapacitors. *J. Colloid Interface Sci.* 552, 712–718. doi: 10.1016/j.jcis.2019.05.093

Yang, H., Ye, S., Zhou, J., and Liang, T. (2019). Biomass-derived porous carbon materials for supercapacitor. *Front. Chem.* 7:274. doi: 10.3389/fchem.2019.00274

Zhang, G., Chen, Y., Chen, Y., and Guo, H. (2018). Activated biomass carbon made from bamboo as electrode material for supercapacitors. *Mater. Res. Bull.* 102, 391–398. doi: 10.1016/j.materresbull.2018.03.006

Zhao, M., Zhang, Q., Huang, J., Tian, G., Chen, T., Qian, W., et al. (2013). Towards high purity graphene/single-walled carbon nanotube hybrids with improved electrochemical capacitive performance. *Carbon* 54, 403–411. doi: 10.1016/j.carbon.2012.11.055

Zhao, X., Wang, S., and Wu, Q. (2017). Nitrogen and phosphorus dual-doped hierarchical porous carbon with excellent supercapacitance performance. *Electrochim. Acta* 247, 1140–1146. doi: 10.1016/j.electacta.2017.07.077

Zhou, M., Pu, F., Wang, Z., and Guan, S. (2014). Nitrogen-doped porous carbons through KOH activation with superior performance in supercapacitors. *Carbon* 68, 185–194. doi: 10.1016/j.carbon.2013.10.079

Zhu, B., Liu, B., Qu, C., Zhang, H., Guo, W., Liang, Z., et al. (2018). Tailoring biomass-derived carbon for high-performance supercapacitors from controllably cultivated algae microspheres. *J. Mater. Chem. A* 6, 1523–1530. doi: 10.1039/C7TA09608A

Conflict of Interest: The authors declare that the research was conducted in the absence of any commercial or financial relationships that could be construed as a potential conflict of interest.

Advantages of publishing in Frontiers

OPEN ACCESS
Articles are free to read for greatest visibility and readership

FAST PUBLICATION
Around 90 days from submission to decision

HIGH QUALITY PEER-REVIEW
Rigorous, collaborative, and constructive peer-review

TRANSPARENT PEER-REVIEW
Editors and reviewers acknowledged by name on published articles

Frontiers
Avenue du Tribunal-Fédéral 34
1005 Lausanne | Switzerland

Visit us: www.frontiersin.org
Contact us: info@frontiersin.org | +41 21 510 17 00

REPRODUCIBILITY OF RESEARCH
Support open data and methods to enhance research reproducibility

DIGITAL PUBLISHING
Articles designed for optimal readership across devices

FOLLOW US
@frontiersin

IMPACT METRICS
Advanced article metrics track visibility across digital media

EXTENSIVE PROMOTION
Marketing and promotion of impactful research

LOOP RESEARCH NETWORK
Our network increases your article's readership